

# UC Riverside

## UC Riverside Electronic Theses and Dissertations

### Title

Analysis of Molecular Cargos in Single Extracellular Vesicle for Identification of Disease-Relevant Vesicles as Liquid Biopsy Markers

### Permalink

<https://escholarship.org/uc/item/8v7051j3>

### Author

Guo, Kaizhu

### Publication Date

2021

Peer reviewed|Thesis/dissertation

UNIVERSITY OF CALIFORNIA  
RIVERSIDE

Analysis of Molecular Cargos in Single Extracellular Vesicle for Identification of  
Disease-Relevant Vesicles as Liquid Biopsy Markers

A Dissertation submitted in partial satisfaction  
of the requirements for the degree of

Doctor of Philosophy

in

Chemistry

by

Kaizhu Guo

September 2021

Dissertation Committee:

Dr. Wenwan Zhong, Chairperson

Dr. Yinsheng Wang

Dr. Haofei Zhang

Copyright by  
Kaizhu Guo  
2021

The Dissertation of Kaizhu Guo is approved:

---

---

---

Committee Chairperson

University of California, Riverside

## Acknowledgement

First, I would like to thank my PhD advisor Dr. Wenwan Zhong for her guidance, support, and encouragement on my research and life. Without her, I can't become who I am today. Her hard-working attitude and full dedication on research always inspire me. I would also like to thank the rest of my dissertation committee members: Dr. Yinsheng Wang and Dr. Haofei Zhang for their help and valuable suggestions during my PhD studies. I would also like to thank the chemistry department, faculty and staff at UCR for their support.

I appreciate the collaborations and help from Dr. Wen Shen, Dr. Emily Wang, Dr. Emma Wilson, Dr. Xinping Cui, Dr. Yadong Yin and Dr. Quan Cheng. I would also like to thank all the members of the Zhong lab, past and present. I would also like to thank all the undergraduates that have worked with me: Allison Win, Erica Sun and Sabrina Sedano.

Lastly, I would like to give my sincere dedication to my family. Their love and support always encourage me to pursue what I love the most.

The material in Chapter 2 was previously published, reprinted with permission from *Angew. Chem. Int. Ed.* **2018**, *57*, 15675-15680. The coauthor, Dr. Wenwan Zhong, directed and supervised the research that formed the basis of this chapter.

The material in Chapter 3 was previously published, reprinted with permission from *Biosens. Bioelectron.* **2021**, *192*, 113502. The coauthor, Dr. Wenwan Zhong, directed and supervised the research that formed the basis of this chapter.

## ABSTRACT OF THE DISSERTATION

Analysis of Molecular Cargos in Single Extracellular Vesicle for Identification of  
Disease-Relevant Vesicles as Liquid Biopsy Markers

by

Kaizhu Guo

Doctor of Philosophy, Graduate Program in Chemistry  
University of California, Riverside, September 2021  
Dr. Wenwan Zhong, Chairperson

Extracellular vesicles (EVs) are membrane-bound vesicles secreted by all cell types and present in various biological fluids. They actively participate in intercellular communication and pathological processes by transporting proteins and nucleic acids between cells; and their molecular cargos may reflect the health status of the cell of origin thus they constitute an emerging target for liquid biopsy in cancer diagnosis. Identifying the molecular cargos of EVs is critical to revealing their biological functions and clinical values, which, however, remains challenging due to their small sizes, high heterogeneity and low quantities of biomolecules carried by each EV.

Herein, we developed a series of methods to amplify the signals from specific EV cargos using DNA nanostructure, and applied these methods to investigate the expression levels of various protein and miRNA targets in individual EV. In Chapter 2, we developed a single-EV flow cytometry analysis approach to realize single EV counting and

phenotyping in a conventional flow cytometer for the first time. This method employs target-initiated engineering of DNA nanostructures on each EV. By illuminating multiple markers on single EVs, statistically significant differences are revealed among the molecular signatures of EVs originating from several breast cancer cell lines, and the cancer cell-derived EVs among the heterogeneous EV populations are successfully recognized.

In Chapter 3, we developed an ultrasensitive method to detect single EVs with an input as low as 100 vesicles/ $\mu$ L using fluorescence microscopy. Taking advantage of both DNA nanostructure labeling and EV membrane staining, this method can also permit calibration-free analysis of the protein profiles among different EV samples, leading to clear EV differentiation by their cell of origin. Moreover, this method allows simple co-localization of dual protein markers on the same EV, and the increased number of EVs carrying dual tumor proteins present in human serum could differentiate cancer patients from healthy controls at the early developmental stage.

In Chapter 4, we developed a method to detect the miRNA cargos enclosed in individual EVs. This method employs nano-stir bars (NSB) for rapid EV capture and isolation from biological fluids. They also permit confinement of miRNA cargos from the same EV onto the same NSB. In this way, DNA nanostructures can be constructed upon recognition of specific miRNA targets for analysis of the miRNA cargos carried by each EV. Again, EV differentiation by their cell of origin can be simply achieved by evaluating the exosomal miRNAs expression profiles among different EV samples. Moreover, our method can provide real-time monitoring of EV secretion and the enclosed miRNA cargos

in cell culture medium, facilitating analysis of EV biogenesis and functions. Overall, I developed various DNA nanostructure based methods for single EV analysis.



## Table of Contents

<b>Acknowledgement</b> .....	<b>iv</b>
<b>ABSTRACT OF THE DISSERTATION</b> .....	<b>v</b>
<b>List of Figures</b> .....	<b>x</b>
<b>List of Tables</b> .....	<b>xix</b>
<b>Chapter 1: Biomarkers Targeted in Liquid Biopsy and Their Detection</b> .....	<b>1</b>
1.1    Liquid biopsy .....	1
1.2    Biomarkers .....	4
1.3    Extracellular Vesicle Classification, Biogenesis and Function .....	8
1.4    Analytical Techniques for Detection of Exosomes and Exosomal Cargos .....	12
1.4.1    Analysis of Exosomal Proteins .....	13
1.4.2    Single Exosome Analysis Based on Protein Contents .....	19
1.4.3    Analysis of Exosomal MicroRNA .....	23
1.5    Signal Amplification Enabling Biomarker Detection.....	33
1.6    Summary .....	37
1.7    Reference .....	39
<b>Chapter 2: A Single Extracellular Vesicle (EV) Flow Cytometry Approach to Reveal EV Heterogeneity</b> .....	<b>47</b>
2.1    Introduction.....	47
2.2    Material and Methods .....	49
2.3    Results and Discussion .....	53
2.4    Conclusion .....	82

2.5	Reference .....	83
<b>Chapter 3: Calibration-Free Analysis of Surface Proteins on Single Extracellular Vesicles Enabled by DNA Nanostructure..... 85</b>		
3.1	Introduction.....	85
3.2	Material and Methods .....	87
3.3	Results and Discussion .....	92
3.4	Conclusion .....	124
3.5	Reference .....	126
<b>Chapter 4: Nano-Stir Bar-Assisted Analysis of microRNAs in Single Extracellular Vesicle..... 129</b>		
4.1.	Introduction.....	129
4.2.	Material and Methods .....	131
4.3.	Results and Discussion .....	137
4.4.	Conclusion .....	167
4.5.	Reference .....	169
<b>Chapter 5: Conclusion and Future Outlook..... 172</b>		
5.1	Conclusion .....	172
5.2	Future Outlook .....	173
5.3	Reference .....	180

## List of Figures

Figure 1.1 Cancer cells and normal cells .....	1
Figure 1.2 Circulating biomarkers in patients with cancer .....	3
Figure 1.3 Advantages and disadvantages of tumor biopsy versus liquid biopsy .....	3
Figure 1.4 Central Dogma.....	5
Figure 1.5 The ‘linear’ canonical pathway of microRNA processing .....	6
Figure 1.6 Extracellular vesicle-mediated cell-cell communication.....	8
Figure 1.7 Number of publications returned from a search on Web of Science with the key word .....	9
Figure 1.8 Main classes of extracellular vesicles.....	10
Figure 1.9 Biogenesis of extracellular vesicles.....	11
Figure 1.10 Biogenesis, secretion, composition, and application of exosomes as liquid biopsy.....	12
Figure 1.11 Composition and structure of extracellular vesicles.....	14
Figure 1.12 Western blotting .....	15
Figure 1.13 ELISA.....	16
Figure 1.14 Mass spectrometry .....	17
Figure 1.15 Flow cytometry.....	18
Figure 1.16 Three primary output measurements of flow cytometry .....	19
Figure 1.17 Confocal microscopy .....	21
Figure 1.18 Single EV analysis (SEA) strategy .....	21
Figure 1.19 Design and workflow of proximity-dependent barcoding assay (PBA) .....	22

Figure 1.20 Aptamer-based DNA nanodevices (ABDN) -based total-internal-reflection-fluorescence (TIFR) assay .....	<b>23</b>
Figure 1.21 Schematic of protein and RNA transfer by extracellular vesicles.....	<b>25</b>
Figure 1.22 Transfer of EV-derived miRNA from donor cell to recipient cells.....	<b>26</b>
Figure 1.23 Northern blotting .....	<b>27</b>
Figure 1.24 miRNA sequencing procedure .....	<b>28</b>
Figure 1.25 Schematic of exosomal miRNA <i>in situ</i> detection by SERS biosensor and Fe <sub>3</sub> O <sub>4</sub> @TiO <sub>2</sub> concentration.....	<b>30</b>
Figure 1.26 <i>in situ</i> detection of exosomal miR-21 using MB for the diagnosis of diseases such as cancer .....	<b>31</b>
Figure 1.27 <i>in situ</i> analysis of exosomal miRNAs by split DNAzyme probe .....	<b>31</b>
Figure 1.28 Nano-bio chip integrated system for liquid biopsy (HNCIB) system for simultaneous detection of membrane protein and mRNA in a single EV .....	<b>32</b>
Figure 1.29 Schematic illustration of the virus-mimicking fusogenic vesicles (Vir-FVs) for the rapid detection of exosomal miRNAs .....	<b>33</b>
Figure 1.30 PCR.....	<b>35</b>
Figure 1.31 Hybridization Chain Reaction .....	<b>36</b>
Figure 1.32 Rolling Circle Amplification.....	<b>37</b>
Scheme 2.1 The Single Extracellular Vesicle Flow Cytometry Analysis Technique enabled by Target-Initiated Engineering of DNA Nanostructures .....	<b>48</b>
Figure 2.1 Hybridization cascade 1 for CD63 .....	<b>55</b>
Figure 2.2 Analysis of the long DNA products by gel electrophoresis .....	<b>55</b>

Figure 2.3 TEM images .....	57
Figure 2.4 AFM images .....	58
Figure 2.5 Size distribution of EVs obtained at various duration of DNA hybridization (0 – 24 hrs) evaluated by NTA.....	59
Figure 2.6 Fluorescence microscopy image of the Engr.EV tagged with rhodamine-nanoparticles or QDs-525 .....	60
Figure 2.7 Fluorescence microscopy images of HCR products and engineered EV .....	61
Figure 2.8 Representative scatter plots and histograms of flow cytometry analysis of the EVs before and after TIE .....	63
Figure 2.9 Representative scatter plots of flow cytometry analysis of the negative controls .....	64
Figure 2.10 Investigation of effects on signal intensity and particle counting from the duration of EV engineering.....	68
Figure 2.11 Investigation of EV engineering at varied duration and self-quenching possibility .....	70
Figure 2.12 The linearity range of our method for standard EV quantification .....	70
Figure 2.13 EV counting by TIE in the EV-free FBS and human serum .....	72
Figure 2.14 Treatment of human serum with sodium citrate (SC) helped to inhibit nuclease activity and kept the DNA probes intact for 8 hours .....	74
Figure 2.15 Hybridization cascade 2 for HER2 .....	77
Figure 2.16 Single hybridization cascade system for detection of CD63 or HER2 .....	77
Figure 2.17 ELISA measurement of protein contents .....	78

Figure 2.18 Hybridization cascade system for recognition of two markers .....	<b>79</b>
Figure 2.19 Flow cytometric analysis of engineered EVs prepared with the dual hybridization cascade system.....	<b>79</b>
Figure 2.20 Flow cytometric analysis of the mixture of EVs from MCF-10A and SKBR3 using TIE-EV .....	<b>82</b>
Scheme 3.1 Schematic illustration of dual-color detection of single EV by dye staining and DNF tagging.....	<b>87</b>
Figure 3.1 Schematic illustration of RCA and analysis of RCA product by gel electrophoresis .....	<b>96</b>
Figure 3.2 AFM and SEM images for RCA product. ....	<b>97</b>
Figure 3.3 NTA analysis of RCA product size distribution in various RCA reaction time (0-5.5 hours).....	<b>98</b>
Figure 3.4 Real-time fluorescence of RCA with (red) and without (black) initiator probe added.....	<b>99</b>
Figure 3.5 RCA efficiency in different ratio of dATP to biotin-dATP added to the reaction mixture, tested by (A) 1.5% native agarose gel and (B) represented by the fluorescence intensity detected in the wells .....	<b>99</b>
Figure 3.6 NTA analysis of EV size distribution with AFM and TEM image of EV ....	<b>101</b>
Figure 3.7 Representative fluorescence microscopy images of the EVs labeled with various dyes .....	<b>101</b>
Figure 3.8 Sensitivity and selectivity test of our assay .....	<b>103</b>

Figure 3.9 Correlation between the EV particle count obtained by DiO-staining (black) or DNF-labeling (specific to HER2) (grey) and the EV input concentration, both in log scale. HER2 recognition was mediated by the anti-HER2 aptamer .....	<b>104</b>
Figure 3.10 Representative CFM images of different samples.....	<b>106</b>
Figure 3.11 Average particle count per image of found in EV samples labeled with the DNFs originated from the direct Ab-DNA conjugation and the aptamer assisted conjugation.....	<b>107</b>
Figure 3.12 Detection of EVs using dual color labeling by antibodies .....	<b>108</b>
Figure 3.13 Comparison of the expression profiles, represented by the particle ratios, of 5 protein markers in the EVs derived from COLO-1 cells .....	<b>110</b>
Figure 3.14 Representative CFM images of the COLO-1-derived EVs labeled with the DNFs specific to CD63, CD9, HER2, EGFR and CD44.....	<b>111</b>
Figure 3.15 Protein profiling using EV engineering.....	<b>112</b>
Figure 3.16 Comparison of the expression profiles .....	<b>113</b>
Figure 3.17 Representative CFM images of the PC-3-derived EVs labeled with the DNFs specific to CD63, CD9, HER2, EGFR and CD44 .....	<b>114</b>
Figure 3.18 Representative CFM images of the A549-derived EVs labeled with the DNFs specific to CD63, CD9, HER2, EGFR and CD44 .....	<b>115</b>
Figure 3.19 Representative CFM images of the MCF-7-derived EVs labeled with the DNFs specific to CD63, CD9, HER2, EGFR and CD44 .....	<b>115</b>
Figure 3.20 Representative CFM images of the MDA-MB-231-derived EVs labeled with the DNFs specific to CD63, CD9, HER2, EGFR and CD44.....	<b>116</b>

Figure 3.21 Representative CFM images of the PDX-derived EVs labeled with the DNFs specific to CD63, CD9, HER2, EGFR and CD44 .....	117
Figure 3.22 Particle count of the EGFR <sup>-</sup> /HER2 <sup>-</sup> EVs, EGFR <sup>+</sup> /HER2 <sup>-</sup> EVs, EGFR <sup>-</sup> /HER2 <sup>+</sup> EVs and EGFR <sup>+</sup> /HER2 <sup>+</sup> EVs obtained with the dual marker colocalization assay.....	119
Figure 3.23 Comparison of the ratio of P <sub>DNF</sub> /P <sub>DiO</sub> obtained from single or dual DNF labeling targeting HER2 and EGFR .....	120
Figure 3.24 Comparison of the ratio of P <sub>DNF</sub> /P <sub>DiO</sub> obtained by detecting the single EVs using DNFs specific to HER2, EGFR, and CD44 in the serum samples collected from breast cancer patients (C) and healthy controls (H).....	121
Figure 3.25 Profiling of EV from serum samples.....	122
Figure 3.26 Particle count of the DiO-stained EVs in the serum samples from breast cancer patients and healthy controls.....	123
Figure 3.27 EV detection by DNF labeling targeting HER2 and CD44, respectively in the serum samples from cancer patients and healthy controls .....	124
Scheme 4.1 Schematic of Exosomal miRNA <i>In Situ</i> Detection by Nano-stir Bar Isolation and DNA Nanoflower Biosensor .....	131
Figure 4.1 TEM images of the FeOOH nanorods, magnetic Fe <sub>3</sub> O <sub>4</sub> NSB@SiO <sub>2</sub> and Fe <sub>3</sub> O <sub>4</sub> NSB@SiO <sub>2</sub> -COOH.....	139
Figure 4.2 Size distribution of Fe <sub>3</sub> O <sub>4</sub> NSB@SiO <sub>2</sub> -COOH .....	139
Figure 4.3 Dye diffusion in a 10-μL droplet with or without NSB spinning.....	140
Figure 4.4 Fluorescence intensity of the fluorescein-labeled streptavidin captured by the biotinylated IgG conjugated to the NSB under different solution agitation conditions .	140



Figure 4.5 AFM images of nano stir bar before and after EV capture .....	<b>142</b>
Figure 4.6 Detectable particle count of EV labeled with CD63-specific DNF under stirring and without stirring, respectively.....	<b>142</b>
Figure 4.7 Detectable particle count of CD63 blocked-EV labeled with CD63-specific DNF under stirring or without stirring.....	<b>143</b>
Figure 4.8 Pixel size of fluorescence microscopy images with and without NSB for protein detection .....	<b>144</b>
Figure 4.9 Fluorescence intensity for RCA reaction by incubating hairpin probes of various stem length with target or without target .....	<b>146</b>
Figure 4.10 Specificity of RCA reaction targeting miR-155 using different target probes .....	<b>148</b>
Figure 4.11 Pixel size of fluorescence microscopy images with flat surface or with NSB for exosomal miRNA detection .....	<b>149</b>
Figure 4.12 Effect of PFA fixation and EDC crosslinking for miRNA <i>in situ</i> detection	<b>151</b>
Figure 4.13 Optimization of EDC crosslinking time for miRNA <i>in situ</i> detection .....	<b>151</b>
Figure 4.14 Representative fluorescence microscopy images for EDC crosslinking time optimization .....	<b>152</b>
Figure 4.15 Optimization of EDC crosslinking concentration for miRNA <i>in situ</i> detection .....	<b>152</b>
Figure 4.16 Representative fluorescence microscopy images for EDC crosslinking concentration optimization.....	<b>152</b>

Figure 4.17 Detectable particle count for EV staining by membrane dye DiB in different time points.....	<b>153</b>
Figure 4.18 Particle ratio for EV staining by membrane dye DiB in different time points .....	<b>154</b>
Figure 4.19 Representative fluorescence microscopy imaging of EV staining by membrane dye, DiB in different time points .....	<b>154</b>
Figure 4.20 Detectable particle count for DiB concentration Optimization for miRNA <i>in situ</i> detection .....	<b>155</b>
Figure 4.21 Particle ratio for DiB concentration optimization for miRNA <i>in situ</i> detection .....	<b>155</b>
Figure 4.22 Pixel size of detectable particles under various DiB concentration .....	<b>156</b>
Figure 4.23 Representative fluorescence microscopy imaging of EV staining by various DiB concentration .....	<b>156</b>
Figure 4.24 Sensitivity test of our assay for miR-155 <i>in situ</i> detection.....	<b>158</b>
Figure 4.25 The particle counts obtained from counting the DiB-stained or the miR-155 specific DNF-tagged EVs at different EV concentrations .....	<b>159</b>
Figure 4.26 Sensitivity and specificity test of our assay for miR-122 <i>in situ</i> detection .	<b>160</b>
Figure 4.27 The particle counts obtained from counting the DiB-stained or the miR-122 specific DNF-tagged EVs at different EV concentrations .....	<b>161</b>
Figure 4.28 Profiling of miRNA expression in EVs derived from COLO1 cell lines using RT-PCR.....	<b>164</b>

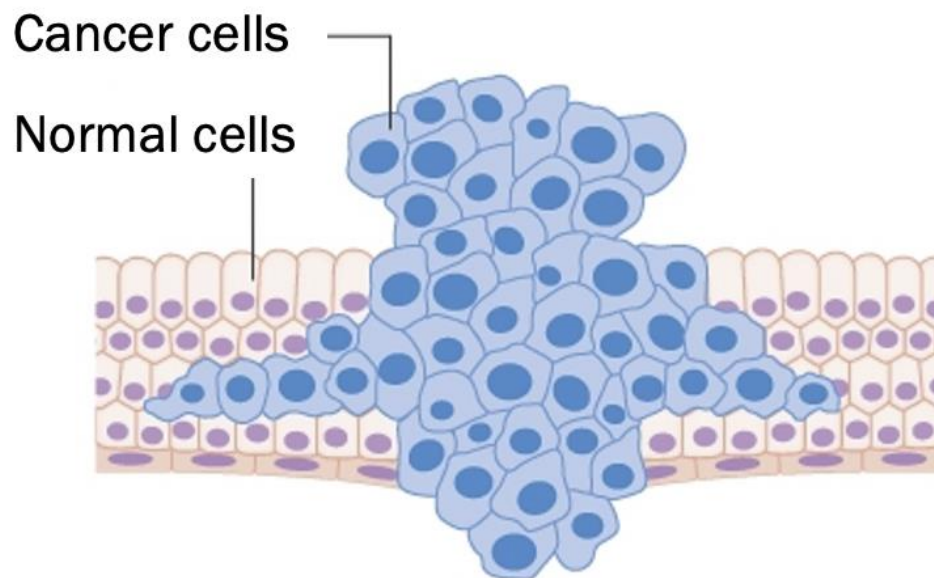
Figure 4.29 Profiling of miRNA expression in EVs derived from COLO1 cell lines using our assay.....	<b>164</b>
Figure 4.30 Profiling of miR-122 expression in CD81 <sup>+</sup> /CD63 <sup>+</sup> /CD9 <sup>+</sup> EVs derived from PDX cell lines with various treatment using our assay.....	<b>165</b>
Figure 4.31 Profiling of miR-122 expression in CD24 <sup>+</sup> EVs derived from PDX cell lines with various treatment using our assay .....	<b>166</b>
Figure 4.32 Profiling of time-based miR-122 expression in cell culture medium of three cell lines using our assay.....	<b>167</b>
Figure 5.1 FCA sort and collect cell based on surface marker profiles .....	<b>174</b>
Figure 5.2 Schematic of AF4-NTA coupling immunoassay .....	<b>175</b>
Figure 5.3 Contour plots showing the single populations and mixed population injections .....	<b>176</b>
Figure 5.4 Protein profiling of EV derived from COLO1 cell lines before and after AF4 separation .....	<b>176</b>
Figure 5.5 Schematic of microfluidic-integrated biosensor for real-time analysis of live cell secretion .....	<b>177</b>
Figure 5.6 Schematic of microfluidic device for automation .....	<b>178</b>
Figure 5.7 Schematic of droplet microfluidic platform .....	<b>179</b>

## List of Tables

Table 2.1 DNA sequences used in TIE system for CD63.....	<b>54</b>
Table 2.2 Readings for the measurements displayed in Figure 2.8 and Figure 2.9 .....	<b>65</b>
Table 2.3 Assessment of measurement reproducibility using TIE for EV engineering ...	<b>71</b>
Table 2.4 DNA sequences used in TIE system for HER2 .....	<b>76</b>
Table 3.1 DNA sequences used in this study.....	<b>95</b>
Table 4.1 DNA sequences used in our system for miR-155 and miR-122.....	<b>147</b>
Table 4.2 Target miRNA sequences used.....	<b>162</b>
Table 4.3 DNA sequences for hairpin probes used in our system .....	<b>163</b>

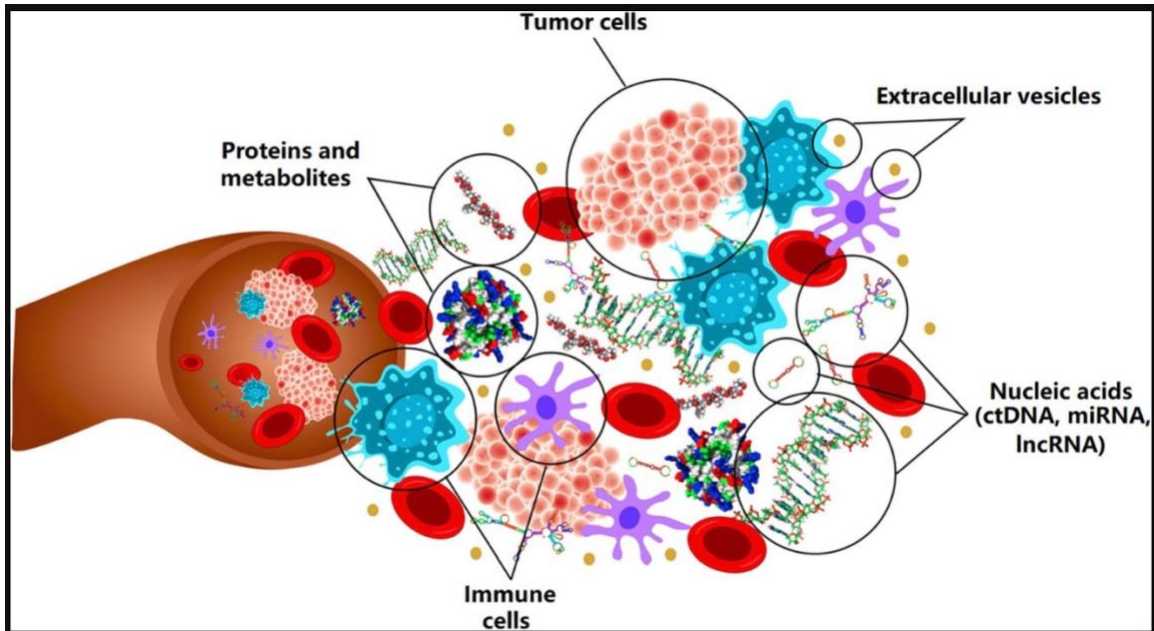
## 1.1 Liquid biopsy

Cancer, the abnormal and uncontrolled growth of cells (Figure 1.1), is one of the leading causes of death in the world, killing nearly 1700 people every day in the United States.<sup>1, 2, 3</sup> Most cancer is detected in late stages, when it is too late for many treatment options to be effective.<sup>4</sup> Therefore, early detection and treatment advances could improve the survival rate and reduce cancer mortality.<sup>5, 6, 7</sup> Tissue biopsy is the conventional approaches in cancer diagnosis and prognosis, relying on biopsy procedures to collect tissues and analyze the pathological signals displayed by the samples.<sup>8</sup> However, tissue biopsy is invasive to patients, and some tumors are not easily accessible.<sup>9</sup> Moreover, tissue biopsy requires long and complex protocols to analyze the solid tissues, which is impractical for early cancer diagnosis.<sup>10</sup>


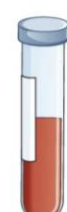


**Figure1.1 Cancer cells and normal cells.** Figure reprinted from Ref.1.

Cancer cells could shred or purposely release tumor-specific molecules into the biological fluids to communicate with other cells; or even the cancer cells can be found as a rare population in the circulation systems.<sup>11</sup> The tumor-related molecules found in the circulation systems include tumor nucleic acids and RNA, extracellular vesicles (EVs), tumor-educated platelets (TEPs) and tumor proteins (Figure 1.2).<sup>12, 13, 14, 15</sup> Derived from the tumor cells, these molecules have the potential to provide information about the tumor cells.<sup>16</sup> So instead of directly detecting the tumor cells, we can detect these tumor-specific analytes in the easily accessible biological fluids, such as blood. This is called liquid biopsy.<sup>17</sup> Performing a liquid biopsy requires collecting biofluids, including blood, urine, saliva, breast milk, and cerebrospinal, synovial, or amniotic fluids.<sup>18</sup> Compared to conventional tissue biopsy, liquid biopsy is safer, less invasive and more convenient to repeat at multiple time intervals (Figure 1.3).<sup>19</sup> Therefore, liquid biopsy could greatly benefit cancer diagnosis, prognosis and treatment supervision by monitoring the levels of the tumor-specific analytes in biofluids, to realize tracking the evolutionary dynamics and heterogeneity of tumors over time, and revealing the very early emergence of therapy resistance, residual disease and recurrence.<sup>20</sup>



**Figure 1.2** Circulating biomarkers in patients with cancer. Figure reprinted from Ref.21.

		At metastatic diagnosis	After subsequent lines of therapy
Tumor biopsy 	Advantages	<ul style="list-style-type: none"> <li>• Key pathological information</li> <li>• Ability to assess non-DNA biomarkers (protein, RNA, etc)</li> </ul>	<ul style="list-style-type: none"> <li>• Important for research and discovery</li> <li>• Critical if assessment of non-DNA biomarkers needed</li> </ul>
	Disadvantages	<ul style="list-style-type: none"> <li>• Longer turnaround time for sequencing limits first-line precision-therapy selection</li> <li>• Limited tissue quantities can constrain breadth of testing or cause assay failure</li> </ul>	<ul style="list-style-type: none"> <li>• Requires repeat invasive procedure</li> <li>• Longer turnaround time for sequencing results may hinder rapid selection of therapy</li> </ul>
Liquid-biopsy cfDNA 	Advantages	<ul style="list-style-type: none"> <li>• High concordance with tissue biopsy</li> <li>• Ready sample availability</li> <li>• Rapid turnaround to facilitate first-line precision-oncology therapies</li> <li>• Baseline for subsequent liquid biopsy</li> </ul>	<ul style="list-style-type: none"> <li>• Non-invasive, easy to obtain serial samples</li> <li>• Captures heterogeneous resistance alterations</li> <li>• Rapid turnaround can enhance clinical-trial enrollment</li> </ul>
	Disadvantages	<ul style="list-style-type: none"> <li>• Parallel assessment with tumor testing increases cost</li> <li>• Cannot assess non-DNA biomarkers</li> </ul>	<ul style="list-style-type: none"> <li>• Cannot assess non-DNA biomarkers</li> </ul>

**Figure 1.3** Advantages and disadvantages of tumor biopsy versus liquid biopsy. Figure reprinted from Ref.19. © 2020, Springer Nature.

## 1.2 Biomarkers

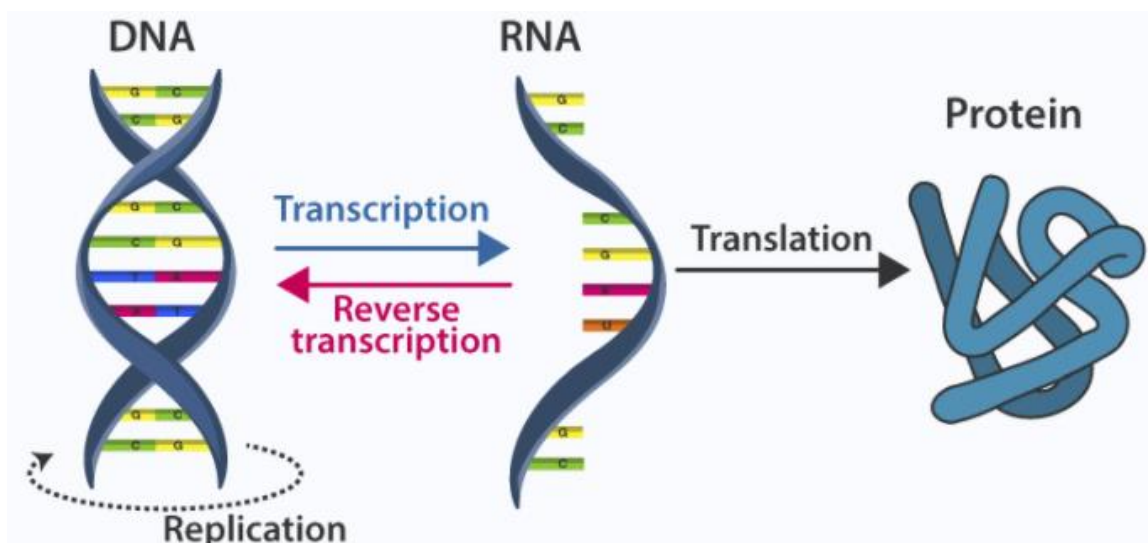
Biological markers (biomarkers) are defined as any substance, structure, or process that can both be measured in the body, and influence or predict the incidence of outcome or disease.<sup>22, 23</sup> They could also be used as an indicator of disease stages, as well as a predictor of pharmacological responses to a therapeutic intervention.<sup>24, 25</sup> As mentioned above, the tumor-specific cells, proteins, nucleic acids and extracellular vesicles secreted into biological fluids have all been considered as promising biomarkers for liquid biopsy.

Proteins are large, complex molecules that encoded by the genes. They are one of the indispensable parts of the structure, function and regulation of the body's tissues and organs.<sup>26</sup> Proteins secreted from different cellular organs play an important role in normal cell mechanisms and signaling.<sup>27, 28</sup> The up or down regulation of protein levels, or alternations of protein functions and distributions, affect cell metabolism and physiology, cell growth and death.<sup>29</sup> Therefore, proteins have become a promising biomarker category for cancer diagnosis.

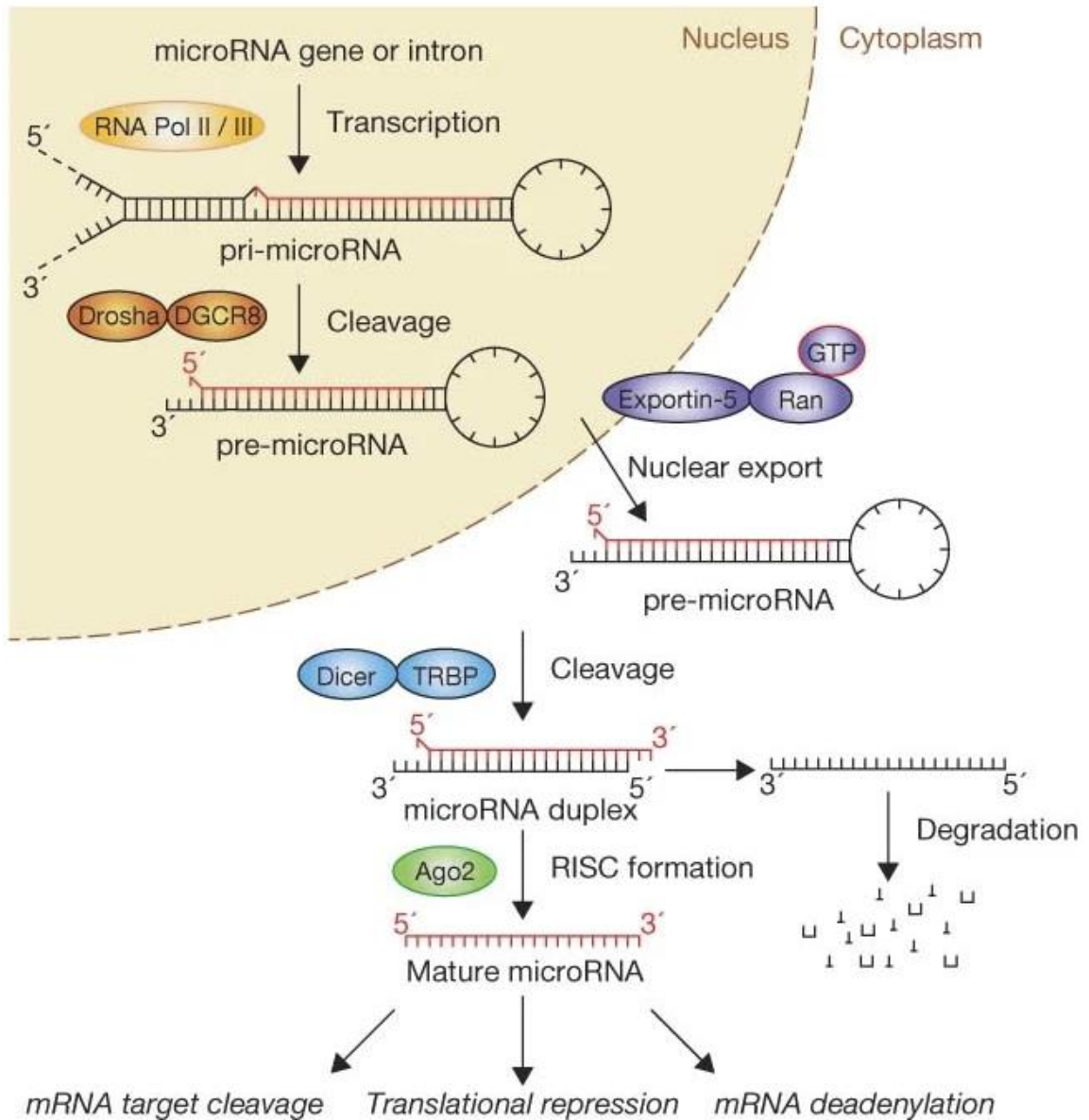
Another promising biomarker family is microRNAs (miRNA), owing to their important regulatory roles in gene expression.<sup>30, 31</sup> In the central dogma, the DNA sequence of a gene is first transcribed into messenger RNA (mRNA). The sequence of mRNA is decoded to specify the amino acid sequence of the protein (Figure 1.4).<sup>32</sup> miRNAs are small noncoding RNAs with a length of 19 – 25 nucleotides. The biogenesis of miRNA is illustrated in Figure 1.5. The miRNA genes are firstly transcribed into primary miRNAs (pri-miRNAs) by RNA polymerase II (pol II).<sup>33, 34</sup> These pri-miRNAs contain a specific hairpin-shaped stem-loop structure that has an embedded miRNA sequence.<sup>35</sup> After



transcription, two-step cleavage of pri-miRNAs would generate mature miRNA.<sup>36, 37</sup> The mature miRNAs could bind to the complementary target messenger RNA (mRNA), which could induce mRNA target cleavage, translational repression or mRNA deadenylation, thereby becoming a crucial part of post transcriptional regulation of mRNA expression.<sup>38</sup> miRNAs are small noncoding RNAs that could bind to the target mRNA through complementary hybridization.<sup>39</sup> In this way, miRNAs could induce either translation repression or degradation of their mRNA targets, thereby becoming a crucial part of post transcriptional regulation of mRNA expression.<sup>40</sup> The abnormal miRNA expression would affect their interactions with mRNA target or dysregulate some crucial pathway, leading to uncontrollable cell growth, which make miRNA a promising biomarker.<sup>41, 42, 43</sup>



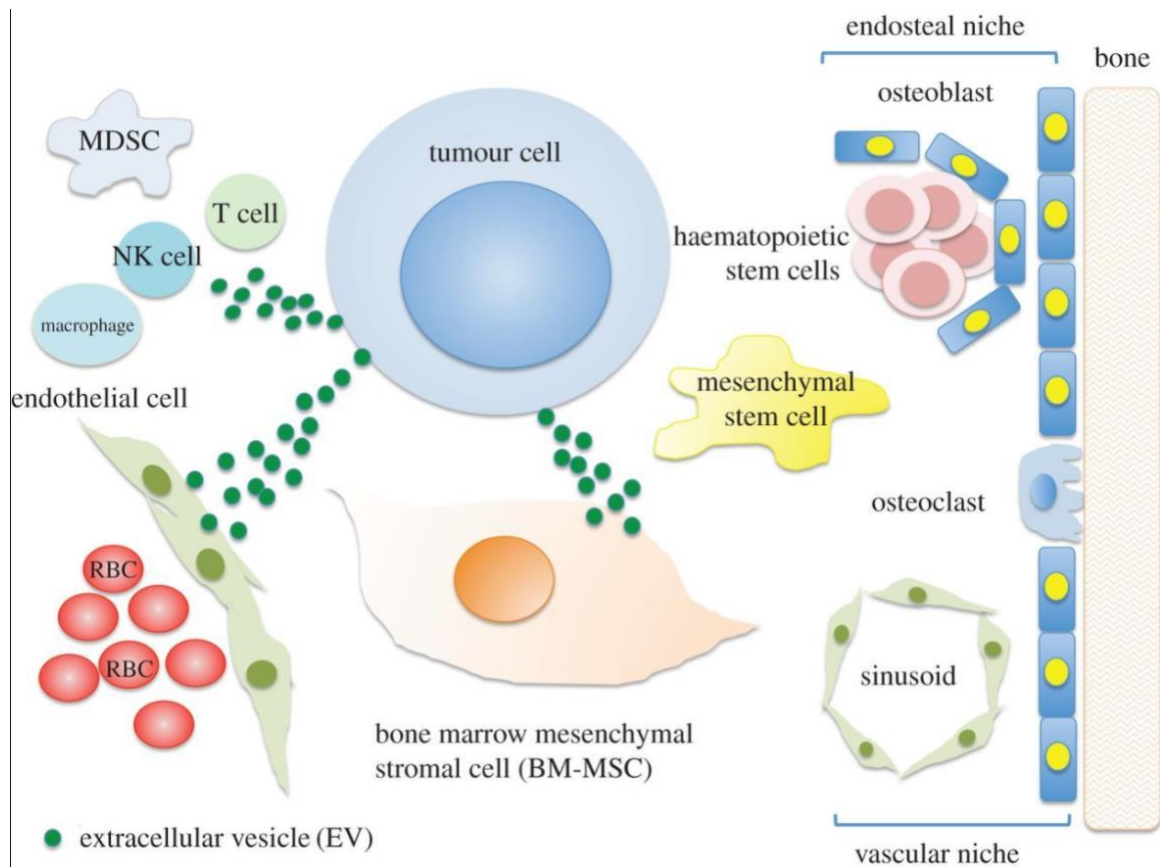
**Figure 1.4 Central Dogma.** Figure reprinted from Ref.32.



**Figure 1.5 The ‘linear’ canonical pathway of microRNA processing.** Figure reprinted from Ref.34. © 2009, Springer Nature.

Extracellular vesicles are an emerging group of biomarkers, the important roles of which in cancer development have been more and more recognized in recent years. Different than proteins and miRNAs, EVs are nano-sized membrane-bound particles secreted by nearly all types of cells that carry diverse molecular cargos like proteins, lipids,

as well as nucleic acids, and transport them from cell to cells, acting as important mediators for intercellular communication (Figure 1.6).<sup>44</sup> EVs released from parental cells could be taken up by other cells, thus carrying the potential to influence the tumor-related functions, such as malignant formation, tumor progression, metastasis and drug resistance, through the release of the functional cargos like miRNAs to the recipient cells. Compared to other cell-free, molecular biomarkers, EV cargos are more stably present in circulation owing to the membrane protection; and one tumor cell can release many EVs, enhancing the chance of their identification through liquid biopsy. Moreover, one EV can contain multiple markers, and detection of the tumor-derived EV is equivalent to identification of a collection of effective tumor markers, which has been found to work more effectively than using a single marker in disease diagnosis and prognosis. These advantages make EV a better biomarker category for liquid biopsy than individual proteins and miRNAs. Thus, the following sections of this chapter are devoted to discussion of EV biogenesis, functions, and potential roles in disease development, as well as the current methods for EV identification and content analysis.

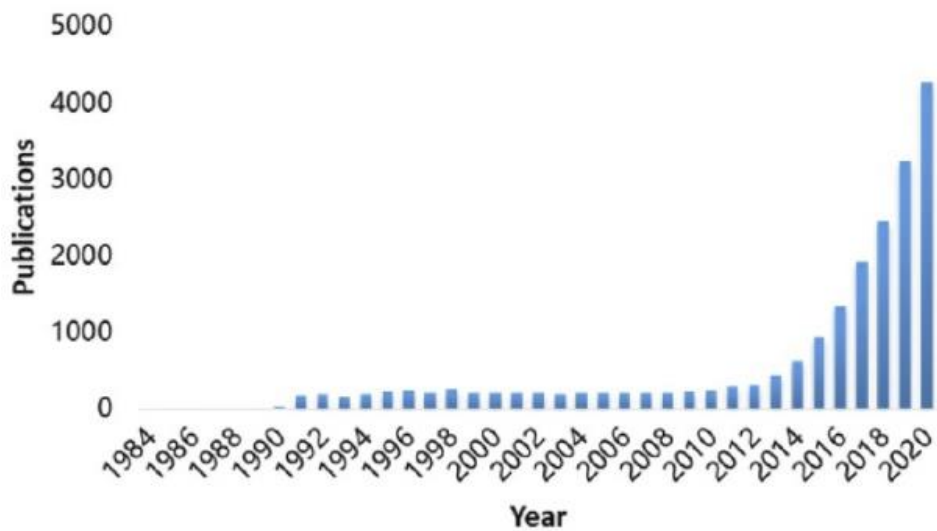


**Figure 1.6 Extracellular vesicle-mediated cell-cell communication.** Figure reprinted from Ref.44. © 2017, Royal Society.

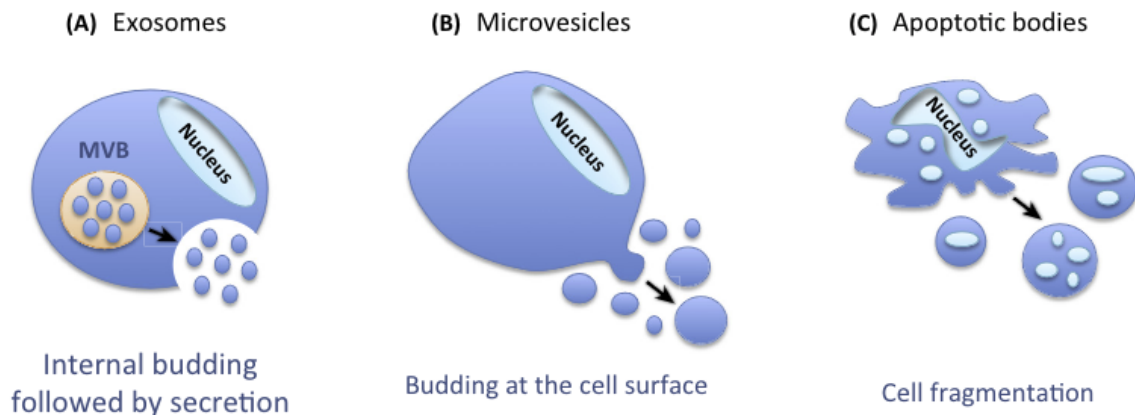
### 1.3 Extracellular Vesicle Classification, Biogenesis and Function

Extracellular vesicles were first discovered in 1946. Early studies treated extracellular vesicles as the cell trash cans for disposing unwanted membrane proteins to maintain cellular health.<sup>45</sup> With more works devoted to EVs, more of the EV functions that go beyond that of discarding proteins, such as acting as messengers for intercellular communication, have been revealed, raising intense research interest. Over the past decade, there has been an exponential rise in EV-related studies in the field of cancer biology (Figure 1.7).<sup>46</sup> This excitement was initially driven by EVs as potential diagnostic

biomarkers, and later as potential therapeutic targets or carriers. EVs are classified into three subtypes based on their biogenesis, release pathways, size, content and function: exosomes (40-120 nm), microvesicles (200-2000 nm) and apoptotic bodies (500-2000nm) (Figure 1.8).<sup>47, 48</sup> Exosomes are one of the primary types of EV studied in disease diagnosis because of their unique biogenesis pathways.



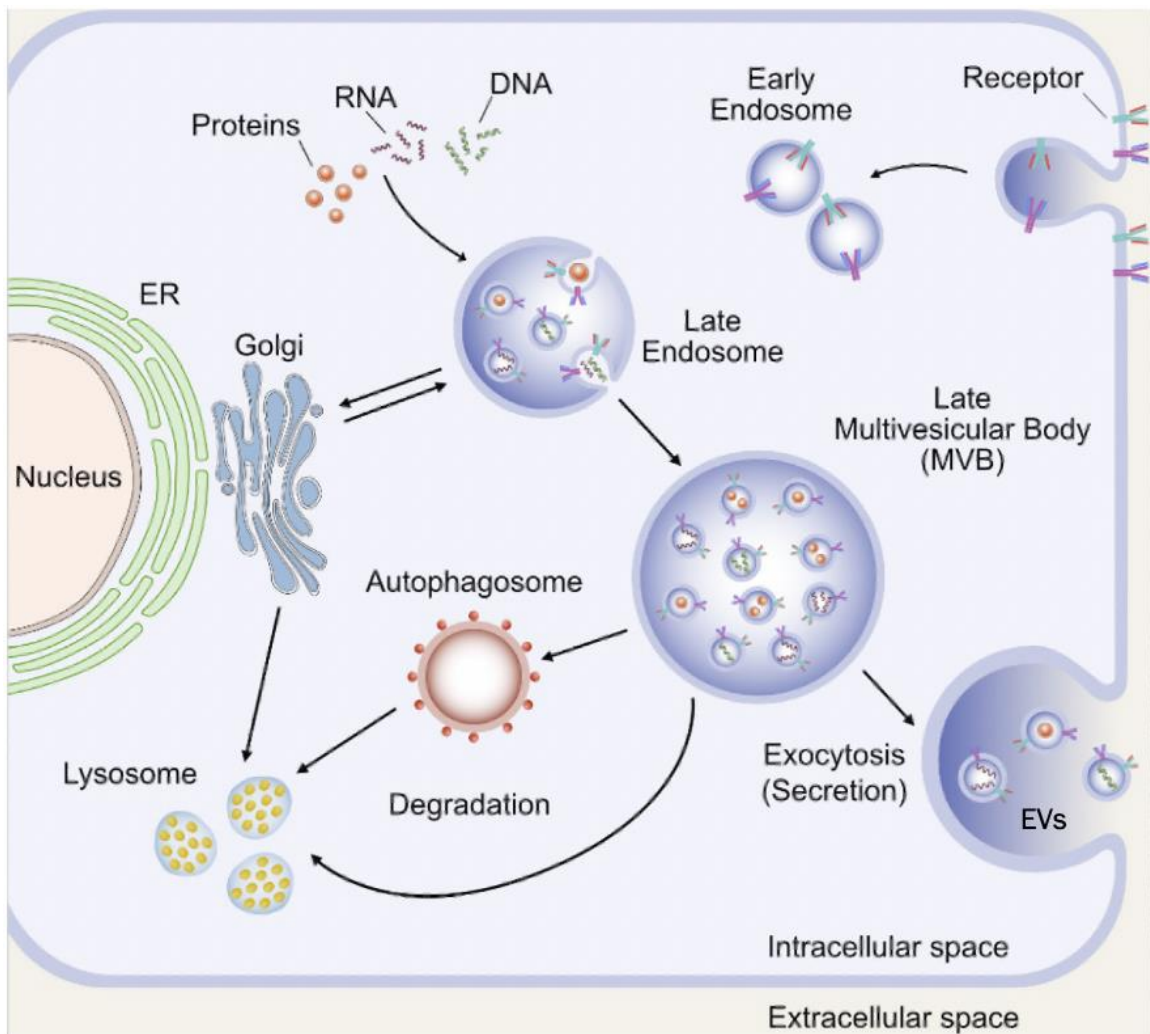
**Figure 1.7** Number of publications returned from a search on Web of Science with the key word “Extracellular Vesicles”. Figure reprinted from Ref.46. © 2021, American Chemical Society.



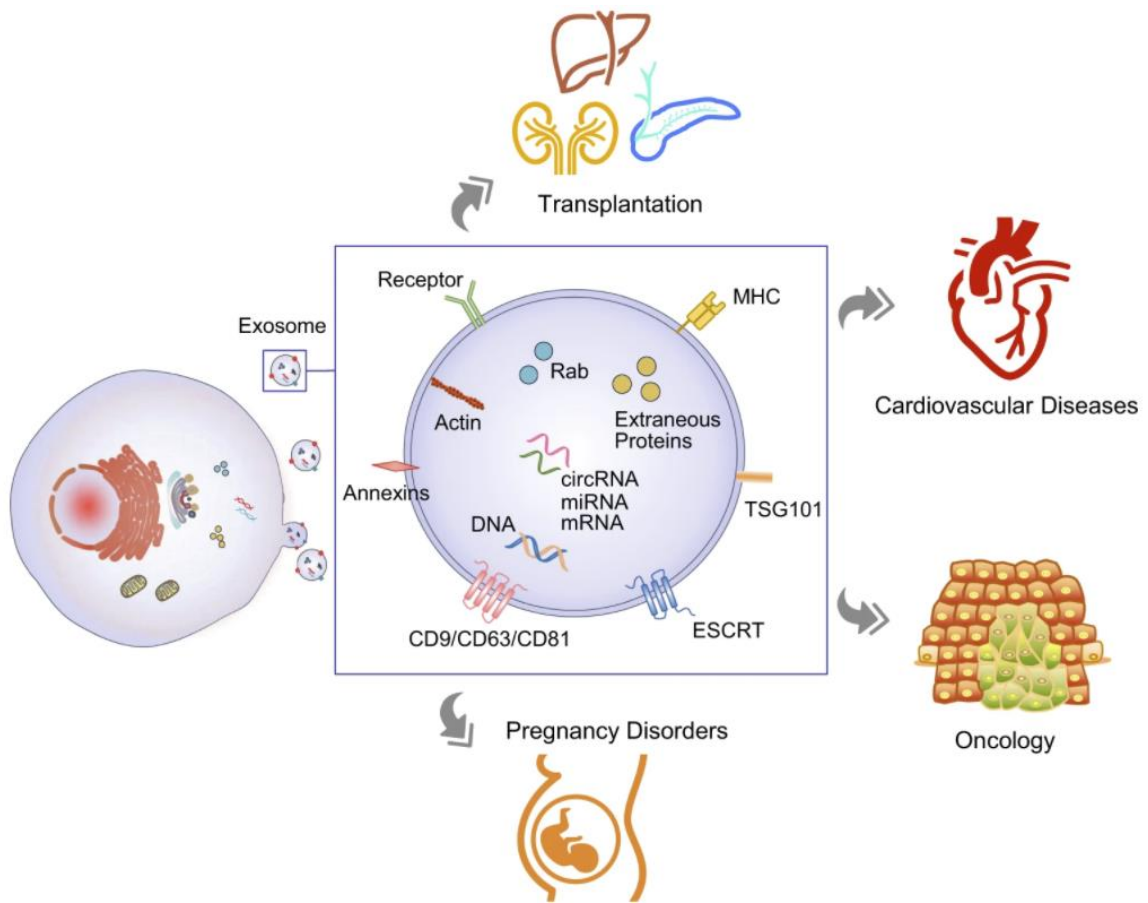
**Figure 1.8 Main classes of extracellular vesicles.** Exosomes are generated by inward budding of endosomal membranes. As these accumulate, they form multivesicular bodies (MVB) that traffic from the cytosol to the cell surface, where they fuse with the cell membrane and release their exosome content to the extracellular space. By contrast, microvesicles (MVs) are formed by outward budding of the plasma membrane. Apoptotic cells release apoptotic bodies (ABs), which are formed by blebbing of the plasma membrane and contain nuclear fragments. Figure reprinted from Ref.47. © 2016, Elsevier.

Exosomes are produced by the endosomal pathway (Figure 1.9).<sup>49</sup> Firstly, endocytic vesicles are produced from the plasma membrane, forming an early endosome. The early endosome subsequently develops into late endosomes. The late endosomes undergo inward budding, leading to the formation and accumulation of intraluminal vesicles inside the lumen, named the multivesicular body (MVB). The MVB merge with lysosome for degradation; otherwise they merge with the plasma membrane, releasing exosomes into extracellular spaces. Based on the biogenesis of exosomes, their protein topology is in the same orientation as in the plasma membrane of cells, which could reflect the origins of the parent cells. In addition, they carry nucleic acids that can regulate gene expression, and proteins and lipids that can participate in specific cellular functions. Therefore, exosome play a critical role in cell-cell communication, and participates in

pathological processes, including immune responses and development of illnesses like cancers, cardiovascular diseases, and pregnancy disorders (Figure 1.10).<sup>50</sup>



**Figure 1.9 Biogenesis of extracellular vesicles.** Figure reprinted from Ref.49.



**Figure 1.10 Biogenesis, secretion, composition, and application of exosomes as liquid biopsy.** Exosomes, originating from the endosomal pathway via the formation of late endosomes or multivesicular bodies, enclose a variable spectrum of molecules characterized by parent cells, including nucleic acids (DNA, mRNA, miRNA, LncRNA, circRNA, etc.), proteins, and lipids, which shows great promise in clinical application in cancer, pregnancy disorders, cardiovascular diseases and organ transplantation. Figure reprinted from Ref.50.

#### 1.4 Analytical Techniques for Detection of Exosomes and Exosomal Cargos

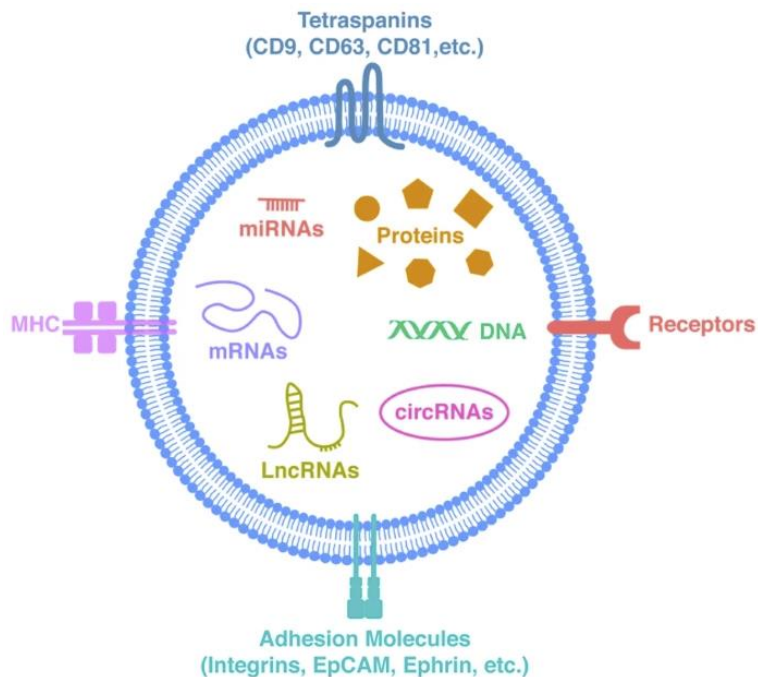
While biomarkers are highly beneficial to cancer diagnosis and treatment decisions, they are largely diluted in the circulation systems, and their presence is very low during the early disease developmental stage. In addition, very few markers have been found to be highly specific, sensitive, and accurate during clinical practices.<sup>51, 52</sup> Therefore, early



cancer diagnosis demands reliable biomarkers and highly sensitive detection technique.<sup>53</sup> The tumor-derived exosomes could carry molecules inherited from the parental cells, potentially reflective to their health state; and the exosomal cargos, in particular, exosomal miRNAs, could be functional molecules that alter the biological processes in the recipient cells, detection of the tumor-derived exosomes and their cargos have been actively pursued for identification of exosome-based biomarkers and development of effective tools for cancer diagnosis. Commonly, method developments target bulk detection of exosomal proteins, nucleic acids, lipids, etc., but recently with the clear recognition of the high heterogeneity of EV populations present in biofluids, more and more development efforts have been geared towards analysis of single exosomes.

#### **1.4.1 Analysis of Exosomal Proteins**

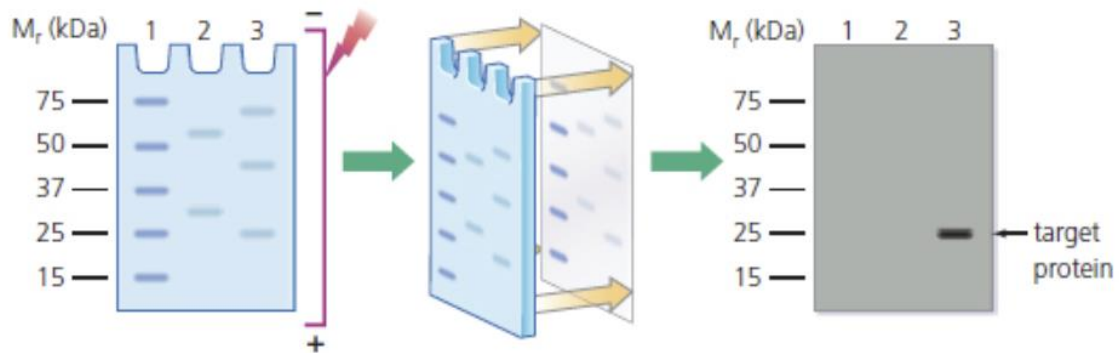
A large proportion of the exosomal proteins are associated with the vesicle membranes: the transmembrane proteins; the peripherally associated membrane proteins and the lipid-anchored membrane proteins (Figure 1.11).<sup>54</sup> Some of these proteins are derived from the biogenesis pathways of exosomes and thus viewed as specific markers for exosomes to differentiate them from other EV sub-populations. The most representative ones are the tetraspanin proteins CD63, CD9 and CD81.<sup>55</sup> Some cytosolic proteins, like ESCRT, annexins and actin, are considered as exosomal markers as well, which exhibit excellent lipid or membrane protein-binding ability. In addition to these exosomal markers, exosomes also enrich specific surface proteins mimicking those found on the membranes of the parental cells, which could reflect their cell of origin and indicate the pathological development, such as the overly expressed cell receptors HER2, EGFR, CD44, etc.



**Figure 1.11 Composition and structure of extracellular vesicles.** Extracellular vesicles are composed of a phospholipid bilayer surrounding protein (membrane protein and cargo protein) and nucleic acid. Membrane proteins include tetraspanins (CD9, CD63, CD81, etc), adhesion molecules (integrins, EpCAM, Ephrin, etc.), MHC, and receptors. Nucleic acid include DNA and RNA (mRNAs, miRNAs, LncRNAs (long non-coding RNAs), and circRNAs (circular RNAs)). Phospholipid bilayer provides protection to the cargo inside. Figure reprinted from Ref.54.

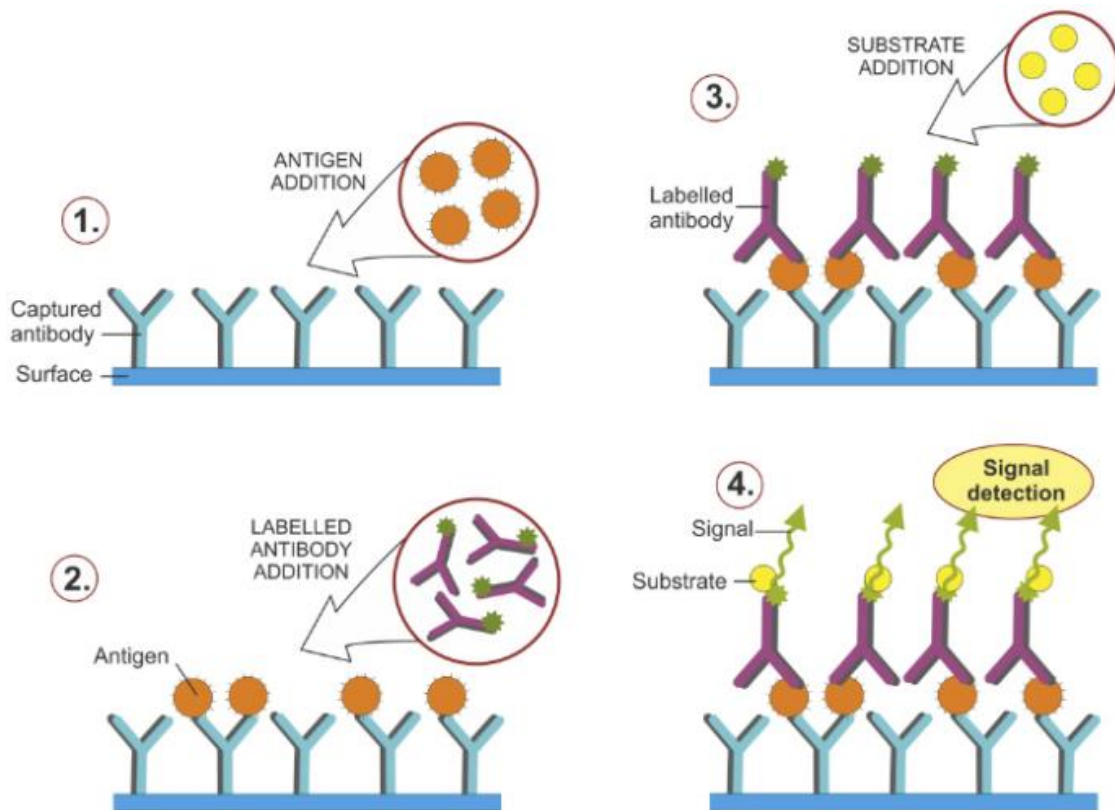
Many techniques have been developed for EV protein quantification. However, these techniques all have limitations. Western blotting (WB) is one of the gold standards to identify the EV proteins.<sup>56</sup> In WB, the proteins are firstly separated by sodium dodecyl sulfate polyacrylamide gel electrophoresis (SDS-PAGE) based on their molecular weights; and then transferred to a membrane for detection of specific protein targets vis immunoblotting (Figure 1.12). WB is suitable for qualitative and semi-quantitative analysis, and routinely implemented in research and clinical labs. However, conventional WB

requires large amounts of pure EVs, which is impractical when EV samples are limited; and it is very time-consuming.



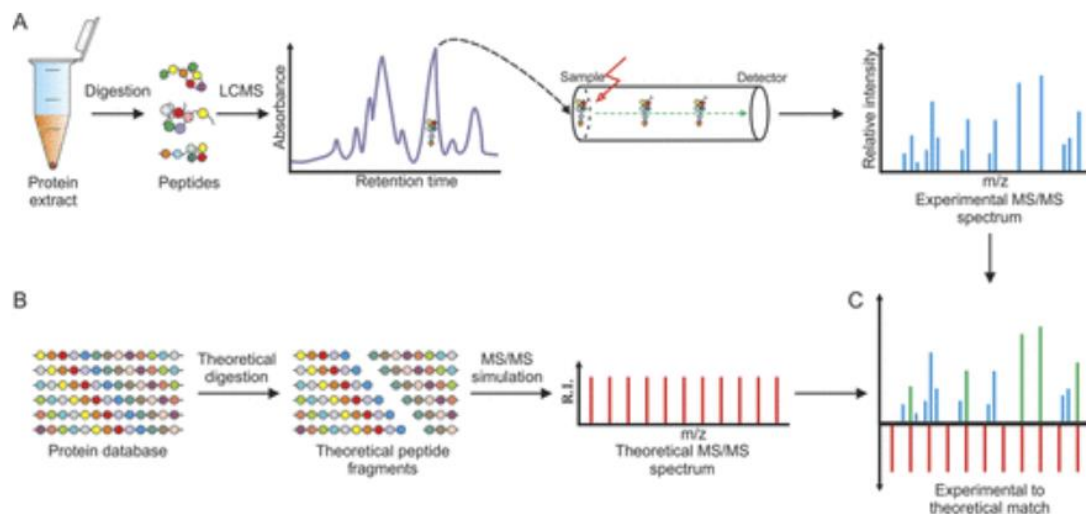
**Figure 1.12 Western blotting.** Figure reprinted from Ref.57.

Enzyme-linked immunosorbent assay (ELISA) is another routinely employed gold standard for EV protein quantification.<sup>56</sup> In ELISA, a sandwich complex is formed between the capture antibody immobilized to the bottom of the 96-well plate, the target protein either from the EV lysates or the surface of the intact EV, and the detection antibody linked to a reporter enzyme. The enzyme can catalyze generation of a large number of signaling molecules for fluorescent, colorimetric, or chemiluminescent detection (Figure 1.13). ELISA can achieve high-throughput analysis, and requires less sample input than WB. Still, it suffers from inadequate sensitivity in EV protein detection, which could be in the range of pg/mL, non-specific adsorption of impurity from biological samples, and lengthy processing. EV enrichment is often required to get sufficient signals.



**Figure 1.13 ELISA.** Figure reprinted from Ref.58.

Unlike ELISA and WB, mass spectrometry (MS) has been used for high-throughput profiling of EV proteins (Figure 1.14).<sup>59, 60, 61, 62</sup> In this technique, the pure EVs are isolated from biofluids, following with EV proteins extraction, purification, and digestion. resultant peptides are then separated using gel electrophoresis or liquid chromatography before MS analysis. MS could identify a large number of proteins simultaneously, but it remains technical demanding for accurate protein quantification and quantity comparison among different samples, and significant EV sample processing is required.

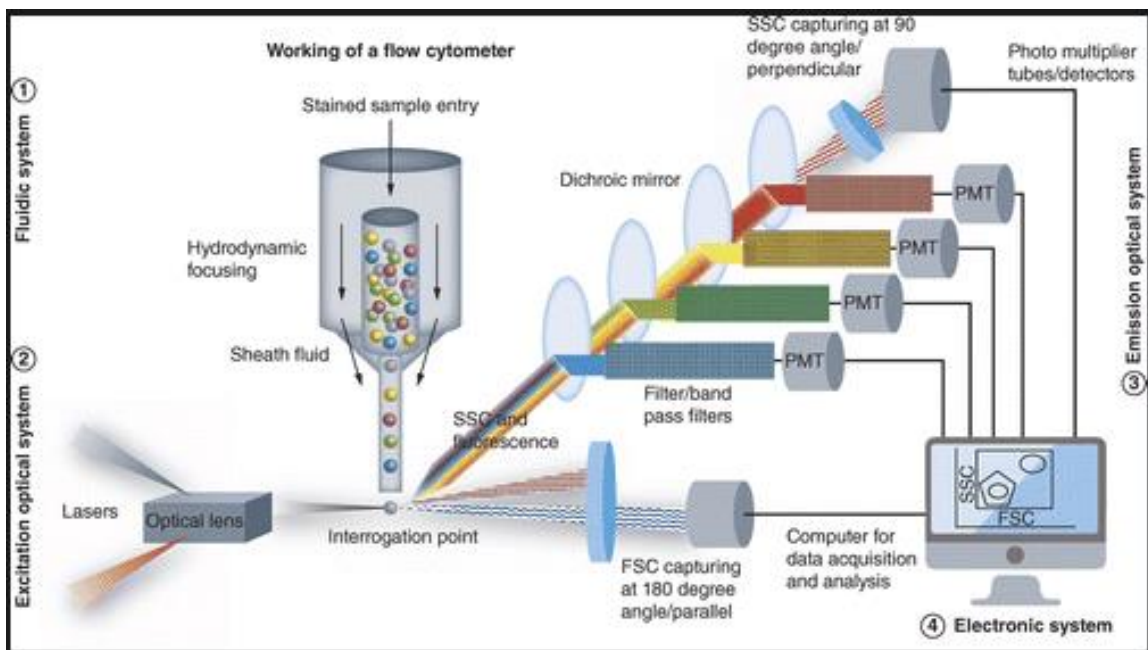


**Figure 1.14 Mass spectrometry.** Figure reprinted from Ref. 63. © 2018, American Chemical Society.

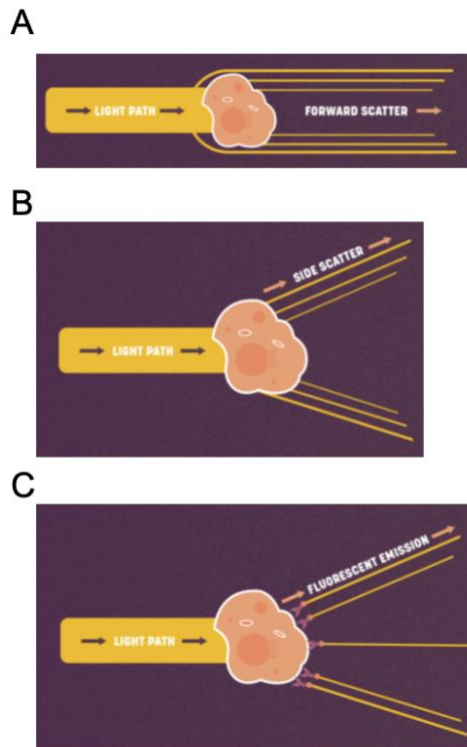
Bead-based flow cytometry (FCM) is another powerful tool for EV protein analysis. FCM is commonly used for single cell multi-parametric analysis.<sup>64</sup> It suspends cells in a stream of fluid and passes them through an electronic detection apparatus one by one using a hydrodynamically focused flow (Figure 1.15). The detector would record the scattered light and the emitted fluorescence signals from each individual cell, and the counting and signal profiles collected from many cells can then represent the average abundance of the protein targets in samples. There are three primary measurements: side scatter (SSC), forward scatter (FSC) and fluorescent signals (Figure 1.16). The SSC measures the scatter at 90 degrees of the laser beam, which can provide the information about the complexity or the granularity of the cell. The FSC measures the scatter coming from the forward direction, which could reflect the size of the cell. The surface markers were labeled with fluorescent antibodies. Using the fluorescence signals, the type of cell could be identified based on the fluorescence color, and the fluorescence intensity would reflect expression

level. Therefore, flow cytometry has been widely used in molecular biology, immunology, virology, bacteriology, infectious disease monitoring and cancer biology.

Similarly, it could be applied to study heterogeneous EVs. In this approach, immunobeads are employed to capture the EVs. The bound EVs are then labeled with the dye-conjugated antibodies for recognition of specific EV proteins. Bead-based FCM can provide fast and multiplexed analysis of EV proteins, and require less sample processing compared to ELISA and WB. Still, sensitivity and stability of EVs during bead capture and FCM analysis could be concerns.



**Figure 1.15 Flow cytometry.** Figure reprinted from Ref.65. © 2009, Future Science Ltd.



**Figure 1.16 Three primary output measurements of flow cytometry.** A: Forward scatter; B: Side scatter; C: Fluorescent signal. Figure reprinted from Ref.66.

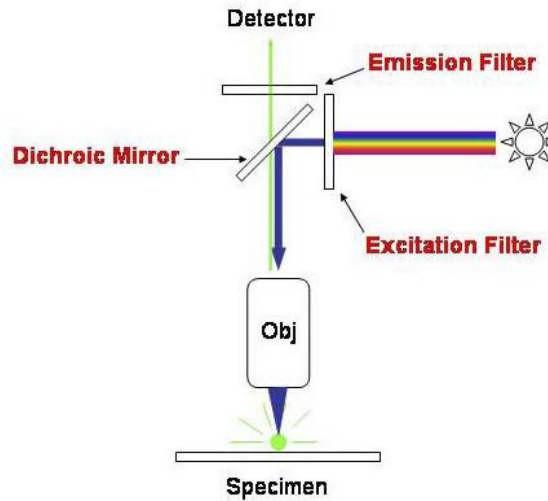
#### 1.4.2 Single Exosome Analysis Based on Protein Contents

The techniques mentioned above are all devoted to bulk analysis of EV protein contents. Although EV concentration in the peripheral circulation can reach  $10^9$  vesicles/mL<sup>67</sup>, the EV with good potential to be disease markers could be very low during early development stage<sup>68</sup>. In addition, the EVs are highly heterogeneous, different in their sizes, content, cell of origin, biogenesis pathways, and functional impact on recipient cells.<sup>69, 70</sup> The high heterogeneity of EVs increase the difficulty in identification of low abundant but unique EV sub-groups reflective to the health states of the parental cell, or

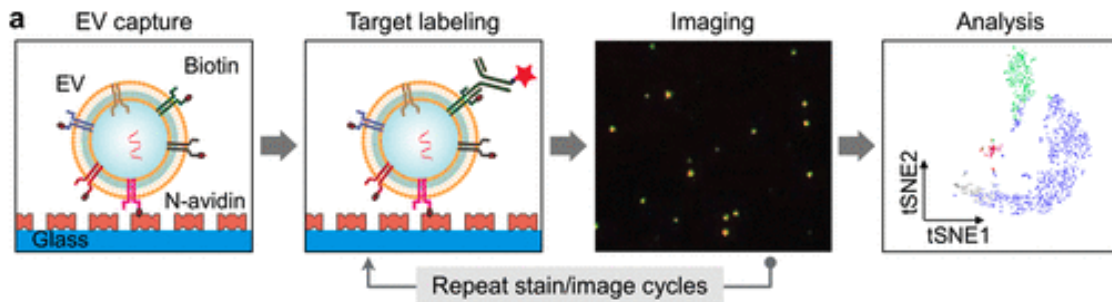
capable of impacting pathological development, among the high abundant, disease-irrelevant EV.

Confocal fluorescence microscopy (CFM) is one powerful tool to profile the surface proteins on individual EVs (Figure 1.17). The first report of single EV phenotyping using CFM labeled the target proteins on individual EVs by antibodies conjugated with bright fluorophores, and labeling and detection cycles which included dye bleaching and new antibody binding were repeated multiple times to detect the colocalization of multiple proteins on individual EVs (Figure 1.18).<sup>71</sup> They proved that the protein profiles could differentiate EVs from different biological origins. While this technique is powerful, it requires lengthy and complicated sample treatments and sophisticated data analysis. Proximity barcoding assay that employs DNA ligation and barcoding, rolling circle amplification and next-generation sequencing was developed for single EV phenotyping (Figure 1.19)<sup>72</sup>, while it requires lengthy and complicated sample treatments. Single EV analysis targeting a few protein markers on EVs for differentiation of EV sub-populations have also been achieved employing high-resolution FCM,<sup>73, 74, 75</sup> super resolution microscopy,<sup>76</sup> and total internal reflection fluorescent microscopy (TIRFM, Figure 1.20),<sup>77</sup> relying on the highly expensive and technically demanding instruments.

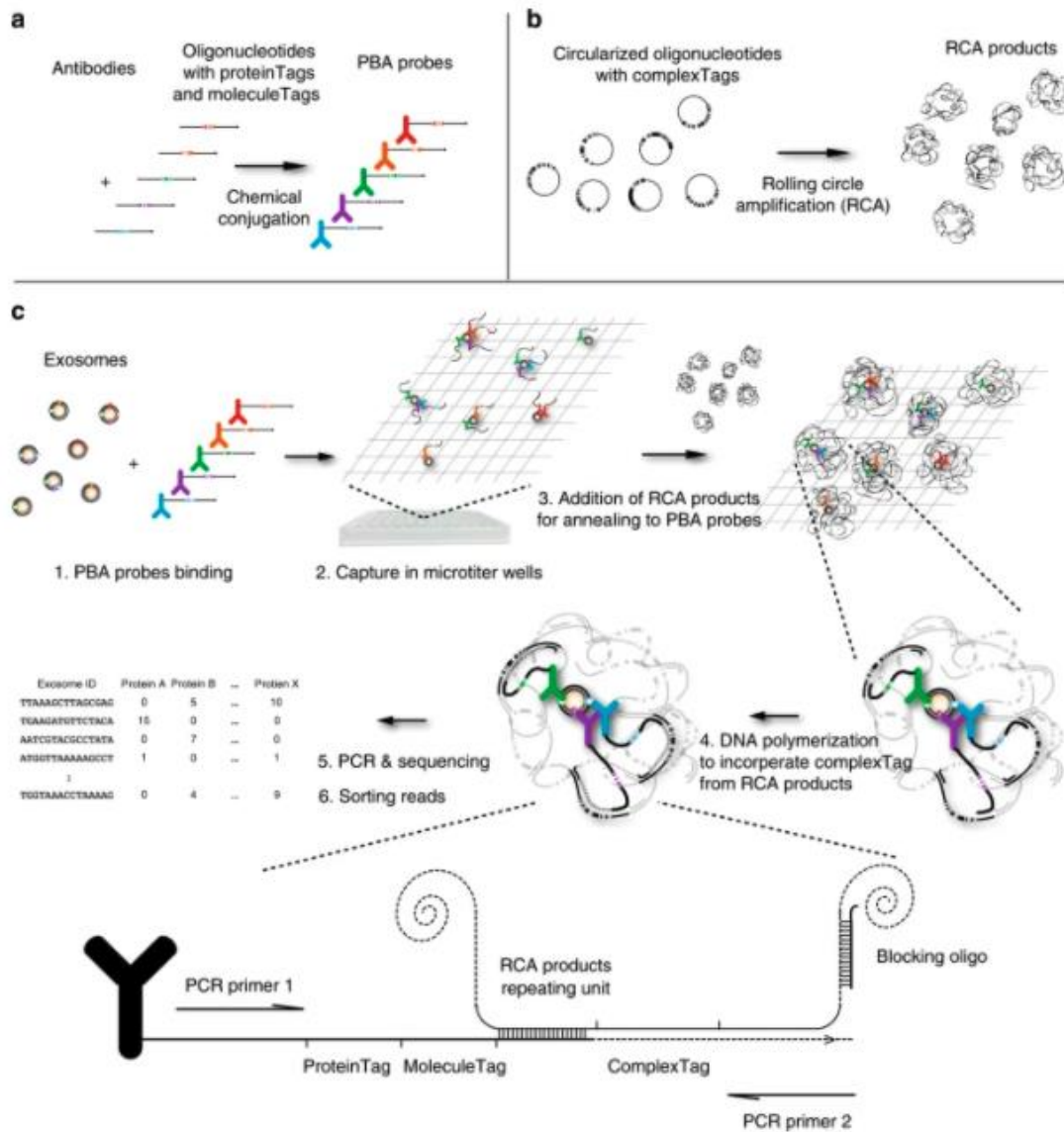




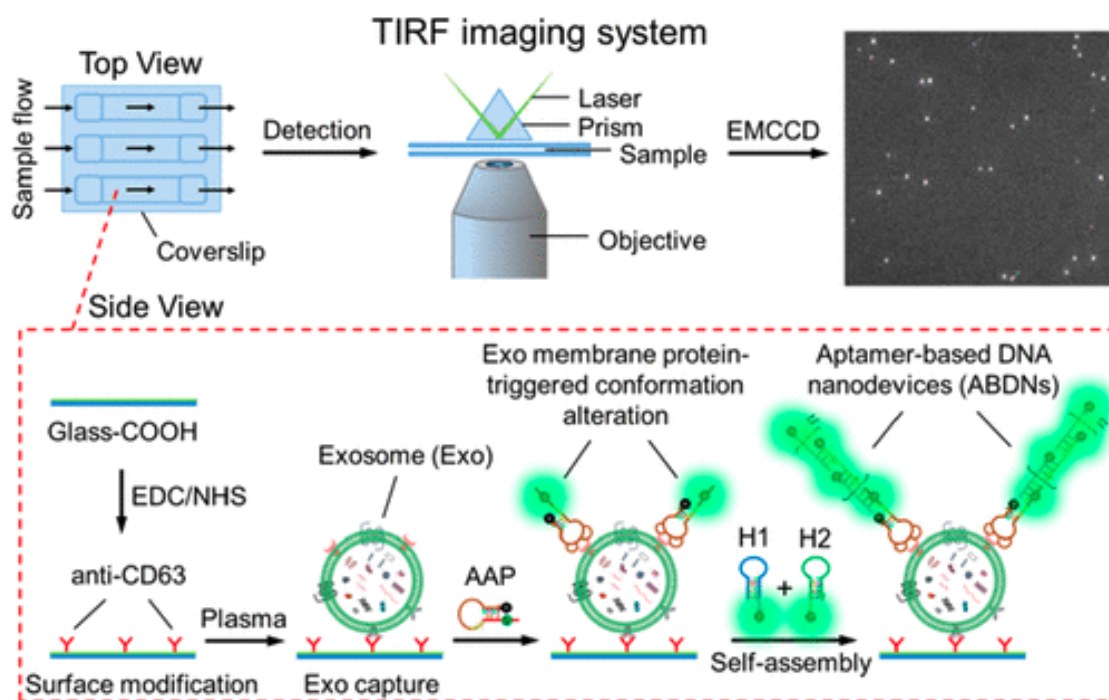
**Figure 1.17 Confocal microscopy.** A: Forward scatter; B: Side scatter; C: Fluorescent signal. Figure reprinted from Ref.78.



**Figure 1.18 Single EV analysis (SEA) strategy.** EV are biotinylated and captured on the device surface coated with neutravidin. The stationary EV are then stained by fluorescence antibodies and imaged by microscopy. Subsequently, fluorochromes are quenched, and the staining process is repeated for a different set of markers. Figure reprinted from Ref.71. © 2017, American Chemical Society.



**Figure 1.19 Design and workflow of proximity-dependent barcoding assay (PBA).** a: Preparation of PBA probes by chemical conjugation of antibodies and DNA oligonucleotides. b: preparation of RCA products from circularized oligonucleotides. c: To profile surface proteins of exosomes by PBA, exosomes are first incubated with PBA probes, followed by capture of exosomes with bound PBA probes in microtiter wells. Oligonucleotides on PBA probes hybridized to a unique RCA product, followed by enzymatic extension. Figure reprinted from Ref.72. © 2019, Springer Nature.



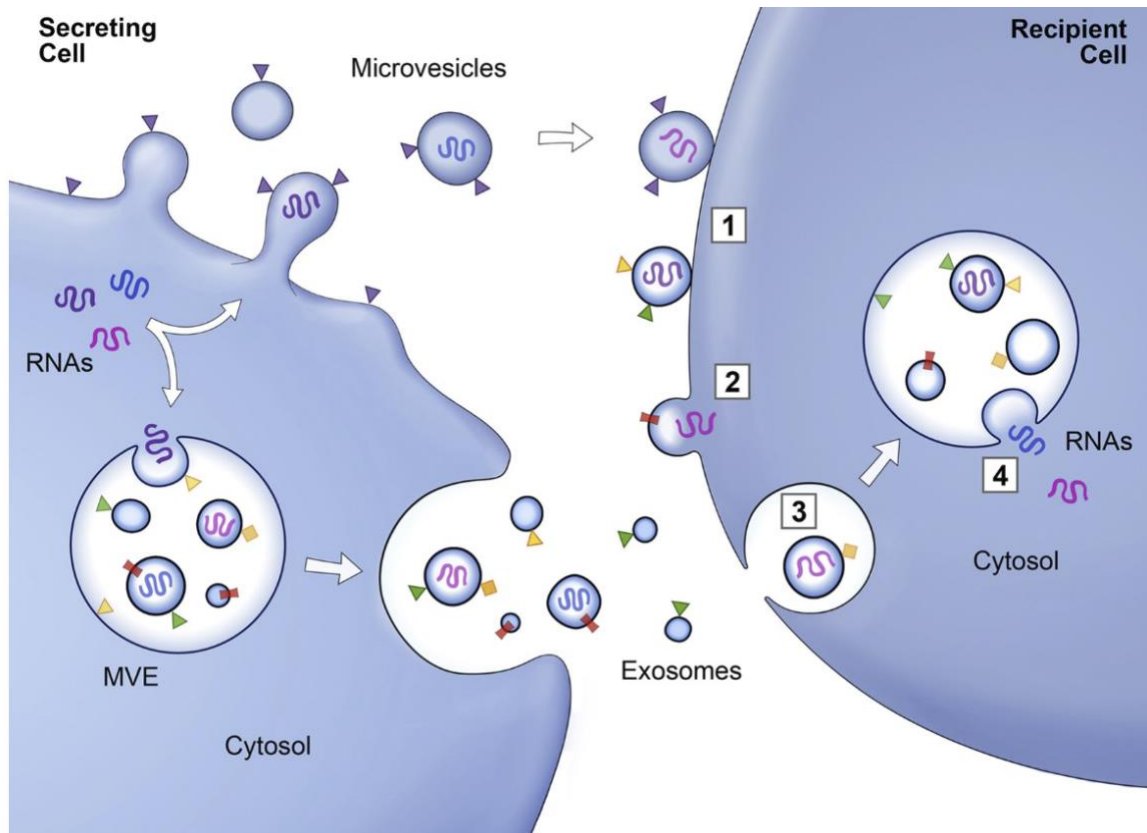
**Figure 1.20 Aptamer-based DNA nanodevices (ABDN) -based total-internal-reflection-fluorescence (TIRF) assay.** Figure reprinted from Ref.77. © 2019, American Chemical Society.

### 1.4.3 Analysis of Exosomal MicroRNA

Circulating miRNAs are stabilized through binding to proteins like the high-density lipoprotein (HDL), argonaute-2 (AGO2), and other RNA-binding proteins.<sup>79</sup> They can also be encapsulated in extracellular vesicles. Both protein binding and EV-encapsulation permit them elongated life-time in biofluids. They can also be detected through enzymatic detection methods with higher sensitivity than proteins. The high stability, easy accessibility, and good detectability make them attractive targets for biomarker discovery and diagnosis assay development.

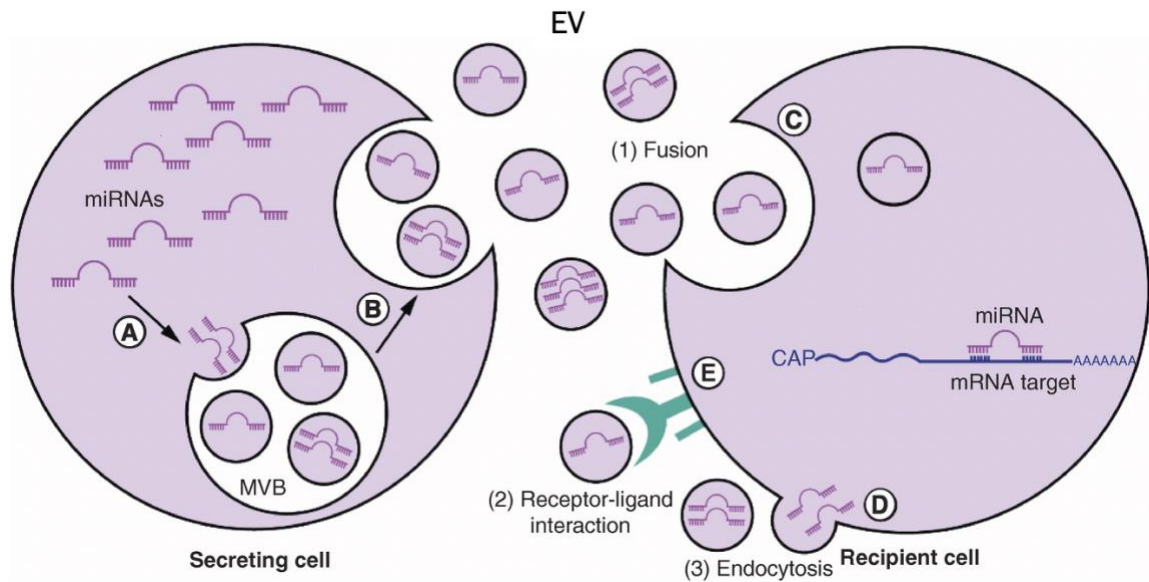
While the circulating miRNAs could be protein-bound or EV-encapsulated, the ones enclosed in EVs raise higher interest in disease marker discovery, because they have

been reported to be specifically transferred to the EVs and carry out dedicated functions (Figure 1.21). Packaging of miRNAs (curved symbols) to EVs starts with their selective incorporation into the intraluminal vesicle (ILV) of multivesicular endosomes (MVEs) or into microvesicles (MVs) budding from the plasma membrane. MVEs fuse with the plasma membrane to release exosomes into the extracellular milieu. MVs and exosomes may dock at the plasma membrane of a target cell. Bound vesicles may either fuse directly with the plasma membrane or be endocytosed. Endocytosed vesicles may then fuse with the delimiting membrane of an endocytic compartment. Both pathways result in the delivery of miRNAs into the membrane or cytosol of the target cell. Fusion and endocytosis are only represented for exosomal vesicles, but plasma membrane-derived MVs may have similar fates.



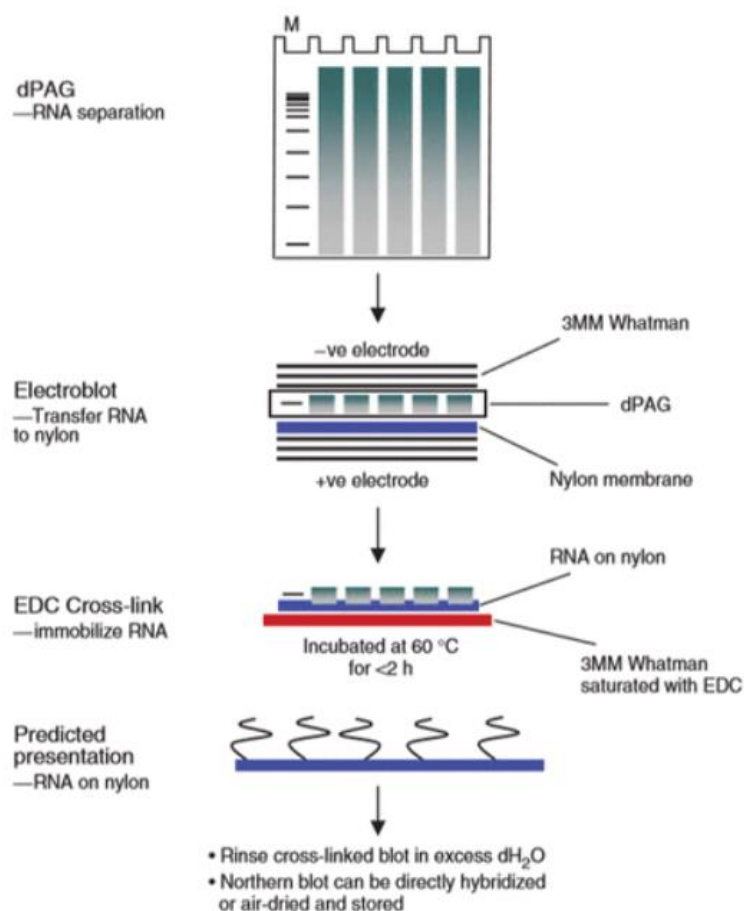
**Figure 1.21 Schematic of protein and RNA transfer by extracellular vesicles.** Figure reprinted from Ref.55. © 2013, Rockefeller University Press.

The EV miRNAs are well protected from nuclease digestion and can be efficiently integrated by specific receptor cells (Figure 1.22).<sup>80</sup> It has also been found that the amount and composition of EV-derived miRNAs differ significantly between healthy individuals and those with cancer. Therefore, EV-derived miRNAs present higher stability and specificity than circulating miRNAs, marking them better biomarkers for cancer diagnosis and prognosis.



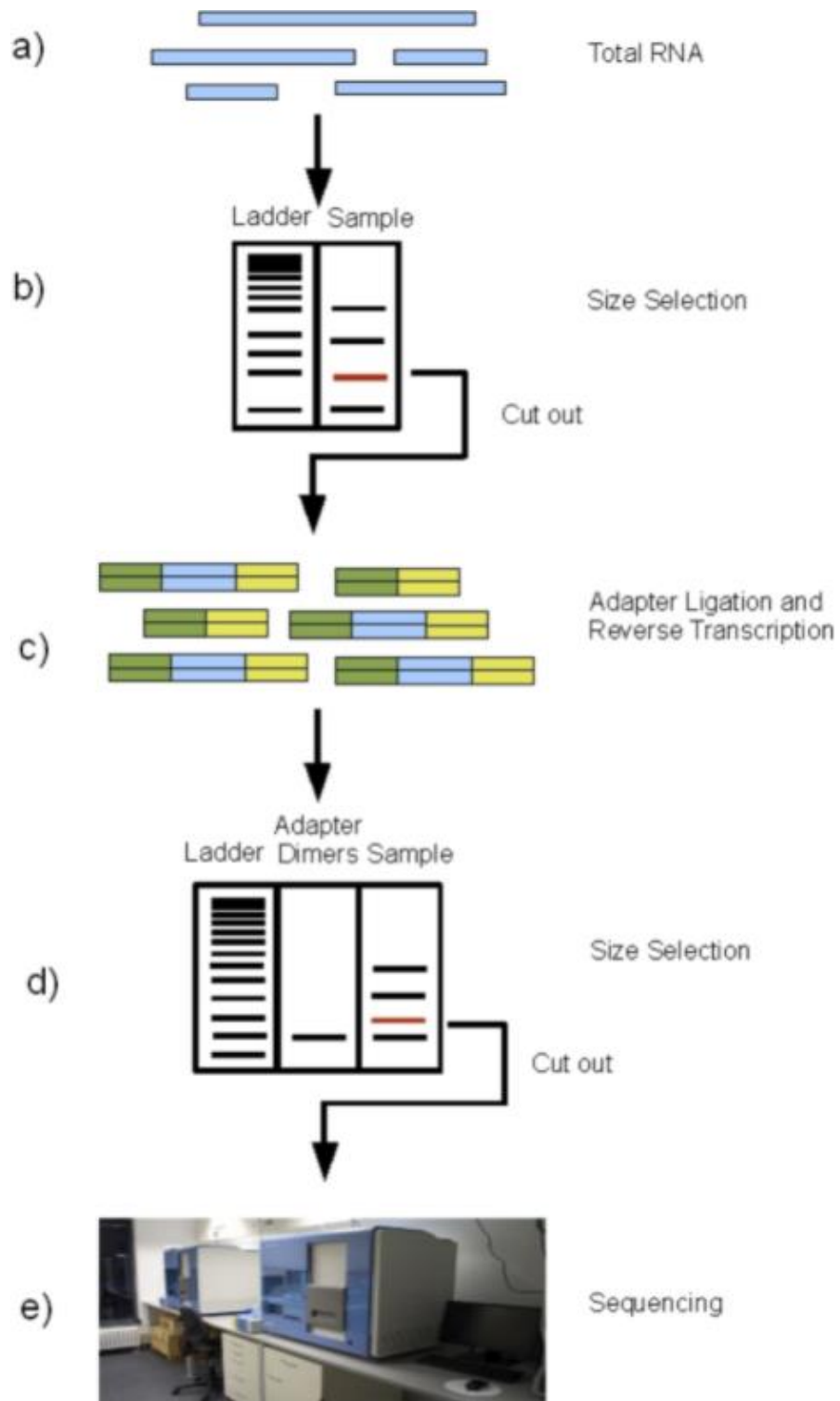
**Figure 1.22 Transfer of EV-derived miRNA from donor cell to recipient cells.** Figure reprinted from Ref.80.

Reverse transcription polymerase chain reaction (RT-PCR) is popular in miRNA quantification because of its high sensitivity.<sup>81, 82</sup> It converts the miRNA into complementary DNA (cDNA), and then amplifies the cDNA using PCR. It is highly sensitive but has low sample throughput. Northern blotting can explore miRNA expression in a relatively high through-put manner (Figure 1.23).<sup>83, 84</sup> It separates the samples using gel electrophoresis after digestion. The separated miRNAs are transferred into a membrane, which will be labeled with isotope or labeled probes for imaging. It can detect not only mature miRNAs, but also its precursors. Even higher throughput miRNA analysis can be achieved by microarray,<sup>85</sup> which modifies the solid phase using capture probes for target miRNA capture. But both northern blotting and microarray suffer from poor sensitivity, narrow dynamic range, and length sample processing.



**Figure 1.23 Northern blotting.** Figure reprinted from Ref.84. © 2019, American Chemical Society.

Next-generation sequencing (NGS) allows the simultaneous analysis of both miRNA sequence and expression (Figure 1.24).<sup>86</sup> The RNA samples are first isolated and purified. Next, the sequencing adapters are ligated to the RNA samples, followed by reverse transcription to cDNA. After that, the cDNA would be separated by agarose gel, and for subsequent sequencing. It has high accuracy and can distinguish miRNAs at a single base resolution. However, it requires high-quality miRNA extraction and preparation of the miRNA libraries.

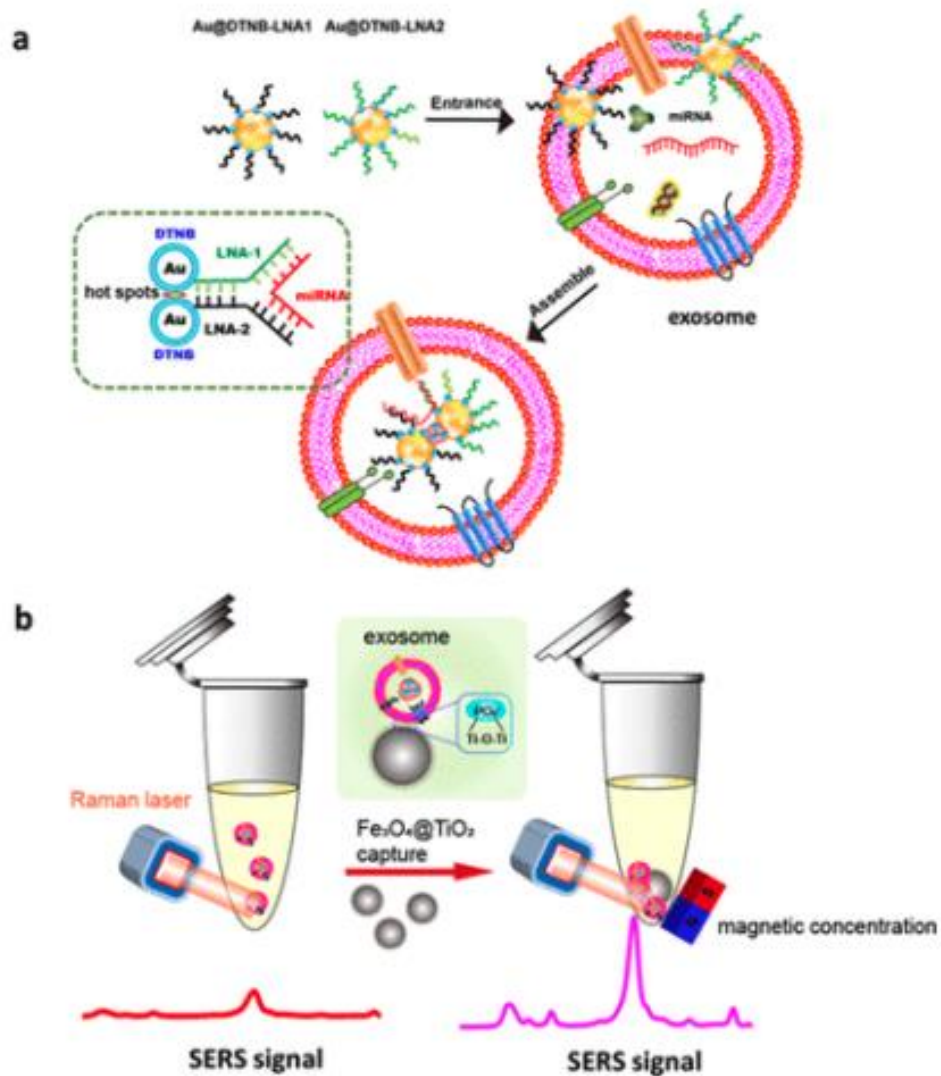


**Figure 1.24 miRNA sequencing procedure.** Figure reprinted from Ref.87.



Employment of the above techniques for analysis of exosomal miRNAs require EV enrichment, lysis and miRNA extraction before miRNA quantification. The entire process could result in poor RNA recovery and have long turn-around time. Moreover, these bulk assays fail to provide information on the molecular content of individual EVs, which promotes the development of miRNA detection in individual EV. Nucleic acid functionalized Au nanoflares were delivered into EV for exosomal miRNA detection (Figure 1.25),<sup>88, 89, 90, 91</sup> but still, it detects the bulk levels of miRNA in EV-containing samples.

Current detection of miRNAs in individual EVs relies on molecular beacons (MB) delivered to each EV through pore formation on the vesicle membrane induced by streptolysin O (Figure 1.26 and Figure 1.27)<sup>92, 93</sup>, fusion with the cationic lipoplexes (Figure 1.28)<sup>94, 95</sup> or merging with the virus-mimicking fusogenic vesicles (Figure 1.29).<sup>96</sup> These methods are insensitive and thus unable to distinguish the low level of target miRNAs in individual vesicles.



**Figure 1.25 Schematic of exosomal miRNA *in situ* detection by SERS biosensor and  $\text{Fe}_3\text{O}_4@\text{TiO}_2$  concentration.** Figure reprinted from Ref.89. © 2021, American Chemical Society.

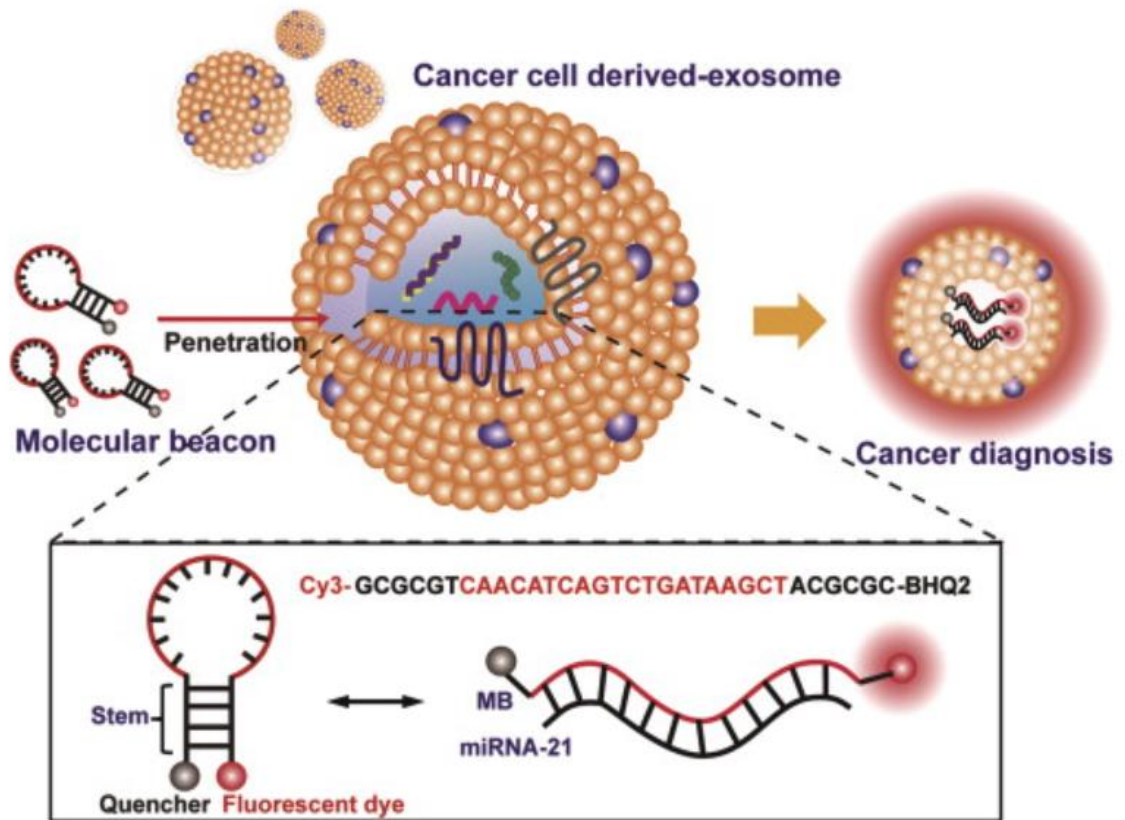


Figure 1.26 *in situ* detection of exosomal miR-21 using MB for the diagnosis of diseases such as cancer. Figure reprinted from Ref.92. © 2015, Elsevier.

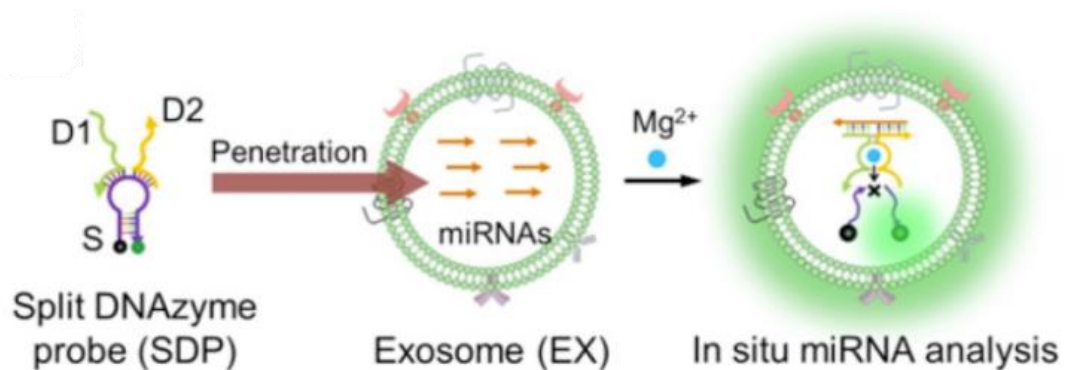
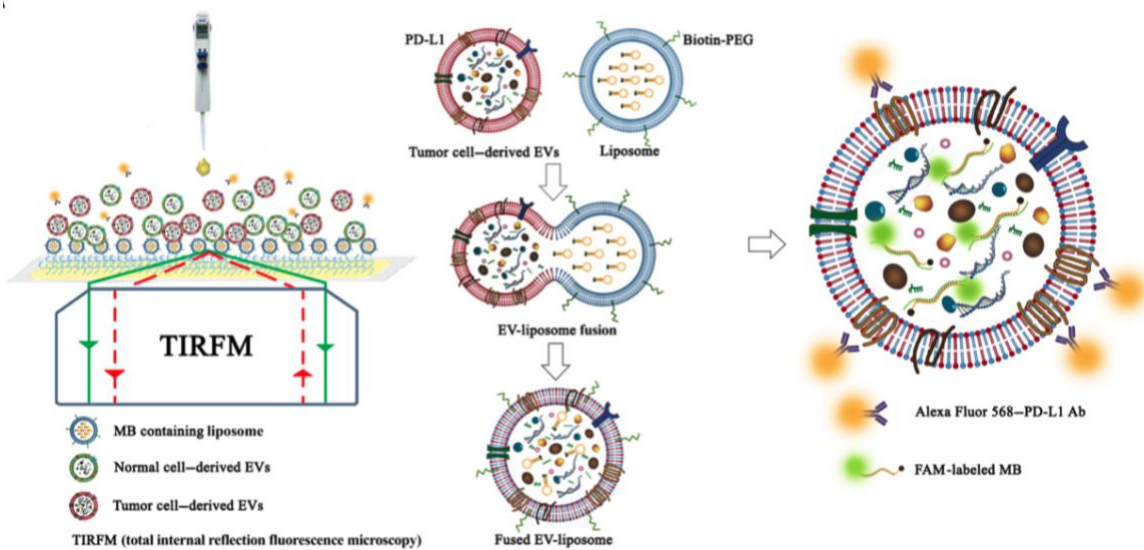
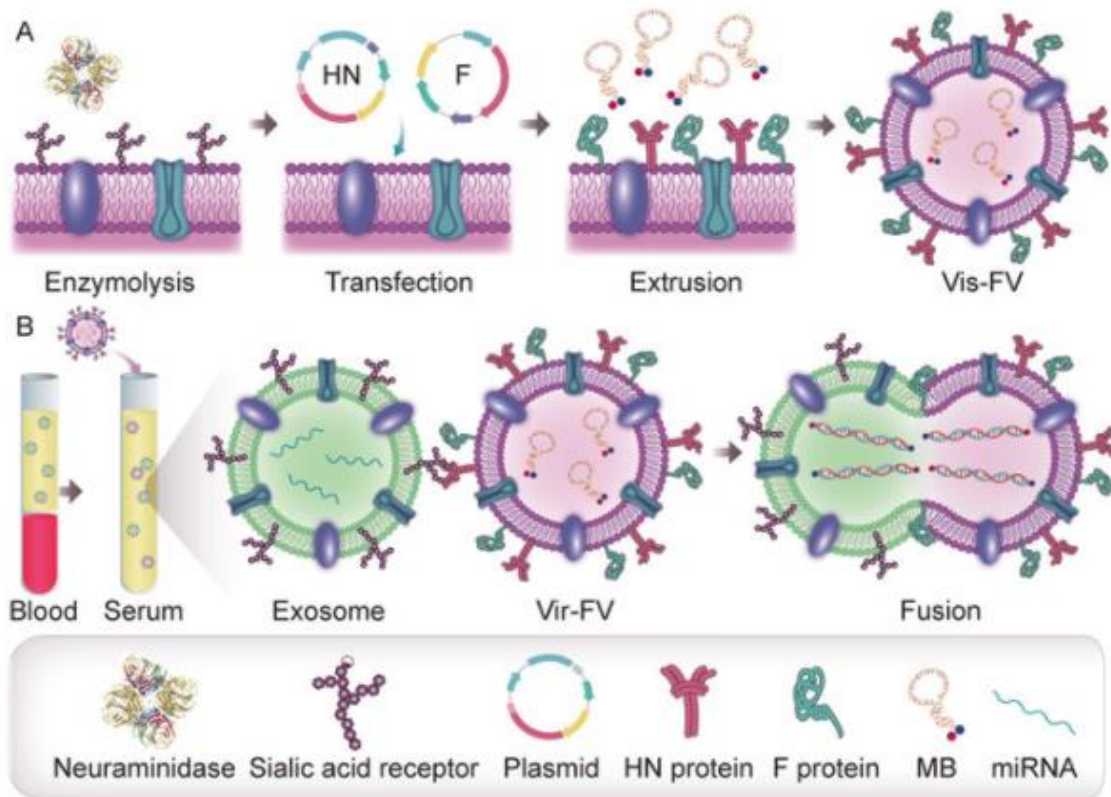


Figure 1.27 *in situ* analysis of exosomal miRNAs by split DNAzyme probe. Figure reprinted from Ref.93.



**Figure 1.28 Nano-bio chip integrated system for liquid biopsy (HNCIB) system for simultaneous detection of membrane protein and mRNA in a single EV. Figure reprinted from Ref.94.**



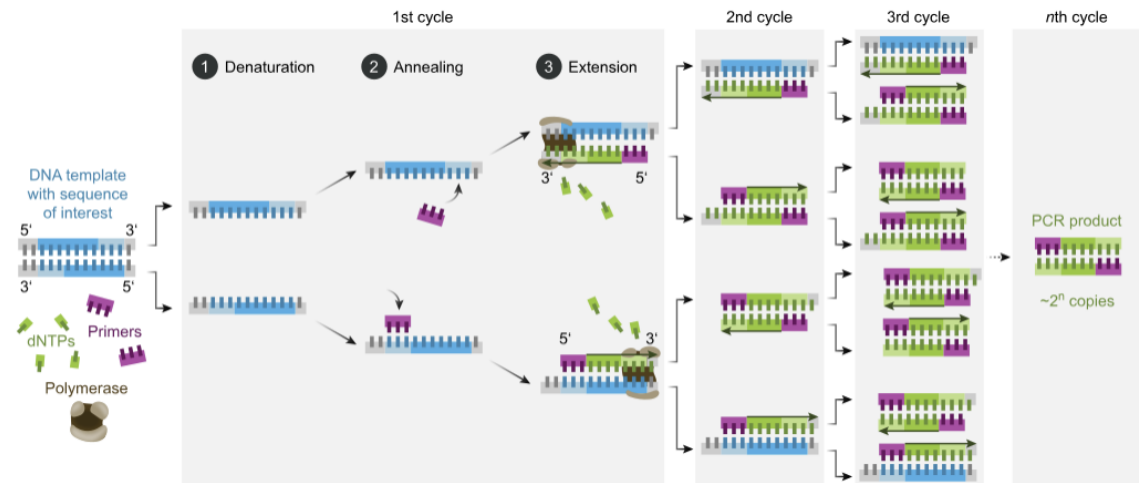
**Figure 1.29 Schematic illustration of the virus-mimicking fusogenic vesicles (Vir-FVs) for the rapid detection of exosomal miRNAs.** A) Preparation of the Vir-FVs. B) The fusion between Vir-FVs and exosomes caused by HN and F protein leads to the hybridization of the MB with the target miRNA. Figure reprinted from Ref.96. © 2019, John Wiley and Sons.

### 1.5 Signal Amplification Enabling Biomarker Detection

Due to the small physical sizes of EVs and the limited amounts of miRNAs enclosed, highly sensitive detection of miRNA expression on single EVs with simple and rapid approaches has not yet been realized, greatly hindering the applications in cancer diagnosis. To bridge the gap, I began my projects with the goal of developing simple and highly specific methods for analysis of exosomal proteins and miRNA in individual EVs.

To deal with the low amount of marker molecules enclosed in the tiny EVs, we have employed the isothermal amplification methods to amplify the target signals.

Nucleic acids, such as DNA (deoxyribonucleic acids) and RNA (ribonucleic acids), are promising biomarkers for cancer diagnosis. Due to their low abundance and short length, nucleic acid amplification is required before detection. Polymerase chain reaction (PCR) is one of the common amplification techniques. It uses a DNA polymerase and a primer to synthesize a new DNA strand complementary to the template strand (Figure 1.30). Typically, it contains three steps: denaturation, annealing and extension. The samples are first heated at high temperature, such as 95 °C, to denature the samples and produce a single-stranded template for the next step. After denaturation, the samples is cooled to about 55 °C, so the primers can bind to the complementary sequences of single-stranded template DNA. At the end, the reaction temperature is raised to about 72 °C, so the DNA polymerase can extend the primers and synthesize a new strand of DNA. This process is carried out by PCR machine in thermal cycling. At the end of the PCR reaction, billions of copies of the template strand are produced, which enables the downstream analysis. However, it requires sophisticated equipment and trained personnel. What's more, the heating step of PCR would destroy the biological molecules, which cannot be applied in living systems.<sup>97</sup> Isothermal DNA amplification was developed to avoid the expensive equipment and heating step.<sup>98</sup>

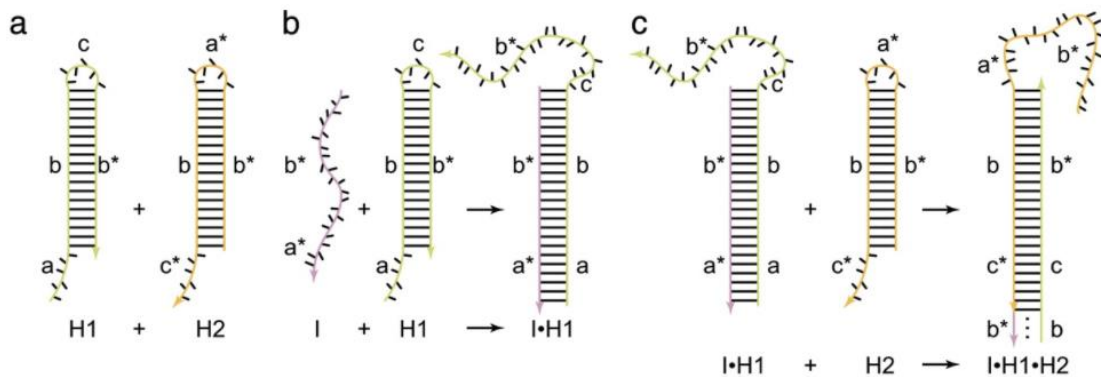


**Figure 1.30 PCR.** Figure reprinted from Ref.99.

Unlike the PCR, isothermal DNA amplification can amplify DNA sequence at a constant temperature.<sup>100</sup> It doesn't require any thermal cycling, which is simple and cost effective. It could produce multiple copies of the target and it is sequence-based amplification, so it has high sensitivity and specificity. What's more, the constant reaction temperature enables its application in clinic samples. There are two kinds of isothermal DNA amplifications: enzyme-based and enzyme-free.

Hybridization chain reaction (HCR), first developed by Dirks and Pierce in 2004, is one of the enzyme-free isothermal amplification methods (Figure 1.31).<sup>101</sup> This reaction employs one initiator and two hairpins DNA probes, H1 and H2.<sup>102</sup> The hairpin DNA probes are composed of a toehold, a long stem and a short loop. For this hairpin structure, the potential energy stored in the short loop is protected by the long stems.<sup>103</sup> Therefore, these two hairpin probes stably coexist in solution in the absence of initiator.<sup>104</sup> Initiator has a complementary sequence to the toehold and stem domains of one of the hairpins, hairpin 1. When introducing the initiator, the initiator would hybridize with hairpin 1

through strand displacement to open the hairpin structure of hairpin 1 and expose the sequence for hybridization with hairpin 2.<sup>105, 106</sup> As a result, the hybridization between hairpin 1 and hairpin 2 would be triggered and produce a long double-stranded DNA. It combines recognition and hybridization, enabling high specificity. Compared to PCR, it is simple, low cost, highly energy efficient as well as high sensitivity and high specificity.<sup>107, 108</sup> Therefore, it is widely used in biosensing, bioimaging and biomedicine.<sup>109</sup>

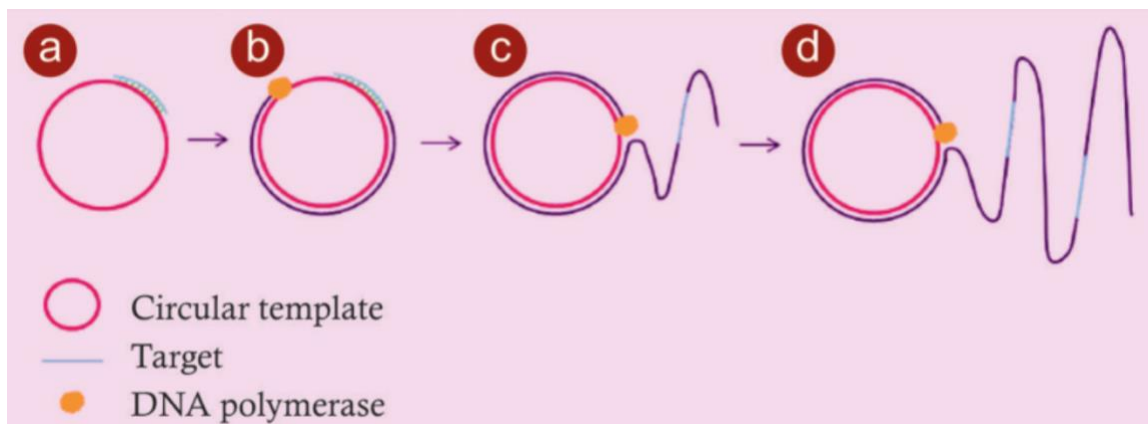


**Figure 1.31 Hybridization Chain Reaction.** Figure reprinted from Ref.101. © 2004, The National Academy of Sciences.

Unlike HCR, rolling circle amplification (RCA) is an enzymatic isothermal amplification method.<sup>110, 111</sup> It employs a circular DNA template, a short primer and a DNA polymerase to synthesize a long single-strand DNA (Figure 1.32).<sup>112, 113</sup> The circular templates were produced from the DNA ligation of a linear probe, named padlock probe. These padlock probes are oligonucleotides whose ends are complementary to the adjacent primer. Upon hybridization to the primer, the two ends are brought into contact, allowing padlock probes circularization by ligation. RCA uses the circular probe as a template.<sup>114,</sup>



<sup>115</sup> By designing the template, the RCA product can be customized into various DNA origami, or DNA based materials containing DNA aptamers or DNAzymes.



**Figure 1.32 Rolling Circle Amplification.** Figure reprinted from Ref.110. © 2020, Springer Science + Business Media, LLC, part of Springer Nature.

## 1.6 Summary

Due to the small physical sizes of EVs and the limited amounts of cargo molecules enclosed, highly sensitive detection of molecular expression on single EVs with simple and rapid approaches has not yet been realized, greatly hindering the discovery and applications of EV-based disease markers. To bridge the gap, I began my projects with the goal of developing simple and highly specific methods for analysis of EV cargos enclosed in individual EVs using the conventional, diffraction-limited flow cytometer and confocal microscopy. These details will be described in Chapter 2 - 4.

Nucleic acid isothermal amplification is a powerful strategy to detect nucleic acids with a low expression level at a constant temperature. In addition to nucleic acids, it also can detect proteins with the assistance of aptamer, antibody or ligand. By converting the

expression level of protein into oligonucleotides level using aptamer or antibody-DNA conjugates, nucleic acid isothermal amplification method can be applied to amplify the signal for detection, enabling individual EV analysis and detection. Thus, to achieve adequate signals from the target EV cargos in my projects, I designed various DNA nanostructures that can be constructed *in situ* using various isothermal DNA amplification methods, such as HCR and RCA, and apply them to profile single EV phenotype information and miRNA expression level.

## 1.7 Reference

---

- 1 Cancer Research UK, How Cancers Grow. <https://www.cancerresearchuk.org/about-cancer/what-is-cancer/how-cancers-grow>.
- 2 J. J. Ofman, A. Raza, A. M. Fendrick, *Evidence-based oncology* **2020**, *26*, SP363.
- 3 G. D. Rubis, S. R. Krishnan, M. Bebawy, *Trends Pharmacol. Sci.* **2019**, *40*, 172-186.
- 4 X. Chen, J. Gole, A. Gore, Q. He, M. Lu, J. Min, Z. Yuan, X. Yang, Y. Jiang, T. Zhang, C. Suo, X. Li, L. Cheng, Z. Zhang, H. u Niu, Z. Li, Z. Xie, H. Shi, X. Zhang, M. Fan, X. Wang, Y. Yang, J. Dang, C. McConnell, J. Zhang, J. Wang, S. Yu, W. Ye, Y. Gao, K. Zhang, R. Liu, L. Jin, *Nat. Commun.* **2020**, *11*, 3475.
- 5 O. Ginsburg, C. Yip, A. Brooks, A. Cabanes, M. Caleffi, J. A. D. Yataco, B. Gyawali, V. McCormack, M. M. de Anderson, R. Mehrotra, A. Mohar, R. Murillo, L. E. Pace, E. D. Paskett, A. Romanoff, A. F. Rositch, J. R. Scheel, M. Schneidman, K. Unger-Saldana, V. Vanderpuye, T. Wu, S. Yuma, A. Dvaladze, C. Duggan, B. O. Anderson, *Cancer* **2020**, *126*, 2379-2393.
- 6 *Nat. Rev. Cancer* **2018**, *18*, 401.
- 7 N. Harbeck, F. Penault-Llorca, J. Cortes, M. Gnant, N. Houssami, P. Poortmans, K. Ruddy, J. Tsang, F. Cardoso, *Nat. Rev. Dis. Primers* **2019**, *5*, 66.
- 8 A. Alba-Bernal, R. Lavado-Valenzuela, M. E. Domínguez-Recio, B. Jiménez-Rodríguez, M. I. Queipo-Ortuño, E. Alba, I. Comino-Méndez, *EBioMedicine* **2020**, *62*, 103100.
- 9 E. Crowley, F. D. Nicolantonio, F. Loupakis, A. Bardelli, *Nat. Rev. Clin. Oncol.* **2013**, *10*, 472.
- 10 J. Wu, S. Hu, L. Zhang, J. Xin, C. Sun, L. Wang, K. Ding, B. Wang, *Theranostics* **2020**, *10*, 4544-4556.
- 11 I. Heidrich, L. Ackar, P. M. Mohammadi, K. Pantel, *Int. J. Cancer* **2020**, *149*, 528-545.
- 12 Y. K. Tong, Y. M. Lo, *Clin. Chim. Acta* **2006**, *363*, 187.
- 13 E. E. Yoruker, S. Holdenrieder, U. Gezer, *Clin. Chim. Acta* **2016**, *455*, 26.

- 
- 14 M. J. Xu, J. F. Dorsey, R. Amaravadi, G. Karakousis, C. B. Simone II, X. Xu, W. Xu, E. L. Carpenter, L. Schuchter, G. D. Kao, *Oncologist* **2016**, *12*, 84.
  - 15 S. Y. Lim, J. H. Lee, R. J. Diefenbach, R. F. Kefford, H. Rizos, *Mol. Cancer* **2018**, *17*, 8.
  - 16 T. K. Y. Tay, P. H. Tan, *Arch. Pathol. Lab. Med.* **2021**, *145*, 678-686.
  - 17 A. H. Cheung, C. Chow, K. To, *J. Thorac. Dis.* **2018**, *10*, S1645-S1651.
  - 18 G. Trecate, P. M. Sinues, R. Orlandi, *Future Oncol.* **2016**, *12*, 1395.
  - 19 R. B. Corcoran, *Nat. Med.* **2020**, *26*, 1815-1816.
  - 20 M. Ignatiadis, G. W. Sledge, S. S. Jeffrey, *Nat. Rev. Clin. Oncol.* **2021**, *18*, 297-312.
  - 21 Y. Wang, M. P. Trinh, Y. Zheng, K. Guo, L. A. Jimenez, W. Zhong, *TrAC* **2019**, *117*, 242-262.
  - 22 K. Strimbu, *J. A. Travel. Curr. Opin. HIV AIDS* **2010**, *5*, 463-466.
  - 23 S. Bratulic, F. Gatto, *J. Nielsen, Regen. Eng. Transl. Med.* **2019** DOI: 10.1007/s40883-019-00141-2.
  - 24 R. Mayeux, *NeuroRx* **2004**, *1*, 182-188.
  - 25 A. A. Hussein, T. Forouzanfar, E. Bloemena, J. de Visscher, R. H. Brakenhoff, C. R. Leemans, M. N. Helder, *Br. J. Cancer* **2018**, *119*, 724-736.
  - 26 E. Heitzer, I. S. Haque, C. E. S. Roberts, M. R. Speicher, *Nat. Rev. Genet.* **2019**, *20*, 71-88.
  - 27 L. Gam, *World J. Exp. Med.* **2012**, *2*, 86-91.
  - 28 P. Kuppusamy, N. Govindana, M. M. Yusoffa, S. J. A. Ichwan, *Saudi J. Biol. Sci.* **2017**, *24*, 1212-1221.
  - 29 P. Maruvada, W. Wang, P. D. Wagner, S. Srivastava, *Biotechniques* **2018**, *38*, 9-15.
  - 30 D. de M. Pérez, A. R. Martínez, A. O. Palomo, M. D. Ureña, J. L. G. Puche, A. R. Remacho, J. E. Hernandez, J. A. L. Acosta, F. G. O. Sánchez, M. J. Serrano, *Sci. Rep.* **2020**, *10*, 3974.

- 
- 31 S. Komatsu, J. Kiuchi, T. Imamura, D. Ichikawa, E. Otsuji, *J. Cancer Metastasis Treat.* **2018**, *4*, 36.
- 32 Central Dogma Inheritance Mechanism. <https://byjus.com/biology/central-dogma-inheritance-mechanism/>.
- 33 M. Ha, V. N. Kim, *Nat. Rev. Mol. Cell Biol.* **2014**, *15*, 509-524.
- 34 J. Winter, S. jung, S. Keller, R. I. Gregory, S. Diederichs, *Nat. Cell Biol.* **2009**, *11*, 228-234.
- 35 T. Treiber, N. Treiber, G. Meister, *Nat. Rev. Mol. Cell Biol.* **2019**, *20*, 5–20.
- 36 L. Quirico, F. Orso, *Cancer Drug Resist.* **2020**, *3*, 117-139.
- 37 L. MacFarlane, P. R. Murphy, *Curr. Genom.* **2010**, *11*, 537-561.
- 38 S. Ono, S. Lam, M. Nagahara, D. S. B. Hoon, *J. Clin. Med.* **2015**, *4*, 1890-1907.
- 39 F. J. Nassar, G. Chamandi, M. A. Tfaily, N. K. Zgheib, *R. Nasr, Front. Med.* **2020**, *7*, 28.
- 40 Y. Toiyama, Y. Okugawa, J. Fleshman, C. R. Boland, A. Goel, *Biochim. Biophys. Acta* **2018**, *1870*, 274-282.
- 41 C. M. Croce, *Nat. Rev. Genet.* **2009**, *10*, 704-714.
- 42 M. Esteller, *Nat. Rev. Genet.* **2011**, *12*, 861-874.
- 43 H. Suzuki, R. Maruyama, E. Yamamoto, M. Kai, *Mol. Oncol.* **2012**, *6*, 567-578.
- 44 J. H. Ohyashiki, T. Umezu, K. Ohyashiki, *Phil. Trans. R. Soc. B* **2017**, *373*, 20160484.
- 45 C. Théry, L. Zitvogel, S. Amigorena, *Nat. Rev. Immunol.* **2002**, *2*, 569-579.
- 46 H. Yan, Y. Li, S. Cheng, Y. Zeng, *Anal. Chem.* **2021**, *93*, 4739-4774.
- 47 M. Kanada, M. H. Bachmann, C. H. Contag, *Trends Cancer* **2016**, *2*, 2.
- 48 Laura M. Doyle and Michael Zhuo Wang, *Cells* **2019**, *8*, 727.
- 49 S. Gurunathan, M. Kang, M. Jeyaraj, M. Qasim, J. Kim, *Cells* **2019**, *8*, 307.

- 
- 50 B. Zhou, K. Xu, X. Zheng, T. Chen, J. Wang, Y. Song, Y. Shao, S. Zheng, *Signal Transduct. Tar.* **2020**, *5*, 144.
- 51 S. Sharma, *Indian J. Med. Paediatr. Oncol.* 2009, *30*, 1.
- 52 G. L. Perkins, E. D. Slater, G. K. Sanders, J. G. Prichard, *Am. Fam. Physician* 2003, *68*, 1075-1082.
- 53 J. D. Schiffman, P. G. Fisher, P. Gibbs, *American Society of Clinical Oncology Educational Book*, **2015**, *35*, 57-65.
- 54 S. Tao, S. Guo, *Cell Commun. Signal.* **2020**, *18*, 163.
- 55 G. Raposo, W. Stoorvogel, *J. Cell Biol.* **2013**, *200*, 373-383.
- 56 H. Shao, H. Im, C. M. Castro, X. Breakefield, R. Weissleder, H. Lee, *Chem. Rev.* **2018**, *118*, 1917 – 1950.
- 57 Bio-Rad, Western Blotting: Introduction. <https://www.bio-rad-antibodies.com/western-blotting-immunoblotting-introduction.html>.
- 58 BioTek, ELISA. <https://www.biotek.com/applications/elisa-and-related-immunoassays.html>.
- 59 A. Mallia, E. Gianazza, B. Zoanni, M. Brioschi, S. S. Barbieri, C. Banfi, *Diagnostics* **2020**, *10*, 843.
- 60 R. Bandu, J. W. Oh, K. P. Kim, *Exp. Mol. Med.* **2019**, *51*, 1-10.
- 61 S. Rontogianni, E. Synadaki, B. Li, M. C. Liefwaard, E. H. Lips, J. Wesseling, W. Wu, M. Altelaar, *Commun. Biol.* **2019**, *2*, 325.
- 62 L. Rosa-Fernandes, V. B. Rocha, V. C. Carregari, A. Urbani, G. Palmisano, *Front. Chem.* **2017**, *5*, 102.
- 63 A. Chugunova, T. Navalayeu, O. Dontsova, P. Sergiev, *J. Proteome Res.* **2018**, *17*, 1-11.
- 64 K. M. McKinnon, *Curr. Protoc. Immunol.* **2018**, *120*, 5.1.1-5.1.11.
- 65 S. M. Manohar, P. Shah, A. Nair, *Bioanalysis* **2021**, *13*, 3.

- 
- 66 M. Wouters, What is Flow Cytometry. **2020**.  
<https://www.technologynetworks.com/cell-science/articles/what-is-flow-cytometry-343977>.
- 67 S. Wang, A. Khan, R. Huang, S. Ye, K. Di, T. Xiong, Z. Li, *Biosens. Bioelectron.* **2020**, *154*, 112056.
- 68 P. Zhang, X. Zhou, Y. Zeng, *Chem. Sci.* **2019**, *10*, 5495-5504.
- 69 G. V. Niel, G. D'Angelo, G. Rapsoso, *Nat. Rev. Mol. Cell Biol.* **2018**, *19*, 213-228.
- 70 S. L. N. Mass, X. O. Breakefield, A. M. Weaver, *Trends Cell Biol.* **2017**, *27*, 172-188.
- 71 Lee, K.; Fraser, K.; Ghaddar, B.; Yang, K.; Kim, E.; Balaj, L.; Chiocca, E. A.; Breakefield, X. O.; Lee, H.; Weissleder, R. *ACS Nano* **2018**, *12*, 494–503.
- 72 D. Wu, J. Yan, X. Shen, Y. Sun, M. Thulin, Y. Cai, L. Wik, Q. Shen, J. Oelrich, X. Qian, K. L. Dubois, K. G. Ronquist, M. Nilsson, U. Landegren, M. Kammali-Moghaddam, *Nat. Commun.* **2019**, *20*, 3854.
- 73 A. Morales-Kastresana, T. A. Musich, J. A. Welsh, W. Telford, T. Demberg, J. C. S. Wood, M. Bigos, C. D. Ross, A. Kachynski, A. Dean, E. J. Felton, J. V. Dyke, J. Tigges, V. Toxavidis, D. R. Parks, W. R. Overton, A. H. Kesarwala, G. J. Freeman, A. Rosner, S. P. Perfetto, L. Pasquet, M. Terabe, K. McKinnon, V. Kapoor, J. B. Trepel, A. Puri, H. Kobayashi, B. Yung, X. Chen, P. Guion, P. Choyke, S. J. Knox, I. Ghiran, M. Robert-Guroff, J. A. Berzofsky, J. C. Jones, *J. Extracell. Vesicles* **2019**, *8*, 1597603.
- 74 Y. Tian, L. Ma, M. Gong, G. Su, S. Zhu, W. Zhang, S. Wang, Z. Li, C. Chen, L. Li, L. Wu, X. Yan, *ACS Nano* **2018**, *12*, 671-680.
- 75 W. Shen, K. Guo, G. B. Adkins, Q. Jiang, Y. Liu, S. Sedano, Y. Duan, W. Yan, S. E. Wang, K. Begersen, D. Worth, E. H. Wilson, W. Zhong, *Angew. Chem. Int. Ed.* **2018**, *57*, 15675-15680.
- 76 Z. Nizamudeen, R. Markus, R. Lodge, C. Parmenter, M. Platt, L. Chakrabarti, V. Sottile, *Biochim. Biophys. Acta Mol. Cell Res.* **2018**, *1865*, 1891–1900.
- 77 D. He, S. Ho, H. Chan, H. Wang, L. Hai, X. He, K. Wang, H. Li, *Anal. Chem.* **2019**, *91*, 2768 – 2775.
- 78 G. Rice, Fluorescent Microscopy.  
[https://serc.carleton.edu/microbelife/research\\_methods/microscopy/fluromic.html](https://serc.carleton.edu/microbelife/research_methods/microscopy/fluromic.html).

- 
- 79 K. Shigeyasu, S. Toden, T. J. Zumwalt, Y. Okugawa, A. Goel, *Clin. Cancer Res.* **2017**, *23*, 2391-2399.
- 80 N. Dilsiz., *Future Sci. OA* **2010**, *6*, FSO465.
- 81 I. Krepelkova, T. Mrackova, J. Izakova, B. Dvorakova, L. Chalupova, R. Mikulik, O. Slaby, M. Bartos, V. Ruzicka, *Biotechniques* **2019**, *66*, 277-284.
- 82 L. Moody, H. He, Y. Pan, H. Chen, *Clin. Epigenetics* **2017**, *9*, 119.
- 83 J. Ye, M. Xu, X. Tian, S. Cai, S. Zeng, *J. Pharm. Anal.* **2019**, *9*, 217-226.
- 84 T. Ouyang, S. Liu, Z. Han, Q. Ge, *Anal. Chem.* **2019**, *91*, 3179-3186.
- 85 E. A. Hunt, D. Broyles, T. Head, S. K. Deo, *Annu. Rev. of Anal. Chem.* **2015**, *8*, 217-237.
- 86 M. Kolanowska, A. Kubiak, K. Jazdzewski, A. Wójcicka, *miRNA Biogenesis* **2018**, *1823*, pp 87-101.
- 87 S. Motameny, S. Wolters, P. Nürnberg, B. Schumacher, *Genes* **2010**, *1*, 70-84.
- 88 W. Lu, Y. Chen, Z. Liu, W. Tang, Q. Feng, J. Sun, X. Jiang, *ACS Nano* **2016**, *10*, 6685-6692.
- 89 S. Jiang, Q. Li, C. Wang, Y. Pang, Z. Sun, R. Xiao, *ACS Sens.* **2021**, *6*, 852-862.
- 90 J. Zhao, C. Liu, Y. Li, Y. Ma, J. Deng, L. Li, J. Sun, *J. Am. Chem. Soc.* **2020**, *142*, 4996-5001.
- 91 L. Zhai, M. Li, W. Pan, Y. Chen, M. Li, J. Pang, L. Zheng, J. Chen, W. Duan, *ACS Appl. Mater. Interfaces* **2018**, *10*, 39478-39486.
- 92 J. H. Lee, J. A. Kim, M. H. Kwon, J. Y. Kang, W. J. Rhee, *Biomaterials* **2015**, *54*, 116-125.
- 93 D. He, H. Wang, S. Ho, H. Chan, L. Hai, X. He, K. Wang, H. Li, *Theranostics* **2019**, *9*, 4494-4507.
- 94 J. Zhou, Z. Wu, J. Hu, D. Yang, X. Chen, Q. Wang, J. Liu, M. Dou, W. Peng, Y. Wu, W. Wang, C. Xie, M. Wang, Y. Song, H. Zeng, C. Bai, *Sci. Adv.* **2020**, *6*, eabc1204.



- 
- 95 Y. Yang, E. Kannisto, G. Yu, M. E. Reid, S. K. Patnaik, Y. Wu, *ACS Appl. Mater. Interfaces* **2018**, *10*, 43375-43386.
- 96 X. Gao, S. Li, F. Ding, H. Fan, L. Shi, L. Zhu, J. Li, J. Feng, X. Zhu, C. Zhang, *Angew. Chem. Int. Ed.* **2019**, *58*, 8719-8723.
- 97 M. G. Mohsen, E. T. Kool, *Acc. Chem. Res.* **2016**, *49*, 11, 2540-2550.
- 98 R. Martzy, C. Kolm, R. Krska, R. L. Mach, A. H. Farnleitner, G. H. Reischer, *Anal. Bioanal. Chem.* **2019**, *411*, 1695–1702.
- 99 Wikipedia, Polymerase Chain Reaction.  
[https://en.wikipedia.org/wiki/Polymerase\\_chain\\_reaction](https://en.wikipedia.org/wiki/Polymerase_chain_reaction).
- 100 P. Subsoontorn, M. Lohitnavy, C. Kongkaew, *Sci. Rep.* **2020**, *10*, 22349.
- 101 R. M. Dirks, N. A. Pierce, *Proc. Natl. Acad. Sci. U.S.A.* **2004**, *101*, 15275-15278.
- 102 C. A. Figg, P. H. Winegar, O. G. Hayes, C. A. Mirkin, *J. Am. Chem. Soc.* **2020**, *142*, 8596-8601.
- 103 Y. Tsuneoka, H. Funato, *Front. Mol. Neurosci.* **2020** DOI: 10.3389/fnmol.2020.00075.
- 104 G. Xu, M. Lai, R. Wilson, A. Glidle, J. Reboud, J. M. Cooper, *Microsyst. Nanoeng.* **2019**, *5*, 37.
- 105 D. Evanko, *Nat. Methods* **2004**, *1*, 186.
- 106 Y. Xu, Z. Zheng, *RNA Detection* **2018**, *1649*, 187-196.
- 107 D. Yang, Y. Tang, P. Miao, *Trends. Anal. Chem.* **2017**, *94*, 1-13.
- 108 C. Zhang, J. Chen, R. Sun, Z. Huang, Z. Luo, C. Zhou, M. Wu, Y. Duan, Y. Li, *ACS Sens.* **2020**, *5*, 2977-3000.
- 109 S. Bi, S. Yue, S. Zhang, *Chem. Soc. Rev.* **2017**, *46*, 4281-4298.
- 110 A. I. Bhat, G. P. Rao, Rolling Circle Amplification (RCA). *Characterization of plant viruses*, **2020**, 377-381, DOI: 10.1007/978-1-0716-0334-5\_39.
- 111 T. Hadi, N. Nozzi, J. O. Melby, W. Gao, D. E. Fuerst, E. Kvam, *Sci. Rep.* **2020**, *10*, 10279.

- 
- 112 M. M. Ali, F. Li, Z. Zhang, K. Zhang, D. Kang, J. A. Ankrum, X. C. Le, W. Zhao, *Chem. Soc. Rev.* **2014**, *43*, 3324-3341.
- 113 R. Johne, H. Müller, A. Rector, M. Ranst, H. Stevens, *Trends Microbiol.* **2009**, *17*, 205-211.
- 114 P. M. Lizardi, X. Huang, Z. Zhu, P. Bray-Ward, D. C. Thomas, D. C. Ward, *Nat. Genet.* **1998**, *19*, 225-232.
- 115 W. Zhao, M. M. Ali, M. A. Brook, Y. Li, *Angew. Chem. Int. Ed.* **2008**, *47*, 6330-6337.

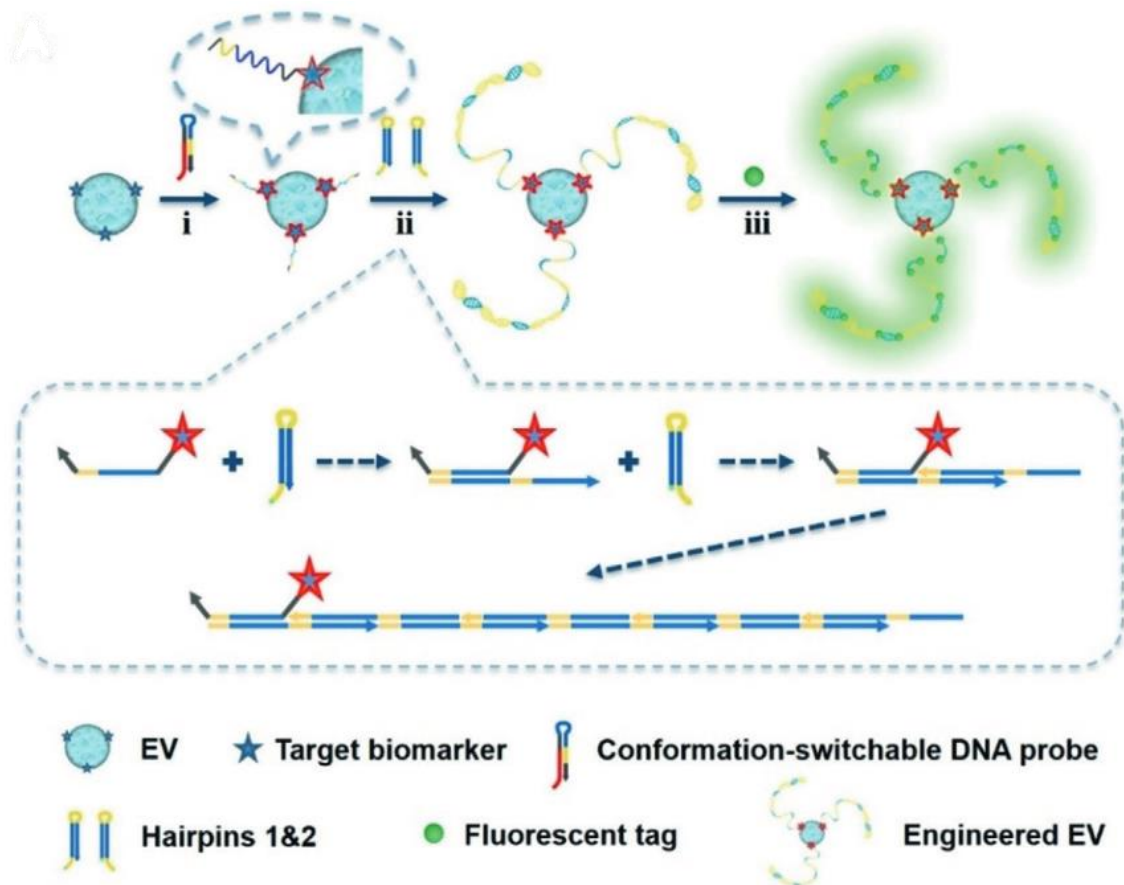
## Chapter 2: A Single Extracellular Vesicle (EV) Flow Cytometry Approach to Reveal EV Heterogeneity

### 2.1 Introduction

Study of the molecular signature of EVs is critical for profoundly understanding their biological functions and clinical values.<sup>1,2</sup> Existing methods for EV study are primarily focused on bulk analysis of a large number of EVs, because the small physical dimensions of EVs limit the total amounts of biomolecules to be carried in each EV, greatly enhancing the difficulty in molecular profiling.<sup>3,4,5,6,7</sup> However, subtle molecular differences at the single EV level may yield significant variation in EV biological functions,<sup>8</sup> and the highly heterogeneous nature of EV population demands the development of techniques capable of profiling individual EVs.<sup>9</sup> Most recently, single EV counting with a nanochip<sup>10,11</sup> and imaging single vesicles with advanced fluorescence microscopy<sup>12</sup> have been reported, and showed that EVs from different cell of origin can carry distinct surface markers mimicking their parent cells. Still, they require EV immobilization steps, limiting the down-stream investigations on EV functions and biogenesis.

Flow cytometry has been widely employed to distinguish different cell types in mixed populations based on the expression of cellular markers.<sup>13</sup> Similarly, it could be used to study the heterogeneous EVs. However, the sizes of EVs fall well below the detection limit of conventional flow cytometers, making it impossible to do single-EV analysis without significant instrumentation development.<sup>14</sup> Herein, we report the first single-EV flow cytometry analysis (FCA) in conventional flow cytometers enabled by target-initiated engineering (TIE) of DNA nanostructures on individual EVs (Scheme 2.1). This technique

employs a conformation-switchable DNA probe to bind to the EV surface marker, which triggers the engineering of a DNA nanostructure by hybridization chain reaction (HCR).<sup>15,16</sup> The HCR products not only enlarge the overall size of the single EV to be beyond 500 nm, but also can bind to multiple fluorophores to amplify the signal from the few marker molecules locating on the limited area of EV surface, both enabling visualization of single EVs in a conventional flow cytometer, and greatly simplifying measurement of multiple markers on the same EV.



**Scheme 2.1 The Single Extracellular Vesicle Flow Cytometry Analysis Technique enabled by Target-Initiated Engineering of DNA Nanostructures.** Figure reprinted from Ref.17. © 2018, John Wiley and Sons.

## 2.2 Material and Methods

**Chemicals and materials.** The standard EVs (lyophilized EVs produced by COLO-1 cells) were obtained from HansaBioMed Life Science Ltd (Tallinn, Estonia). CD63 protein was obtained from Sino Biological Inc. (Beijing, P.R.China). Qdot™ 525 Streptavidin Conjugate and Alexa Fluor® 488 streptavidin were obtained from Thermo Fisher Scientific Inc. (Waltham, MA). All other chemicals in this study were purchased from Sigma-Aldrich (St.Louis, MO) or Fisher Scientific (Fairlawn, NJ), and used as received. All DNA oligos were obtained from Integrated DNA Technologies Inc. (Coralville, Iowa). Flow Cytometry Nano Fluorescent Size Standard Kit was obtained from Spherotech Inc. (Lake Forest, IL).

**Cell lines and cell culture.** The three cell lines used were purchased from the American Type Culture Collection (ATCC) and cultured at the recommended media containing 1% penicillin streptomycin. MCF-10A cells were cultured in a 1:1 mixture of Dulbecco's modified Eagles medium (DMEM) and Ham's F-12 medium supplemented with 5% horse serum, 0.1 µg/ml cholera toxin (Sigma Aldrich), 10 µg/ml insulin, 1.4 µM cortisol, and 20 ng/ml epidermal growth factor (EGF). DMEM supplied with 10% fetal bovine serum (FBS) was used for MCF-7; and DMEM with 20% FBS and 1% penicillin streptomycin was for SKBR3. All cell lines were maintained at 37 °C in a humidified 5% CO<sub>2</sub> incubator and routinely screened for Mycoplasma contamination. Except for cortisol (Sigma Aldrich), all chemicals were attained from Thermofisher Scientific.

**EVs extraction.** Once the cell culture reached a confluency of 75%, the medium was changed into the EV-depleted culture medium. After 24 h, the EVs were harvested using an Optima XPN-80 S-2 ultracentrifuge (Beckman Coulter Inc.). First, the culture medium

(30 ml) was collected and spun at 500g for 15 min to remove cells. The second centrifugation step was at 15,000g for 20 min, aiming to remove cell debris. Then the supernatant was centrifuged twice at 110,000 g, each lasting for 70 mins. All centrifugation steps were carried out at 4 °C. The EV pellet was resuspended in 1×PBS, and used immediately. Before measurement by TIE enabled EV counting, the particle concentration was measured by NTA and the total protein concentration was determined by BCA.

**EV engineering.** EV engineering was carried out by mixing 10 µL of EV suspension at  $1 \times 10^{12}$  particles/mL (concentration varied for measurement of EV detection range) with 12.5 nM aptamer- containing P and 1 µM H1 and H2. The mixture was incubated at 37 °C for 8 h. The resultant engineered EVs were then incubated with 2 µl QD-525 (for CD63 detection) or the Alexa660- labeled DNA tag (for HER2 detection) for 30 mins at RT, and diluted with 400 µl water before measurement.

**The kinetics of TIE.** Upon mixing the EVs with the DNA probes and hairpins, the sample was incubated for 2, 4, and 8 hrs. After the flow cytometric analysis, a gate was applied on the flow plots to identify the particle cluster displaying higher fluorescence and larger forward scatter than background, which were considered as the “detectible events”. The “particle count” within the gate and the “mean fluorescence intensity (MFI)” were assessed.

**Flow cytometry.** Single EV counting was carried out in a BD FACS Canto II Flow Cytometer (BD Biosciences), using a red laser for excitation wavelength of 633 nm (FL4 channel, for HER2 detection) and a blue laser at 488 nm (FL1 channel, for CD63 detection). The sample was added to a 12 × 75 mm polypropylene round-bottom flow tube, and run at

the speed setting of “medium”, with the data acquisition time fixed at 3 mins. The typical settings for the FSC, SSC, FL1, and FL4 channel were 330, 330, 385, and 300, respectively, with the threshold for FSC set at 4,000, and that for SSC set at 2,000. All data were acquired and analyzed by the BD FACSDiva and FlowJo software. Measurements of engineered EV were always done in parallel with the negative control of EV+H1+H2+QDs (no target-binding probe) to ensure the scatter pattern was from the individual engineered EV.

**TEM and AFM.** Transmission electron microscopy (TEM) was taken with a JEOL 2011 microscope operated at 100 kV and Atomic Force Microscopy (AFM) was carried out on a Horiba LabRam/ AIST-NT AFM. Purified EVs were deposited on formvar-carbon-coated EM grids. The unmodified EVs were stained with 2% uranyl acetate and the engineered EVs with HCR product on the surface were stained with 0.5% uranyl acetate. Both were embedded in 1% methyl cellulose, dried at room temperature and viewed using a Tecnai12 TEM. AFM was carried out in air under the tapping mode with a Dimension 5000 Scanning Probe Microscope on a freshly cleaved mica, on which 10  $\mu$ l of the diluted sample was deposited and left to absorb for 10 min. Sample were then rinsed with deionized water for 3 times and dried by N<sub>2</sub>. The image background was flattened by NanoScope Analysis software.

**Expression of CD63 and HER2 tested by ELISA.** Expression of CD63 and HER2 level was determined by ELISA. The 96-well immuno plates were coated for 8h at RT with 50ul of diluted exosome solution (for exosome standard, we used 0.03  $\mu$ g/ml) and blocked overnight at 4°C with a blocking solution (5% milk in 1xPBS). After washing with 1xPBS, 100  $\mu$ l of diluted primary antibody (0.2  $\mu$ g/ml anti-CD63 or anti-HER2; antibodies from

ThermoFisher) was applied to each well for 2 hrs at RT. After washing with 1xPBS, bound protein was detected by labelling with an HRP-conjugated goat anti-mouse IgG (ThermoFisher) and subsequent incubation with supersignal west pico chemiluminescent substrate (ThermoFisher). Absorbance was recorded at 450 nm on a Qubit 2.0 Fluorescence reader.

**Gel electrophoresis.** Gel electrophoresis to confirm formation of the long DNA chains was carried out in 1% Agarose gel in 1xTBE. The DNAs were stained by SYBR gold (Invitrogen Inc.). The imaging was taken under a Spectroline® UV transilluminator.

**Fluorescence microscopy.** The EV sample (10  $\mu$ L of EV suspension at  $1 \times 10^{12}$  particles/mL) was incubated with anti-CD9 (0.1  $\mu$ g/ml) and the TIE probe (10 nm) targeting CD63 overnight. Then H1 and H2 (10 nm) were added to generate the long DNA chains on EVs. Before detection, the sample was incubated with streptavidin conjugate Qdot (Thermo Fisher) and Rh-IONPs for 30 mins. Then 10  $\mu$ L of the sample was deposited onto the poly-L-lysine coated glass slide conjugated to protein G, and incubated for 10 min, allowing protein G to capture the anti-CD9 and thus immobilize the EVs. After three rinses with deionized water and dried by N<sub>2</sub>, fluorescence imaging was performed on a Leica Inverted SP5 Confocal Microscope. The measurement was performed using an Ar laser at  $\lambda_{ex} = 488$  nm for fluorescence from QD-525, and the HeNe laser at  $\lambda_{ex} = 543$  nm for fluorescence from the rhodamine dye.

**Nanoparticle tracking analysis.** Suspensions containing EVs from plasma or cell culture medium were analyzed using an NTA instrument (NanoSight NS300, Malvern Instruments). For this analysis, a monochromatic laser beam at 532 nm was applied to the



dilute suspension of EVs. A video of 30–60 s duration was taken with a rate of 25 frames/s, and EV movement was analyzed using NanoSight NS300 Software (Version 3.2). NTA post-acquisition settings were optimized and kept constant between samples, and each video was then analyzed to give an estimate of the concentration.

**Statistical analyses.** Data are presented as mean  $\pm$  SD as indicated for each graph. Means and standard deviations were calculated using OriginPro 2017 (Origin Lab Corp.). Student's t-test was used for evaluation of differences in means for normally distributed data. All P values are two-tailed, and values of less than 0.05 were considered to indicate statistical significance: \* $p < 0.05$ , \*\* $p < 0.01$ .

## 2.3 Results and Discussion

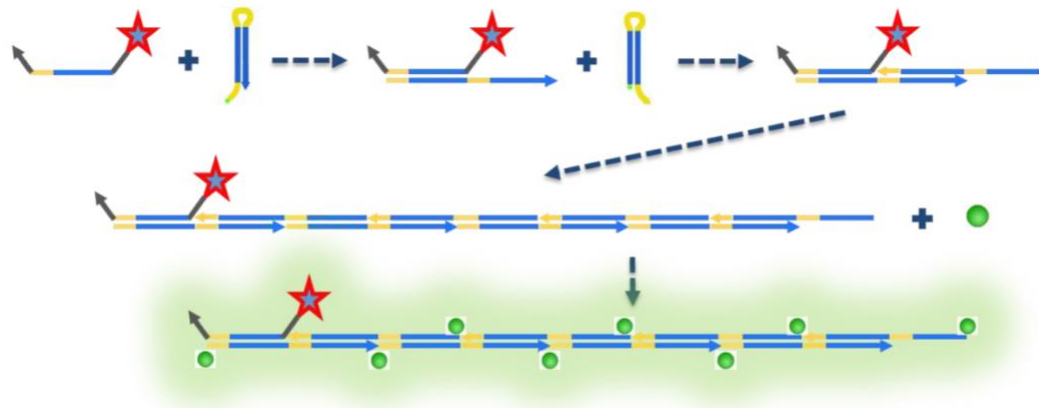
To test the working principle, we designed the conformation-switchable probe to recognize CD63, a classic tetraspanin marker that is highly abundant in various EVs (Scheme 2.1). This probe contained a target recognition domain with the sequence of an anti-CD63 aptamer<sup>18</sup> and a trigger domain for initiation of DNA growth via HCR. These two domains were flanked by a hinge sequence to achieve conformation change triggered by aptamer–target interaction (Table 2.1 and Figure 2.1): apart of the target recognition domain hybridized with the trigger domain (that is, “deactivated state”) to form a hairpin structure, which could be opened upon target binding to expose the sequence (“activated state”) for hybridization with Hairpin 1(H1). Then sequential hybridization between H1 and H2 would occur to build the long dsDNA product on EV (Scheme 2.1 and Figure 2.1). The design of target-initiated engineering of DNA nanostructure could effectively

eliminate non-specific DNA growth without the target. Furthermore, the DNA nanostructures constructed upon recognition of the free, non-EV bound target would not locate on EV surface and should not reach the size range detectable by the conventional flow cytometer. Both features significantly reduce the background in FCA and render our technique ultra-high simplicity: no washing is necessary to remove the unreacted probes.

**Table 2.1 DNA sequences used in TIE system for CD63.**

Name	Sequences (5'-3')
Initiator Probe 1 (IP1) targeting CD63	CAC CCC ACC TCG CTC CCG TGA CAC TAA TGC TAA CAC GCC AGT CTA GGA TTC GGC GTG TTA GCA TTA G/3SpC3/
Simple initiator probe (SI)	AGT CTA GGA TTC GGC GTG TTA GCA
Hairpin 1 (H1)	Biotin-TGC TAA CAC GCC GAA TCC TAG ACT CAA AGT AGT CTA GGA TTC GGC GTG /3SpC3/
Hairpin 2 (H2)	Biotin- AGT CTA GGA TTC GGC GTG TTA GCA CAC GCC GAA TCC TAG ACT ACT TTG/3SpC3/

The regions sharing the same color in different strands are the complementary sequences used for hybridization. Underline sequences indicate complementary regions of the probes to form hairpin structure. Initiator Probe 1 includes a CD63 recognition domain (red), and a trigger domain (yellow and blue) for growth of a long dsDNA via DNA hybridization cascade, connected by a hinge domain (grey). The 5' end of both hairpins labeled with biotin for binding with the streptavidin conjugated fluorescent tag.



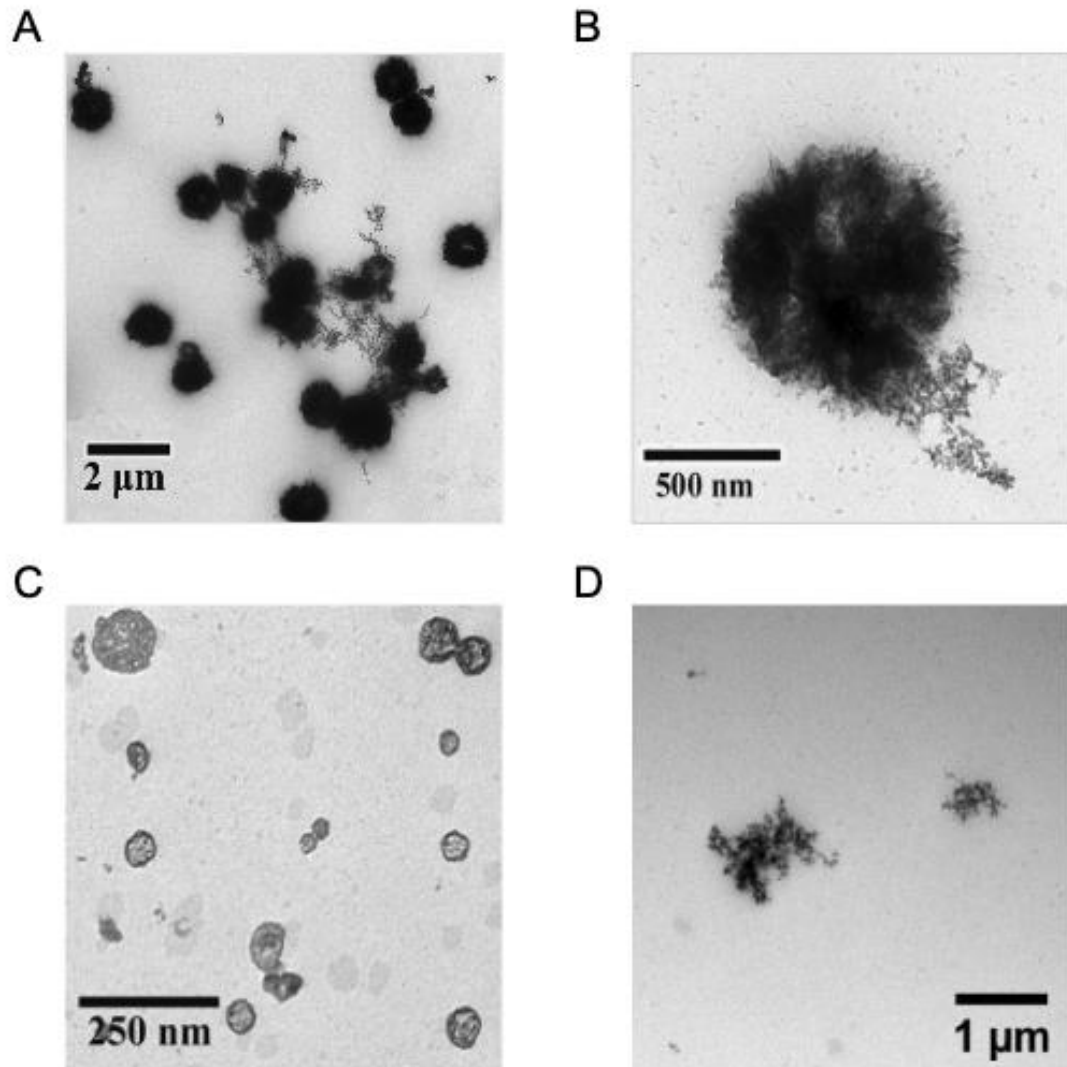
**Figure 2.1 Hybridization cascade 1 for CD63.** Figure reprinted from Ref.17. © 2018, John Wiley and Sons.



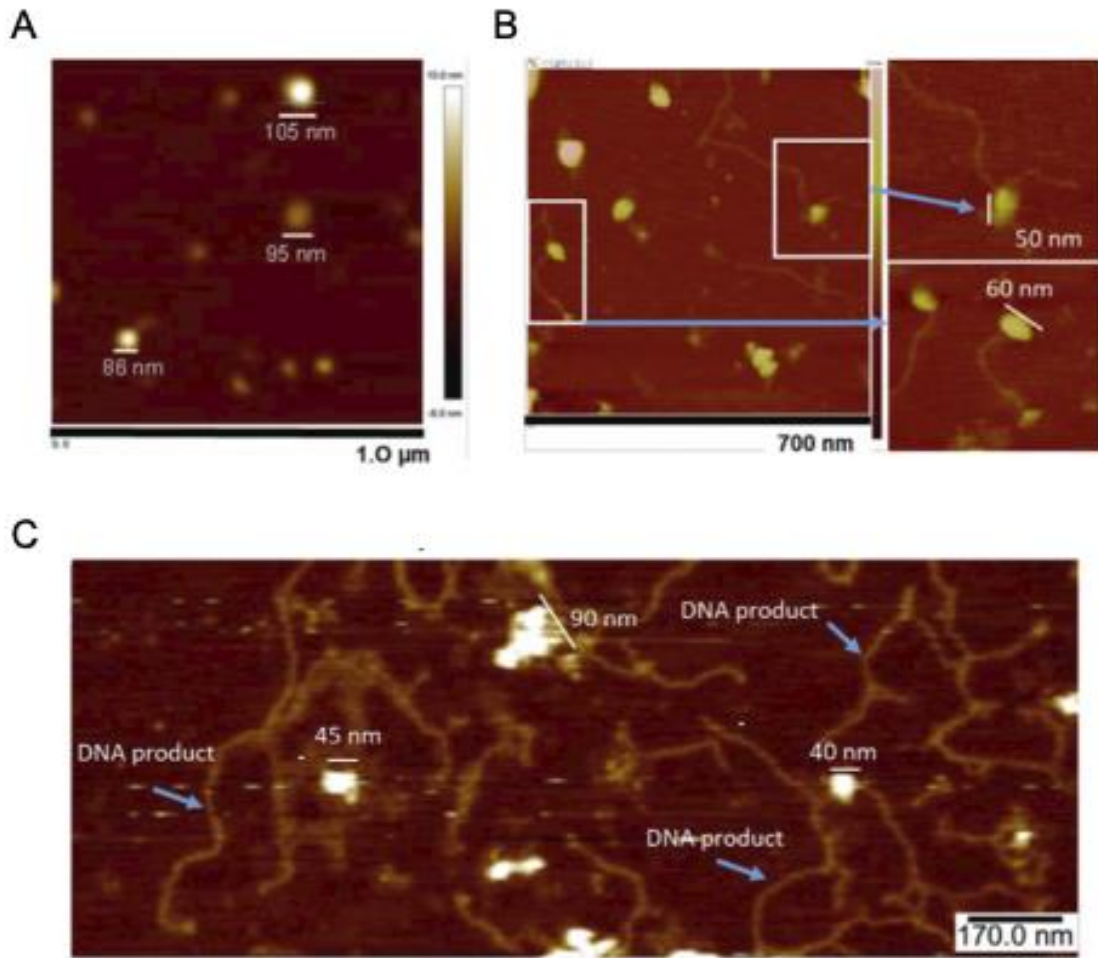
**Figure 2.2 Analysis of the long DNA products by gel electrophoresis.** Lane 1: reaction probes only; Lane 2, 3, and 4: reaction triggered by the simple initiator, CD63 protein, and CD63+ EVs, respectively. Figure reprinted from Ref.17. © 2018, John Wiley and Sons.

Successful DNA hybridization cascade initiated by CD63 or the CD63-containing EVs was verified by native agarose gel electrophoresis. We can see from the gel image (Figure 2.2) that, long DNA products were formed in the presence of CD63 protein (Lane

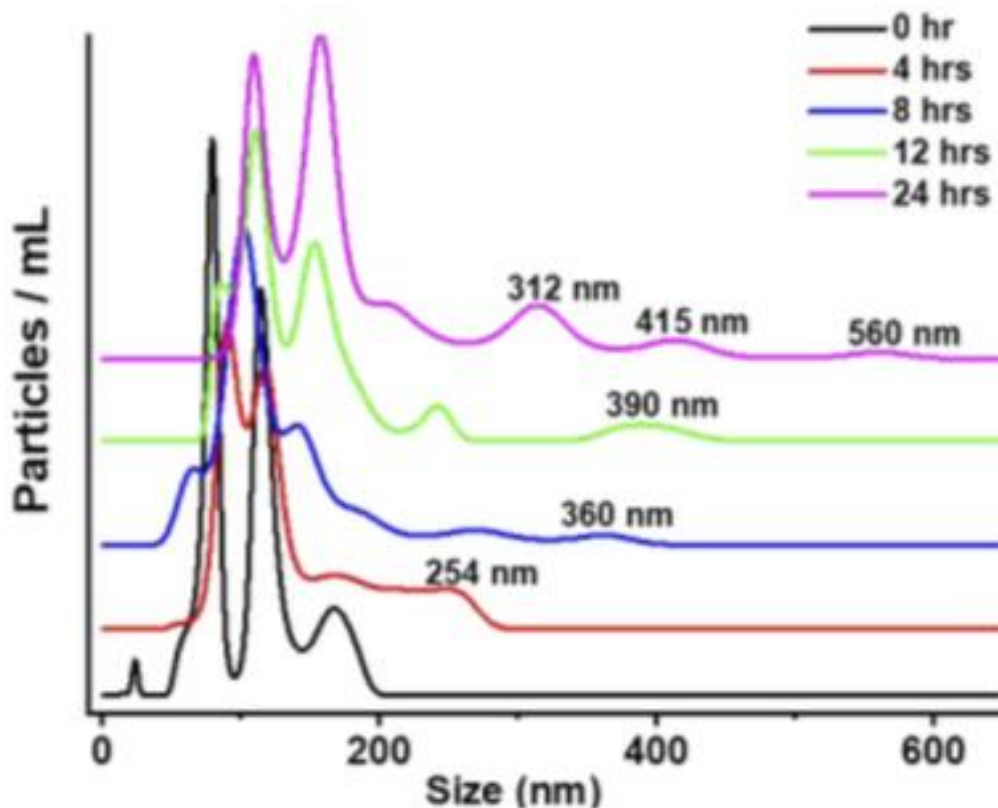
3), accompanied with significant consumption of H1 and H2, similar to the reaction between the hairpins and a simple initiator (Lane 2), a sequence of the trigger domain that can directly hybridize with H1 without target recognition and initiate DNA growth. With the CD63-containing EVs (referred to as “standard EVs” hereafter), most of the long DNA products were trapped inside the loading well probably by binding to the EVs (Lane 4). We employed transmission electron microscopy (TEM) to confirm the size enlargement in EVs produced by TIE. As clearly illustrated in Figure 2.3A, after TIE, each standard EV exhibited the “hairy” morphology on its surface, with the overall size increasing from the original tens of nanometers to hundreds of nanometers and maintaining the spherical shape (Figure 2.3 B and C). In contrast, the DNA hybridization products triggered by simple initiator were in random shapes without the densely stained core (Figure 2.3 D). The growth effect was also viewed by atomic force microscopy (AFM) (Figure 2.4) and nanoparticle tracking analysis (NTA) Supporting Information, (Figure 2.5): after TIE, DNA strands up to 250 nm long were seen surrounding the individual EVs under AFM; and the size distribution profile in NTA shifted to the larger size region with a new peak at 500 nm appeared.



**Figure 2.3 TEM images.** TEM images of A) the Engineered EVs, B) single engineered EV, C) EVs before engineering, and D) DNA hybridization products triggered by SI. Figure reprinted from Ref.17. © 2018, John Wiley and Sons.



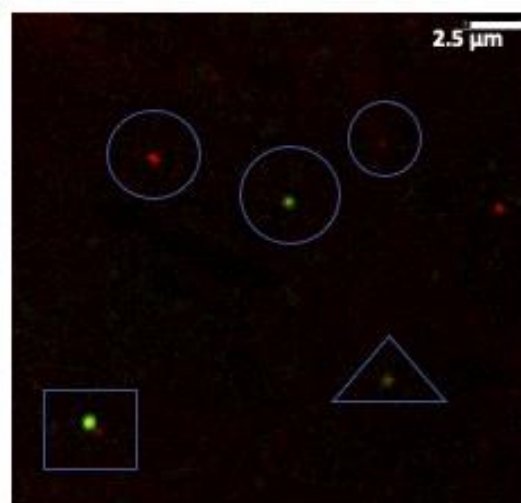
**Figure 2.4 AFM images.** AFM images of the EVs A) before and B) after engineering. The lines drawn on the images represent the length of the subjects. DNA products longer than 250 nm can be seen around C) the EV after engineering, increasing the overall size of the EVs. Figure reprinted from Ref.17. © 2018, John Wiley and Sons.



**Figure 2.5** Size distribution of EVs obtained at various duration of DNA hybridization (0 – 24 hrs) evaluated by NTA. Traces obtained at various reaction duration were stacked to increase visibility. Figure reprinted from Ref.17. © 2018, John Wiley and Sons.

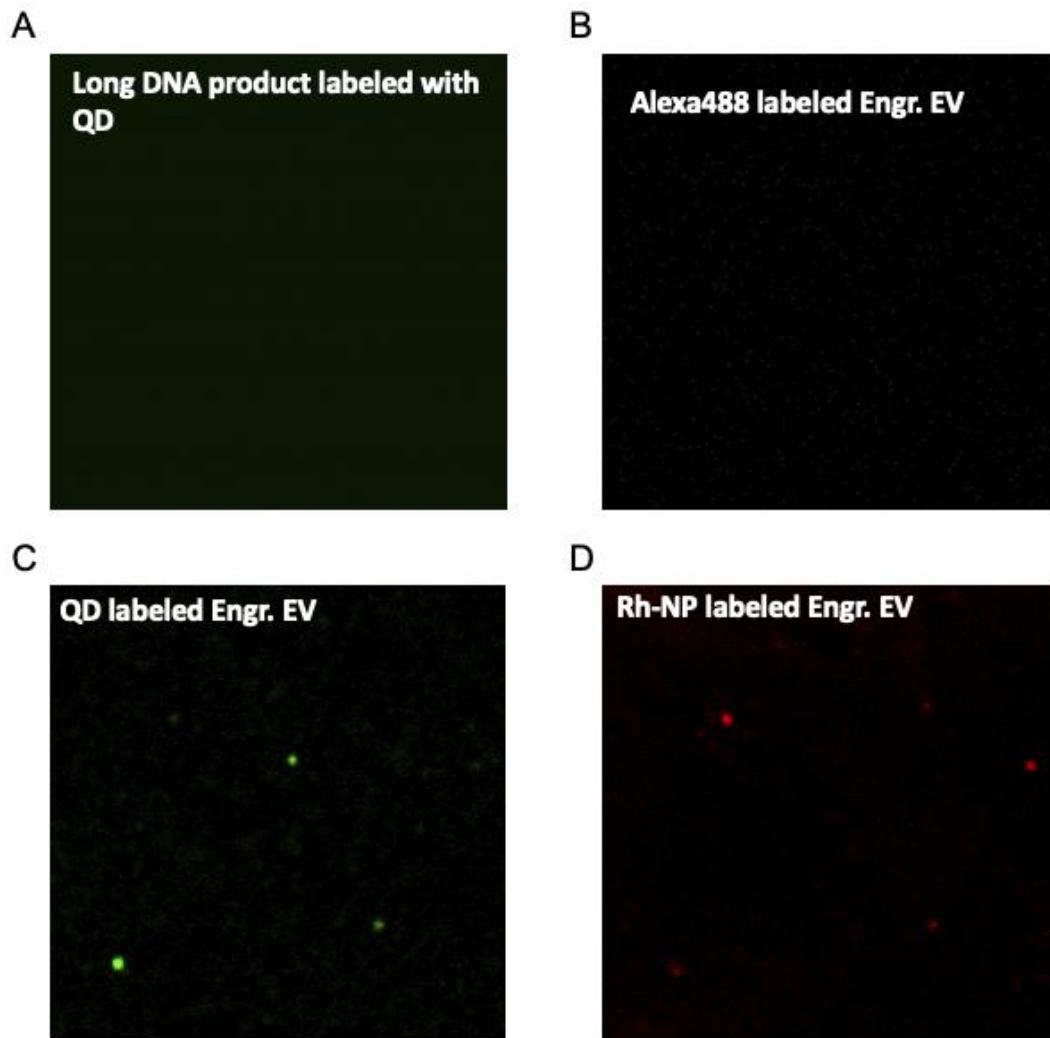
We examined the enlarged EVs by a confocal fluorescence microscope. Labeled the hairpins with biotin, the long DNA products can be tagged with the streptavidin-conjugated fluorescent probes, like the Qdot 525 streptavidin conjugate (QDs, Ex488 nm/Em 525 nm) and the streptavidin/rhodamine-conjugated iron oxide nanoparticles (RhNPs, Ex 547 nm/Em 572 nm). These two tags were used to produce two distinct EV populations in separate reaction tubes, which were mixed and inspected under microscope. Indeed, the engineered EVs labeled with either the QDs or the RhNPs were clearly discernible in the confocal mode with an objective of 40x (Figure 2.6). We even found

particles that were overlapped (highlighted by a triangle), located close to each other (highlighted by a square), or completely separated (indicated by circles), showing that each fluorescent particle represented one individual vesicle. The negative controls, that is, the QD-labeled DNA nanostructure established by the simple initiator, and the RhNPs or QDs by themselves, were not observable even under a higher magnification of 60x or 100x (Figure 2.7), which was due to the few numbers of QDs on each DNA nanostructure. On contrary, each EV could carry multiple surface markers, and be labeled by multiple dsDNAs (Figure 2.4) that not only enlarge the overall size, but also amplify the total fluorescence signal, making the single EV visible under the same imaging setting. This result confirms that the EVs enlarged by TIE were visible by conventional optical imaging tools.



**Figure 2.6** Fluorescence microscopy image of the Engr.EV tagged with rhodamine-nanoparticles or QDs-525. Engr. EV-RhNPs show in red, and Engr. EV-QDs show in green. Circles – Engr. EV-RhNPs or Engr. EV-QDs, well separated from each other; Square – One Engr. EV-QDs located nearby another Engr. EV-RhNPs; Triangle – Engr. EV labeled with both QDs and Rh-NPs. Figure reprinted from Ref.17. © 2018, John Wiley and Sons.

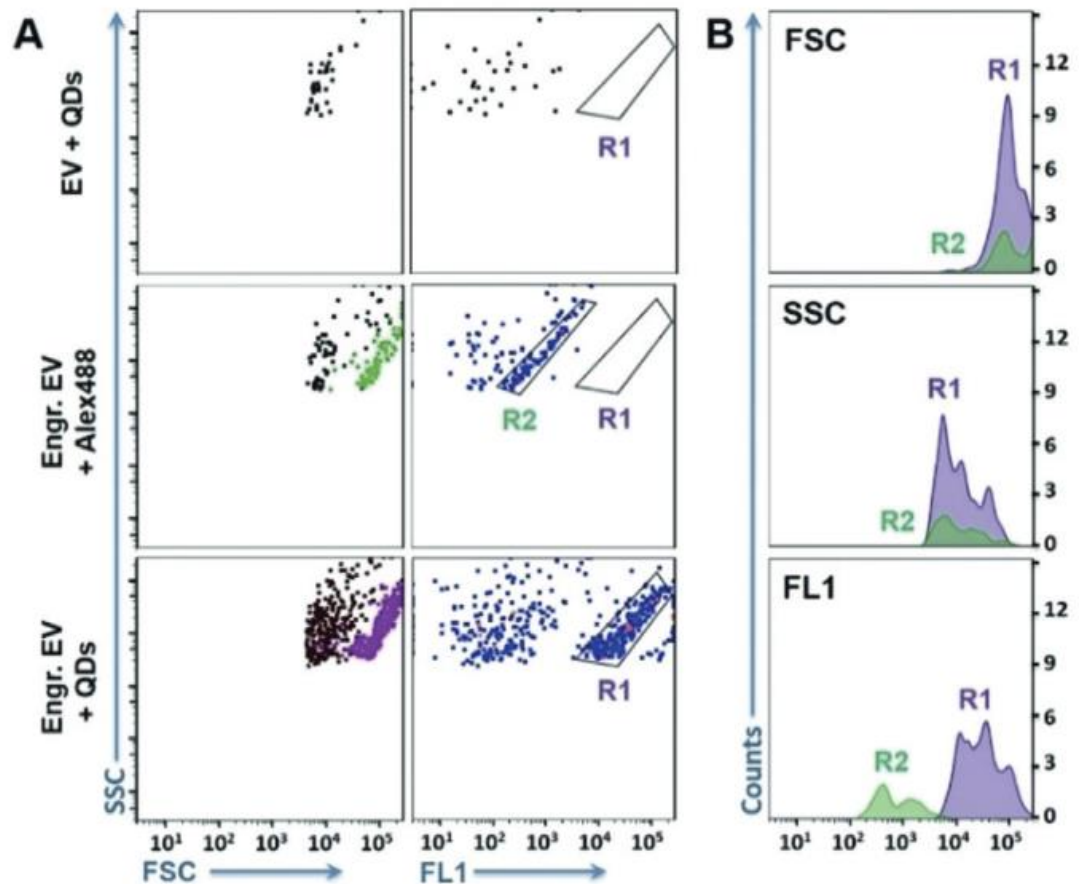




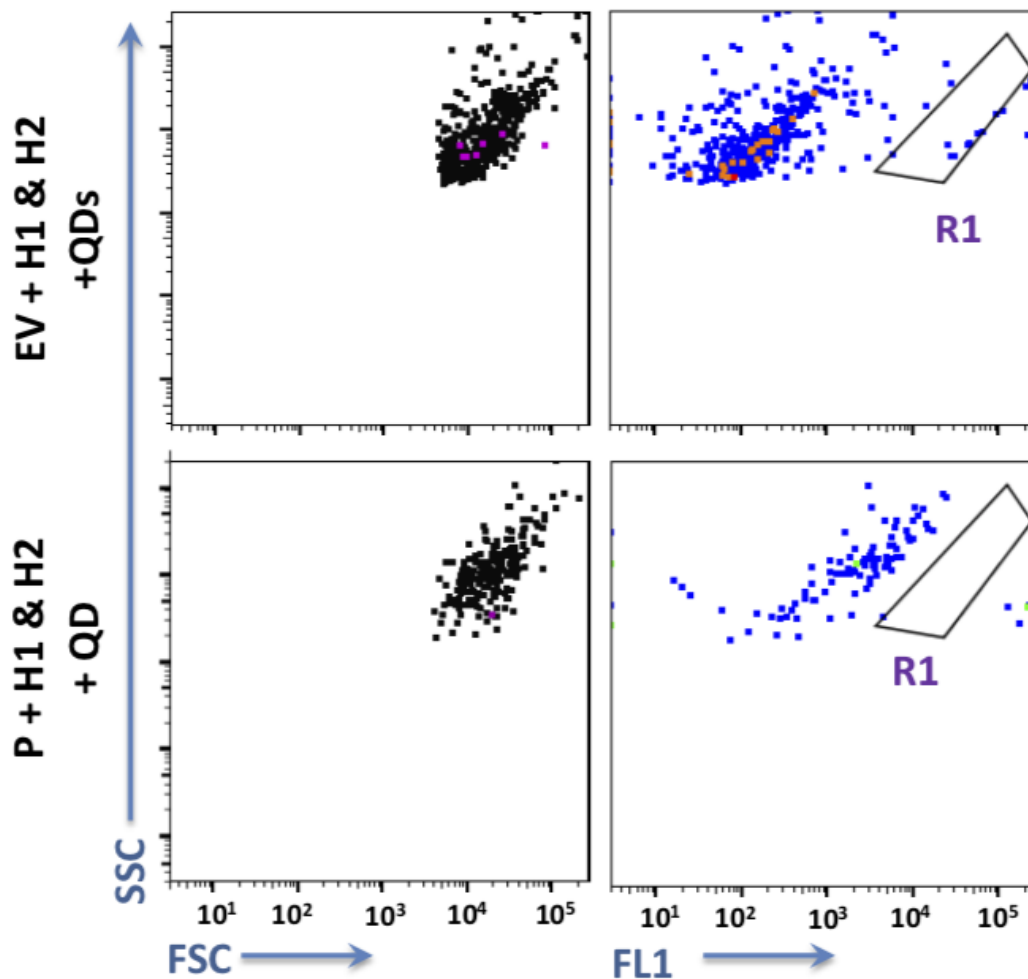
**Figure 2.7 Fluorescence microscopy images of HCR products and engineered EV.** A): HCR products (long chain DNA); B): Engineered EV labeled with Alexa488; C): Engineered EV labeled with QD; D): Engineered EV labeled with rhodamine (Rhod) - nanoparticle (NP). Figure reprinted from Ref.17. © 2018, John Wiley and Sons.

Compared to microscopic imaging, flow cytometry provides fast and automatic particle counting at the rate of thousands particles per second; and can sort pure particle populations defined by fluorescence patterns, much more ideal for interrogating single biological particles. Thus, we explored whether the engineered EVs could be detected in a conventional flow cytometer FACSCanto that is widely used in research and clinical

settings. Analysis of the standard beads confirmed that this instrument could not see particles smaller than 500 nm. In this experiment, the DNA nanostructure carried by the engineered EVs were tagged by either Alexa Fluor 488 streptavidin conjugates (that is, Engr.EV-Alexa488) or the green QDs-525 (Engr.EV-QDs). Interestingly, both EV samples revealed a significant particle cluster in the flow cytometry plots of FSC (forward scatter) vs. SSC (side scatter) and FL1 (fluorescence channel, ex = 488 nm) vs. SSC (Figure 2.8A). These particles exhibited larger FSC and higher fluorescence (FL) than the background particles, confirming the significant EV size enlargement induced by the CD63-initiated EV engineering; and the signal amplification from the multiple fluorescent tags bound to the long DNA chains on each EV. Gating the particle cluster by R1 (for the QD label) or R2 (for the Alexa488 label) illustrated that the enlarged EVs represented about 50% of the total particles detected for each sample (Table 2.2). In contrast, no distinct particle cluster was detected on the flow plots obtained from the negative control samples, including the EVs labeled by the anti-CD63-conjugated QDs without any size enlargement (that is, EV-QDs) (Figure 2.8A), and the EVs mixed with just the hairpins and QDs (Figure 2.9). The background particles present in Figure 2.8A and the Figure 2.9 with low forward scatter and fluorescence signals might be produced from non-specific adsorption of the hairpins and QDs on the EVs, as well as random aggregation of QDs in solutions. Furthermore, TIE on free CD63 did not produce observable particles, ensuring the counting was from intact EVs instead of free markers released by cells or from vesicle breakage.



**Figure 2.8 Representative scatter plots and histograms of flow cytometry analysis of the EVs before and after TIE.** A): Representative scatter plots of flow cytometry analysis of the EVs before and after TIE. Top to bottom: Standard EVs directly labeled with QDs (EV + QDs); engineered EVs labeled with Alexa488 or QDs-525. The particle populations shown in green and purple on the light scatter plots of FSC vs. SSC were those included in R2 and R1, respectively, on the flow plots of FL1 vs. SSC. B): Histograms for the signals of FSC, SSC, and fluorescence produced by the engineered EVs labeled with Alexa488 (green) and QDs-525 (purple). All samples started with about  $10^9$  EV particles. Figure reprinted from Ref.17. © 2018, John Wiley and Sons.



**Figure 2.9 Representative scatter plots of flow cytometry analysis of the negative controls.** Negative controls (the mixture containing only the DNA probes used in reaction and QDs (P + H1&H2 + QD); and the mixture of EV, hairpins, and QDs (EV + H1&H2 + QDs)) for the positive samples measured by flow cytometry with results shown in Figure 2.8. Figure reprinted from Ref.17. © 2018, John Wiley and Sons.

**Table 2.2 Readings for the measurements displayed in Figure 2.8 and Figure 2.9.**  
Table reprinted from Ref.17. © 2018, John Wiley and Sons.

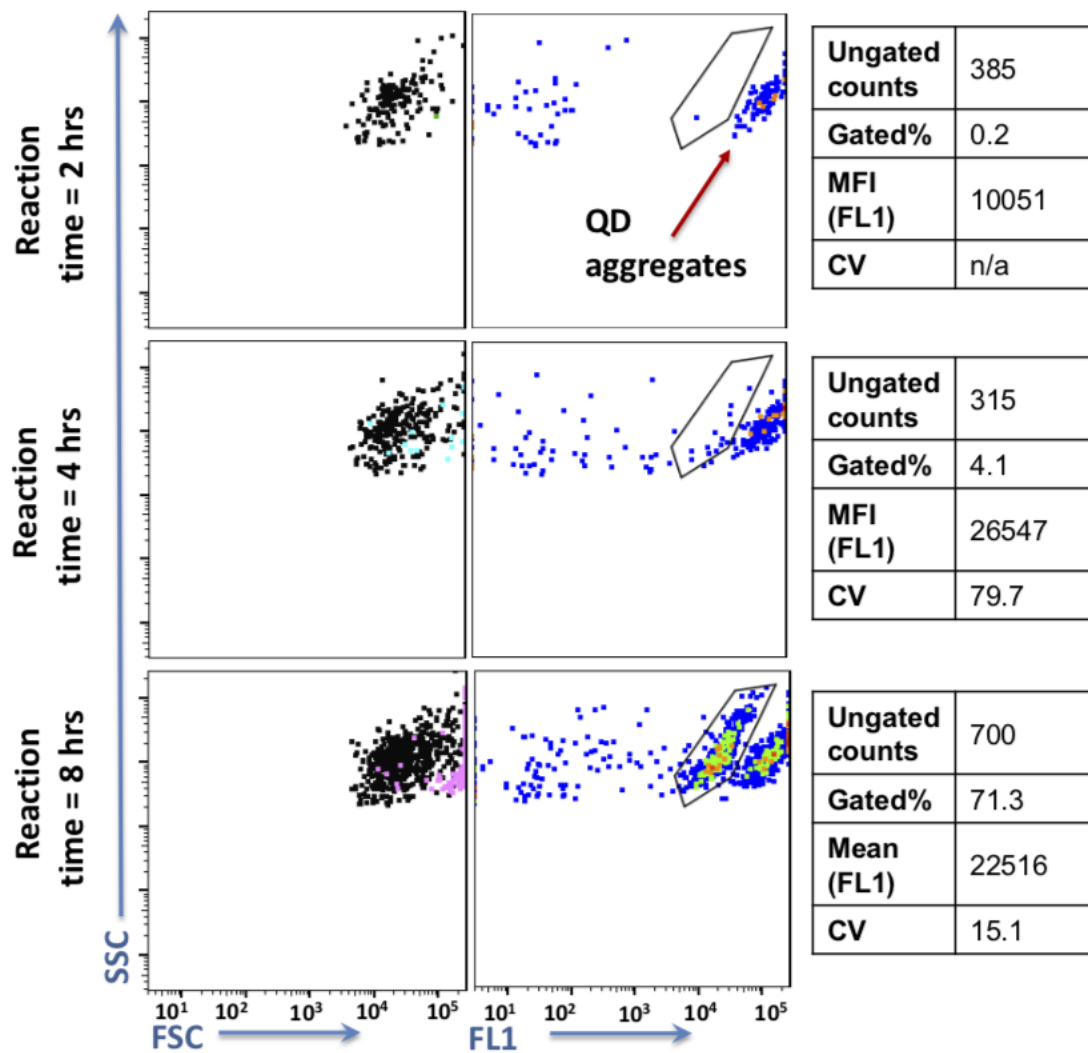
Sample Name	Total counts	%Counts in R1
EV-QDs	35	0
Engr. EV-Alexa488	140	52%
Engr. EV-QDs	525	51%
Control 1: EVs + H1&H2 + QDs	420	1.6%
Control 2: P + H1&H2 + QDs	210	0

Using R1 and R2, we compared the scatter and FL signals obtained with Alexa488 and QDs (Figure 2.8B). Both labels gave out comparable FSC readings (the mean FSC intensity ratio of QD/Alexa = 0.92 : 0.07 ( n = 3)), indicating the size enlargement effect was mainly resulted from the growth of the dsDNA, not the additional size of the fluorescent tag. Labeling with QDs resulted in 70.5 : 6.2 ( n = 3) times higher FL than with Alexa488. The higher FL shifted the enlarged EVs further away from the background particles, making the population more distinct, which is acritical characteristic for future sorting of specific EV populations. This is the first time a new population of detectible EVs appearing on the flow cytometric plots to enable clear and unambiguous recognition of pure EV population in a conventional flow cytometer, owing to TIE-enabled transformation of the invisible EVs to the visible particles.

The kinetics of TIE was studied by changing the HCR time from 0 h to 24 h. A gate was applied on the flow plots to identify the particle cluster displaying higher FL and larger FSC than background, which were considered as the detectible events. We found that, a

reaction time of 2h produced only very few numbers of the detectible events, which dramatically increased at 4 and 8h (Figure 2.10). NTA measurement also confirmed that with the reaction time increasing to 4 and 8h, more engineered EVs larger than 250 nm were produced (Figure 2.5). The mean fluorescence intensity (MFI) gradually increased with the reaction time going from 0 to 8 h (Figures 2.10 and 2.11). However, extending the reaction to 12 h did not induce significant changes in the number of detectible events and the MFI value detected in the flow cytometer, neither big change was observed in the size distribution profile obtained with NTA. This result indicates that recognition of the CD63-positive EVs may have reached a steady state and no new engineered EVs could be produced with longer reaction time. Still, the length of the DNA product continued to increase with longer reaction duration, which generated the engineered EVs larger than 500 nm at 24 h observed by NTA (Figure 2.5). However, space hindrance and winding of the long DNA strand may have prevented more QDs from binding to the DNA; and after being kept at 37 C for 24 h, the EVs may no longer be stable, both leading to the decrease in MFI and detectible events measured by flow cytometry (Figure 2.11). While detailed study of the kinetics of engineering DNA nanostructures on EVs needs to be conducted in future works, the present work employed overnight reaction to obtain stable signals in flow cytometric analysis of single EVs. Under the optimized TIE conditions, we confirmed that the number of detectible events was linearly ( $R^2 = 0.9974$ ) proportional to the number of EVs in the sample within the range of  $20 \text{ mg mL}^{-1}$  to  $500 \text{ mg mL}^{-1}$  (Figure 2.12), proving the capability of our method in EV quantification. Furthermore, the robustness of our method was verified by the intraday and interday replicates (Table 2.3). The Student's t test

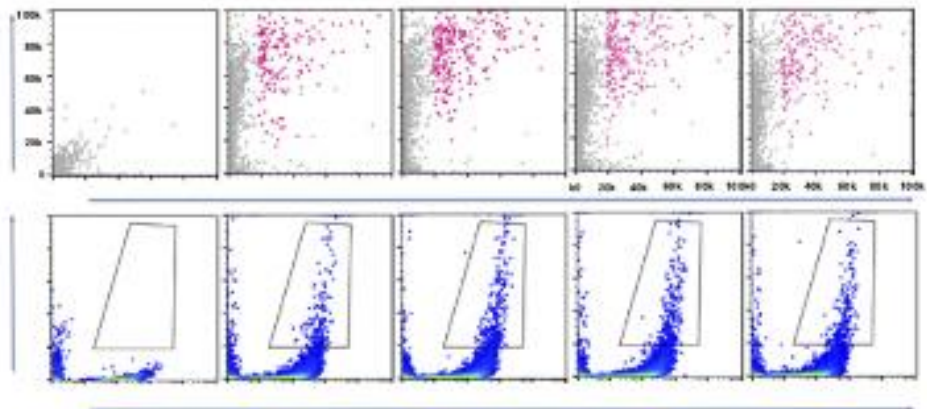
obtained a p value smaller than  $10^{-4}$  when evaluating the MFI or mean forward scatter (MFS) among all these replicates, showing that EV engineering is highly reproducible. More importantly, we showed that our method can directly engineer the EVs in biofluids such as cell culture medium (Figure 2.13) and serum (Figure 2.14) by simply treating the matrix with sodium citrate to inhibit exonuclease activity.<sup>19</sup> Direct EV detection in biological samples with minimum sample pretreatment and without EV enrichment or immobilization is a big advancement compared to existing technologies and makes our method highly suitable for studying the heterogeneity of EV populations and examining their clinical values.



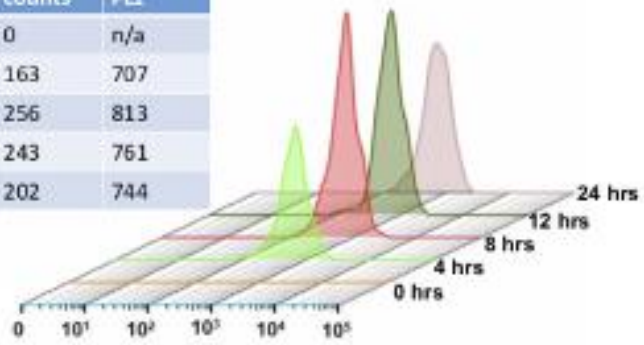
**Figure 2.10 Investigation of effects on signal intensity and particle counting from the duration of EV engineering.** QD aggregates were detected here due to reduction of the power setting for the FL1 channel, which was set to 350, instead of 385, the common setting for all other measurements. Figure reprinted from Ref.17. © 2018, John Wiley and Sons.



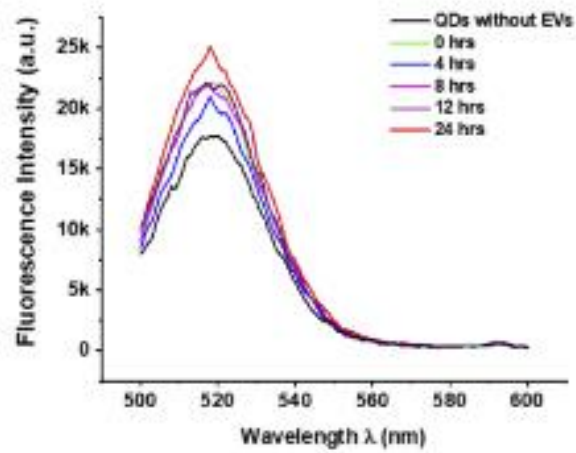
A



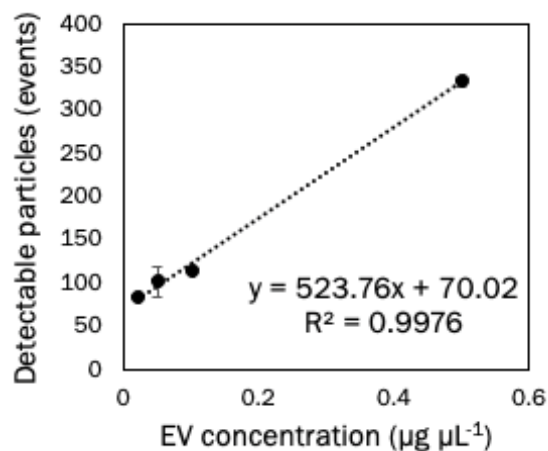
HCR Duration	Gated counts	Mean FLI
0 hr	0	n/a
4 hrs	163	707
8 hrs	256	813
12 hrs	243	761
24 hrs	202	744



B



**Figure 2.11 Investigation of EV engineering at varied duration and self-quenching possibility.** A): Investigation of EV engineering at varied duration (from 0 to 24 hrs) by MoFlo Astrios EQ™ from Beckman Coulter. B): Investigation of self-quenching possibility using a fluorometer (PTI QuantaMaster™ 400, Horiba, Ltd.;  $\lambda_{ex} = 488 \text{ nm}$ ,  $\lambda_{em} = 520 \text{ nm}$ ). The engineered EVs were constructed by 2, 4, 8, 12, and 24 hrs of HCR and the QDs were added right before fluorescence measurement in the fluorometer. No significant decrease in QD fluorescence upon addition of the engineered EVs even at long HCR duration up to 24 hrs, supporting that no self-quenching occurred in our system under the present reaction conditions. Figure reprinted from Ref.17. © 2018, John Wiley and Sons.

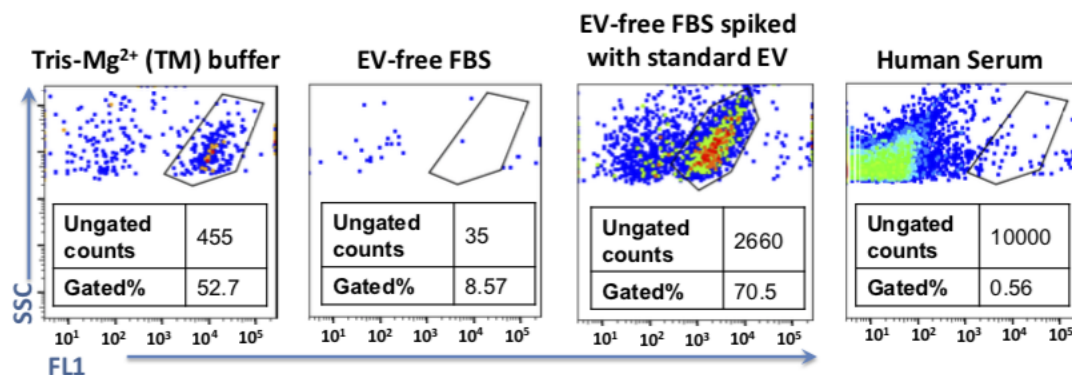


**Figure 2.12 The linearity range of our method for standard EV quantification.** Figure reprinted from Ref.17. © 2018, John Wiley and Sons.

**Table 2.3 Assessment of measurement reproducibility using TIE for EV engineering.**  
Table reprinted from Ref.17. © 2018, John Wiley and Sons.

		Mean Count%	Mean Fluorescence Intensity Ratio	Mean Forward Scatter Intensity Ratio
CD63	Intraday (n = 6)	47.6 ± 11.5	765.3 ± 269.5	5.7 ± 1.8
	Interday (n = 16)	52.7 ± 21.1	704.3 ± 532.6	5.5 ± 1.9
HER2	Intraday (n = 6)	50.1 ± 16.0	523.3 ± 139.0	8.7 ± 1.5
	Interday (n = 13)	43.4 ± 17.4	374.0 ± 182.9	6.8 ± 2.3

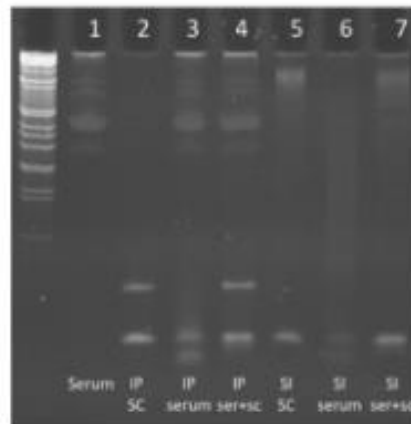
The standard EV (lyophilized EVs produced by COLO-1 cells, HansaBioMed Life Science Ltd) concentration was at 0.1 µg/µL. The mean fluorescence and forward scatter ratio was calculated between the particles locating within the gate (positive reading with higher fluorescence or forward scatter) and outside of the gate (i.e. background). Thus, the ratio represents signal improvement in fluorescence and forward scatter. The robustness of our method by carrying out repeated measurements in different days. The “%counts” within the gated region for a total of 16 replicates was found to be 52.7 ± 21.1%. Consistent enhancements in EV size and fluorescence were also achieved: the gated events exhibited 704 ± 532.6 and 5.5 ± 1.4 folds increase in mean fluorescence intensity (MFI) and mean forward scatter (MFS), respectively, compared to the ungated ones.



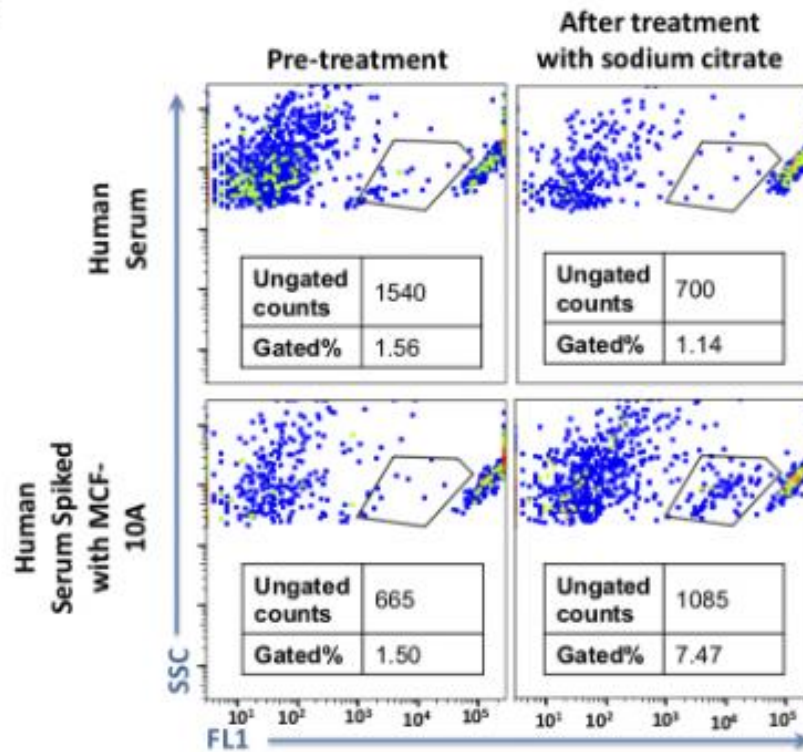
**Figure 2.13 EV counting by TIE in the EV-free FBS and human serum.** Comparison was made among reactions taking place in the TM buffer, in EV-free FBS, and in FBS spiked with  $10^9$  EV particles. The last 6 nucleotides at 3' ends of the hairpins were modified with phosphorothioate. No reaction could be detected without PS modification (data not shown). After modification, EV engineering was successful in EV-free FBS. Figure reprinted from Ref.17. © 2018, John Wiley and Sons.

A

- 1: Human serum
- 2: IP + Hairpins in SC
- 3: IP + Hairpins in serum
- 4: IP + Hairpins in serum + SC
- 5: SI + Hairpins in SC
- 6: SI + Hairpins in serum
- 7: SI + Hairpins in serum + SC



B



**Figure 2.14 Treatment of human serum with sodium citrate (SC) helped to inhibit nuclease activity and kept the DNA probes intact for 8 hours.** A): Gel electrophoresis results confirming the presence of intact DNA probes (PS modified hairpins and initiator probe) after 8-hr incubation in the SC-treated serum (lane 4 and 7), while significant degradation was observed without SC treatment in lane 3 and 6. The large Mw bands observed in lane 1, 3, & 4 were from serum proteins. B): Flow cytometric analysis of EV engineering in human serum with or without SC treatment. Without SC treatment, the spiked EV was not detectable in serum. QD aggregates were detected here due to reduction of the power setting for the FITC channel, which was set to 350, instead of 385, the common setting for all other measurements. Figure reprinted from Ref.17. © 2018, John Wiley and Sons.

Differentiation of heterogeneous EVs requires recognition of multiple markers. The TIE system can be easily adjusted to target different surface biomarkers by simply switching the aptamer sequence in the conformation-switchable DNA probe. To demonstrate this, we designed another TIE system to target human epidermal growth factor receptor 2 (HER2), a typical breast cancer marker overexpressed in about 20 % of breast cancer patients and present on a subset of EVs derived from breast cancer cell lines.<sup>20</sup> We substituted the anti-CD63 aptamer with an anti-HER2 aptamer<sup>21,22</sup> in the target-recognition domain, and kept the trigger domain intact. The hinge domain was adjusted slightly to achieve effective conformational switching upon HER2 recognition (Table 2.4). Since the HCR triggered by HER2 remains the same as that by CD63, we define it as the “single hybridization cascade system”, and applied it to analyze HER2 and CD63 expression separately on single EVs secreted by three different cell lines: the breast cancer cells of SKBR3 (highly metastatic) and MCF-7 (poorly metastatic) and the non-tumor epithelial cell MCF-10A. We found that the anti-HER2 system produced more detectable events from the SKBR3-derived EVs than those from MCF-7 and MCF-10A (Figure 2.16). Furthermore, two times more events were detected by the anti-HER2 system on the SKBR3

EVs than by the anti-CD63 system. On the other hand, the EVs originating from MCF-10A and MCF-7 resulted in comparable numbers of detectable events for detection of CD63 or HER2. These results agree well with the bulk analysis by ELISA (Figure 2.17), which confirmed the overexpression of HER2 in SKBR3 cells as reported previously,<sup>23</sup> and found two times more HER2 than CD63 in the SKBR3-derived EVs, but comparable amounts of HER2 and CD63 in the EVs from MCF-7 and MCF-10A cells. If the signals from both markers can be acquired simultaneously, the flow plots should directly show the presence of EV sub-populations in a heterogeneous EV mixture without the help of statistical tools, which is necessary for single vesicle analysis using microscopic methods. Herein, we designed a dual hybridization cascade system to simultaneously amplify signals from HER2 and CD63 on a single EV by two separate hybridization cascade reactions (Table 2.4). In this system, CD63 signal was still derived from the streptavidin-conjugated QDs, but HER2 signal was from the Alexa660 labeled DNA tag hybridized with the overhang in H3 on the HCR product (Figure 2.15 and 2.18B). The fluorescence of QDs and Alexa660 were detected in the FACSCanto fluorescence channel of FL1 and FL4, respectively. As expected, the detectible events from the EVs produced by SKBR3, MCF-7, and MCF-10A located at distinct positions on the fluorescence flow cytometric plots, each EV sub-population exhibiting characteristic distribution patterns (Figure 2.18A and 2.19). Viewing CD63 as the internal standard, we calculated the MFI ratio of FL4/FL1 to represent the relative content of HER2 and CD63 on the same EV. Significant difference in the MFI ratios between EVs from the MCF-10A and SKBR3 cells ( $p = 0.009$ ), or between those from the MCF-7 and SKBR3 cells ( $p = 0.02$ ) was confirmed with Students t test (Figure

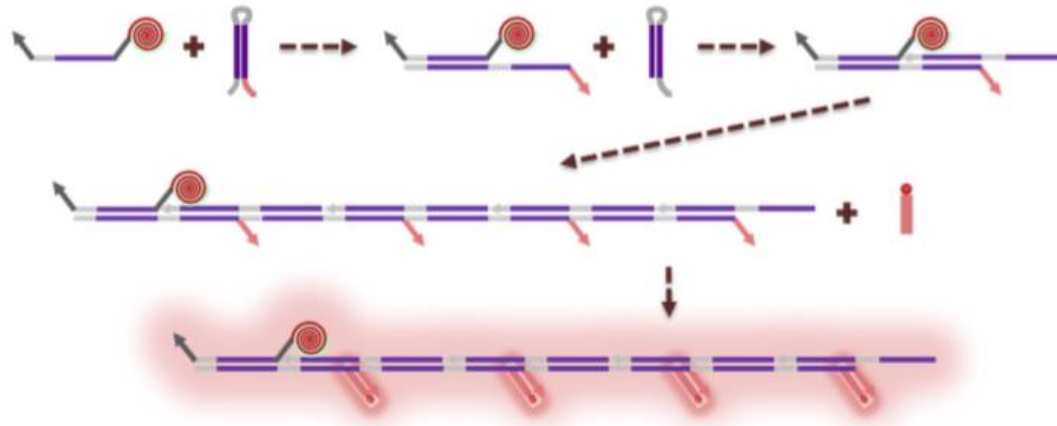
2.18C), confirming the effectiveness of dual labeling on the same EV for robust differentiation of the SKBR3-derived EVs from those produced by the MCF cells. The EVs from MCF-7 and MCF-10A were not differentiable using these two markers, because the expression levels of both markers were comparable in these two EVs (Figure 2.17).

**Table 2.4 DNA sequences used in TIE system for HER2.** Table reprinted from Ref.17. © 2018, John Wiley and Sons.

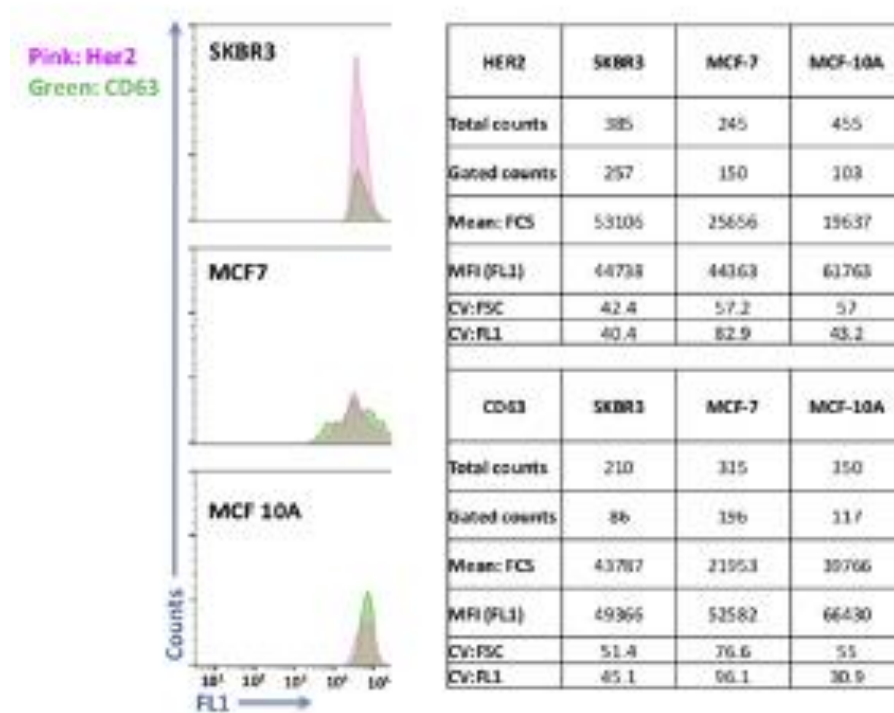
Name	Sequences (5'-3')
Initiator Probe 2 (IP2) targeting HER2	<u>CTG CA TAA GTT CGC TGT GGC ACC TGC ACG</u> <u>AAC TTA T GCA GCG GTG TGG GG</u>
Hairpin 3 (H3)	<u>CCT CCA CCA CGC TGT GGC ACC TGC ACG</u> CAC CCA <u>CGT GCA GGT GCC ACA GCG</u> AAC TTA
Hairpin 4 (H4)	TGG GTG <u>CGT GCA GGT GCC ACA GCG</u> TAA GTT <u>CGC TGT GGC ACC TGC ACG</u>
DNA tag for IP2/H3/H4 system	<u>TGG TGG AGG</u> /3AlexF660N

The regions sharing the same color in different strands are the complementary sequences used for hybridization. Underline sequences indicate complementary regions of the probes to form hairpin structure. Initiator Probe 2 includes a HER2 recognition domain (red), and a trigger domain (purple and grey) for growth of a long dsDNA via DNA hybridization cascade, connected by a hinge domain (grey). The overhand design at the 5' end of one of the hairpins is for tagging of a short ssDNA detection probe. The DNA tag to be hybridized with the overhang in H3 is marked pink.

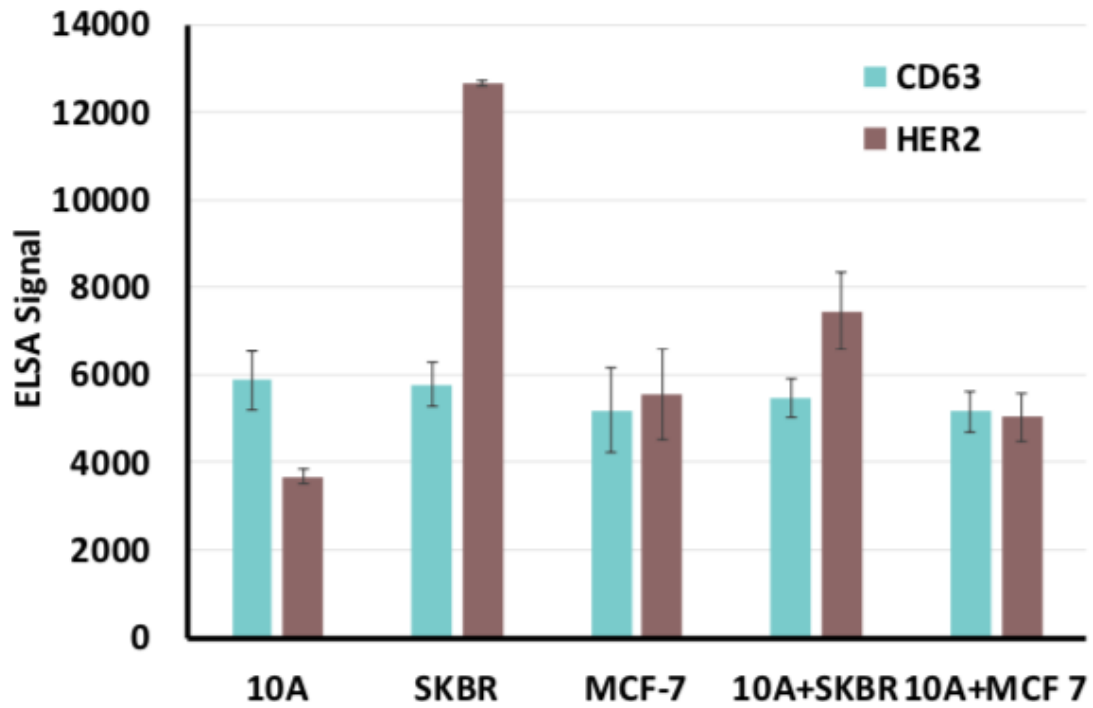




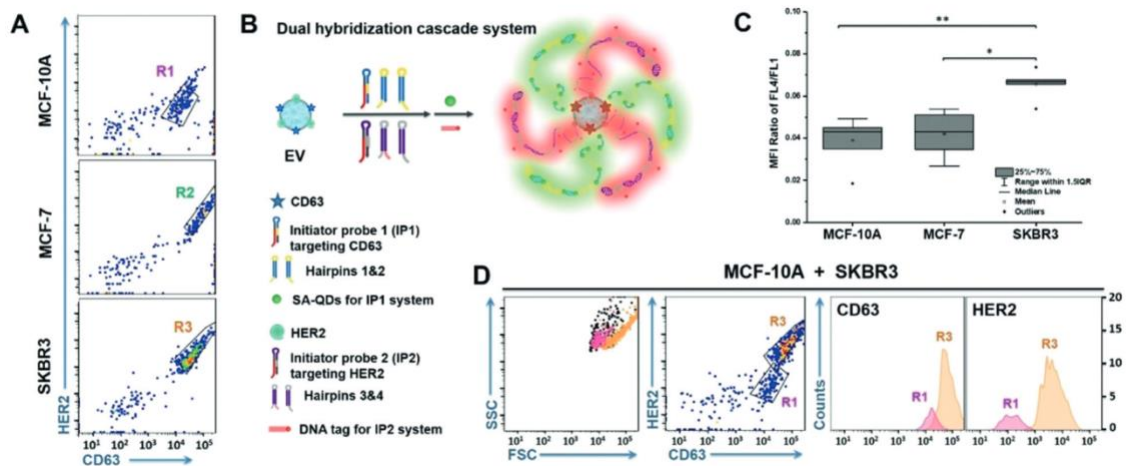
**Figure 2.15 Hybridization cascade 2 for HER2.** Figure reprinted from Ref.17. © 2018, John Wiley and Sons.



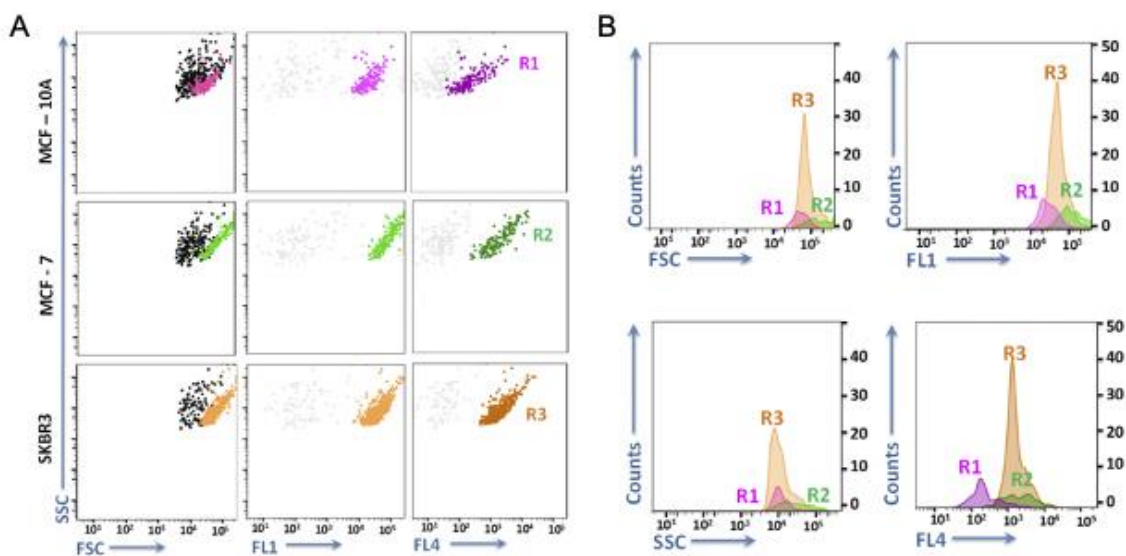
**Figure 2.16 Single hybridization cascade system for detection of CD63 or HER2.** Representative flow cytometry histogram of fluorescence and data summary of using the single hybridization cascade system for detection of CD63 or HER2 on individual EVs produced by three cell lines: MCF-10A, MCF-7, and SKBR3. The anti-HER2 and anti-CD63 probes were mixed with the EV sample separately to obtain two reactions for flow cytometric analysis. Figure reprinted from Ref.17. © 2018, John Wiley and Sons.



**Figure 2.17 ELISA measurement of protein contents.** It cannot reveal the presence of different EV populations. Figure reprinted from Ref.17. © 2018, John Wiley and Sons.



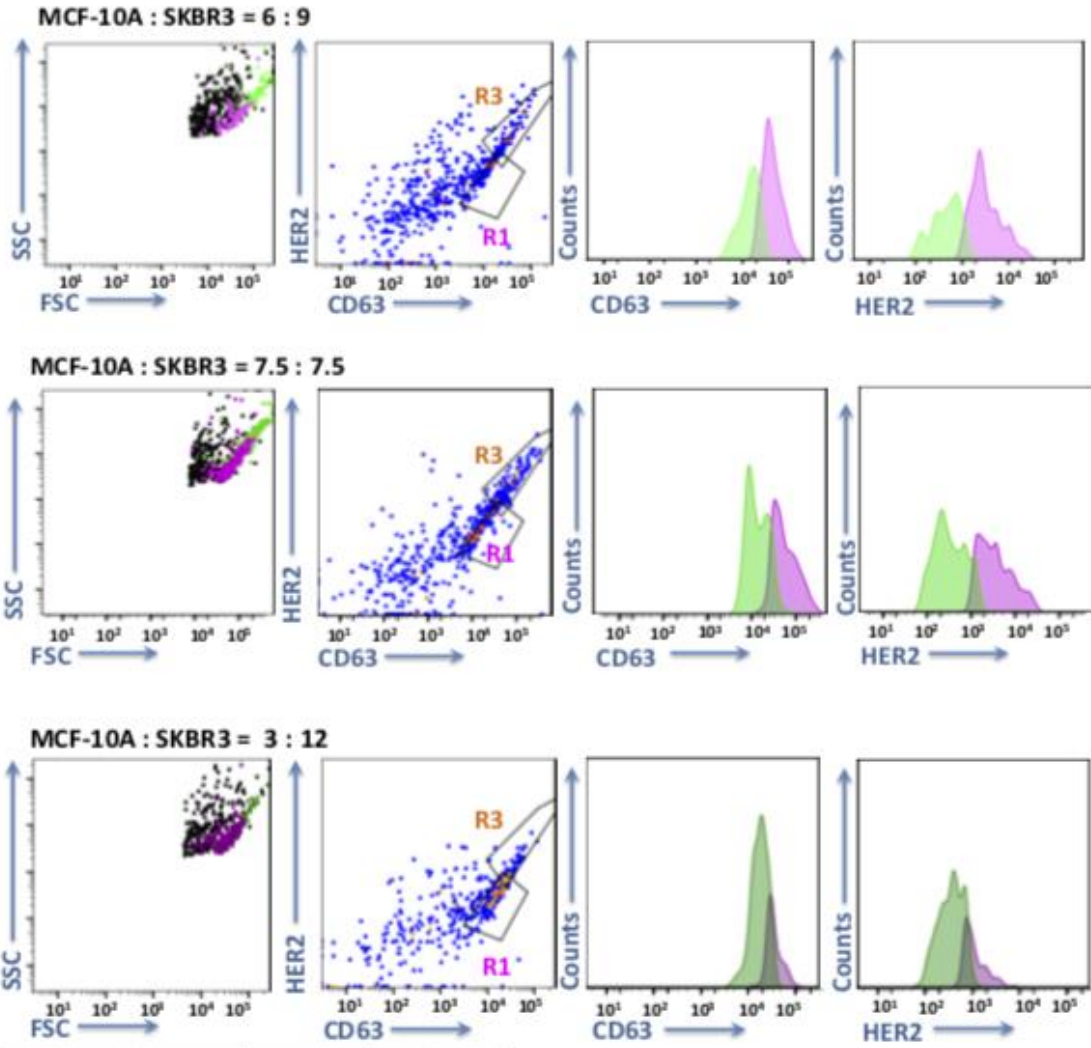
**Figure 2.18 Hybridization cascade system for recognition of two markers.** A): Representative flow cytometry plots of the particle cluster determined by the relative expression levels of HER2 and CD63 for the EVs from different cell lines. B): The dual hybridization cascade system for recognition of two markers on the same EV. C): Box chart of the mean fluorescence intensity (MFI) ratio between FL4 and FL1 of the EVs from three cell lines. \*P < 0.05, \*\*p < 0.01, n = 5. IQR = interquartile range. D): Flow cytometry scatter plots and fluorescence histograms for analysis of EV mixtures. R1 and R3 are defined in Figure 3 A using the EVs from the corresponding cell lines. The particle clusters were colored on the scatter plot of FSC vs. SSC and the histograms based on the gates defined in the HER2 vs. CD63 plots. Figure reprinted from Ref.17. © 2018, John Wiley and Sons.



**Figure 2.19 Flow cytometric analysis of engineered EVs prepared with the dual hybridization cascade system.** A): Flow cytometry plots of FSC vs. SSC, and FL1 (for CD63) or FL4 (for HER2) vs. SSC from engineered EVs prepared with the dual hybridization cascade system. B): histograms for plots of A. Particles locating in R1, R2, and R3, i.e. with enhanced fluorescence, were highlighted with colors in the scatter plots, proving that they also experienced size enlargement after engineering. Figure reprinted from Ref.17. © 2018, John Wiley and Sons.

The significant difference between the MFI values from different EV sub-populations indicates that our technique has the power to reveal the presence of EV sub-populations among heterogeneous mixtures. To confirm this, we tested the mixture of EVs

from MCF-10A and SKBR3 prepared at a 1:1 ratio. Using the distribution patterns identified with the pure EV populations, we could clearly see the presence of two EV populations in the mixture (Figure 2.18D). The particle count ratio for those locating within R1 and R3 was equal to 0.98:0.07 (n=3), agreeing with the mixing ratio of the two EV sub-populations. In contrast, bulk analysis of the same EV mixture using ELISA only reflected as light increase in the HER2 content, but failed to recognize the presence of two distinct EV sub-populations (Figure 2.17). More strikingly, varying the mixing ratios of these two EV sub-populations, the ratio of the particle counts in the gated regions of R1 and R3 showed a strongly linear relationship ( $R^2 = 0.9581$ ) with the ratio of the added EV numbers between two cell lines (Figure 2.20). These results demonstrate the great potential of our method in recognizing EV heterogeneity and differentiating EV sub-populations.



	of	for EV	SKBR3		
	3	10A)			
		60.00	85.00	1.5	1.4
		154.00	123.00	1	0.8
		226.00	79.00		



**Figure 2.20 Flow cytometric analysis of the mixture of EVs from MCF-10A and SKBR3 using TIE-EV.** The table summarized the readings collected from the cytometric analysis, and the plot of EV amount ratio vs. Count ratio showed good linear correlation. Vol. = volume of pure EV stock solution taken to prepare the EV mixture, in  $\mu\text{L}$ . Figure reprinted from Ref.17. © 2018, John Wiley and Sons.

## 2.4 Conclusion

In summary, we have developed a single-EV FCA technique to visualize individual EV in a conventional flow cytometer for the first time, which can help gain in-depth insights into the molecular signatures of EV sub-populations under regular lab settings. While our work demonstrates simultaneous recognition of dual surface markers on the same vesicle, more markers can be targeted by simply revising the conformation-switchable probes to improve more effective differentiation of more EV sub-populations. Furthermore, our technique opens the opportunity for EV sorting and collection based on surface marker profiles under typical clinical lab settings. The pure EV sub-populations obtained will definitely benefit clear correlation between EV composition and their biogenesis and functions. Overall, we believe this single-EV FCA technique is a valuable tool for gaining more understanding on the roles of EVs in cell-cell communication and pathological development, and its high simplicity and good adaptivity to clinical labs will be highly beneficial for screening for EV markers for liquid biopsy applications.

## 2.5 Reference

---

- 1 C. F. Ruivo, B. Adem, M. Silva, S. A. Melo, *Cancer Res.* **2017**, *77*, 6480–6488.
- 2 L. Han, J. Xu, Q. Xu, B. Zhang, E. W. Lam, Y. Sun, *Med. Res. Rev.* **2017**, *37*, 1318–1349.
- 3 Y. Jiang, M. Shi, Y. Liu, S. Wan, C. Cui, L. Zhang, W. Tan, *Angew.Chem. Int. Ed.* **2017**, *56*, 11916–11920.
- 4 D. W. Greening, R. Xu, H. Ji, B. J. Tauro, R. J. Simpson, *Methods Mol. Biol.* **2015**, *1295*, 179–209.
- 5 G. Pocsfalvi, C. Stanly, I. Fiume, K. Vekey, *J. Chromatogr. A* **2016**, *1439*, 26–41.
- 6 Z. Zhao, Y. Yang, Y. Zeng, M. He, *Lab Chip* **2016**, *16*, 489–496.
- 7 M. A. Rider, S. N. Hurwitz, D. G. Meckes, *Sci. Rep.* **2016**, *6*, 23978.
- 8 M. Leslie, *Science* **2011**, *331*, 24–26.
- 9 M. Tkach, C. Thery, *Cell* **2016**, *164*, 1226–1232.
- 10 R. Friedrich, S. Block, M. Alizadehheidari, S. Heider, J. Fritzsche, E. K. Esbjergner, F. Westerlund, M. Bally, *Lab Chip* **2017**, *17*, 830–841.
- 11 K. Liang, F. Liu, J. Fan, D. Sun, C. Liu, C. J. Lyon, D. W. Bernard, Y. Li, K. Yokoi, M. H. Katz, E. J. Koay, Z. Zhao, Y. Hu, *Nat. Biomed. Eng.* **2017**, *1*, 0021.
- 12 K. Lee, K. Fraser, B. Ghaddar, K. Yang, E. Kim, L. Balaj, E. A. Chiocca, X. O. Breakefield, H. Lee, R. Weissleder, *ACS Nano* **2018**, *12*, 494–503.
- 13 M. Brown, C. Wittwer, *Clin. Chem.* **2000**, *46*, 1221–1229.
- 14 Y. Tian, L. Ma, M. Gong, G. Su, S. Zhu, W. Zhang, S. Wang, Z. Li, C. Chen, L. Li, L. Wu, X. Yan, *ACS Nano* **2018**, *12*, 671–680.
- 15 R. M. Dirks, N. A. Pierce, *Proc. Natl. Acad. Sci. USA* **2004**, *101*, 15275–15278.
- 16 A. Cangialosi, C. Yoon, J. Liu, Q. Huang, J. Guo, T. D. Nguyen, D. H. Gracias, R. Schulman, *Science* **2017**, *357*, 1126–1130.

- 
- 17 W. Shen, K. Guo, G. B. Adkins, Q. Jiang, Y. Liu, S. Sedano, Y. Duan, W. Yan, S. E. Wang, K. Begersen, D. Worth, E. H. Wilson, W. Zhong, *Angew. Chem. Int. Ed.* **2018**, *57*, 15675-15680.
- 18 Q. Zhou, A. Rahimian, K. Son, D. S. Shin, T. Patel, A. Revzin, *Methods* **2016**, *97*, 88–93.
- 19 A. Kolarevic, D. Yanchev, G. Kocic, A. Smelcerovic, *Eur. J. Med. Chem.* **2014**, *88*, 101–111.
- 20 S. E. Wang, R. J. Lin, *MicroRNA* **2013**, *2*, 137–147.
- 21 G. Mahlknecht, R. Maron, M. Mancini, B. Schechter, M. Sela, Y. Yarden, *Proc. Natl. Acad. Sci. USA* **2013**, *110*, 8170–8175.
- 22 M. L. Squadrito, C. Cianciaruso, S. K. Hansen, M. De Palma, *Nat. Methods* **2018**, *15*, 183–186.
- 23 K. Subik, J. F. Lee, L. Baxter, T. Strzepak, D. Costello, P. Crowley, L. Xing, M. C. Hung, T. Bonfiglio, D. G. Hicks, P. Tang, *Breast Cancer Basic Clin. Res.* **2010**, *4*, 35–41.



## Chapter 3: Calibration-Free Analysis of Surface Proteins on Single Extracellular Vesicles Enabled by DNA Nanostructure

### 3.1 Introduction

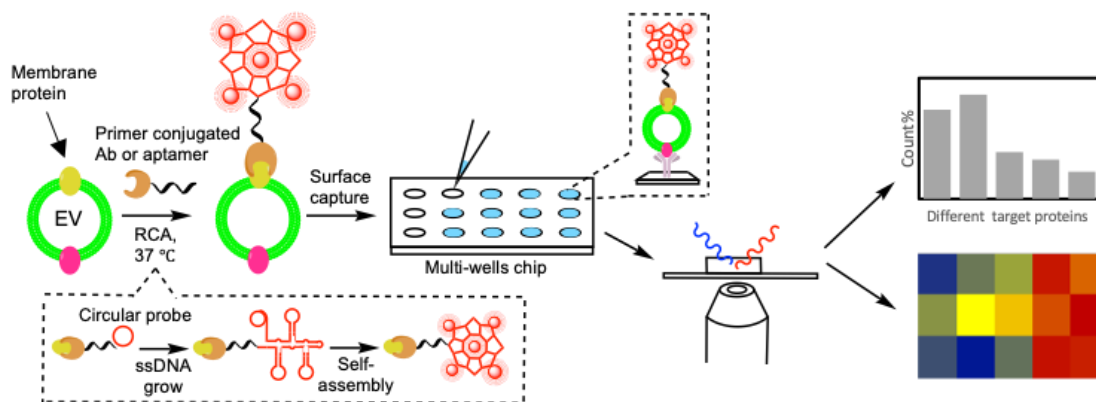
Extracellular vesicles (EVs) carry diverse cargos like proteins, lipids, as well as nucleic acids, and transport them from cells to cells, acting as important mediators for cell-cell communication.<sup>1,2</sup> EVs are stably present in biofluids, easily accessible with minimal invasion. Their biogenesis involves distinct intracellular regulatory processes that likely determines the close relationship between their molecular composition and the parental cell's biological states; and their cargos have been reported to be highly relevant to pathological developments.<sup>3,4</sup> Thus, analyzing the molecular profiles of the circulating EVs may not only gain information about the remote tissues only reachable through surgery, but also reveal disease progression.<sup>5</sup> These unique characteristics of EVs have attracted active research efforts to explore their potential as promising biomarkers in liquid biopsies.<sup>6,7</sup>

However, the EVs found in biofluids are highly heterogeneous, consisting of many sub-populations different in sizes, cargo composition, cell of origin, biogenesis pathways, and functions.<sup>8,9,10</sup> Conventional EV analysis relies on bulk measurement methods, like enzyme-linked immunosorbent assays (ELISAs)<sup>11,12</sup>, Western blots (WB)<sup>13</sup> and bead-based flow cytometry (FCM)<sup>14</sup>, that produce the ensemble average of the varying signals from a swarm of heterogeneous EVs. It is very likely for such bulk measurements to miss the molecular information carried by the few EVs derived from the diseased cells that are the most relevant to pathological development. Single EV phenotyping can well overcome the heterogeneity issue and differentiate EVs from different biological origins, as

demonstrated by counting individual EVs under confocal fluorescence microscopy (CFM) with repeated dye bleaching and antibody binding cycles<sup>15</sup>; or by the proximity barcoding assay that employs DNA ligation and barcoding, rolling circle amplification, and next-generation sequencing<sup>16</sup>. While these techniques are powerful at EV differentiation and thus valuable in discovery of EV markers useful for disease diagnosis, they require lengthy and complicated sample treatments and sophisticated data analysis. Promising liquid biopsy tools often focus on detection of the specific EV sub-populations carrying a few markers among a heterogeneous mixture, which has also been achieved employing high-resolution FCM<sup>17, 18, 19</sup>, super resolution microscopy<sup>20</sup>, and total internal reflection fluorescent microscopy (TIRFM)<sup>21</sup>. Still, the small physical sizes of EVs and the limited amounts of cargo molecules enclosed represent great challenges for rapid, simple, and highly sensitive detection of single EVs.

Herein, we report an innovative method for detection of single EVs with low sample inputs that permits rapid and calibration-free comparison of surface protein expression among different EV samples. Our design takes advantage of a long ssDNA grown *in situ* on the EV surface by rolling circle amplification (RCA) upon recognition of the surface protein of single EV (Scheme 3.1). The ssDNA contains repeated regions or numerous labeled nucleotides for the binding of multiple fluorophores. With judicious design of the template sequence, the single-stranded RCA product can self-assemble into a compact structure, which is called DNA nanoflower (DNF), in the following text. Such a DNF not only enlarges the size of EV, but also amplifies the signal from the surface protein, enabling easy visualization of individual EVs in the diffraction-limited CFM with an EV

input EVs as low as  $\sim 100$  vesicles/ $\mu\text{L}$ . Coupling with a membrane-staining dye, accurate comparison of the protein expression profiles in different EV samples can be achieved to differentiate the EVs by their cell-of-origin. By simply changing the primer sequence, dual protein markers can be simultaneously labeled by DNFs to realize duplex detection, enhancing the specificity in EV differentiation. Moreover, this method can directly detect EVs carrying tumor-specific proteins in biofluids, leading to clear recognition of cancer patients at early stages from healthy controls.



**Scheme 3.1 Schematic illustration of dual-color detection of single EV by dye staining and DNF tagging.** Figure reprinted from Ref.22. © 2021, Elsevier.

### 3.2 Material and Methods

**Chemicals and materials.** Human breast cell line MCF-10A and MDA-MB-231 were purchased from ATCC. The standard EVs were obtained from HansaBioMed Life Science Ltd (Tallinn, Estonia) (lyophilized EVs produced by COLO-1 cells) and System biosciences (lyophilized EVs produced by PC-3 cells and A549 Cells). Human breast cancer patient serum samples and healthy patient serum samples were provided by the NCI funded Cooperative Human Tissue Network (CHTN). MFGE8 protein, anti-EGFR

antibody and epidermal growth factor (EGF) were purchased from Sino Biological. Anti-CD9 antibody, anti-mouse IgG, cholera toxin, hydrocortisone and poly-L-lysine coated glass slide were purchased from Sigma Aldrich. Anti-CD63 antibody and anti-CD44 antibody were purchased from Novus Biologicals. All oligonucleotides were purchased from Integrated DNA Technologies. Phi29 DNA polymerase was purchased from New England Biolabs. DBCO-PEG5-NHS ester was purchased from Click Chemistry Tools. All other chemicals, including anti-HER2 antibody, penicillin streptomycin, DMEM/F-12, insulin, DMEM, biotin-14-dATP and fetal bovin serum (FBS), were purchased from ThermoFisher Scientific.

**Cell culture and EV extraction.** Human breast cell line MCF-10A, MCF-7 and MDA-MB-231 were cultured at the recommended media containing 1% penicillin streptomycin. MCF-10A cells were cultured in the DMEM/F-12 media supplied with 5% horse serum, 0.1  $\mu\text{g}/\text{mL}$  cholera toxin, 10  $\mu\text{g}/\text{mL}$  insulin, 0.5  $\mu\text{g}/\text{mL}$  hydrocortisone, and 20  $\text{ng}/\text{mL}$  EGF. MDA-MB-231 cells were cultured in DMEM media supplemented with 10% FBS. All cell lines were maintained at 37 °C in a humidified 5% CO<sub>2</sub> incubator and routinely screened for Mycoplasma contamination. When the cells reached a confluency of 75%, the medium was replaced with the EV-depleted culture medium. After 24 hours incubation, the culture medium was collected and centrifuged at 500 g for 15 min and 15,000 g for 20 min to remove the cell debris. Next, the medium was ultra-centrifuged at 110,000 g for 70 min twice to pellet the EVs secreted by the cells. The EVs pellet was resuspended in 1  $\times$  PBS. Particle concentration in the EV solution was measured by NTA.

**Gel electrophoresis.** Gel electrophoresis for the confirmation of the growth of DNA long chain and DNA-antibody conjugation, and optimization of biotin-dATP ratio were carried out in 1.5% Agarose gel in 1 x TBE. The DNAs were stained by SYBR gold. The images were taken under a Spectroline® UV transilluminator.

**Atomic force microscopy (AFM), transmission electron microscopy (TEM) and scanning electron microscopy (SEM).** 10  $\mu$ L sample was deposited on a freshly cleaved mica for 10 min. Before imaging, the samples were rinsed with deionized water for 3 times and then dried by N<sub>2</sub>. AFM images were recorded in air under the tapping mode using a Dimension 5000 Scanning Probe Microscope. The images were flattened by NanoScope Analysis software.

TEM was carried out using a Tecnail2 TEM. The EVs were stained with 2% uranyl acetate, embedded in 1% methyl cellulose, dried at room temperature and deposited on formvar-carbon-coated EM grids for imaging.

SEM was done with a Zeiss XB 1540 instrument. The sample solutions were prepared using the typical procedures for EV suspension and DNF labeling. Then 10  $\mu$ L of each solution was dropped on the silicon wafers which were soaked in piranha solution for 8 hrs, cleaned by ethanol and acetone sequentially, and dried before usage. The samples were dried again at 70 °C for 2 hrs, and coated by Ag sputtering before SEM imaging.

**Nanoparticle tracking analysis (NTA).** Particle concentration and size distribution of EVs and DNA nanoflowers were measured by NanoSight NS300 using a low volume flow cell manifold and a 405 nm laser module. A video of 30–60 s duration was taken with a rate of 25 frame/s.

**Real-time fluorescence.** The RCA reaction was monitored in 96-well PCR plated and controlled using a Bio-Rad CFX Connect Real-Time PCR Detection System. The reaction mixture was incubated at 37 °C and fluorescence curves were recorded at 30 s intervals.

**Circular probe preparation and rolling circle amplification (RCA) for construction of DNA nanoflower (DNF)** For circular probe preparation, the phosphorylated template for DNFs (0.6 μM) and the initiator (1.2 μM) were mixed and annealed in the hybridization buffer (20 mM Tris-HCl, 5 mM MgCl<sub>2</sub>, 137 mM NaCl, pH 7.5) by heating at 95 °C for 5 min, followed by cooling to room temperature over 3 hrs. The annealed product was incubated with the T4 DNA ligase in the ligation buffer (50 mM Tris-HCl, 10 mM MgCl<sub>2</sub>, 1mM ATP, 10mM DTT) at 37 °C for 3hrs. The reaction was terminated by heating the solution at 65 °C for 20 min. Exonuclease I and Exonuclease III were then added to digest the un-ligated, linear template and initiator overnight at 37 °C. The reaction was terminated by incubation at 80 °C for 20 min. The concentration of the resultant circular probe was quantified by Nanodrop.

For a typical RCA used in our work, 5 nM of the circular probe was incubated with 25 nM of the RCA initiator in the reaction buffer (50 mM Tris-HCl, 10 mM MgCl<sub>2</sub>, 10 mM (NH<sub>4</sub>)<sub>2</sub>SO<sub>4</sub> and 4 mM DTT) at 37 °C for 30 min. Then, 80 μM of dNTPs and 2.5 U/μL of phi29 DNA polymerase were added to grow the DNF at 37 °C for 1 hr.

**EV labeling and imaging by confocal fluorescence microscopy.** EV engineering was carried out by mixing 2 μL of EV suspension with 25 nM initiator probe and 5 nM circular template probe in 50 mM Tris-HCl, 10 mM MgCl<sub>2</sub>, 10 mM (NH<sub>4</sub>)<sub>2</sub>SO<sub>4</sub> and 4 mM DTT. After incubation, 80 μM dNTPs (20 μM for each of dATP, dGTP, dTTP, and dCTP), 20uM

biotinylated dATP and 2.5 U/  $\mu\text{L}$  phi29 DNA polymerase were added to initiate the growth of DNA nanoflower. Before depositing the sample onto the glass slide, the EV was incubated with 50 nM Alexa 633-conjugated streptavidin for DNFs labelling and with 10  $\mu\text{g}/\text{mL}$  DiO dye to stain EVs for 30 min. The glass slides were modified with 20  $\text{ng}/\mu\text{L}$  MFGE8 protein or 15 $\mu\text{g}/\text{mL}$  anti-CD63 antibody through EDC coupling for EV on-chip capturing. For serum samples, 10  $\mu\text{L}$  of diluted sample were incubated on chip first before DNF construction. For imaging, 10  $\mu\text{L}$  of the sample was subsequently deposited onto the microwell chip, and incubated for 1 hour at room temperature, allowing the EVs immobilization. After five rinses with 0.1% BSA, fluorescence imaging was performed on a Zeiss 880 Inverted Confocal Microscope. The measurement was performed using an Argon laser at  $\lambda_{\text{ex}} = 488 \text{ nm}$  for fluorescence from DiO dye, and an HeNe laser at  $\lambda_{\text{ex}} = 633 \text{ nm}$  for fluorescence from the Alexa 633 dye. All of the CFM images were collected at a resolution of 512 x 512 pixels. The viewing area are 21  $\mu\text{m}$  x 21  $\mu\text{m}$  or 50  $\mu\text{m}$  x 50  $\mu\text{m}$ . For each sample, 10 independent images on 10 different locations were acquired respectively from a single well.

The image analysis was carried out using Image J. Each bright spot on the CFM images represents a single target EV. The particle count of EV in each image was determined by counting the number of single fluorescence particles computationally. The threshold was set as 3 times the standard deviation of the intensity of the background and size of the particles was set as 2 – 10 pixels to reduce the false positive signals generated from noises or aggregation. The fluorescent spots in 10 independent images were counted and summed up. All experiments were done in triplicate to prove their reproducibility.

**DNA-protein conjugation.** DBCO-PEG5-NHS ester was used as a linker for the conjugation. The protein first reacted with DBCO-PEG5-NHS at room temperature for 30 mins. Excess cross-linkers were then removed from DBCO-activated proteins with Zeba spin columns (40-kDa MWCO). The DBCO-activated proteins were mixed with azide-labeled RCA initiators at 4 °C overnight. The resulted conjugation was characterized using gel electrophoresis.

**Fabrication of multi-well chip.** The multi-well chip was fabricated via pouring polydimethylsiloxane (PDMS) to the mold and curing the polymer in an oven (55 °C, overnight). The cured PDMS structure and a glass substrate were oxygen plasma treated and irreversibly bonded. The wells were washed with 1M NaOH, water, ethanol and dried by air. After that, the bottom of the well was modified with 10% (v/v) (3-Aminopropyl)triethoxysilane (APTES) in ethanol for 10 min at room temperature and washed for several times. The bottom of the well was then modified with 20 ng/ $\mu$ L MFGE8 protein or 15  $\mu$ g/mL anti-CD63 antibody in EDC coupling buffer (40  $\mu$ g/mL EDC (1-Ethyl-3-(3-dimethylaminopropyl)carbodiimide), 0.1 mM MES (4-morpholinoethanesulfonic acid), pH 4.7). The wells were blocked with 1% BSA (Bovine Serum Albumin) before sample loading.

### 3.3 Results and Discussion

We hypothesized that a relatively large DNA nanostructure formed *in situ* upon target recognition and carrying multiple fluorophores could enlarge the overall size of a single EV and enhance its visibility in a diffraction-limited confocal microscope (Scheme



3.1). Such a DNA structure can be grown by RCA (Scheme 3.1). RCA employs a polymerase capable of strand displacement to rapidly extend a primer (referred as “initiator” in the following text) that hybridizes to a circular template to a long ssDNA product at a constant temperature. The ssDNA product contains the repeated sequences complementary to the circular probe. Since each of the sequences can be bound with a labeling probe, the RCA product can be labeled by multiple signaling units, providing effective signal amplification for biomarker detection.<sup>23, 24</sup> More attractively, the circular template can be designed to adopt a T-shaped design (Table 3.1; Figure 3.1A), so that the repeated sequences on the single-stranded RCA product can hybridize with each other (Figure 3.1B), causing the self-assembly of the long ssDNA into a compact nanostructure, i.e. DNF.<sup>25</sup>

Indeed, 1-hr RCA using a simple initiator (Initiator 1 in Table 3.1, with no target-binding sequence) and a T-shaped circular template (Template 1 in Table 3.1) produced long DNAs that could not migrate out of the agarose gel during electrophoresis (Figure 3.1C). We also inspected the size and morphology of the RCA products by Atomic Force Microscopy (AFM) and Scanning Electron Microscopy (SEM). We can see from the AFM images that, the RCA products did display a globular structure with the average diameter around 100-150 nm, which were not observed if no polymerase was added to the reaction (Figure 3.2A). Both the size and morphology of the DNF was also confirmed by SEM (Figure 3.2B). In addition, we analyzed the hydrodynamic size of these RCA products by Nanoparticle Tracking Analysis (NTA). Particles larger than 150 nm were detected, the mean size of which gradually increased with the RCA time (Figure 3.3A&C). In contrast,

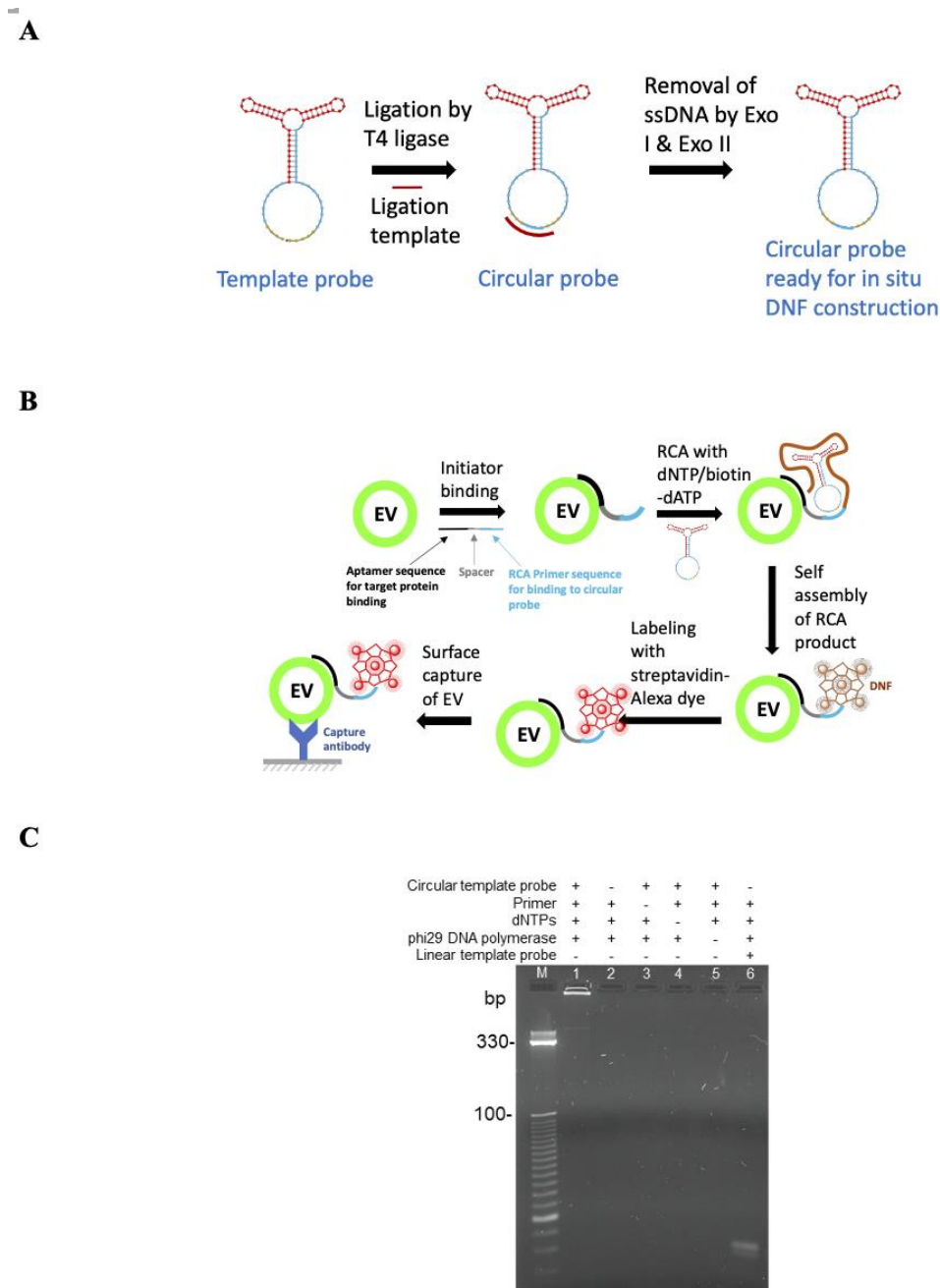
if a circular template without the self-hybridization regions was used for RCA, the RCA products did not show the reaction time-dependent increase in the mean size detected by NTA (Figure 3.3B&C), because it could not fold into a compact, globular structure but rather form the flexible random coil structure.

We further optimized the RCA conditions by monitoring the product growth in a real-time PCR (rtPCR) instrument. We found that the rate of growth started to slow down after 1 hr (Figure 3.4), at which time an obvious peak of the DNA particles larger than 150 nm detected by NTA (Figure 3.3A). Although more large particles were produced with longer RCA times, 1 hr was chosen in our assay to keep the procedure short. The dNTP used for RCA contained the biotinylated dATP so that the RCA product can be labeled by the streptavidin conjugated with fluorescent probes afterwards. The optimal ratio of dATP/biotin-dATP was found to be 4:1 to gain a high number of labeling sites without compromising the reaction efficiency (Figure 3.5). The reaction time of 1 hr yielded 10× increase in the fluorescence observed in the real-time PCR machine, which indicated the RCA product was probably 10× longer than the circular probe (84 nt). With a ratio of 4:1 of dATP : biotin-dATP used in RCA, the ~ 800 nt long RCA product could maximally contain 36 biotin-dATP for streptavidin labeling.

**Table 3.1 DNA sequences used in this study.**

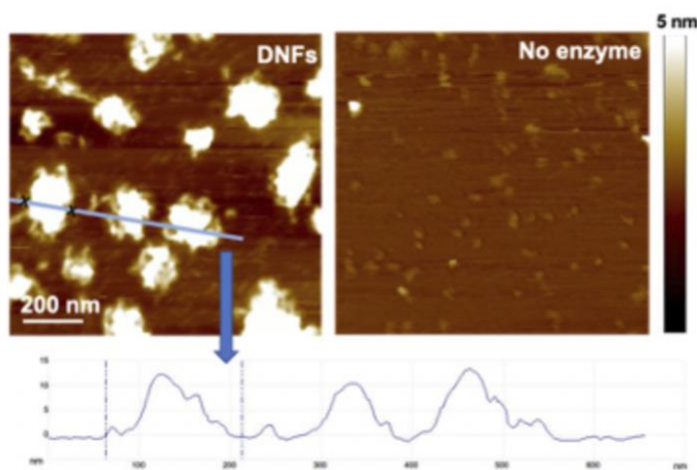
Name	Sequences (5'-3')
Initiator 1 for RCA 1	CGT TGT CGT TAG TCT AGG ATT CGG CGT GTT AGC A
Initiator 2 targeting CD63 in RCA 1	CAC CCC ACC TCG CTC CCG TGA CAC TAA TGC TAA CAC GCC AGT CTA GGA TTC GGC GTG TTA GCA
Initiator 3 targeting HER2 in RCA 1	GCA GCG GTG TGG GGG CAG CGG TGT GGG GGC AGC GGT GTG GGG AGA GGT TAA GTT GTC GTT AGT CTA GGA TTC G
Template probe 1 for RCA 1	Phosphate-GAC TAA CGA CAA <u>CGC GTG TTA GCA AGC</u> <u>GAT ACG CGT ATC GCT ATG GCA TAT CGT ACG ATA TGC</u> <u>CTG CTA ACA CGC CGA ATC CTA</u>
Detection probe 1	CGA ATC CTA GAC TAA CG /3AlexF546N/
Initiator 4 for RCA 2	CCA TTA GAC CAC CAC CAG TCG AGA GAA GAT CAT AGC TT
Initiator 5 targeting HER2 in RCA 2	GCA GCG GTG TGG GGG CAG CGG TGT GGG GGC AGC GGT GTG GGG AGA GGT TAA CCA TTA GAC CAC CAC CAG TCG AGA GAA GAT CAT AGC TT
Template probe 2 for RCA 2	Phosphate-GTG GTC TAA TGG <u>AGA TCA TAG CTT AGA</u> <u>CGT TCC GGA ACG TCT CGC TCG TAA CTA GTT ACG</u> <u>AGA AGC TAT GAT CTT CTC TCG ACT GGT G</u>
Detection probe 2	TGG TGG TGG/3AlexF660N/

The initiators contain a target protein recognition domain (black), a trigger domain (blue) for growth of a DNF via RCA, and a spacer (grey) to connect the recognition domain and trigger domain. The sequences in red in the template probes are the regions initiating self-assembly into the DNF through the underline nucleotides.

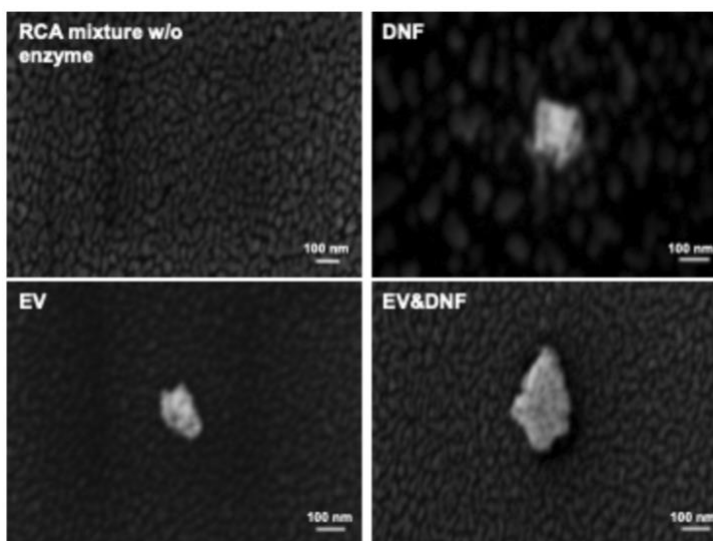


**Figure 3.1 Schematic illustration of RCA and analysis of RCA product by gel electrophoresis.** Schematic illustration of A) circular probe generation and B) RCA on EV surface. C) Scheme of Analysis of the long DNA products by agarose gel electrophoresis: Lane M: DNA marker; Lane 1: RCA product; Lane 2, 3, 4, and 5: reaction without circle template probe, initiator probe, dNTPs, phi29 DNA polymerase, respectively; Lane 6: reaction with linear template probe. Figure reprinted from Ref.22. © 2021, Elsevier.

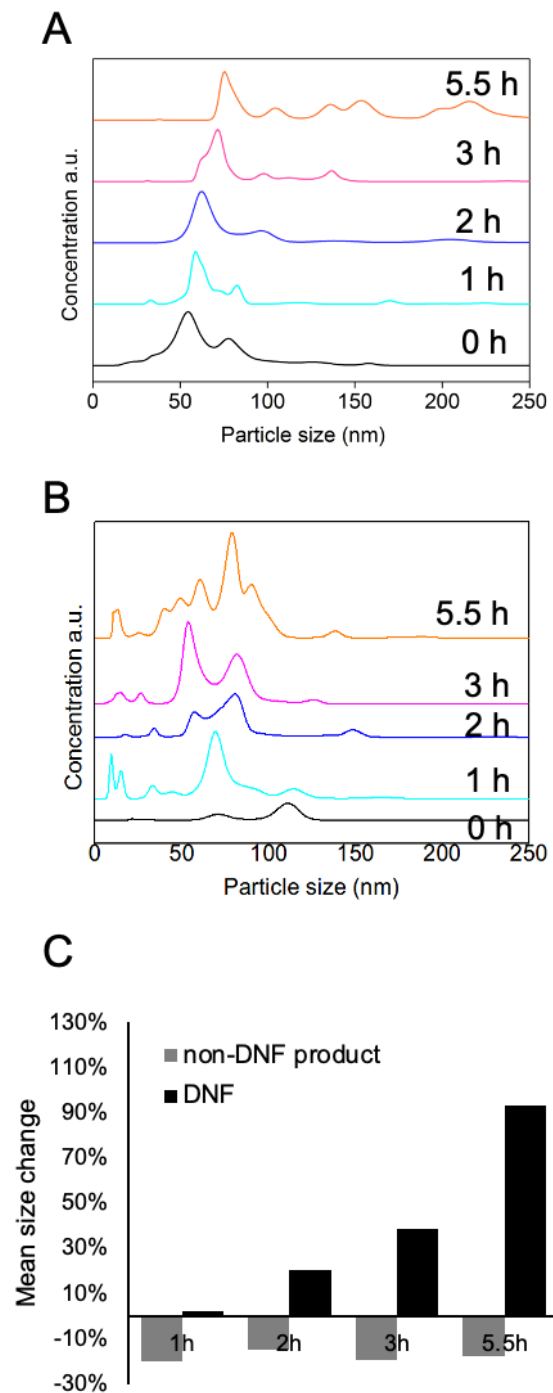
A



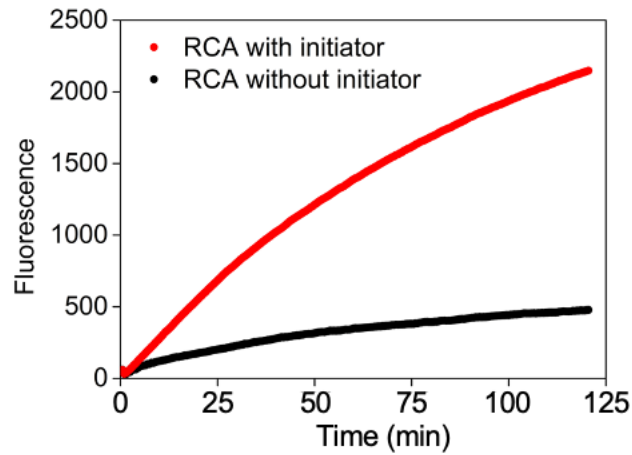
B



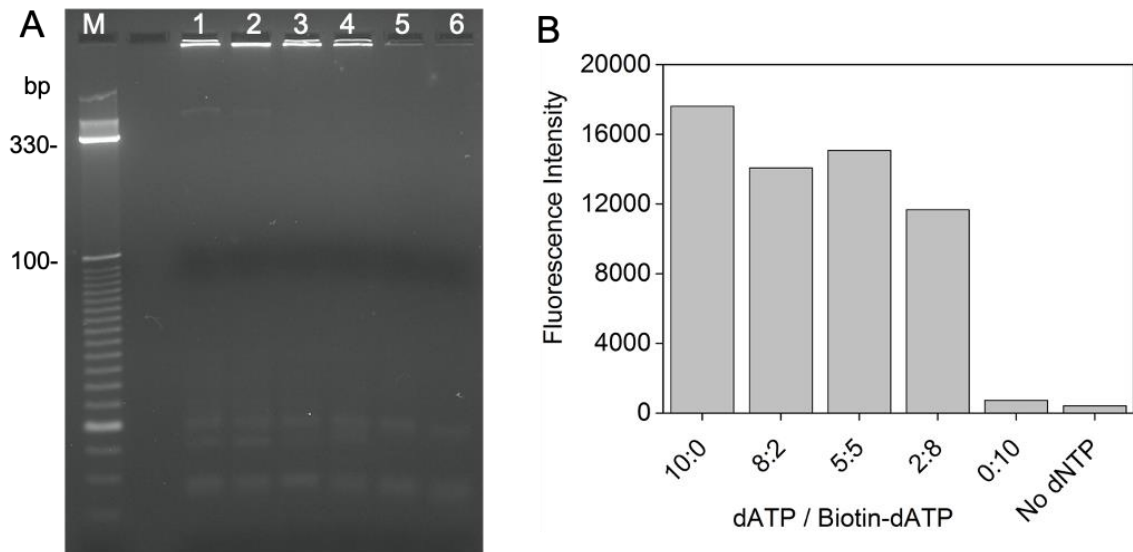
**Figure 3.2 AFM and SEM images for RCA product.** A) AFM images for the DNFs (left) and the reaction mixture with no enzyme added (right). The diameter of each globular DNF was measured to be  $\sim 100 - 150$  nm (bottom). B) SEM results for the DNF and its control - RCA mixture with no enzyme; as well as the EV and the DNF grown on the EV. Both the DNF and the EV only showed structures with diameters around 100 nm; but the sample that grew the DNF on the EV showed structures  $> 250$  nm after drying. Figure reprinted from Ref.22. © 2021, Elsevier.



**Figure 3.3 NTA analysis of RCA product size distribution in various RCA reaction time (0-5.5 hours).** Analysis of A) DNF and B) non-DNF in various reaction time (0-5.5 hours). C) Mean size change of RCA product. Figure reprinted from Ref.22. © 2021, Elsevier.



**Figure 3.4 Real-time fluorescence of RCA with (red) and without (black) initiator probe added.** Figure reprinted from Ref.22. © 2021, Elsevier.

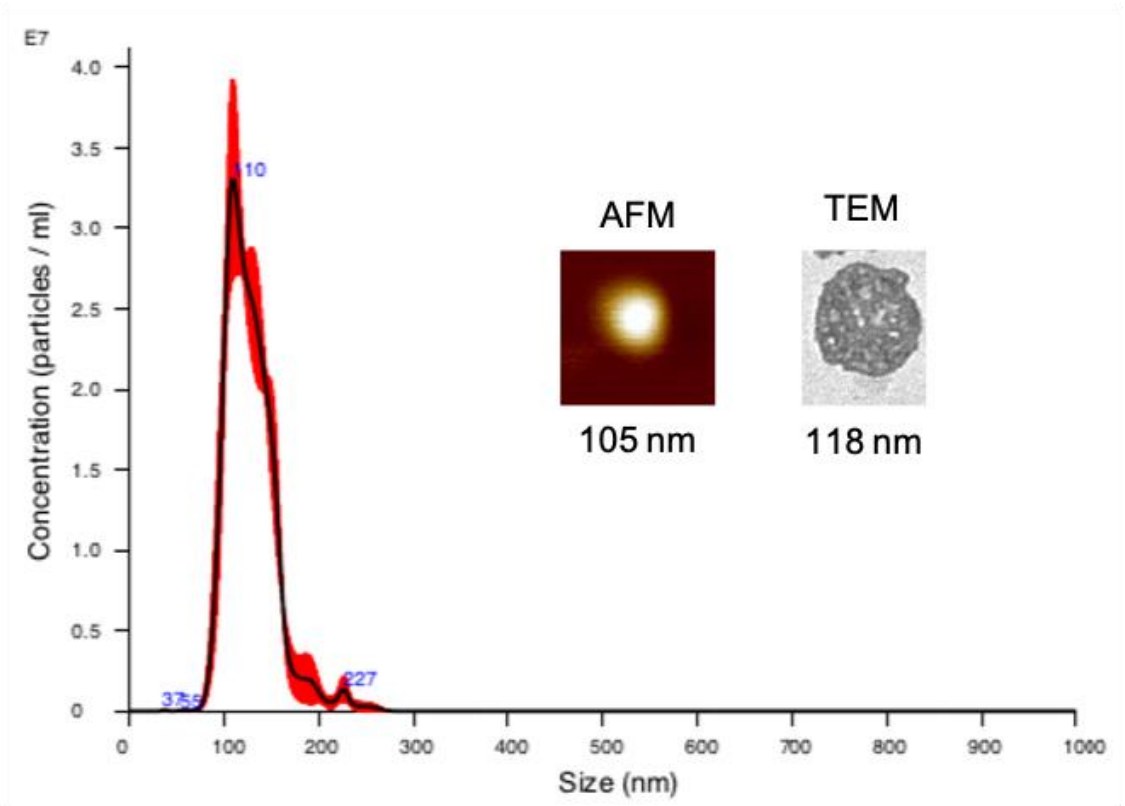


**Figure 3.5 RCA efficiency in different ratio of dATP to biotin-dATP added to the reaction mixture, tested by A) 1.5% native agarose gel and B) represented by the fluorescence intensity detected in the wells.** Figure reprinted from Ref.22. © 2021, Elsevier.

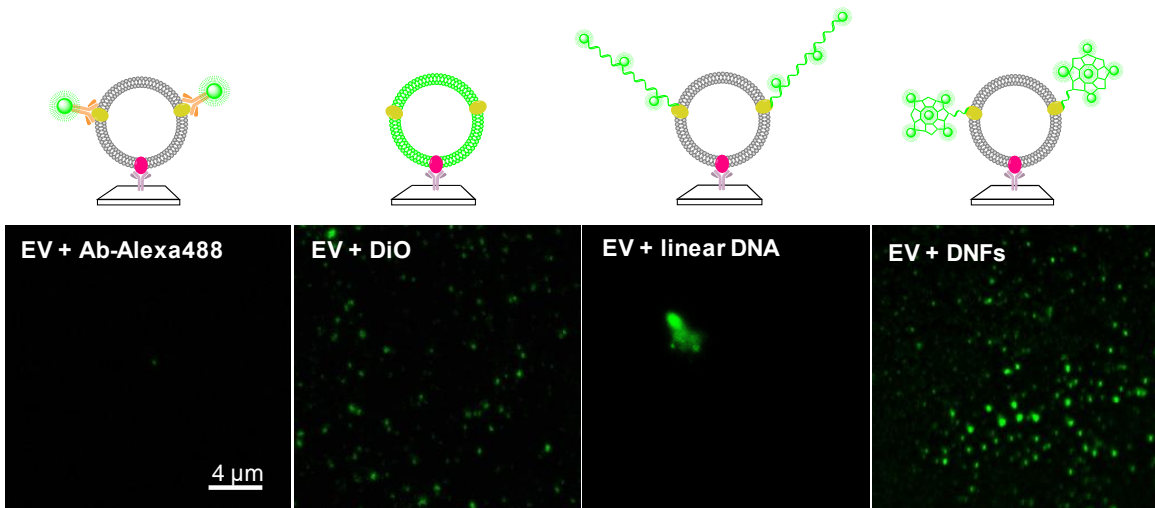
We hypothesized that EVs labeled by the DNF with comparable sizes (Figure 3.2B, Figure 3.3 and Figure 3.6), and carrying tens of fluorophores through biotin-streptavidin

interaction should be easily observable by the conventional CFM. Thus, we designed the RCA initiator that can recognize CD63 on the EV surface, a classic tetraspanin membrane protein with high abundance on a particular EV population, exosome<sup>26, 27</sup> This initiator contains the primer sequence complementary to a region on the circular template at its 3' end for strand extension, and the anti-CD63 aptamer at the 5' end for EV binding through CD63 recognition (Initiator 2 in Table 3.1). These two sequences were separated by a short spacer to ensure stable EV attachment. The initiator was incubated with the standard EVs derived from COLO-1 cells, and then the RCA reagents were added to the mixture for DNF construction. We confirmed that growing the DNF *in situ* on EV surface did not alter its compact structure of the DNF by SEM (Figure 3.2B). At last, the DNF was labeled by the Alexa 488-conjugated streptavidin (SA-Alexa 488) before the EVs were captured onto the anti-CD9 modified coverslip for CFM (Scheme 3.1). Indeed, many bright fluorescent particles were found by CFM, each occupying a region with a diameter of 5 – 9 pixels (200 – 400 nm) (Figure 3.7, last image). In contrast, the EVs directly labeled with the Alexa 488-conjugated anti-CD63 Ab were not detectable (Figure 3.7). In addition, labeling the EVs with the RCA product from a circular template without the self-assembly regions did not show countable fluorescent particles, other than very few but large particles (Figure 3.7) that might be the result of the entanglement of multiple, long, freely straining single-stranded RCA products on the nearby EVs.



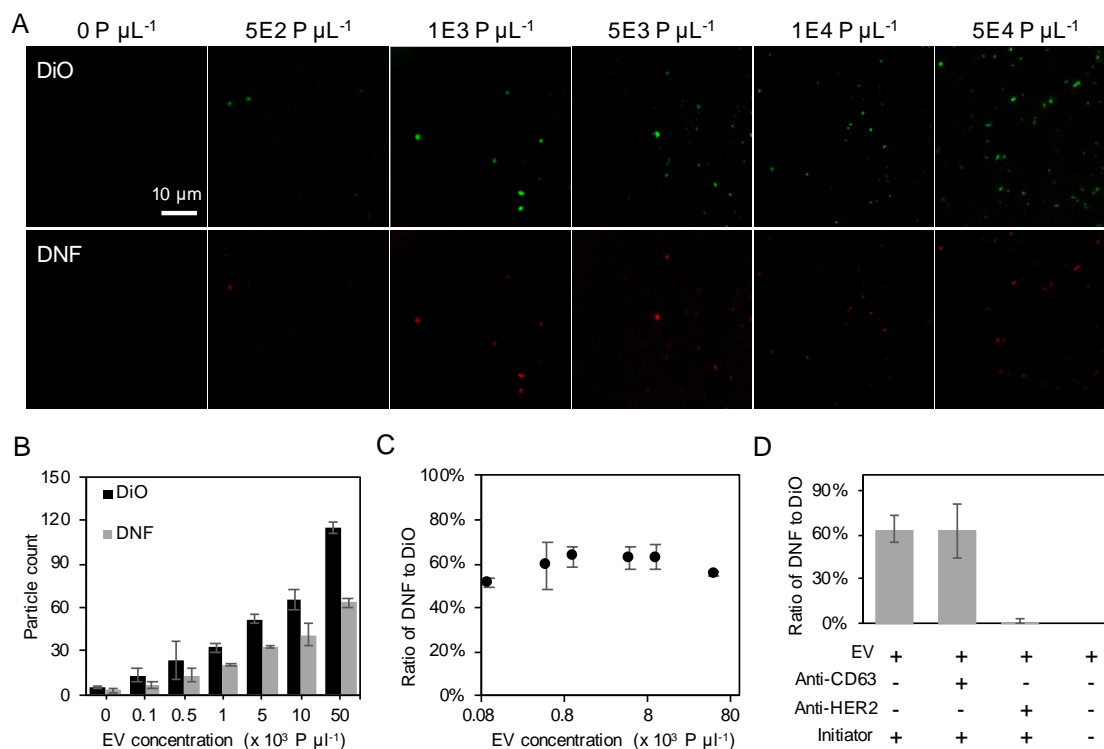


**Figure 3.6** NTA analysis of EV size distribution with AFM and TEM image of EV. Figure reprinted from Ref.22. © 2021, Elsevier.

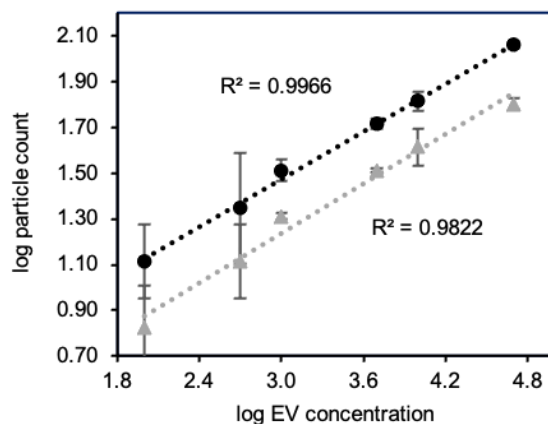


**Figure 3.7** Representative fluorescence microscopy images of the EVs labeled with various dyes: Alexa 488 conjugated antibody, DiO dye, linear RCA product and CD63-specific DNFs. All images have the same scale bar. Figure reprinted from Ref.22. © 2021, Elsevier.

With the DNF allowing single EV visualization, the binding of the RCA initiator that recognizes a specific EV surface protein should be positively related to the target abundance on each EV. Therefore, the number of EVs illuminated by the DNFs in each EV sample could represent the sample's target protein content. To prove this, we carried out the assay using the RCA initiator containing the anti-human epidermal growth factor receptor 2 (HER2)<sup>28</sup> aptamer (Initiator 3 in Table 3.1) to grow the DNF, and capturing the EV sample to the imaging surface by anti-CD63 Ab (Figure 3.8A, lower panel). The DNF was tagged by the Alexa 633-labeled streptavidin. We can see that the particle counts acquired in the red channel (detecting the DNF),  $P_{\text{DNF}}$ , was indeed proportional to the EV concentration in the range of  $100 - 5 \times 10^4$  particle/ $\mu\text{l}$  with a high linear regression coefficient ( $R^2 = 0.982$ ) (Figure 3.8B; Figure 3.9). Using the  $3\sigma$  method, the limit of detection (LOD) with DNF labeling was 82 particle/ $\mu\text{l}$ , 100 times lower than that obtained by tagging single EVs with fluorescent antibodies<sup>29</sup>. This result confirms that we can “digitally” count the number of fluorescent particles for EV quantification with high sensitivity.



**Figure 3.8 Sensitivity and selectivity test of our assay.** A) Representative CFM images for detection of the EVs stained by the DiO dye and tagged by the HER2-specific DNFs at different EV concentration. All images share the same scale bar. B) The particle count obtained from counting the DiO-stained or the DNF-tagged EVs at different EV concentrations. C) Ratio of  $P_{\text{DNFs}}/P_{\text{DiO}}$  measured at different EV concentrations. D) Ratios of the EVs labeled with the HER2-specific DNFs to that stained by DiO stained in EV samples going through different labeling conditions. All error bars represent the standard deviations from three measurements. Figure reprinted from Ref.22. © 2021, Elsevier.



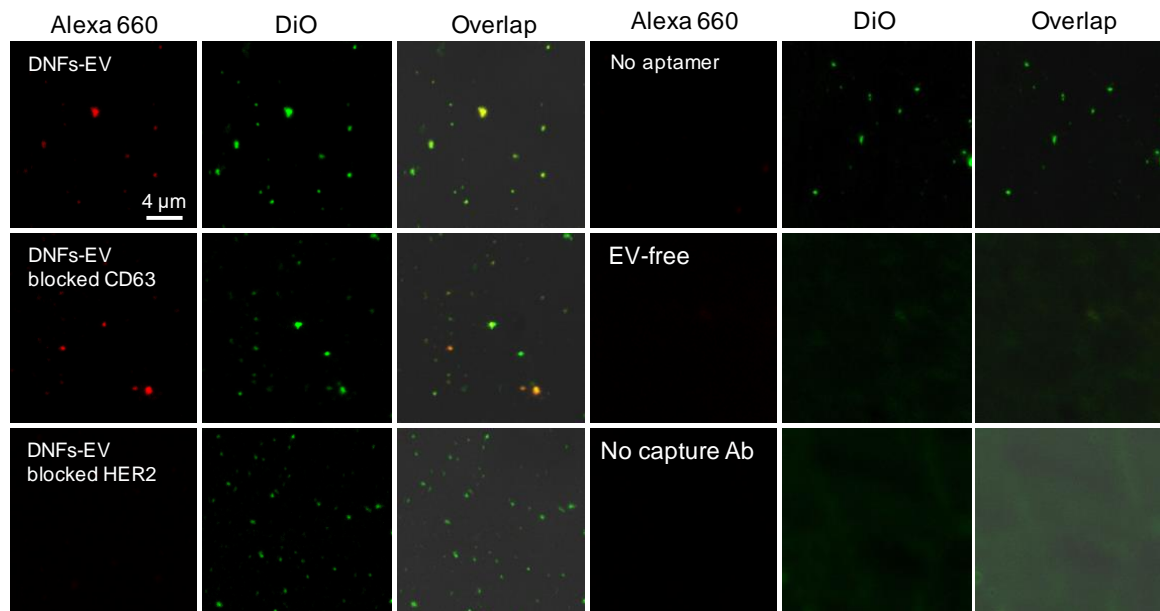
**Figure 3.9 Correlation between the EV particle count obtained by DiO-staining (black) or DNF-labeling (specific to HER2) (grey) and the EV input concentration, both in log scale. HER2 recognition was mediated by the anti-HER2 aptamer. Figure reprinted from Ref.22. © 2021, Elsevier.**

However, EV capture efficiency on the imaging surface could vary and the input EV number could be different from sample to sample, preventing the usage of the absolute particle counts for accurate comparison of the EV protein expression profiles among samples. In conventional approaches like WB and ELISA, total EV counts and total protein amounts should be determined prior to protein expression analysis. To avoid these tedious sample characterization steps, we stained the EVs with the lipophilic fluorescent dye, DiO<sup>30</sup>, to directly count the total EVs captured on the viewing surface. The DiO-stained EVs were visible under the same imaging condition as that for the DNF-labeled EVs (Figure 3.8A, upper panel; Figure 3.7), and provided similar detection sensitivity as the DNF, probably because of the multiple dyes incorporated into the EV membrane (Figure 3.8B; Figure 3.9;  $R^2 = 0.996$ ). Since the number of DiO-stained EVs obtained in the green channel of the CFM (detecting the DiO dye),  $P_{\text{DiO}}$ , should be proportional to all the EVs

captured on the imaging surface, using  $P_{\text{DiO}}$  as the internal standard to normalize  $P_{\text{DNF}}$ , we can correct for variations in EV input or capture efficiency. Indeed, the ratio of  $P_{\text{DNFs}}/P_{\text{DiO}}$  remained constant and  $\sim 60\%$  with different EV concentrations (Figure 3.8C), meaning that  $\sim 60\%$  of this EV population (standard EVs derived from PC-3 cells) carries HER2. This result proves that, using  $P_{\text{DiO}}$  as the internal reference, we can compare the expression levels of the same protein marker in repeated measurements and across different EV samples, without the need of prior quantification of the total EV numbers or the total protein contents, nor to use any external calibration methods for quantification of the absolute target amount. Eliminating these steps could greatly save the time, effort, and sample consumption in evaluation of EV protein expression difference in samples. It is worth noting that our method does not rely on the particle fluorescence intensity for protein quantification, which could vary with the length of the RCA product and demands more time and efforts in data processing.

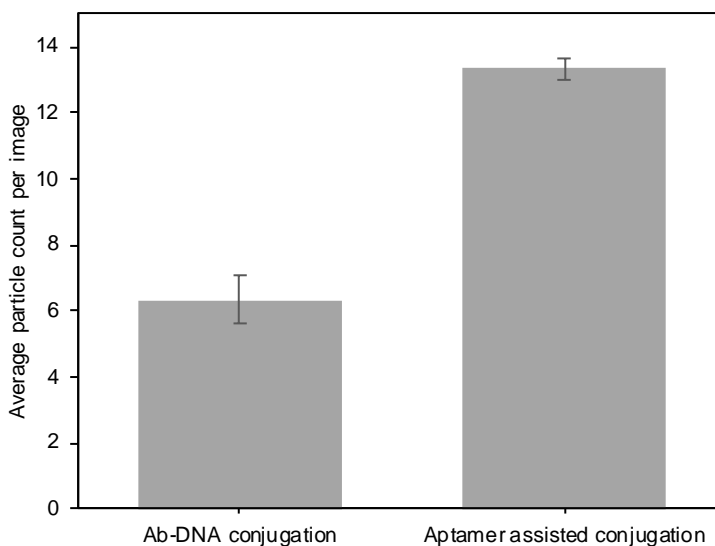
Another advantage of our assay is that, we only count the DNF-labeled particles co-localized with the DiO-stained ones, to eliminate the background DNF grown from the probes non-specifically adsorbed on the imaging surface, enhancing detection specificity. To verify the fluorescent particles detected by CFM were the EVs specifically labeled by DNF, we tested EV labeling by the HER2-targeting DNF: in the presence of 1) anti-HER2 Ab that should block the HER2 protein on EV surface and thus prevent the binding of the aptamer-based initiator probe needed for DNF construction; and 2) anti-CD63 Ab that does not compete with the initiator binding to HER2. We can see from Figure 3.8D and 3.10 that, anti-HER2 Ab completely blocked the growth of DNF on the EVs, leaving no EVs

stained by red fluorescence. On contrary, anti-CD63 Ab did not affect the DNF labeling. Additionally, if the RCA initiator contained only the template-hybridizing primer but not the anti-HER2 aptamer sequence (Initiator 1 in Table 3.1), no fluorescent particles was detected (Figure 3.10). The same negative results were obtained in the controls that had no EV in the sample or no capturing Ab on the surface. These results demonstrate that, DNF labeling is specific to the EV target protein, and experiences little non-specific absorption to the detection surface. Since EV capture and DNF labeling target different surface proteins, our method can also avoid detection of the freely floating proteins in biospecimen, but report the co-localization of both targets on the same EV particle.

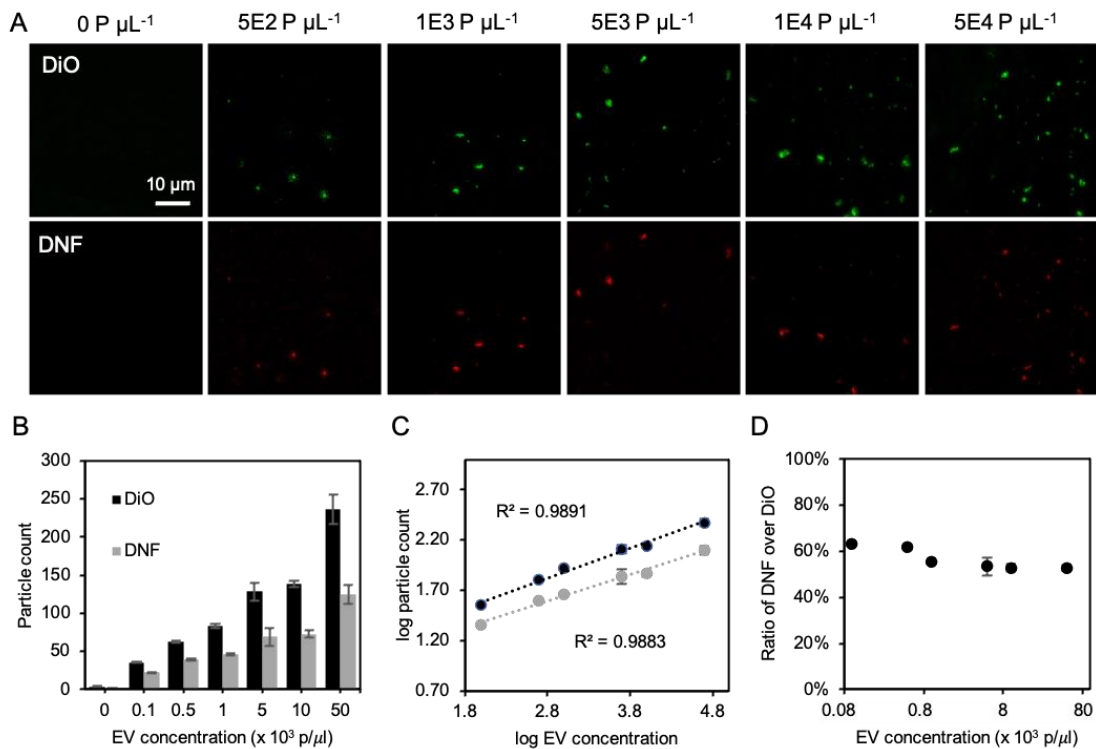


**Figure 3.10 Representative CFM images of different samples** containing the DiO-stained EVs which were also labeled by the DNFs targeting HER2 through the anti-HER2 aptamer (DNFs-EV). Several controls were included. They were the EV samples undergoing the same DiO and DNF labeling but with the presence of 1) anti-CD63 (DNFs-EV blocked CD63) or 2) anti-HER2 (DNFs-EV blocked HER2). Or, the RCA initiator did not have the anti-HER aptamer region (No aptamer); the reaction was conducted in the EV-free sample (EV-free); or the EV sample was applied on a glass slide with no capture antibody on the surface (No capture Ab). All images have the same scale bar. Figure reprinted from Ref.22. © 2021, Elsevier.

The above works uses aptamers for target recognition, which can be conveniently incorporated into the sequence of the RCA initiator. To allow detection of more protein targets, we also conjugated the simple RCA initiator (Initiator 1 in Table 3.1) to the secondary Ab which can bind to the primary Ab used for recognition of specific surface proteins on EV surface<sup>31</sup>. To better preserve the secondary Ab's affinity to the primary Ab, we employed the proximity-induced site-specific labeling strategy<sup>32</sup>: the azide-modified primer was hybridized with an anti-IgG aptamer that recognizes the Fc region of IgG, so that crosslinking only occurred in the Fc region (Figure 3.11). Using the primer-conjugated Ab, the  $P_{DNFs}/P_{DiO}$  of HER2 in the same EV sample was also found to be  $\sim 60\%$  (Figure 3.12), proving that both Ab and aptamer can be used in our design, and the ratio of  $P_{DNFs}/P_{DiO}$  is not affected by experimental conditions and consistent among different batches of measurements of the same EV population.



**Figure 3.11 Average particle count per image of found in EV samples labeled with the DNFs originated from the direct Ab-DNA conjugation and the aptamer assisted conjugation.** Figure reprinted from Ref.22. © 2021, Elsevier.



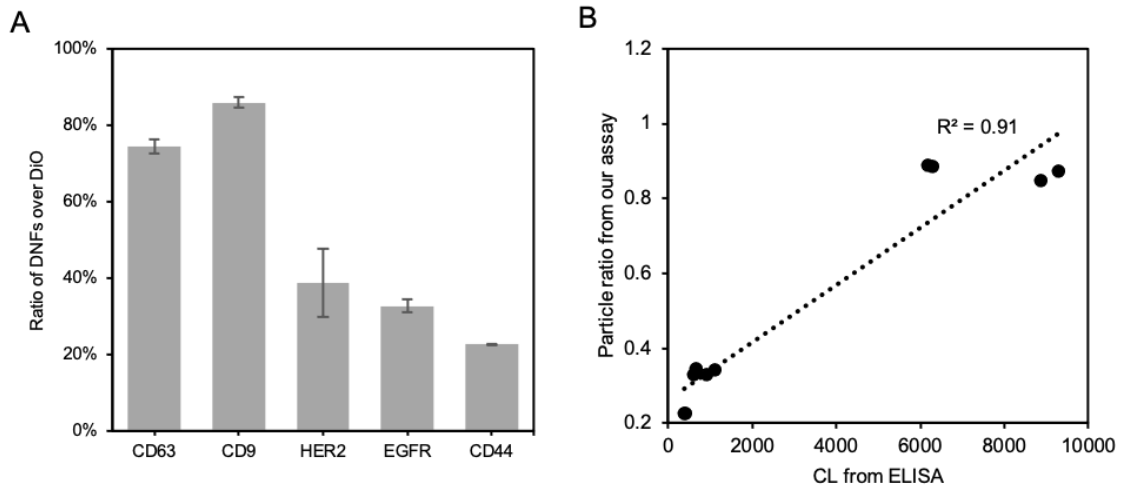
**Figure 3.12 Detection of EVs using dual color labeling by antibodies.** A) Representative CFM images of the EV stained by DiO and labeled by the HER2-specific DNFs with various EV input concentrations. All images share the same scale bar. B) Particle count of the EVs labeled by DiO (black) and DNFs (grey). C) Correlation of the EVs particle count obtained using DiO staining (black) or HER2-specific DNF labeling (grey) with the EV concentration. D) Particle count ratio of DNFs to DiO under various EV concentrations. Figure reprinted from Ref.22. © 2021, Elsevier.

DNF can be used to label different target proteins by simply switching the aptamer sequence on the RCA initiator, or using the simple initiator-conjugated secondary Ab to bind to the primary Ab that recognizes different targets of interest. Thus, we attempted to profile the expression of different markers on EVs using our method. Since the standard EVs are derived from tumor cell lines, we chose to detect several well-known tumor proteins on the EV surface, including HER2, epidermal growth factor receptor (EGFR)<sup>33</sup>;

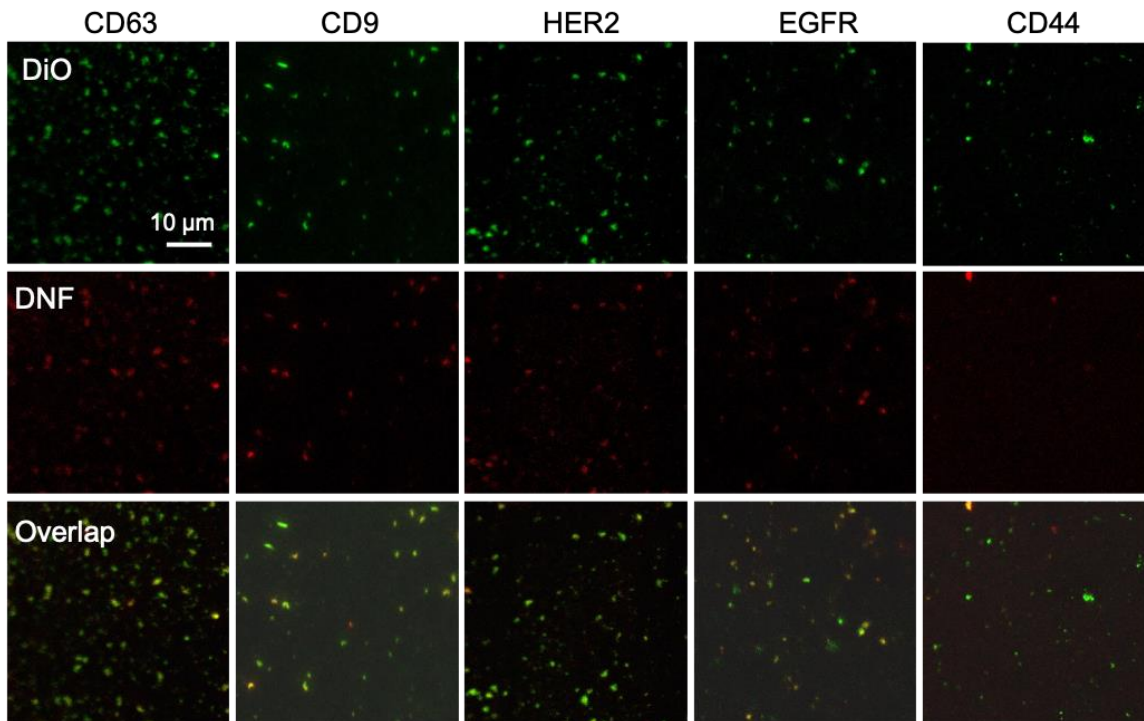


and CD44<sup>34</sup>. Exosomes are one of the EV sub-populations that have demonstrated to be highly relevant to cancer development<sup>35, 36</sup>. Therefore, we also included two exosomal markers, CD63 and CD9. The 18-microwell chip was used to simultaneously process 18 samples in parallel, with each well detecting one EV protein in 10  $\mu$ L of the dilute EV solution.

The standard EVs derived from COLO-1 were labeled by DNF and DiO, and captured by the Milk fat globule epidermal growth factor 8 (MFG-E8), which binds to the phosphatidylserine (PS) exposed on EVs<sup>37</sup>. Individual EVs were counted in both the green and red channels, and the ratio of  $P_{\text{DNS}}/P_{\text{DiO}}$  for each of the protein target was measured. Higher  $P_{\text{DNS}}/P_{\text{DiO}}$  ratios ( $\sim 80\%$ ) were found for CD63 and CD9 among 5 markers, agreeing with their roles as the general exosome markers (Figure 3.13 and Figure 3.14). A high positive correlation ( $R^2 = 0.91$ ; Figure 3.13) was detected between the  $P_{\text{DNS}}/P_{\text{DiO}}$  ratio and the chemiluminescence obtained by ELISA for these 5 markers, further confirming that the ratio of  $P_{\text{DNS}}/P_{\text{DiO}}$  is proportional to the expression level of the target protein in EVs. Our method only requires few  $\mu$ l of EVs sample and is much more sensitive than ELISA, avoiding EV enrichment prior to measurement that could take hours or even days<sup>38</sup>.

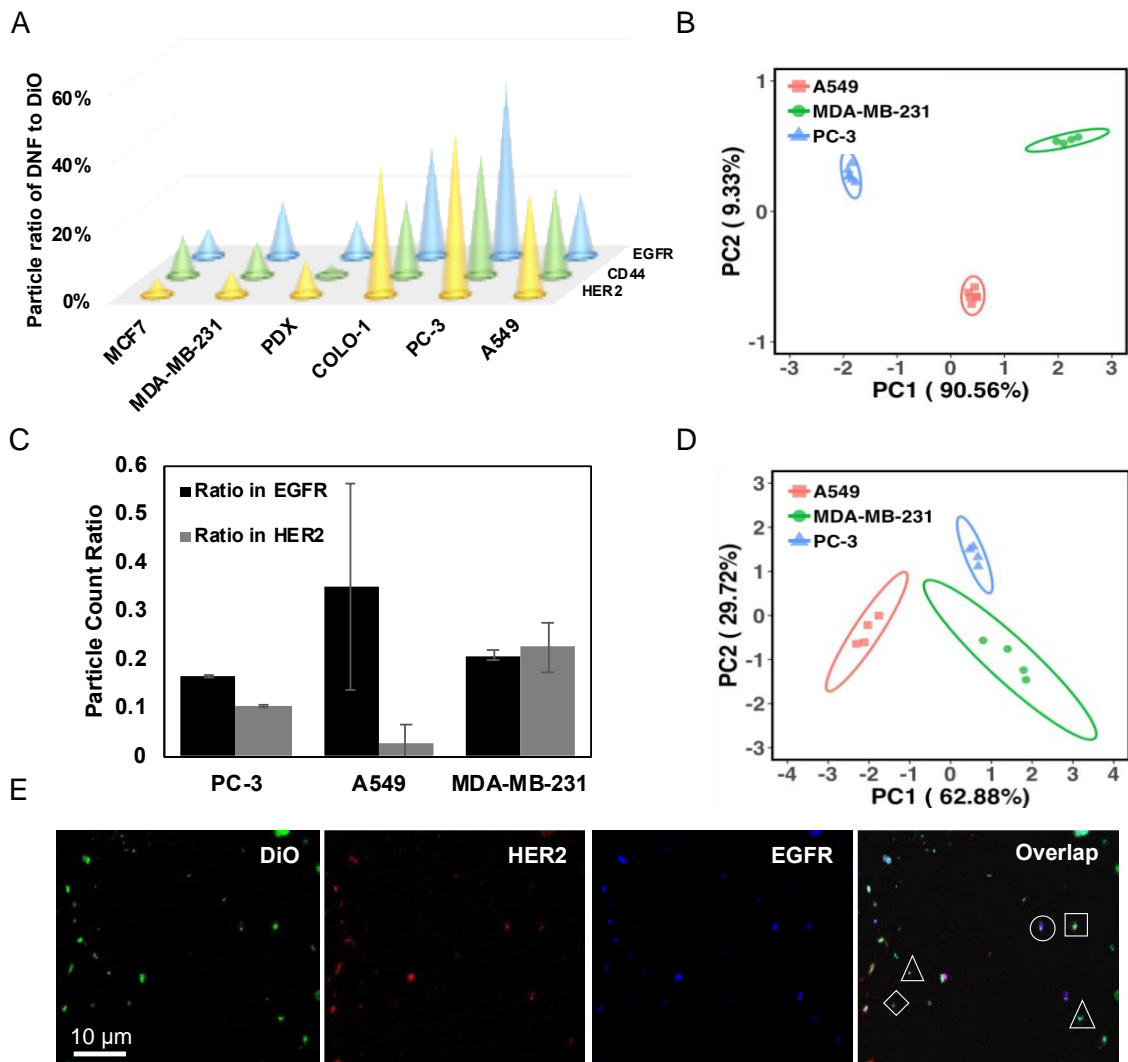


**Figure 3.13 Comparison of the expression profiles, represented by the particle ratios, of 5 protein markers in the EVs derived from COLO-1 cells.** A) Comparison of the expression profiles, represented by the particle ratios, of 5 protein markers in the EVs derived from COLO-1 cells. B) Correlation of particle ratio obtained from our assay with chemiluminescence signals from ELISA. Figure reprinted from Ref.22. © 2021, Elsevier.

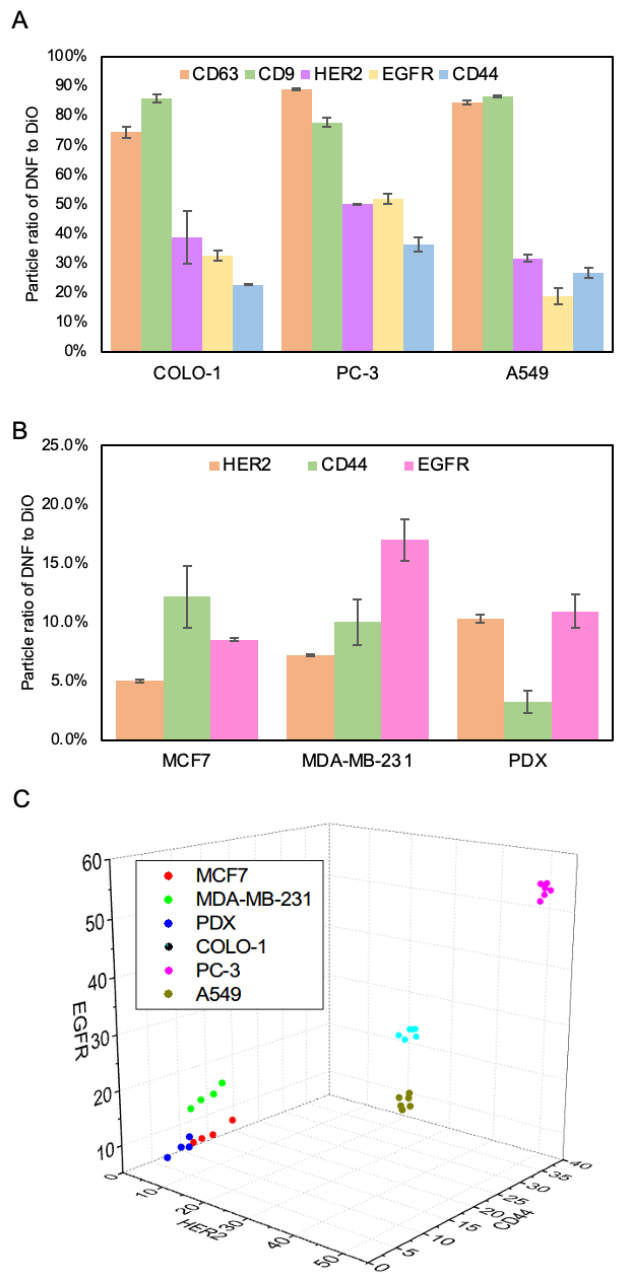


**Figure 3.14 Representative CFM images of the COLO-1-derived EVs labeled with the DNFs specific to CD63, CD9, HER2, EGFR and CD44.** All images have the same scale bar. Figure reprinted from Ref.22. © 2021, Elsevier.

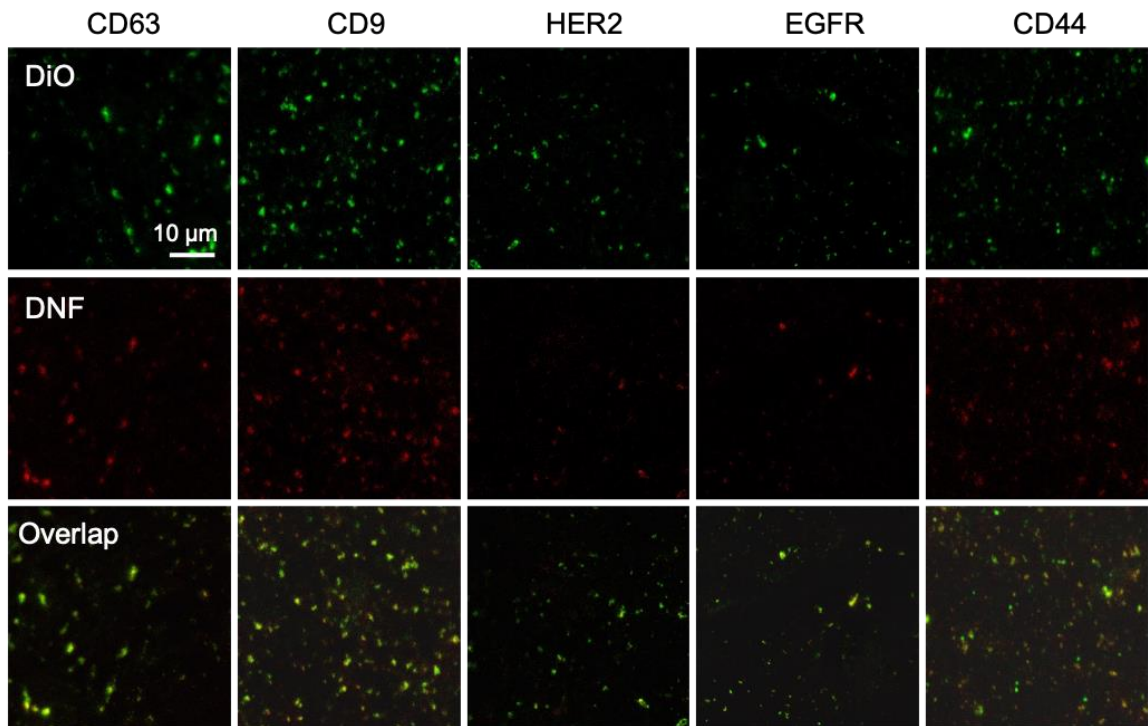
We also tested the EVs derived from other cells, including PC-3, A549, and three breast-cancer (BC) related cells: MCF-7, MDA-MB-231, and the primary cells (PDX) taken from the tumor tissue of a female patient carrying triple-negative BC.<sup>39, 40, 41</sup> Strikingly, the protein expression profiles illustrated by the ratios of  $P_{\text{DNS}}/P_{\text{DIO}}$  were significantly different among all EV samples tested (Figure 3.15A; Figure 3.16 – 3.21). The expression levels of EGFR were the highest in the MDA-MB-231-derived EVs compared to those from other cells; and those from PDX cells had the highest  $P_{\text{DNS}}/P_{\text{DIO}}$  for HER2. The scores plot obtained from subjecting the profiles to Principal Component Analysis (PCA) also proved significant clustering of the EVs by the cell of origin (Figure 3.15B); and even plotting the ratios of  $P_{\text{DNFS}}/P_{\text{DIO}}$  of HER2, EGFR and CD44 could lead to good clustering of the EVs originated from the same source (Figure 3.14C). All of the lab-prepared EVs derived from the BC-related cell lines located closer to each other, but further apart from the standard EVs purchased from commercial sources with different cells of origin on the PCA plot. Although we could not exclude the contribution from the source of EVs to the protein expression difference observed, among the lab-prepared EVs, those originated from the two triple negative (Basel) cell lines – PDX and MDA-MB-231 – were clustered closer compared to their relative location to those from the MCF-7 cells (ER<sup>+</sup>/PR<sup>+</sup>/HER2<sup>-</sup>, Luminal A). This result strongly supports the feasibility of our method in EV differentiation based on the cell of origin.



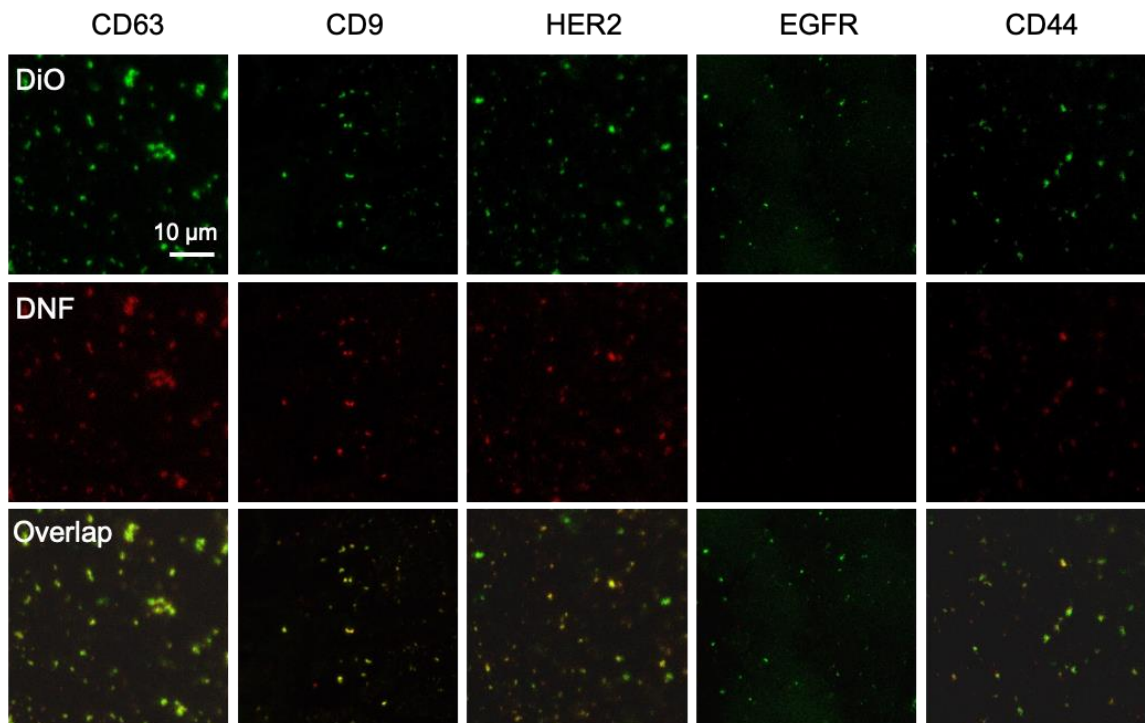
**Figure 3.15 Protein profiling using EV engineering.** A) Comparison of the expression profiles, represented by the average particle ratios ( $n = 6$ ), of 3 protein markers in the EVs derived from six cell lines. Average relative standard deviation of all measurements  $< 5\%$ . B) PCA score plot showing EV differentiation by the cell of origin based on the protein profiles shown in A). C) Ratio of EV carrying both markers detected in the EV population captured by anti-EGFR and anti-HER2 Ab, respectively, using the dual-marker colocalization assay. D) PCA score plot to identify EVs derived from three cell lines based on the particle counts obtained from DiO staining or DNF tagging in the dual-marker assay. E) Representative 3-color CFM images for the DiO-stained EV with dual-DNF labeling. Triangle – EV labeled with DiO; Square – EV labeled with both DiO and EGFR-specific DNFs; diamond – EV labeled with both DiO and HER2-specific DNFs; Circles – EV labeled with DiO, HER2-specific DNFs and EGFR-specific DNFs. Ellipses indicate 95% confidence. Scale bar = 10  $\mu$ m. Figure reprinted from Ref.22. © 2021, Elsevier.



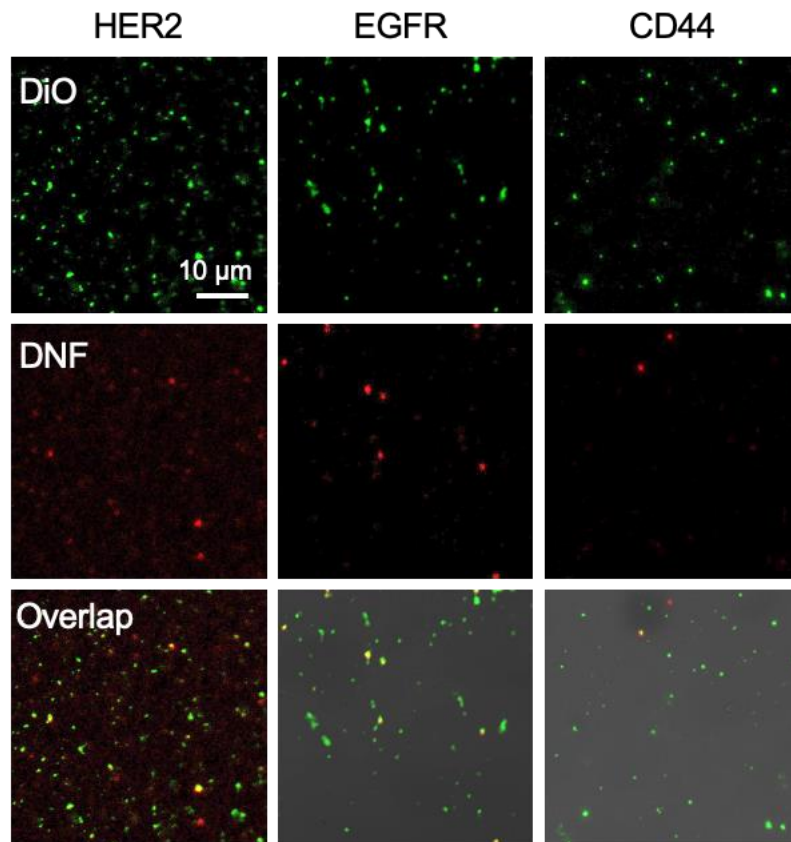
**Figure 3.16 Comparison of the expression profiles.** A) Comparison of the expression profiles, represented by the particle ratios, of 5 protein markers in the EVs derived from COLO-1, PC-3 and A549 cells. B) Comparison of the expression profiles, represented by the particle ratios, of 3 protein markers in the EVs derived from MCF-7, MDA-MB-231, PDX cells. C) The 3D plot to differentiate EVs derived from six cell lines (MCF-7, MDA-MB-231, PDX, COLO-1, PC-3, A549) using the particle counts obtained from DNF labeling targeting HER2, EGFR and CD44, respectively. Figure reprinted from Ref.22. © 2021, Elsevier.



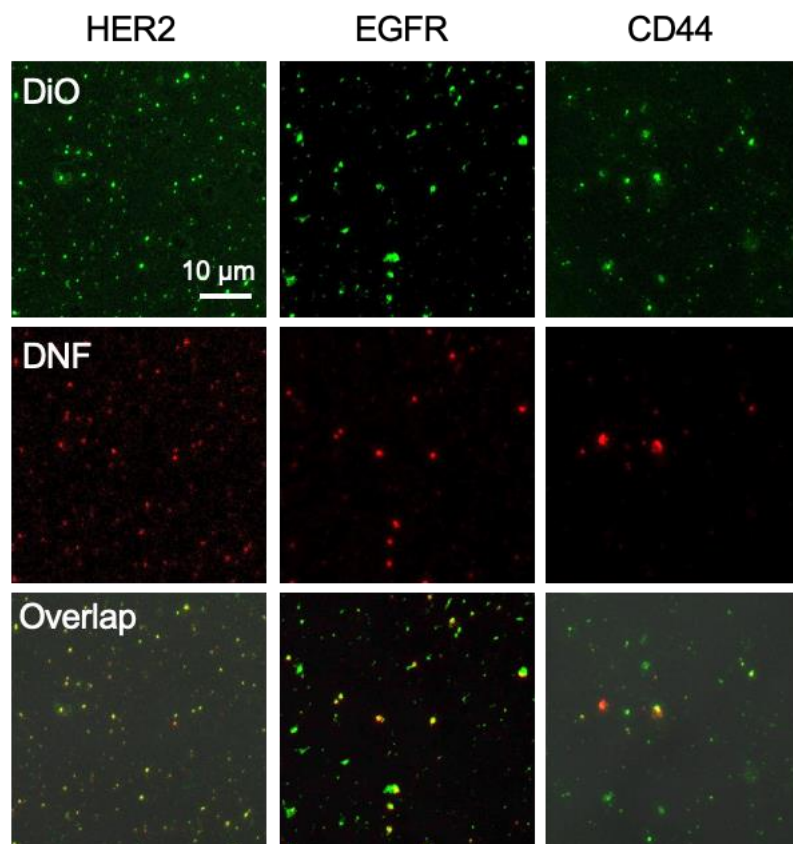
**Figure 3.17 Representative CFM images of the PC-3-derived EVs labeled with the DNFs specific to CD63, CD9, HER2, EGFR and CD44.** All images have the same scale bar. Figure reprinted from Ref.22. © 2021, Elsevier.



**Figure 3.18** Representative CFM images of the A549-derived EVs labeled with the DNFs specific to CD63, CD9, HER2, EGFR and CD44. All images have the same scale bar. Figure reprinted from Ref.22 © 2021, Elsevier.

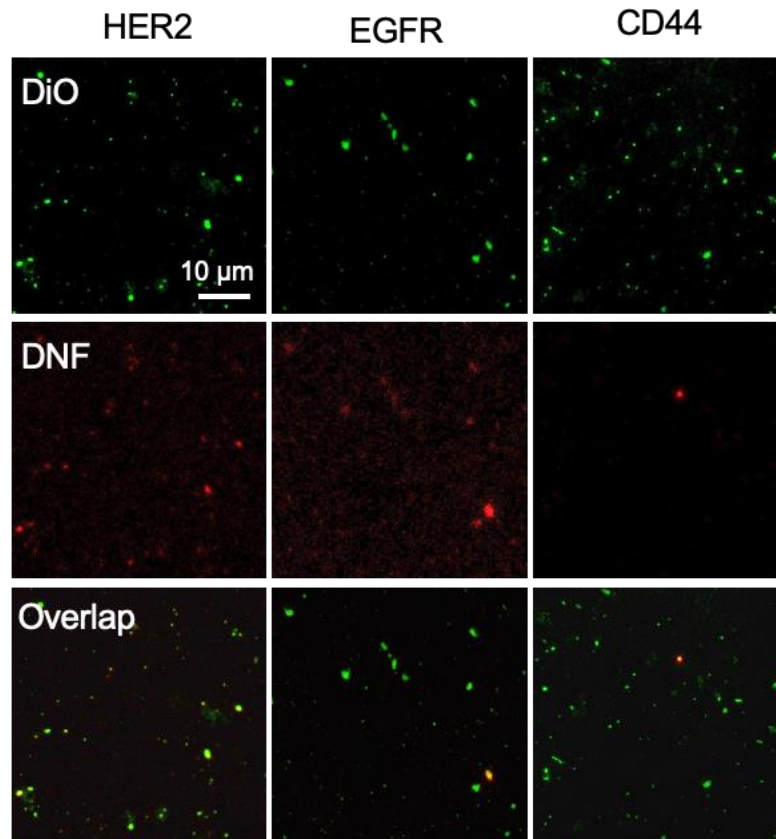


**Figure 3.19** Representative CFM images of the MCF-7-derived EVs labeled with the DNFs specific to CD63, CD9, HER2, EGFR and CD44. All images have the same scale bar. Figure reprinted from Ref.22. © 2021, Elsevier.



**Figure 3.20** Representative CFM images of the MDA-MB-231-derived EVs labeled with the DNFs specific to CD63, CD9, HER2, EGFR and CD44. All images have the same scale bar. Figure reprinted from Ref.22. © 2021, Elsevier.





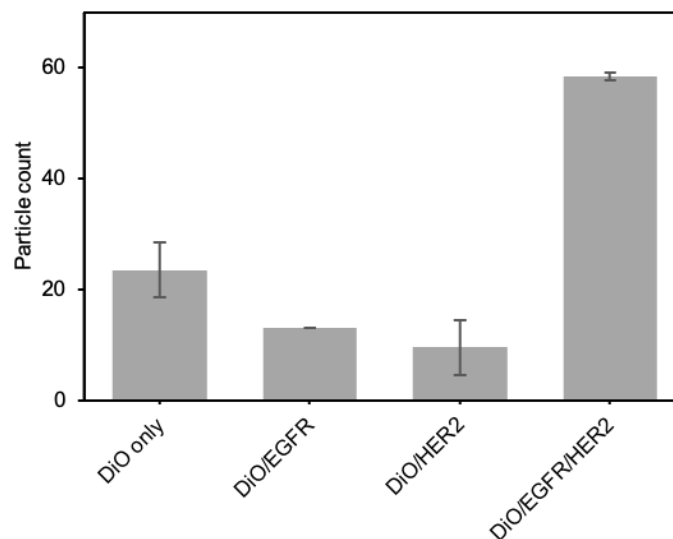
**Figure 3.21** Representative CFM images of the PDX-derived EVs labeled with the DNFs specific to CD63, CD9, HER2, EGFR and CD44. All images have the same scale bar. Figure reprinted from Ref.22. © 2021, Elsevier.

Co-localizing multiple biomarkers on the same EV can specifically detect the EV sub-groups carrying unique molecular signatures, as proved by the pioneering works.<sup>15, 16</sup> Different than these previous works that aim to discover the EV sub-groups with significantly different biological roles, our method focuses on sensitive detection of the EVs carrying dual protein targets in clinical samples for disease diagnosis. This can be simply done by targeting different proteins for EV capture and DNF construction, respectively. Using the anti-EGFR Ab for EV capture and the anti-HER2 Ab for DNF

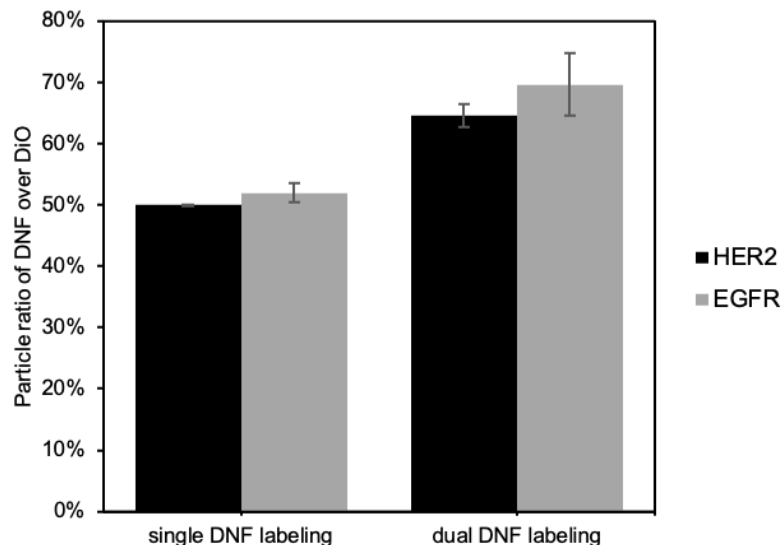
construction (labeled with the Alexa 633-conjugated streptavidin), we obtained the number of EVs carrying EGFR by counting the particles emitting green fluorescence (resulted from DiO staining), i.e.  $P_{\text{EGFR}}$ , and those also having HER2 on the surface (emitting red fluorescence from Alexa-633), i.e.  $P_{\text{EGFR/HER2}}$ . Switching the capture and labeling targets, we can then get the number of EVs carrying HER2 ( $P_{\text{HER2}}$ ) and the number of HER2<sup>+</sup> EVs that also contain EGFR ( $P_{\text{HER2/EGFR}}$ ). The different expression situations of EGFR and HER2 in the EVs derived from PC-3, A549, and MDA-MB-231 cells were evaluated in Figure 3.15C. Interestingly, we can see the proportion of EGFR<sup>+</sup>/HER2<sup>+</sup> EVs among the EGFR<sup>+</sup> or HER2<sup>+</sup> EVs were comparable in the EVs derived from the MDA-MB-231 cells. In contrast, a significantly larger proportion of the EVs carrying both markers was detected in the EGFR<sup>+</sup> EVs derived from the PC3 and A549 cells, compared to that in the HER2<sup>+</sup> EVs. Moreover, dual-marker detection can lead to satisfactory EV differentiation (Figure 3.15D), using the  $P_{\text{EGFR}}$ ,  $P_{\text{EGFR/HER2}}$ ,  $P_{\text{HER2}}$ , and  $P_{\text{HER2/EGFR}}$  found in the above capture/label schemes.

Protein co-localization can also be attained by simultaneously labeling two proteins with the DNF tagged by different fluorophores on the same EVs. Different than the biotin-streptavidin labeling strategy used above, fluorophore-conjugated short DNA probes were employed for dual-target labeling. These probes can complementarily bind to the repeated sequences on the DNFs. To demonstrate this, two DNFs were grown on the EV surface from two RCA initiators, one containing the anti-HER2 aptamer sequence (Initiator 5 in Table 3.1), and the other (Initiator 1 in Table 3.1) attached to the secondary Ab bound to the anti-EGFR primary Ab, with their corresponding templates (Template 1 & 2 in Table

3.1). The EVs were captured by anti-CD63 Ab; and the DNFs targeting HER2 and EGFR were tagged by Alexa 660 and Alexa 546, respectively, using Detection probe 1 and 2 (Table 3.1). The CFM images (Figure 3.15E) revealed that, even among the EVs derived from the same cell of origin, i.e. PC3, there exist particles carrying different protein combinations: some particles emitted only green fluorescence (marked by a triangle), i.e. the CD63<sup>+</sup>/EGFR<sup>-</sup>/HER2<sup>-</sup> EVs; green plus red or yellow fluorescence (marked by a square or diamond), i.e. the CD63<sup>+</sup>/EGFR<sup>+</sup>/HER2<sup>-</sup> EVs or CD63<sup>+</sup>/EGFR<sup>-</sup>/HER2<sup>+</sup> EVs; or all 3 fluorescence (marked by a circle), i.e. the CD63<sup>+</sup>/EGFR<sup>+</sup>/HER2<sup>+</sup> EVs (Figure 3.22). The ratio of  $P_{DNFs}/P_{DiO}$  for EGFR and HER2 is 69.6% and 64.6%, respectively, comparable to that obtained by single marker labeling (Figure 3.23). This result hints that dual marker detection exhibits little space hindrance, probably owing to the compact structure of the DNF.



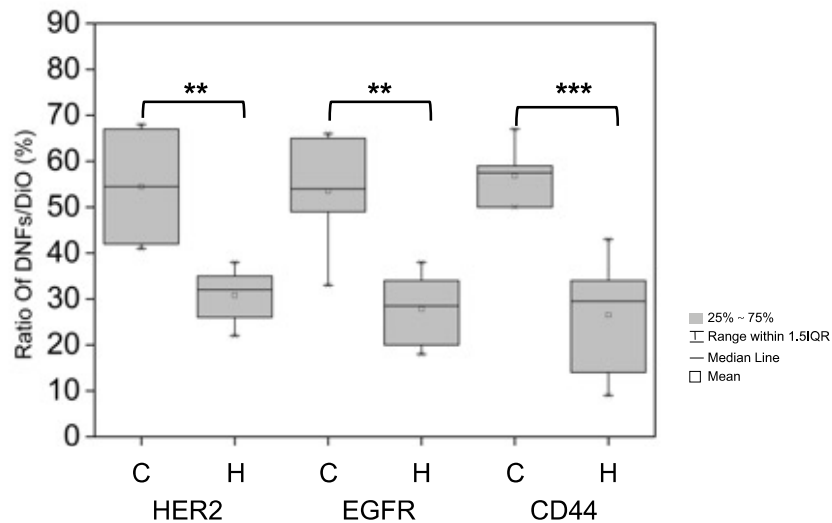
**Figure 3.22 Particle count of the EGFR<sup>-</sup>/HER2<sup>-</sup> EVs, EGFR<sup>+</sup>/HER2<sup>-</sup> EVs, EGFR<sup>-</sup>/HER2<sup>+</sup> EVs and EGFR<sup>+</sup>/HER2<sup>+</sup> EVs obtained with the dual marker colocalization assay.** Figure reprinted from Ref.22. © 2021, Elsevier.



**Figure 3.23 Comparison of the ratio of  $P_{DNF}/P_{DiO}$  obtained from single or dual DNF labeling targeting HER2 and EGFR.** Figure reprinted from Ref.22. © 2021, Elsevier.

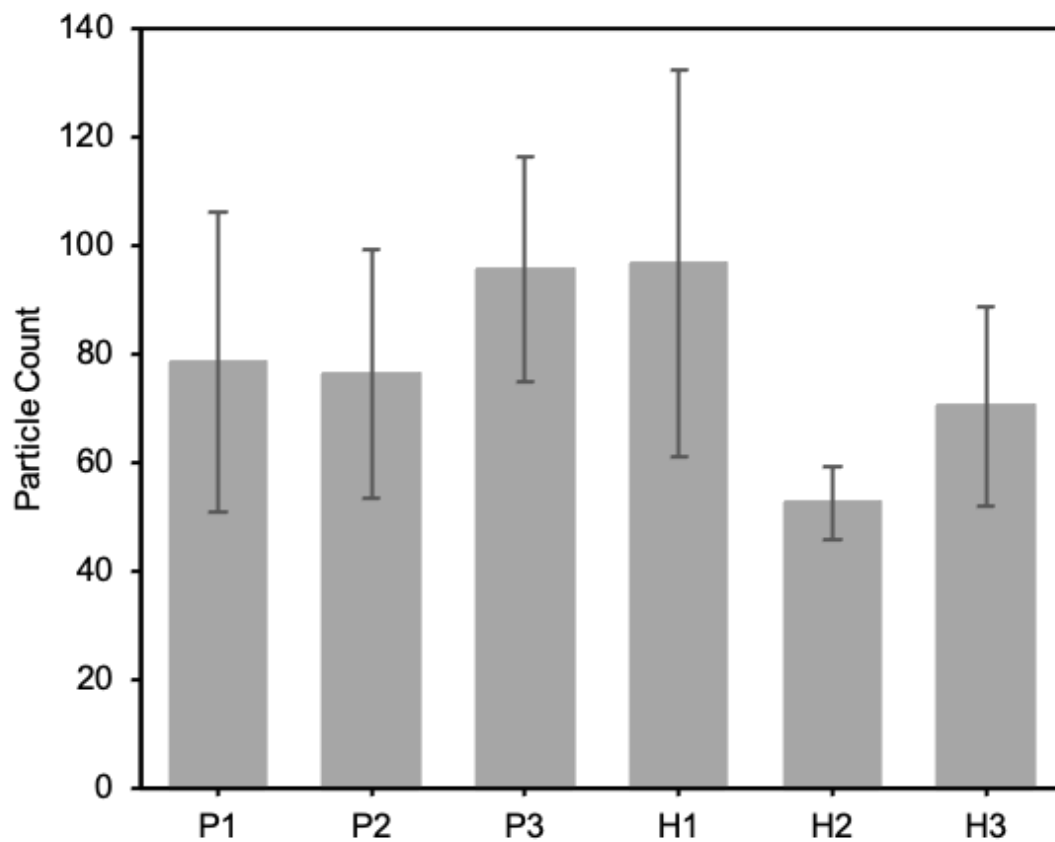
Our method is simple (one-pot incubation) and sensitive (detecting down to 100 EV/ $\mu$ L) in detection of the specific EV sub-populations carrying the high potential markers, promising for disease diagnosis. To prove this, we detected the EVs in serum samples collected from healthy patients and breast cancer (BC) patients (Stage IA with the same molecular profiles of ER<sup>+</sup>/PR<sup>-</sup>/HER2<sup>+</sup>). The EVs were captured directly on the well surface without any sample pretreatment. Firstly, all three tumor markers of EGFR, HER2, and CD44 were assessed, with the ratios of  $P_{DNFs}/P_{DiO}$  obtained for each protein. We found that the  $P_{DNFs}/P_{DiO}$  ratios in the BC patients were all significantly higher than those in the healthy controls (Figure 3.24, with  $p$  values < 0.01 by Student's  $t$  test). The 3D plot of the particle ratios of these 3 markers also clearly separated the BC patients from the healthy control samples (Figure 3.25). In contrast, BC patient and healthy control differentiation cannot be attained by the total counts of particles stained by DiO (Figure 3.26).

We also noticed that, the serum samples from BC patients and healthy controls in fact can be well separated by using the particle ratios of both HER2 and CD44 (Figure 3.27A). Thus, we used the dual-marker co-localization assay to detect the EVs carrying both HER2 and CD44, by capturing the EVs via anti-CD44, and labeling HER2 by DNF. In this way, each sample (10  $\mu$ L) was only measured one time to get the particle counts of the CD44<sup>+</sup>/HER2<sup>+</sup> EVs, and the number of such particles was significantly higher in the BC patients than in the healthy controls (Figure 3.25B,  $p \leq 0.0001$ ; Figure 3.27B). These results prove that, co-localizing two markers on the same EV could enhance the detection throughput and exhibit more significant difference between BC patients and healthy controls than detection of single protein markers on the EVs.

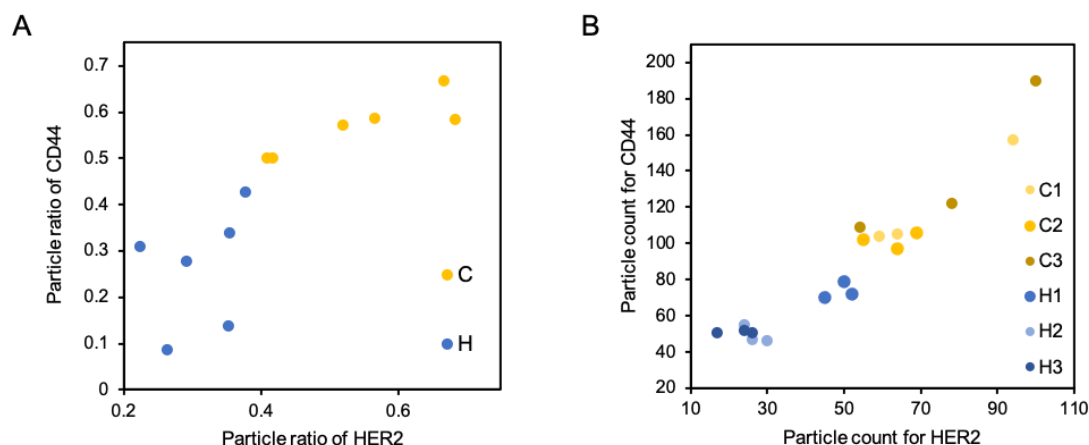


**Figure 3.24 Comparison of the ratio of  $P_{DNF}/P_{DiO}$  obtained by detecting the single EVs using DNFs specific to HER2, EGFR, and CD44 in the serum samples collected from breast cancer patients (C) and healthy controls (H). \*\* $p < 0.01$ , \*\*\* $p < 0.001$ . Figure reprinted from Ref.22. © 2021, Elsevier.**





**Figure 3.26 Particle count of the DiO-stained EVs in the serum samples from breast cancer patients and healthy controls.** Figure reprinted from Ref.22. © 2021, Elsevier.



**Figure 3.27 EV detection by DNF labeling targeting HER2 and CD44, respectively in the serum samples from cancer patients and healthy controls.** A) Particle ratio of  $P_{\text{DNF}}/P_{\text{DiO}}$  obtained by detecting one marker at a time with the EV captured by anti-CD9 & anti-CD63. B) Particle counts obtained by simultaneously detecting dual markers on the same EV with the EV captured by anti-CD44 and labeled by the DNF targeting HER2. Figure reprinted from Ref.22. © 2021, Elsevier.

### 3.4 Conclusion

To summarize, we have developed a technique to profile the surface protein contents on individual EVs. Different affinity probes, like aptamers, antibodies, and ligands, can be easily adopted to recognize diverse targets locating on the membrane of the EV. Construction of DNF on the surface of EVs not only enables single EV visualization by the diffraction-limited microscopes, but also greatly improves the sensitivity of EV detection. Evaluation of the surface protein expression profiles among different EV samples can be simply done with low sample consumption, and without the need of calibration curve construction, EV pre-concentration, and quantification of total EV counts or protein contents. Our method can also assess the co-localization of multiple markers on



the same EV to improve EV differentiation, which can give higher specificity and sensitivity in EV detection. Overall, by enabling rapid and sensitive analysis of EV proteins on single EVs using a one-pot reaction on a multiwell chip and fluorescence microscopy, our technique could be a valuable tool for disease diagnosis and EV biogenesis and functional study that require rapid and high-throughput molecular analysis of the EVs in biofluids or secreted by stimulated cells.

### 3.5 Reference

---

- 1 A. G. Thompson, E. Gray, S. M. Heman-Ackah, I. Mäger, K. Talbot, S. E. Andaloussi, M. J. Wood, M. R. Turner, *Nat. Rev. Neurol.* **2016**, *12*, 346–357.
- 2 A. Koponen, E. Kerkelä, T. Rojalín, E. Lazaro-Ibanez, T. Suutari, H. O. Saari, P. Siljander, M. Yliperttula, S. Laitinen, T. Viitala, *Biosens. Bioelectron.* **2020**, *168*, 112510.
- 3 M. L. Broekman, S. L. N. Maas, E. R. Abels, T. R. Mempel, A. M. Krichevsky, X. O. Breakefield, *Nat. Rev. Neurol.* **2018**, *14*, 482–495.
- 4 R. Kalluri, V. S. LeBleu, *Science* **2020**, *367*, eaau6977.
- 5 S. Wang, A. Khan, R. Huang, S. Ye, K. Di, T. Xiong, Z. Li. *Biosens. Bioelectron.* **2020**, *154*, 112056.
- 6 R. Kalluri, *J. Clin. Investig.* **2016**, *126*, 1208–1215.
- 7 M. Oliveira-Rodríguez, E. Serrano-Pertierra, A. C. García, S. López-Martín, M. Yañez-Mo, E. Cernuda-Morollón, M. C. Blanco-López, *Biosens. Bioelectron.* **2017**, *87*, 38-45.
- 8 E. Cocucci, G. Racchetti, J. Meldolesi, *Trends Cell Biol.* **2019**, *19*, 43–51.
- 9 G. V. Niel, G. D’Angelo, G. Raposo, *Nat. Rev. Mol. Cell Biol.* **2018**, *19*, 213–228.
- 10 S. L. N. Maas, X. O. Breakefield, A. M. Weaver, *Trends Cell Biol.* **2017**, *27*, 172–188.
- 11 S. Gurunathan, M. Kang, M. Jeyaraj, M. Qasim, J. Kim, *Cells* **2019**, *8*, 307.
- 12 B. Zhou, K. Xu, X. Zheng, T. Chen, J. Wang, Y. Song, Y. Shao, S. Zheng, *Signal Transduct. Tar.* **2020**, *5*, 144.
- 13 H. Shao, H. Im, C. M. Castro, X. Breakefield, R. Weissleder, H. Lee, *Chem. Rev.* **2018**, *118*, 1917–1950.
- 14 K. M. McKinnon, *Curr. Protoc. Immunol.* **2018**, *120*, 5.1.1-5.1.11.
- 15 K. Lee, K. Fraser, B. Ghaddar, K. Yang, E. Kim, L. Balaj, E. A. Chiocca, X. O. Breakefield, H. Lee, R. Weissleder, *ACS Nano* **2018**, *12*, 494–503.

- 
- 16 D. Wu, J. Yan, X. Shen, Y. Sun, M. Thulin, Y. Cai, L. Wik, Q. Shen, J. Oelrich, X. Qian, K. L. Dubois, K. G. Ronquist, M. Nilsson, U. Landegren, M. Kammali-Moghaddam, *Nat. Commun.* **2019**, *20*, 3854.
- 17 A. Morales-Kastresana, T. A. Musich, J. A. Welsh, W. Telford, T. Demberg, J. C. S. Wood, M. Bigos, C. D. Ross, A. Kachynski, A. Dean, E. J. Felton, J. V. Dyke, J. Tigges, V. Toxavidis, D. R. Parks, W. R. Overton, A. H. Kesarwala, G. J. Freeman, A. Rosner, S. P. Perfetto, L. Pasquet, M. Terabe, K. McKinnon, V. Kapoor, J. B. Trepel, A. Puri, H. Kobayashi, B. Yung, X. Chen, P. Guion, P. Choyke, S. J. Knox, I. Ghiran, M. Robert-Guroff, J. A. Berzofsky, J. C. Jones, *J. Extracell. Vesicles* **2019**, *8*, 1597603.
- 18 Y. Tian, L. Ma, M. Gong, G. Su, S. Zhu, W. Zhang, S. Wang, Z. Li, C. Chen, L. Li, L. Wu, X. Yan, *ACS Nano* **2018**, *12*, 671-680.
- 19 W. Shen, K. Guo, G. B. Adkins, Q. Jiang, Y. Liu, S. Sedano, Y. Duan, W. Yan, S. E. Wang, K. Begersen, D. Worth, E. H. Wilson, W. Zhong, *Angew. Chem. Int. Ed.* **2018**, *57*, 15675-15680.
- 20 Z. Nizamudeen, R. Markus, R. Lodge, C. Parmenter, M. Platt, L. Chakrabarti, V. Sottile, *Biochim. Biophys. Acta Mol. Cell Res.* **2018**, *1865*, 1891-1900.
- 21 D. He, S. Ho, H. Chan, H. Wang, L. Hai, X. He, K. Wang, H. Li, *Anal. Chem.* **2019**, *91*, 2768 – 2775.
- 22 K. Guo, Z. Li, A. Win, R. Coreas, G. B. Adkins, X. Cui, D. Yan, M. Cao, S. E. Wang, W. Zhong, *Biosens. Bioelectron.* **2021**, *192*, 113502.
- 23 M. M. Ali, F. Li, Z. Zhang, K. Zhang, D. Kang, J. A. Ankrum, X. C. Le, W. Zhao, *Chem. Soc. Rev.* **2014**, *43*, 3324-3341.
- 24 J. Yao, K. Flack, L. Ding, W. Zhong, *Analyst* **2013**, *138*, 3121-3125.
- 25 R. Hu, X. Zhang, Z. Zhao, G. Zhu, T. Chen, T. Fu, W. Tan, *Angew. Chem.* **2014**, *53*, 5821-5826.
- 26 Y. Jiang, M. Shi, Y. Liu, S. Wan, C. Cui, L. Zhang, W. Tan, *Angew. Chem.* **2017**, *56*, 11916-11920.
- 27 C. Théry, L. Zitvogel, S. Amigorena, *Nat. Rev. Immunol.* **2002**, *2*, 569-579.
- 28 C. Gutierrez, R. Schiff, *Arch. Pathol. Lab. Med.* **2011**, *135*, 55-62.

- 
- 29 J. Min, T. Son, J. Hong, P. S. Cheah, A. Wegemann, K. Murlidharan, R. Weissleder, H. Lee, H. Im, *Adv. Biosyst.* **2020**, *4*, 2000003.
- 30 M. Rodrigues, N. Richards, B. Ning, C. J. Lyton, T.Y. Hu, *Nano Lett.* **2019**, *19*, 7623–7631.
- 31 B. Schweitzer, S. Wiltshire, J. Lambert, S. O’Malley, K. Kukanskis, Z. Zhu, S. F. Kingsmore, P. M. Lizardi, D. C. Ward, *Proc. Natl. Acad. Sci. U.S.A.* **2000**, *97*, 10113–10119.
- 32 C. Yu, J. Tang, A. Loredó, Y. Chen, S. Y. Jung, A. Jain, A. Gordon, H. Xiao, *Bioconjugate Chem.* **2018**, *29*, 3522–3526.
- 33 B. R. Voldborg, L. Damstrup, M. Spang-Thomsen, H. S. Poulsen, *Ann. Oncol.* **1997**, *8*, 1197–1206.
- 34 C. Chen, S. Zhao, A. Karnad, J. W. Freeman, *J. Hematol. Oncol.* **2018**, *11*, 64.
- 35 A. Becker, B. K. Thakur, J. M. Weiss, H. S. Kim, H. Peinado, D. Lyden, *Cancer Cell* **2016**, *30*, 836–848.
- 36 S. Rontogianni, E. Synadaki, B. Li, M. C. Liefwaard, E. H. Lips, J. Wesseling, W. Wu, M. Altelaar, *Biol. Commun.* **2019**, *2*, 325.
- 37 T. Ooishi, D. Nadano, T. Matsuda, K. Oshima, *Genes Cells* **2017**, *22*, 885–899.
- 38 D. W. Greening, R. Xu, H. Ji, B. J. Tauro, R. J. Simpson, *Methods Mol. Biol.* **2015**, *1295*, 179 – 209.
- 39 W. Zhou, M. Y. Fong, Y. Min, G. Somlo, L. Liu, M. R. Palomares, Y. Yu, A. Chow, S. T. F. O’Conner, A. R. Chin, Y. Yen, Y. Wang, E. G. Marcusson, P. Chu, J. Wu, X. Wu, A. X. Li, Z. Li, H. Gao, X. Ren, M. P. Boldin, P. C. Lin, S. E. Wang, *Cancer Cell.* **2015**, *25*, 501-515.
- 40 W. Yan, X. Wu, W. Zhou, M. Y. Fong, M. Cao, J. Liu, X. Liu, C. Chen, O. Fadare, D. P. Pizzo, J. Wu, L. Liu, X. Liu, A. R. Chin, X. Ren, Y. Chen, J. W. Locasale, S. E. Wang, *Nat. Cell Biol.* **2018**, *20*, 597-609.
- 41 M. Y. Fong, W. Zhou, L. Liu, A. Y. Alontage, M. Chandra, J. Ashby, A. Chow, S. T. F. O’Connor, S. Li, A. R. Chin, G. Somlo, M. Palomares, Z. Li, J. R. Tremblay, A. Tsuyada, G. Sun, M. A. Reid, X. Wu, S. Piotr, X. Ren, Y. Shi, M. Kong, W. Zhong, Y. Chen, S. E. Wang, *Nat. Cell Biol.* **2015**, *17*, 183-94.

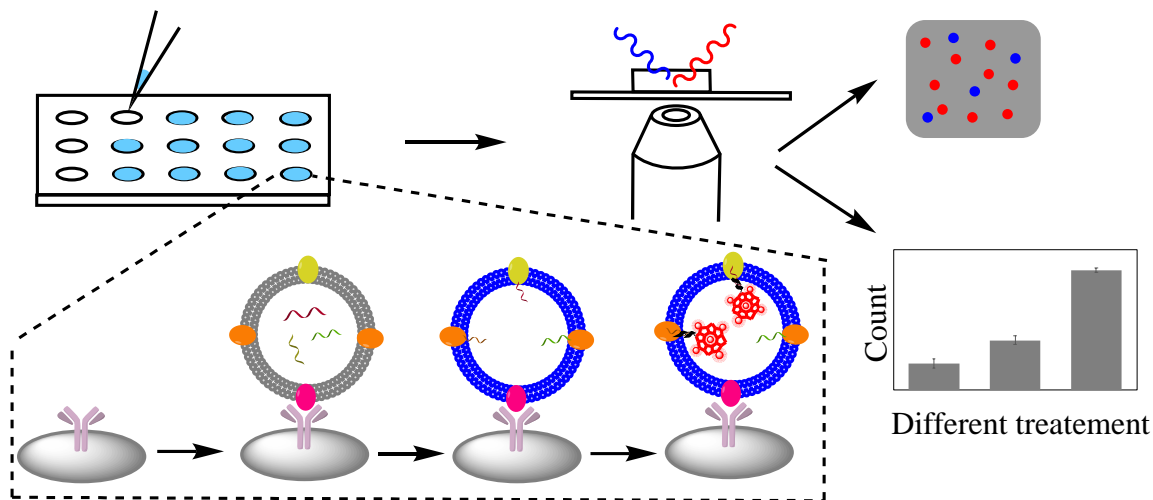
## Chapter 4: Nano-Stir Bar-Assisted Analysis of microRNAs in Single Extracellular Vesicle

### 4.1. Introduction

MicroRNAs (miRNAs) are crucial players in post translational regulation of mRNA expression.<sup>1, 2, 3</sup> A portion of cell-free miRNAs is encapsulated in extracellular vesicles (EVs).<sup>4, 5</sup> EVs protect miRNAs from degradation and transfer miRNAs between cells for intercellular communication, making them promising biomarkers for profiling tumor progression and metastasis.<sup>6, 7</sup> Conventional exosomal miRNAs quantification and detection methods are reverse transcription polymerase chain reaction (RT-PCR),<sup>8</sup> northern blotting,<sup>9</sup> microarray,<sup>10</sup> and next-generation sequencing.<sup>11</sup> These require EV lysis and miRNA extraction before quantification, which is time-consuming and inefficient. Nucleic acid functionalized nanoparticle, such as Au nanoflares,<sup>12, 13</sup> magnetic nanoparticle,<sup>14</sup> and gold nanoparticle<sup>15</sup> were delivered into EVs for *in situ* detection of the bulk levels of exosomal miRNAs with little sample processing. Still, bulk analysis fails to provide information of the discrepancy between EV miRNA function and the rareness of miRNA in EV, which promotes the development of miRNA detection in individual EV.

Current methods for analysis of miRNA in single EVs rely on molecular beacons (MB),<sup>16</sup> which can be delivered into EVs through the membrane pore-generation reagent streptolysin O,<sup>17, 18</sup> or fusion with the cationic lipoplexes<sup>19, 20</sup> or virus-mimicking fusogenic vesicles<sup>21</sup> containing the MBs. However, these methods are difficult to detect the low levels of target miRNAs in individual EVs. Additionally, fusion time and efficiency limit its application. Moreover, these methods cannot access the miRNA content in individual EVs with high accuracy.

Herein, continuing our success in the development of a calibration-free method for detection of exosomal proteins on single EVs, we have developed the method to explore the miRNA contents in individual EVs, with both the miRNA target and the EV labeled by different fluorophores. In this way, semi-quantitative evaluation of miRNA content in individual EVs can be accessed. While the miRNA target is still labeled by the DNA nanoflowers (DNF) reported in Chapter 3, in this new method, we synthesized the nano-stir bars (NSB) that have comparable dimension as the EVs, to enable highly efficient immunocapture and isolation of EVs from biological fluids prior to single EV analysis. Owing to space hindrance, each NSB only binds to one EV, and also permits rapid immobilization of the EV contents, including proteins and miRNAs, on the NSB. In this way, the miRNA contents in each individual EV can be probed using DNA nanoflowers (DNF) grown upon recognition of the target miRNA. Since each DNF carries multiple fluorophores, counting individual EVs based on their miRNA contents can be realized under confocal fluorescence microscopy (CFM). In addition, coupling with a membrane-staining dye, accurate comparison of the miRNA expression profiles in different EV samples can be achieved to differentiate the EVs by their cell-of-origin. Moreover, our method permits continuous monitoring of EV secretion and enclosed miRNA expression in cell culture medium without prior EV enrichment.



**Scheme 4.1 Schematic of Exosomal miRNA *In Situ* Detection by Nano-stir Bar Isolation and DNA Nanoflower Biosensor.**

#### 4.2. Material and Methods

**Chemicals and materials.** Human breast cell line MCF-10A, MCF-7 and MDA-MB-231 were purchased from ATCC. The standard EVs were obtained from HansaBioMed Life Science Ltd (Tallinn, Estonia) (lyophilized EVs produced by COLO-1 cells). Anti-CD9 antibody, anti-CD81 antibody, cholera toxin, hydrocortisone were purchased from Sigma Aldrich. Anti-CD63 antibody were purchased from Novus Biologicals. Anti-CD24 antibody was purchased from BioLegend. (1-ethyl-3-(3-dimethylaminopropyl)carbodiimide hydrochloride) (EDC) and paraformaldehyde (PFA) were purchased from Acros Organics. Lipophilic carbocyanine dye was purchased from Biotium. miRNeasy mini kit was purchased from Qiagen. All oligonucleotides were purchased from Integrated DNA Technologies. Phi29 DNA polymerase was purchased from New England Biolabs. All other chemicals, including TRIzol™ LS reagent, penicillin

streptomycin, DMEM/F-12, insulin, DMEM, biotin-14-dATP and fetal bovin serum (FBS), were purchased from ThermoFisher Scientific.

**Cell culture and EV extraction.** All cells were cultured at the recommended media containing 1% penicillin streptomycin. MCF-10A cells were cultured in the DMEM/F-12 media supplied with 5% horse serum, 0.1  $\mu\text{g/mL}$  cholera toxin, 10  $\mu\text{g/mL}$  insulin, 0.5  $\mu\text{g/mL}$  hydrocortisone, and 20 ng/mL EGF. MDA-MB-231 and MCF-7 cells were cultured in DMEM media supplemented with 10% FBS. Patient-derived PDX265922 cancer cells (propagated in NSG mice and denoted as PDX) were cultured in Iscove's Modified Dulbecco's medium supplemented with 20% FBS. All cell lines were maintained at 37 °C in a humidified 5% CO<sub>2</sub> incubator and routinely screened for Mycoplasma contamination. When the cells reached a confluency of 75%, the medium was replaced with the EV-depleted culture medium. After 24 hours incubation, the culture medium was collected and centrifuged at 500 g for 15 min and 15,000 g for 20 min to remove the cell debris. Next, the medium was ultra-centrifuged at 110,000 g for 70 min twice to pellet the EVs secreted by the cells. The EVs pellet was resuspended in 1  $\times$  PBS. Particle concentration in the EV solution was measured by NTA.

**Preparation of Nano-stir bar.** The synthesis of nano-stir bar was based on a previous report with slight modifications.<sup>22, 23, 24</sup> 108 mg of FeCl<sub>3</sub>•6H<sub>2</sub>O were dissolved in 4 mL of deionized water, and heated at 87 °C for 18 hrs. The precipitation was isolated by centrifugation, washed with water for three times, and then dispersed in 400  $\mu\text{L}$  of DI water. The surfaces of as-synthesized FeOOH nanorods were functionalized with polyacrylic acid (PAA) by mixing with 0.36 mg/mL PAA solution overnight. The excess



PAA was removed by centrifugation and the PAA modified FeOOH was dispersed in 60  $\mu\text{L}$  of DI water. To synthesize FeOOH@SiO<sub>2</sub>, the PAA modified FeOOH was added to 600  $\mu\text{L}$  ethanol followed by 7.5  $\mu\text{L}$  ammonia hydroxide and 4.5  $\mu\text{L}$  of tetraethyl orthosilicate (TEOS) twice with 1 h interval. The mixture was magnetically stirred overnight. The FeOOH@SiO<sub>2</sub> was isolated by centrifugation and washed with ethanol and water separately, and redispersed into 800  $\mu\text{L}$  of DI water. The FeOOH@SiO<sub>2</sub> was heated to 280 °C under nitrogen, and then reduced by DEG.

To modify the NSB with antibody, it was functionalized with carboxyl group by incubating with carboxyl modified APTES at 130 °C for 30 hrs. Carboxyl modified APTES was prepared by incubating 1 mL of APTES and 85.5 mg/mL of Succinic anhydride at room temperature for 24 hrs. The Fe<sub>3</sub>O<sub>4</sub>@SiO<sub>2</sub>-COOH were isolated and washed with acetone, ethanol and water separately and dispersed in 5 mL of water. For antibody modification, 1 mL of Fe<sub>3</sub>O<sub>4</sub>@SiO<sub>2</sub>-COOH were incubated in 1.6 mg/mL EDC and 0.8 mg/mL NHS at RT for 2 h. The pretreated particles were isolated and washed with 1xPBS. And then the particles were incubated with 50 ng antibody at 4 °C overnight. The Ab-modified NSB were pulled down and washed with 1xPBS twice. After blocking with the glycine, the particles were dispersed in 1ml 1xPBS.

**Exosomal miRNA *in situ* detection by confocal fluorescence microscopy.** We performed the reaction in an 18 sample format. EV isolation was carried out by incubating antibody-functionalized nano-stir bar with EV suspension for 30 min at room temperature with gentle mixing. After isolation, the nano-stir bars were washed with 10  $\mu\text{L}$  PBS to remove impurity, following with 10  $\mu\text{L}$  4% PFA for EV fixation. After fixation, the nano-

stir bars were washed with 10  $\mu$ L 0.1 M imidazole, and incubated with EDC fixation buffer (0.2 M EDC, 0.1 M imidazole, pH 8.0) for 30 min at room temperature with gentle mixing. The non-react EDC were quenched with 0.2 % glycine. For DNA nanoflower construction, the nano-stir bars were incubated with 25 nM hairpin probes, 5 nM circular template probe and 0.5 x DiB dye in 1x phi 29 buffer for 30 min. After incubation, 80  $\mu$ M dNTPs mix, 20  $\mu$ M biotinylated dATP and 2.5 U/  $\mu$ L phi29 DNA polymerase were added to initiate the growth of DNA nanoflower. Before imaging, the EV was incubated with 50 nM Alexa 633-conjugated streptavidin for DNFs labelling for 30 min. Fluorescence imaging was performed on a Zeiss 880 Inverted Confocal Microscope. The measurement was performed using an Argon laser at  $\lambda_{ex} = 355$  nm for fluorescence from DiB dye, and an HeNe laser at  $\lambda_{ex} = 633$  nm for fluorescence from the Alexa 633 dye. All the CFM images were collected at a resolution of  $512 \times 512$  pixels. The viewing area are  $100 \mu\text{m} \times 100 \mu\text{m}$ . For each sample, 10 independent images on 10 different locations were acquired respectively from a single well.

The image analysis was carried out using Image J. Each bright spot on the CFM images represents a single target EV. The particle count of EV in each image was determined by counting the number of single fluorescence particles computationally. The threshold was set as 3 times the standard deviation of the intensity of the background and size of the particles was set as 2 – 10 pixels to reduce the false positive signals generated from noises or aggregation. The fluorescent spots in 10 independent images were counted and summed up. All experiments were done in triplicate to prove their reproducibility.

**Fabrication of multi-well chip.** The multi-well chip was fabricated via pouring polydimethylsiloxane (PDMS) to the mold and curing the polymer in an oven (55 °C, overnight). The cured PDMS structure and a glass substrate were oxygen plasma treated and irreversibly bonded. The wells were washed with 1M NaOH, water, ethanol and dried by air. After that, the bottom of the well was modified with 10% (v/v) (3-Aminopropyl)triethoxysilane (APTES) in ethanol for 10 min at room temperature and washed for several times. The bottom of the well was then modified with 20 ng/ $\mu$ L MFGE8 protein or 15  $\mu$ g/mL anti-CD63 antibody in EDC coupling buffer (40  $\mu$ g/mL EDC (1-Ethyl-3-(3-dimethylaminopropyl)carbodiimide), 0.1 mM MES (4-morpholinoethanesulfonic acid), pH 4.7). The wells were blocked with 1% BSA (Bovine Serum Albumin) before sample loading.

**Exosomal miRNA quantification using reverse transcription polymerase chain reaction (RT-PCR).** The EVs were first lysed using TRIzol<sup>TM</sup> LS reagent. After EV lysis, exosomal miRNAs were extracted using miRNeasy mini kit. For RT reaction, 5  $\mu$ L of sample extract was mixed with 0.13  $\mu$ L of RNase inhibitor, 0.1  $\mu$ L of dNTP mix, 0.67  $\mu$ L of reverse transcriptase and 2  $\mu$ L of a corresponding stem-loop RT primer for each miRNA target strand and 1  $\mu$ L silicone oil in 1x RT buffer. The reverse transcription was conducted on a Bio-Rad CFX Connect Real-Time PCR Detection System. The RT reaction consisted of a 30-minute annealing step at 16 °C, a 32-minute reverse transcription step at 42 °C, and a 5-minute denaturing step at 85 °C. After RT, the samples underwent quantitative PCR (qPCR). On the qPCR plate, 1  $\mu$ L of the RT product was mixed with 1  $\mu$ L ethylene glycol, 0.1  $\mu$ L DMSO, 0.5  $\mu$ L 25 mM magnesium chloride and 5  $\mu$ L silicone oil in 1 x Taq master

mix and 1 x qPCR primer mix (specific forward and reverse PCR primers, and specific TaqMan fluorescent probe). The qPCR analysis was conducted with an initial activation step at 95 °C for 90 s followed by an initial annealing step at 59 °C for 50 s, followed by a 40-cycle PCR with 30 s denaturation at 95 °C and 70 s annealing/extension at 53 °C in each cycle.

**Atomic force microscopy (AFM) and Transmission electron microscopy (TEM).** 10  $\mu$ L sample was deposited on a freshly cleaved mica for 10 min. Before imaging, the samples were rinsed with deionized water for 3 times and then dried by N<sub>2</sub>. AFM images were recorded in air under the tapping mode using a Dimension 5000 Scanning Probe Microscope. The images were flattened by NanoScope Analysis software. TEM was carried out using a Tecnai2 TEM. The NSB were deposited on formvar-carbon-coated EM grids for imaging.

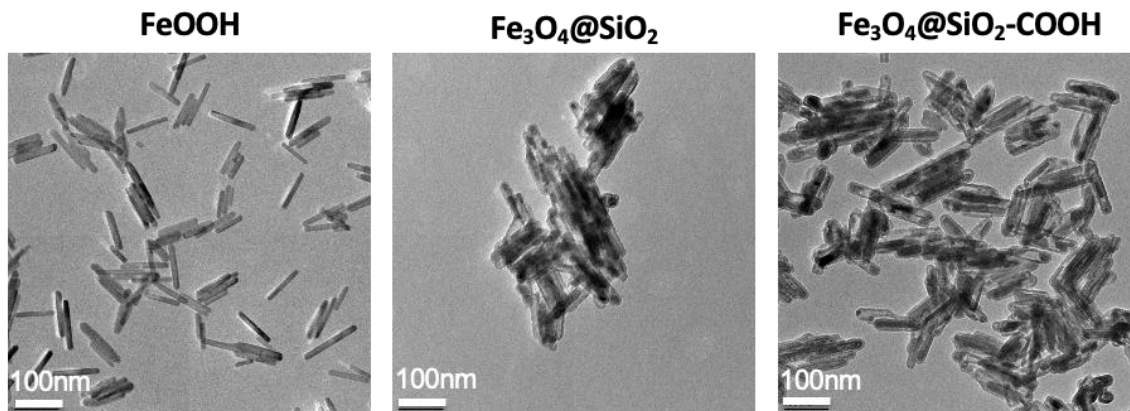
**Nanoparticle tracking analysis (NTA).** Particle concentration and size distribution of EVs and nano-stir bar were measured by NanoSight NS300 using a low volume flow cell manifold and a 405 nm laser module. A video of 30–60 s duration was taken with a rate of 25 frame/s.

**Real-time fluorescence.** The RCA reaction was monitored in 96-well PCR plated and controlled using a Bio-Rad CFX Connect Real-Time PCR Detection System. The reaction mixture was incubated at 37 °C and fluorescence curves were recorded at 30 s intervals.

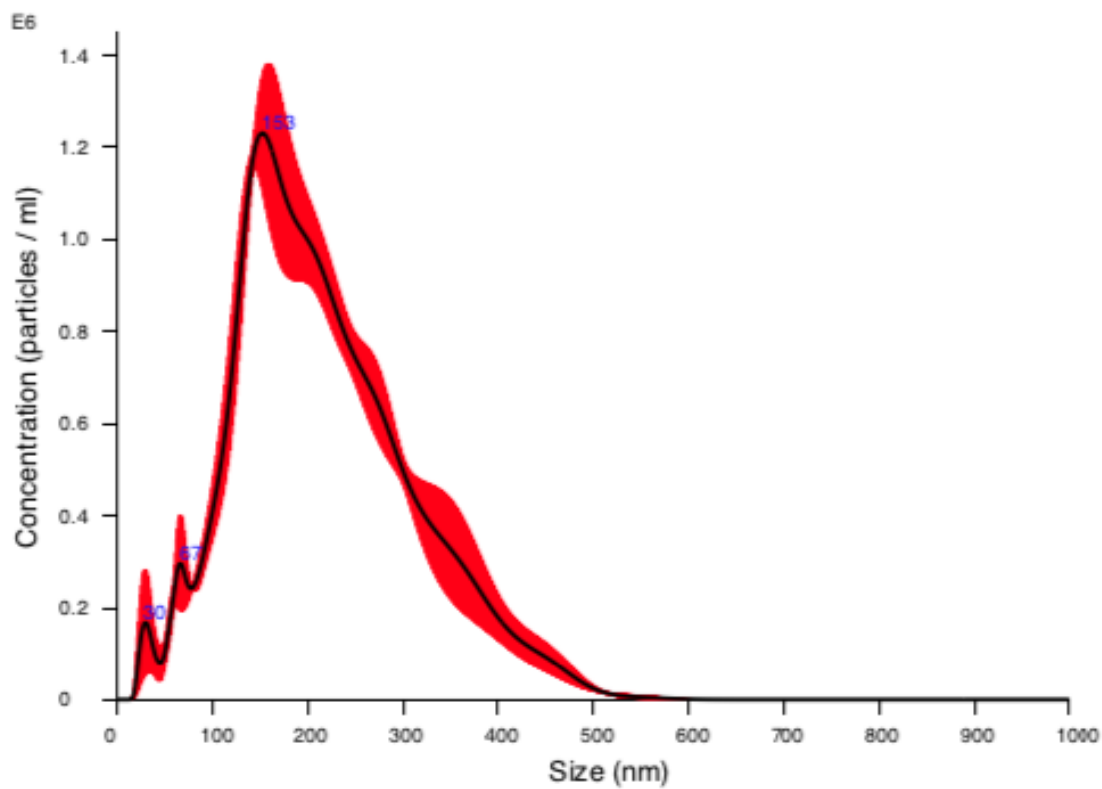
### 4.3. Results and Discussion

Our method contains two main enabling components (Scheme 4.1): nano-stir bar (NSB) for EV isolation and DNA nanoflower (DNF) for signal amplification. Exosomal miRNA detection in biological samples suffers from low efficiency and high background from the auto-fluorescence of the matrix molecules, which requires EV pre-concentration.<sup>25</sup> Current EV isolation methods, however, are often time-consuming with low recovery.<sup>26, 27, 28, 29, 30</sup> Therefore, we first isolate the EVs from biological fluids using the antibody-functionalized NSB. The NSB is about 150 nm in length and 50 nm in diameter, each of which can capture up to one EV to facilitate single EV analysis. In addition, single EV per NSB allows EV fixing without significant diffusion of the released contents, which cannot be done if not limiting EV on a confined area. With the presence of the antibody, NSB can capture the EVs carried target antigen with high specificity. The NSB can also stir under the magnetic field to speed up EV capture and removal of impurities adsorbed non-specifically on the NSB surface. Moreover, the NSB can be pulled down within 5 min using external magnet to isolate EVs from biological fluids, enabling easy handling and simple buffer exchange. Upon single EV capture, the EVs are treated with 10% PFA and EDC to expose the cytosolic contents and crosslink them to the NSB. Then, the target miRNA would trigger RCA to construct a DNF *in situ*, which is subsequently labeled with multiple dyes to amplify the detection signal and enable detection of miRNA content in individual EVs. The whole procedure only takes 3 hrs, much shorter than the previous protein detection method that lasts for at least 6 hrs.

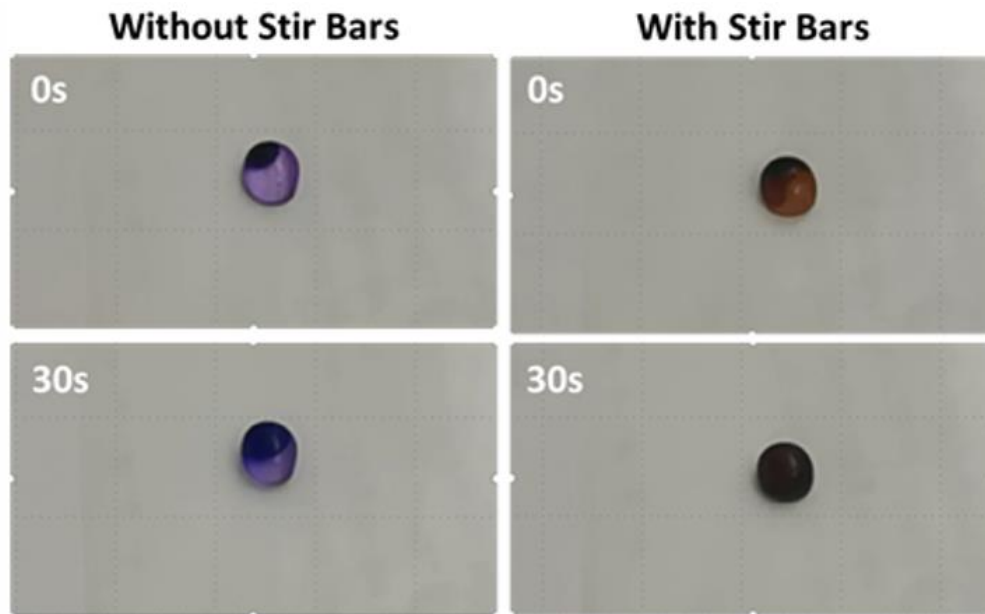
For the nano stir bar preparation, we first synthesized the iron oxyhydroxide (FeOOH) nanorods with highly uniform sizes, then coated them with silica, followed by reducing them into magnetic metallic iron ( $\text{Fe}_3\text{O}_4$  NSB@ $\text{SiO}_2$ ). For antibody functionalization, we modified silica with carboxyl groups, which can easily conjugate with antibody using carbodiimide crosslinking. The nanorods exhibit excellent superparamagnetic properties, which allow them to remain well dispersed in solution in the absence of external magnetic field, while becoming magnetic responsive when an external field is applied. Figure 4.1 shows the TEM image of the FeOOH nanorods, magnetic  $\text{Fe}_3\text{O}_4$  NSB@ $\text{SiO}_2$  and  $\text{Fe}_3\text{O}_4$  NSB@ $\text{SiO}_2$ -COOH. A uniform ellipsoidal morphology with an iron oxide core and silica shell structure was observed. The size of the magnetic  $\text{Fe}_3\text{O}_4$  NSB@ $\text{SiO}_2$ -COOH was  $150 \pm 6.8$  nm (Figure 4.2). This allowed that at most one EV was captured per NSB due to space hindrance, which minimized aggregation. These nanorods can be pulled down within 10 seconds under magnetic field. In addition, they can spin in solution under a low-gradient rotating magnetic field generated by a stirrer plate, acting like nanosized stir bars. Such NSBs can speed up solution mixing in a 10- $\mu\text{L}$  droplet (Figure 4.3). The mild spinning action can greatly aid molecule transfer to the surface while promoting target binding. After modification of biotinylated IgG, the stirring NSB captured >40% fluorescein-labeled streptavidin from a 30- $\mu\text{L}$  solution compared to no stirring, and even outperformed vortex (Figure 4.4).



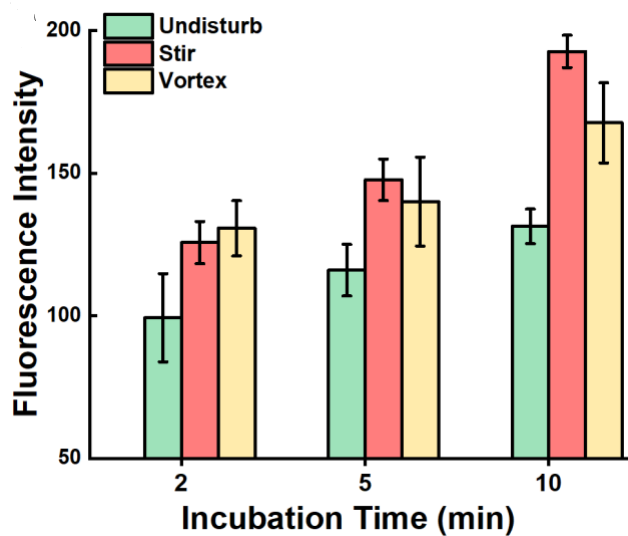
**Figure 4.1** TEM images of the FeOOH nanorods, magnetic Fe<sub>3</sub>O<sub>4</sub> NSB@SiO<sub>2</sub> and Fe<sub>3</sub>O<sub>4</sub> NSB@SiO<sub>2</sub>-COOH.



**Figure 4.2** Size distribution of Fe<sub>3</sub>O<sub>4</sub> NSB@SiO<sub>2</sub>-COOH.



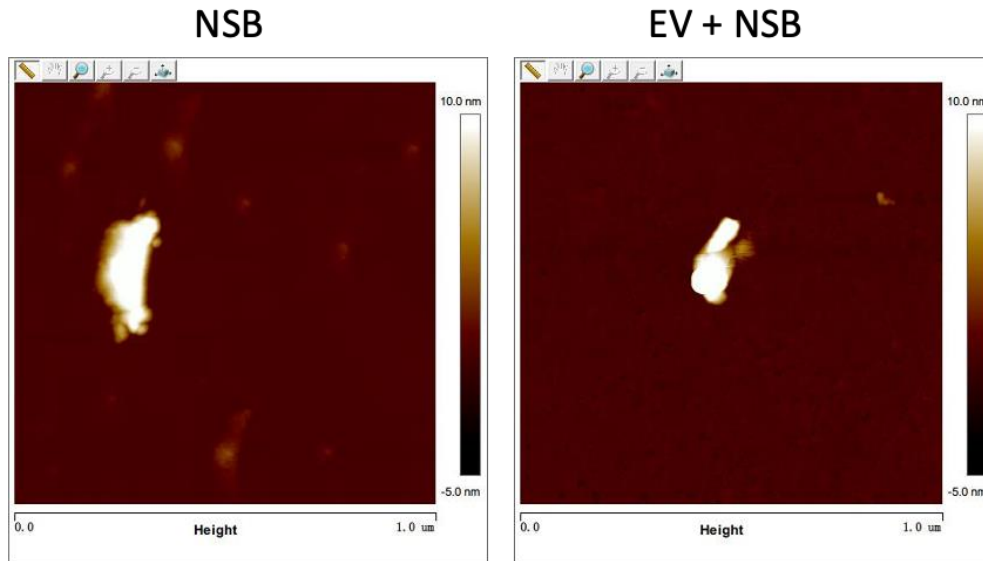
**Figure 4.3** Dye diffusion in a 10- $\mu$ L droplet with or without NSB spinning.



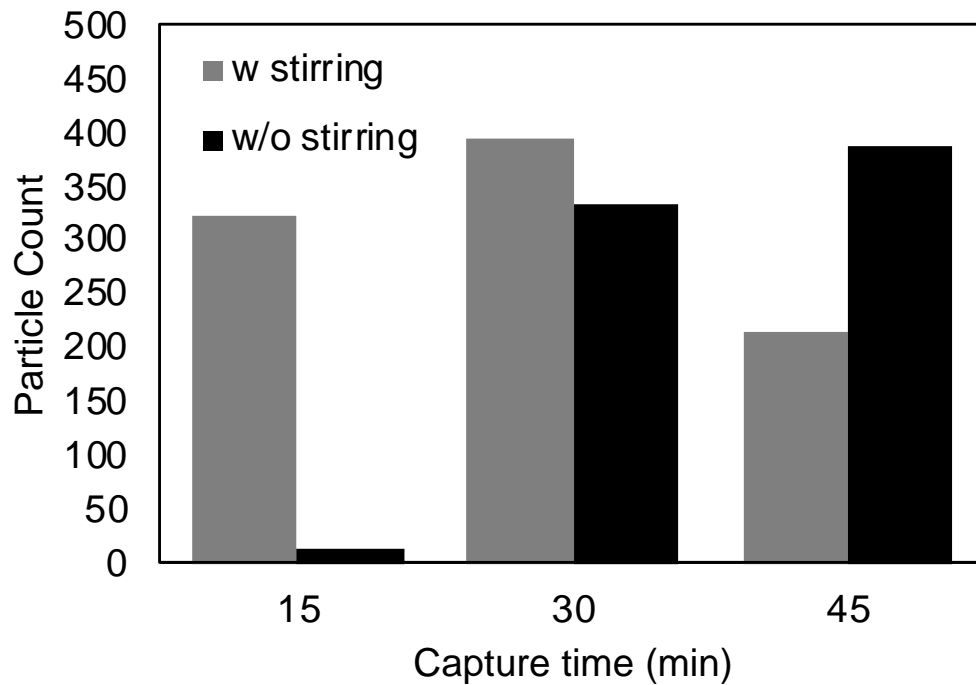
**Figure 4.4** Fluorescence intensity of the fluorescein-labeled streptavidin captured by the biotinylated IgG conjugated to the NSB under different solution agitation conditions. All error bars represent the standard deviations from three repeated measurements.



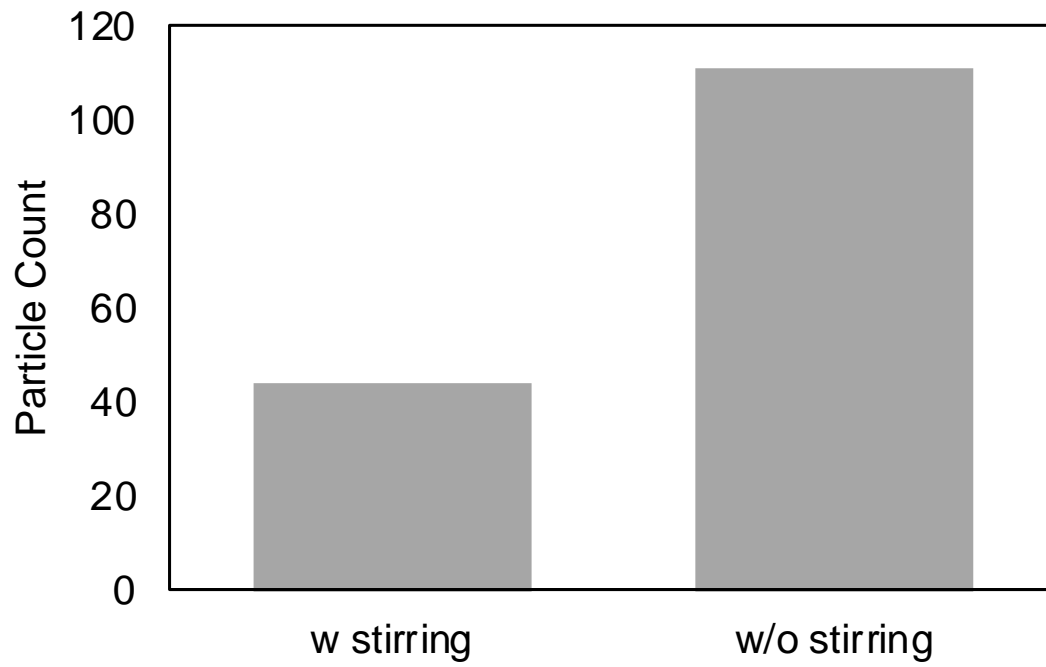
We then characterized the capture performance of the NSB for EV isolation. After antibody functionalization, the immuno-NSB was mixed with EV at room temperature for 30 min. The AFM images confirmed each NSB only can capture at most one EV (Figure 4.5). To prove that NSB can speed up reaction and avoid EV aggregation, we performed rolling circle amplification (RCA) to construct DNA nanoflowers (DNFs) that can specifically bind to the membrane proteins on EV surface under stirring and without stirring, respectively. The detectable particle count of the reaction under stirring after 15 mins was comparable with that without stirring after 30 mins (Figure 4.6). The detectable particle count of the reaction under stirring reached plateau after 30mins, while it took 45 mins for the reaction without stirring. These results suggested the stirring function of NSB can speed up reaction. Moreover, stirring during washing step can efficiently remove non-specific adsorption of CD63-specific DNF to CD63-blocked EV (Figure 4.7). We also measured the pixel size of each fluorescence dot in the DNF channel of each fluorescence microscopy image. The pixel size of the samples with NSB are smaller than that without NSB, demonstrating that NSB can avoid EV aggregation (Figure 4.8).



**Figure 4.5 AFM images of nano stir bar before and after EV capture.**



**Figure 4.6 Detectable particle count of EV labeled with CD63-specific DNF under stirring and without stirring, respectively.**



**Figure 4.7 Detectable particle count of CD63 blocked-EV labeled with CD63-specific DNF under stirring or without stirring.**

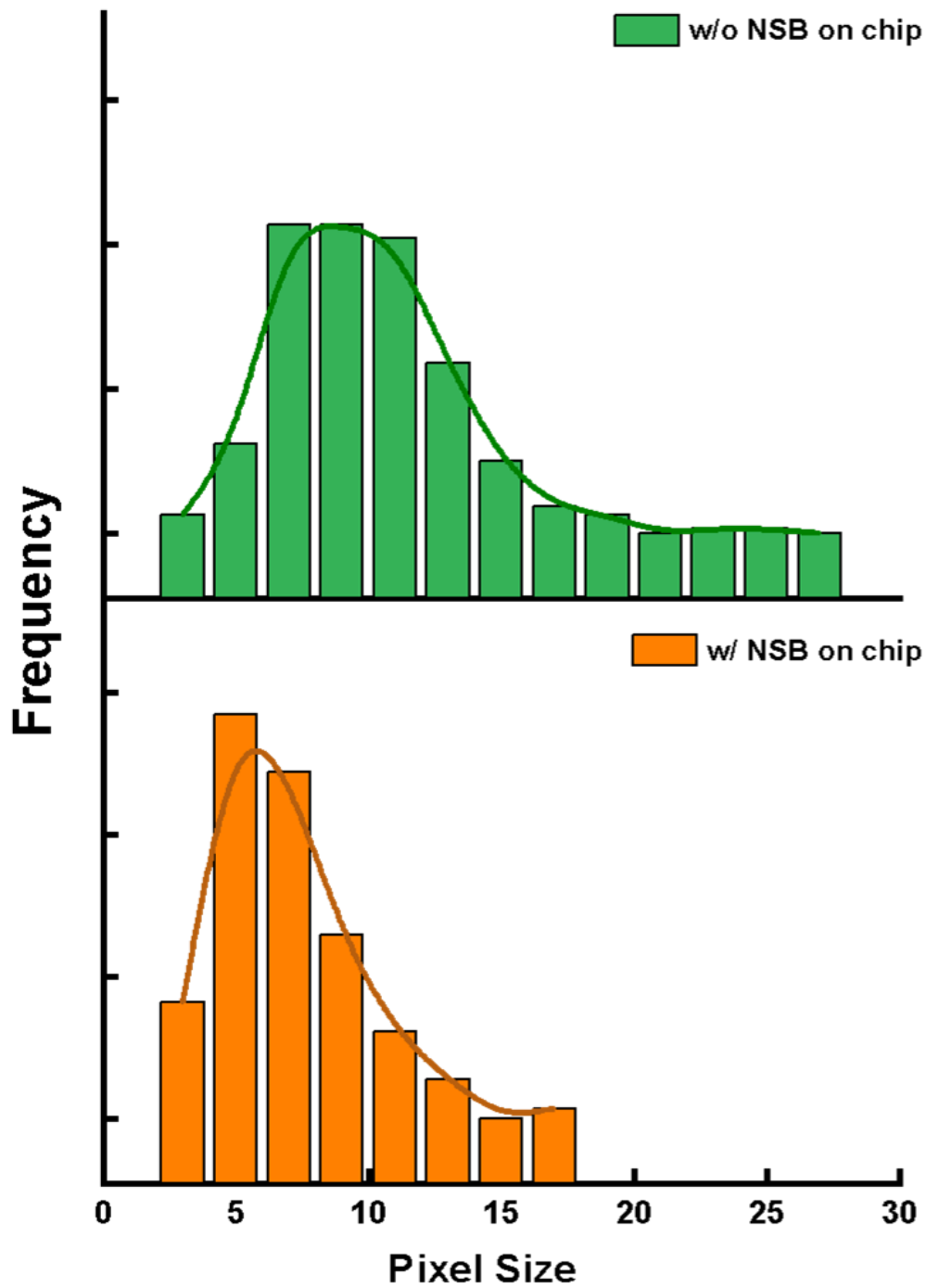
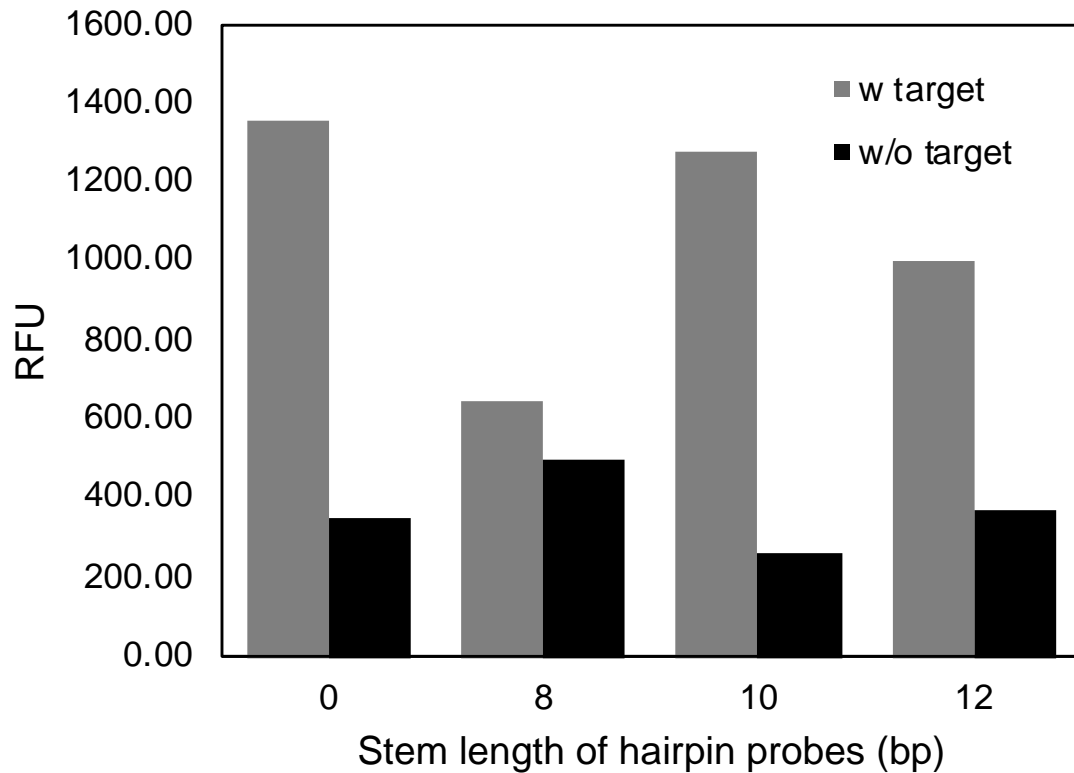


Figure 4.8 Pixel size of fluorescence microscopy images with and without NSB for protein detection.

After EV isolation via antibody functionalized NSB, miRNAs inside each captured EV were visualized *in situ*. Since the expression level of miRNAs are too low to detect, we amplified the signal before imaging. RCA, an DNA isothermal amplification method, can produce a long single-strand DNA with repeated regions, which can be labeled with multiple dye for signal amplification.<sup>31, 32</sup> With judicious design of the template sequence, the single-strand RCA product can self-assemble into a compact flower-like structure.<sup>33</sup> Therefore, we used RCA to construct a DNA nanostructure inside EV for exosomal miRNA *in situ* detection. To eliminate non-specific reaction, a hairpin probe was designed. Without the target miRNA, the hairpin probe presented in the system stably, yielding no amplification. When introducing the target miRNA, the hairpin would bind to the target miRNA and switch its structure to expose the initiator sequence for RNA amplification.<sup>34</sup> The stem length of the hairpin probes is crucial to the specificity of the reaction, since the short stem length causes high background noise and long stem length results in a weak fluorescence signal. Therefore, the stem length of the hairpin probes needs to be optimized. We chose miR-155 as our target model and designed 4 hairpin probes with various stem lengths: 0, 8, 10 and 12 base pairs (bp, Table 4.1). The hairpin with 8 bp-stem showed significant background noise and that with 12 bp-stem had a weaker fluorescence signal than the linear DNA probe (Figure 4.9). Hairpin probe with 10-bp stem showed the highest signal-to-noise ratio, so we selected it in our system. To investigate the specificity of our hairpin designs targeting miR-155, we conducted a series of control experiments using single-base-mismatched miR-155 and two-base-mismatched miR-155 as negative controls, which did not show any enhancement (Figure 4.10). Similarly, reaction with non-target

miRNA, such as miR122, miR21, let-7a, showed no fluorescence enhance, suggesting our hairpin designs can detect miRNA with single-base mismatch discrimination.

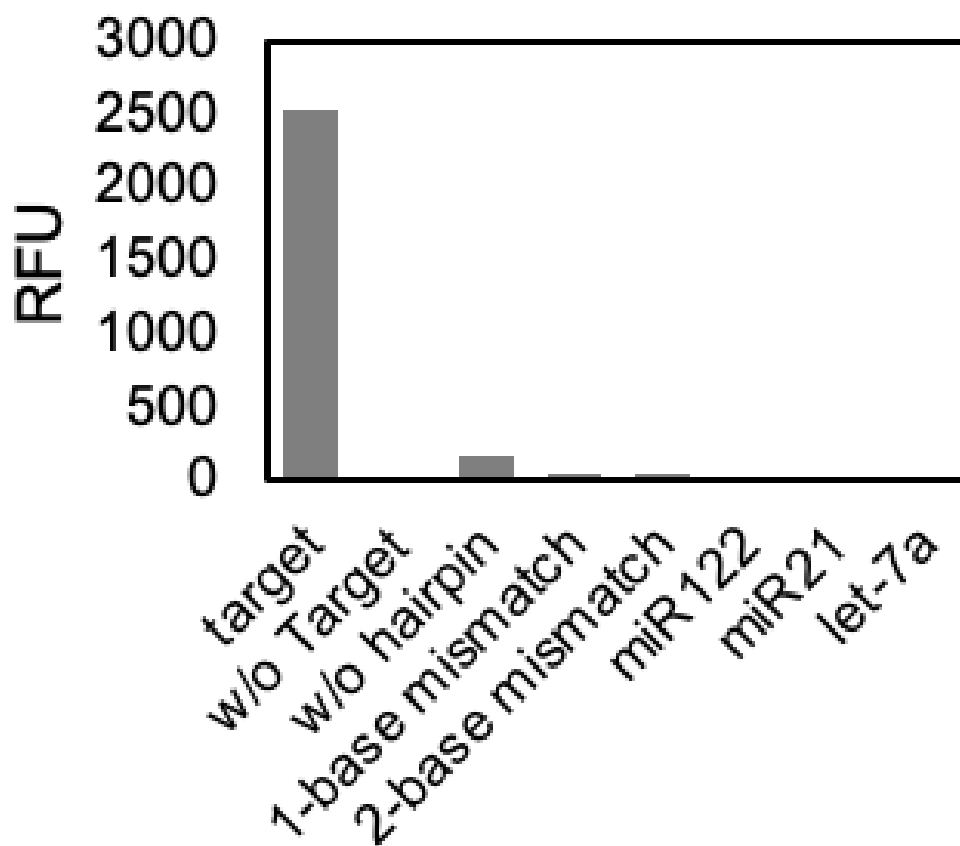


**Figure 4.9** Fluorescence intensity for RCA reaction by incubating hairpin probes of various stem length with target or without target.

**Table 4.1 DNA sequences used in our system for miR-155 and miR-122.**

Name	Sequences (5'-3')
Ligation probe	CGT TGT CGT TAG TCT AGG ATT CGG CGT GTT AGC A
Template probe	Phosphate-GAC TAA CGA CAA <u>CGC</u> GTG TTA GCA <u>AGC</u> GAT <u>ACG</u> CGT ATC GCT ATG GCA TAT CGT ACG ATA TGC <u>CTG</u> CTA <u>ACA</u> <u>CGC</u> <u>CGA</u> ATC CTA
miR-155	UU AAU GCU AAU CGU GAU AGG GGU
Linear primer for miR-155	<u>ACC CCT ATC ACG ATT AGC ATT AAG</u> TCT CCC <u>AGT CTA GGA TTC GGC GTG TTA GCA</u>
Hairpin 1 for miR-155 (HP-155-1)	<u>ACC CCT ATC ACG ATT AGC ATT AAG</u> TCT CCC <u>AGT CTA GGA TTC GGC GTG TTA GCA</u> <u>TTA ATG CT</u>
Hairpin 2 for miR-155 (HP-155-2)	<u>ACC CCT ATC ACG ATT AGC ATT AAG</u> TCT CCC <u>AGT CTA GGA TTC GGC GTG TTA GCA</u> <u>TTA ATG CTA A</u>
Hairpin 3 for miR-155 (HP-155-3)	<u>ACC CCT ATC ACG ATT AGC ATT AAG</u> TCT CCC <u>AGT CTA GGA TTC GGC GTG TTA GCA</u> <u>TTA ATG CTA ATC</u>
One-base mismatch for miR-155	TTA ATG CTA ATC GTG ATA <span style="background-color: #c8e6c9;">■</span> GG GT
Two-base mismatch for miR-155	TTA ATG CTA ATC <span style="background-color: #c8e6c9;">■</span> TG ATA <span style="background-color: #c8e6c9;">■</span> GG GT
miR-122	UGG AGU GUG ACA AUG GUG UUU G
Hairpin for miR-122 (HP-122)	<u>CAA ACA CCA TTG TCA CAC TCC A</u> GT GTG TGA <u>GTC TAG GAT TCG GCG TGT TAG CAT</u> <u>GGA GTG T</u>
One-base mismatch for miR-122	TGG AGT GTG ACA ATG GT <span style="background-color: #c8e6c9;">■</span> TTT G
Two-base mismatch for miR-122	TGG A <span style="background-color: #c8e6c9;">■</span> T GTG ACA ATG GT <span style="background-color: #c8e6c9;">■</span> TTT G

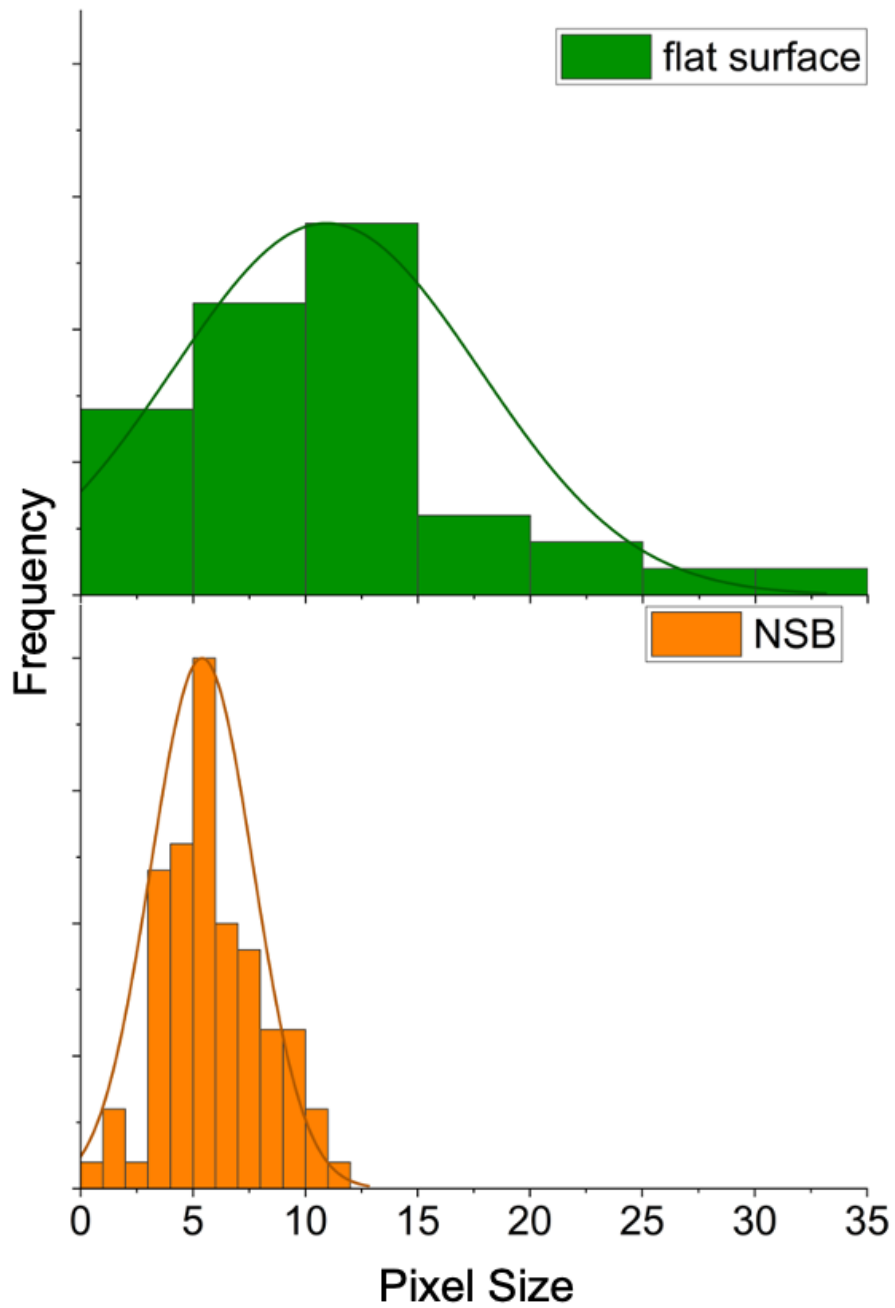
Underline sequences indicate complementary regions of the probes to form hairpin structure. Each hairpin includes a target miRNA recognition domain (red), and a trigger domain (blue) for growth of a long dsDNA via DNA hybridization cascade, connected by a hinge domain (grey). The mismatch bases are highlighted with green.



**Figure 4.10 Specificity of RCA reaction targeting miR-155 using different target probes.**

We next constructed DNFs that can specifically bind to the target miRNA inside EV after EV fixation and EDC crosslinking on NSB and flat surface, respectively. We measured the pixel size of each fluorescence dot in the DNF channel. The pixel size of the samples in NSB were smaller than that in flat surface, demonstrating the necessity of confining the EV first to a small area carrying functional groups before fixing and exposing its contents (Figure 4.11).





**Figure 4.11 Pixel size of fluorescence microscopy images with flat surface or with NSB for exosomal miRNA detection.**

After confirming EV isolation using NSB and signal amplification by DNA nanoflowers, we would like to apply our assay for exosomal miRNA *in situ* detection. We found that PFA fixation and EDC crosslinking were indispensable for miRNA *in situ* detection. There is less detectable particle for samples without PFA fixation or EDC crosslinking (Figure 4.12). The incubation time and concentration of EDC buffer were optimized by counting the number of detectable particles under fluorescence microscopy. As the incubation time increased, the number of detectable particles also increased (Figure 4.13 and 4.14). To shorten the total assay time, we used 30 min in the following experiment. For the EDC concentration optimization, the particle count increased when EDC concentration increased from 0.05 M to 0.1 M then decreased from 0.1 M to 0.2 M (Figure 4.15 and 4.16). 0.1 M was selected as the EDC crosslinking concentration. To track the EV, we stained EV using membrane dye, DiB. We incubated the DiB dye with EV in different time point: during EV capture, EDC crosslinking, target recognition, RCA amplification and DNF labeling. EV stained with DiB during target recognition yielded higher detectable particle count (Figure 4.17-19). Therefore, we stained EV with DiB during target recognition. We also optimized the concentration of DiB dye. Samples stained with 0.5× DiB had higher particle ratio and less pixel size than those stained with 1× DiB. Therefore, 0.5× DiB was the optimal condition (Figure 4.20-23).

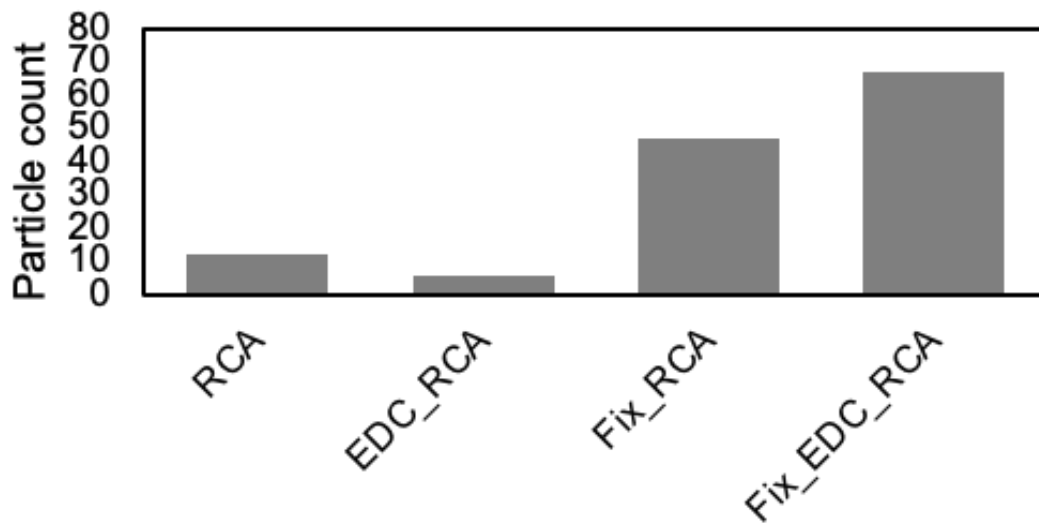


Figure 4.12 Effect of PFA fixation and EDC crosslinking for miRNA *in situ* detection.

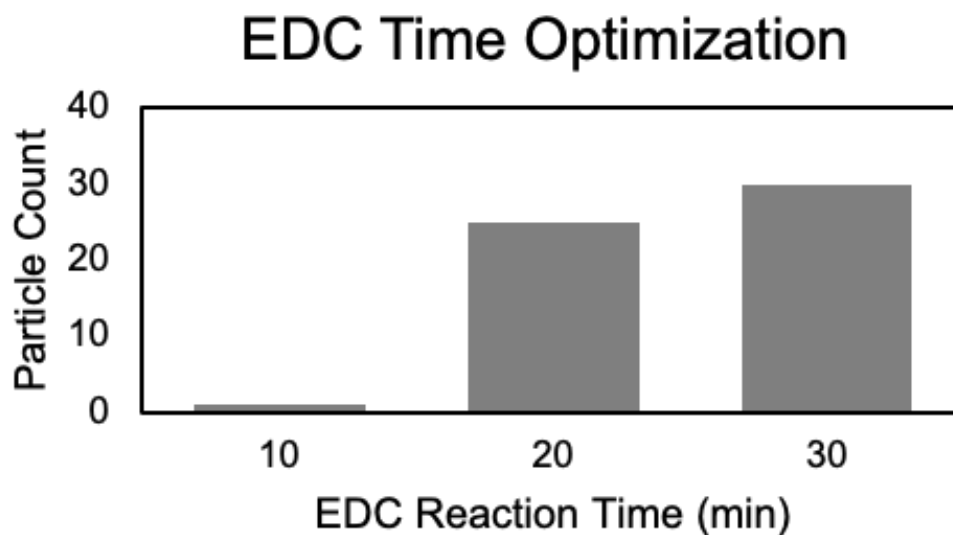


Figure 4.13 Optimization of EDC crosslinking time for miRNA *in situ* detection.

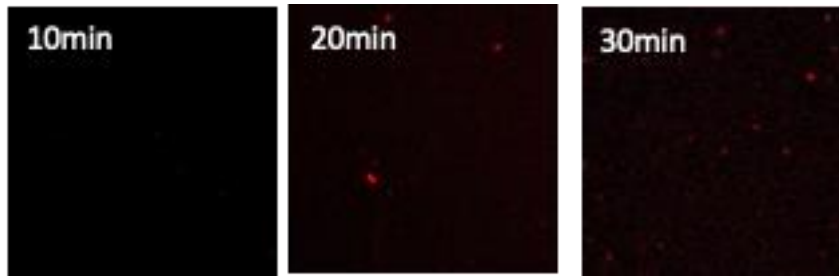


Figure 4.14 Representative fluorescence microscopy images for EDC crosslinking time optimization.

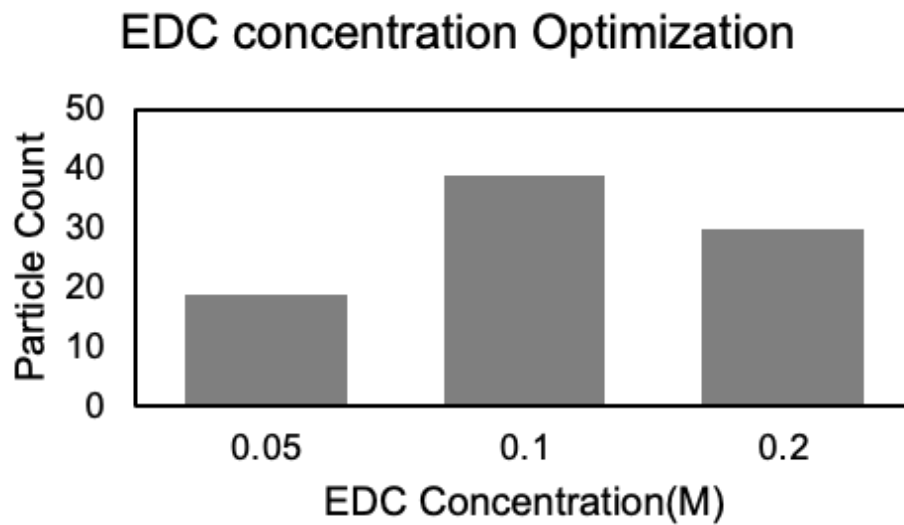


Figure 4.15 Optimization of EDC crosslinking concentration for miRNA *in situ* detection.

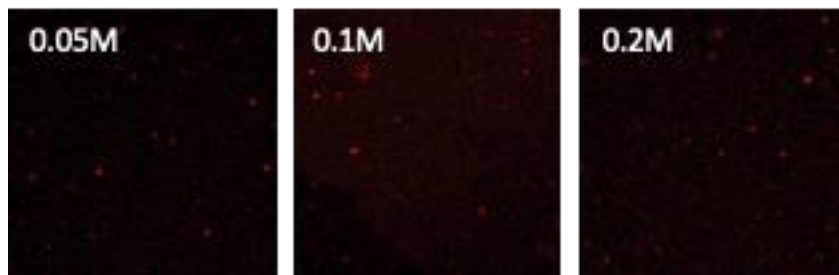
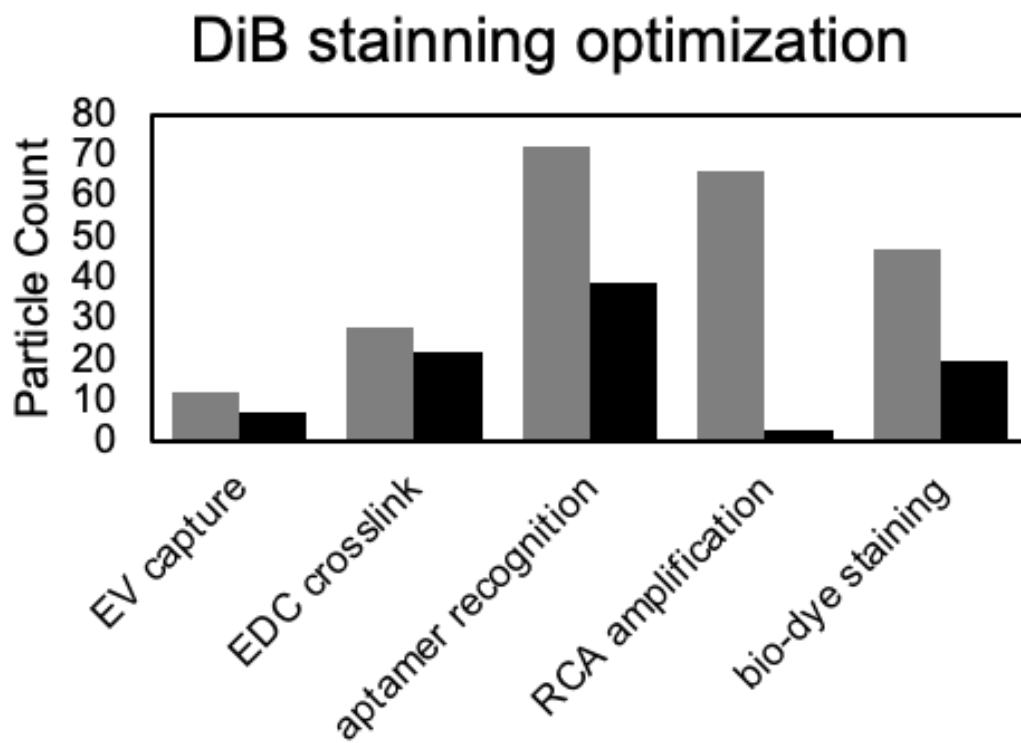


Figure 4.16 Representative fluorescence microscopy images for EDC crosslinking concentration optimization.



**Figure 4.17** Detectable particle count for EV staining by membrane dye DiB in different time points.

## DiB staining Optimization

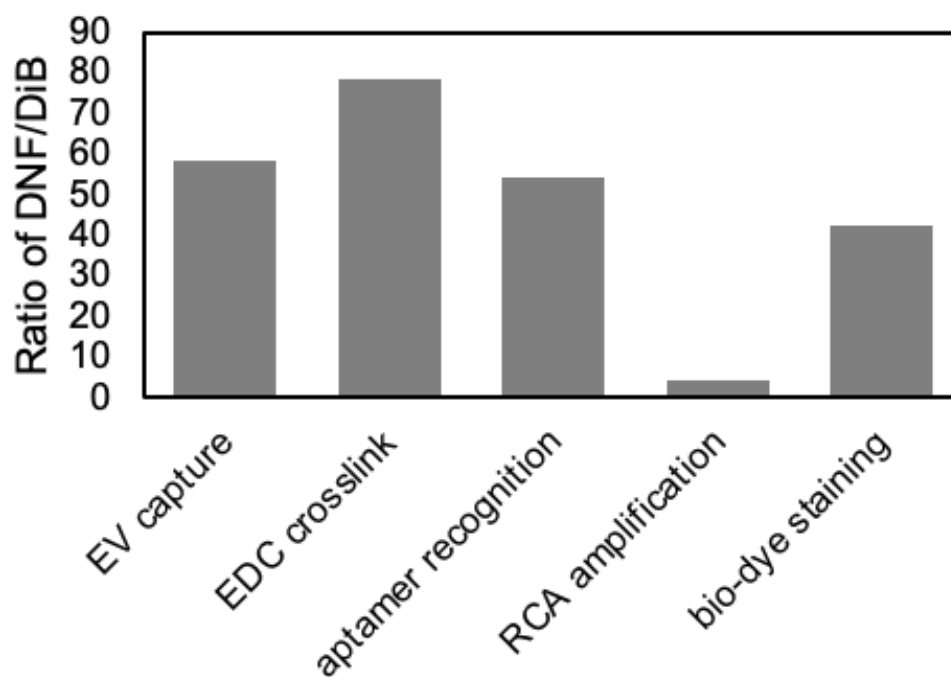


Figure 4.18 Particle ratio for EV staining by membrane dye DiB in different time points.

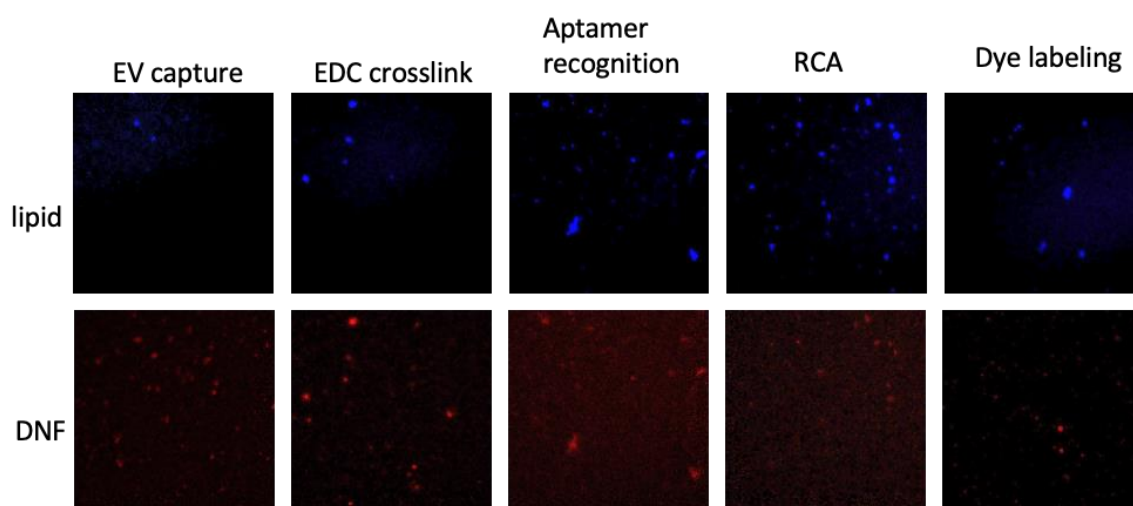
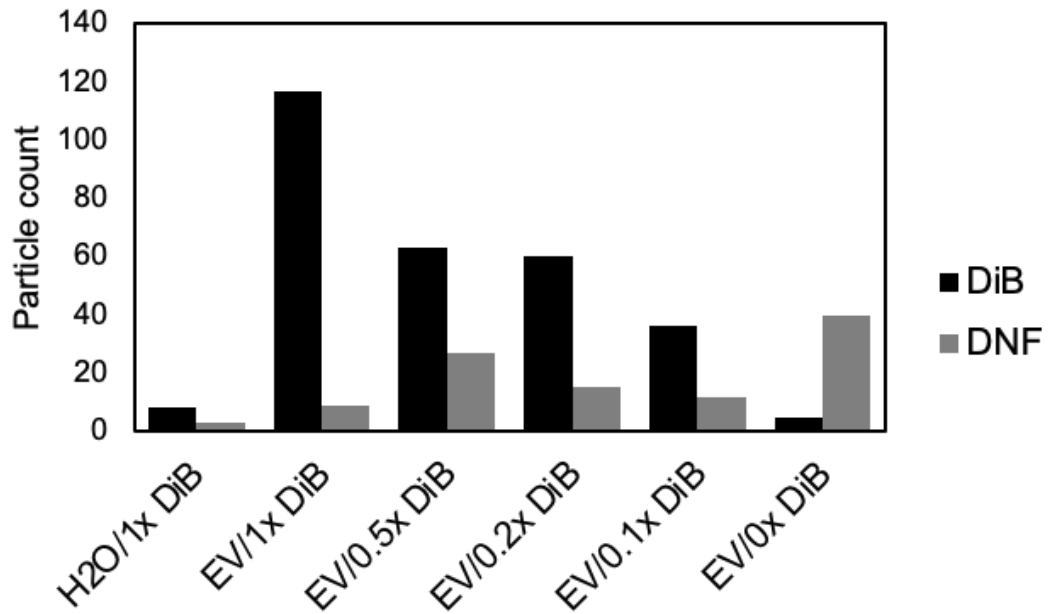
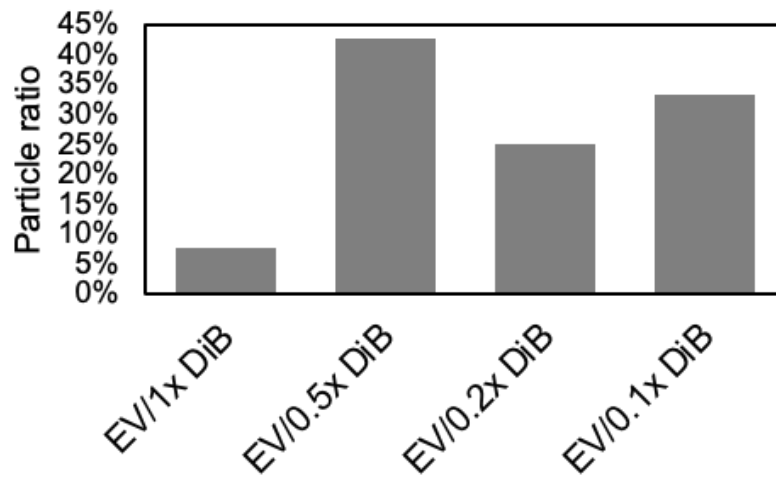


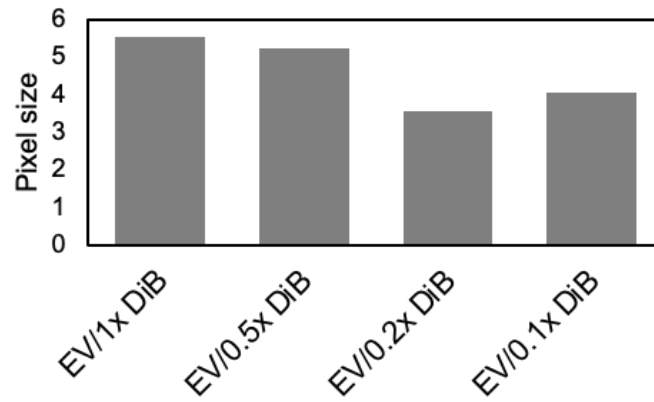
Figure 4.19 Representative fluorescence microscopy imaging of EV staining by membrane dye, DiB in different time points.



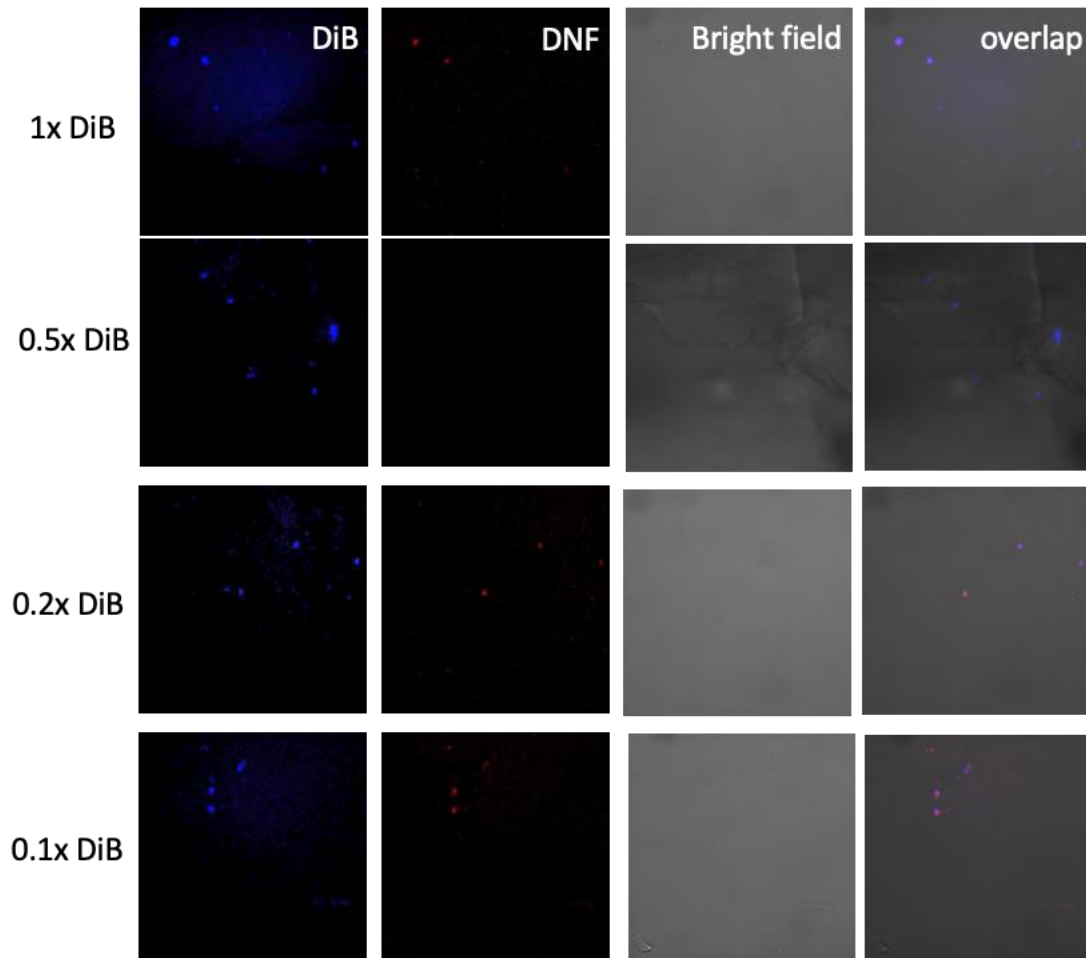
**Figure 4.20** Detectable particle count for DiB concentration Optimization for miRNA *in situ* detection.



**Figure 4.21** Particle ratio for DiB concentration optimization for miRNA *in situ* detection.



**Figure 4.22 Pixel size of detectable particles under various DiB concentration.**

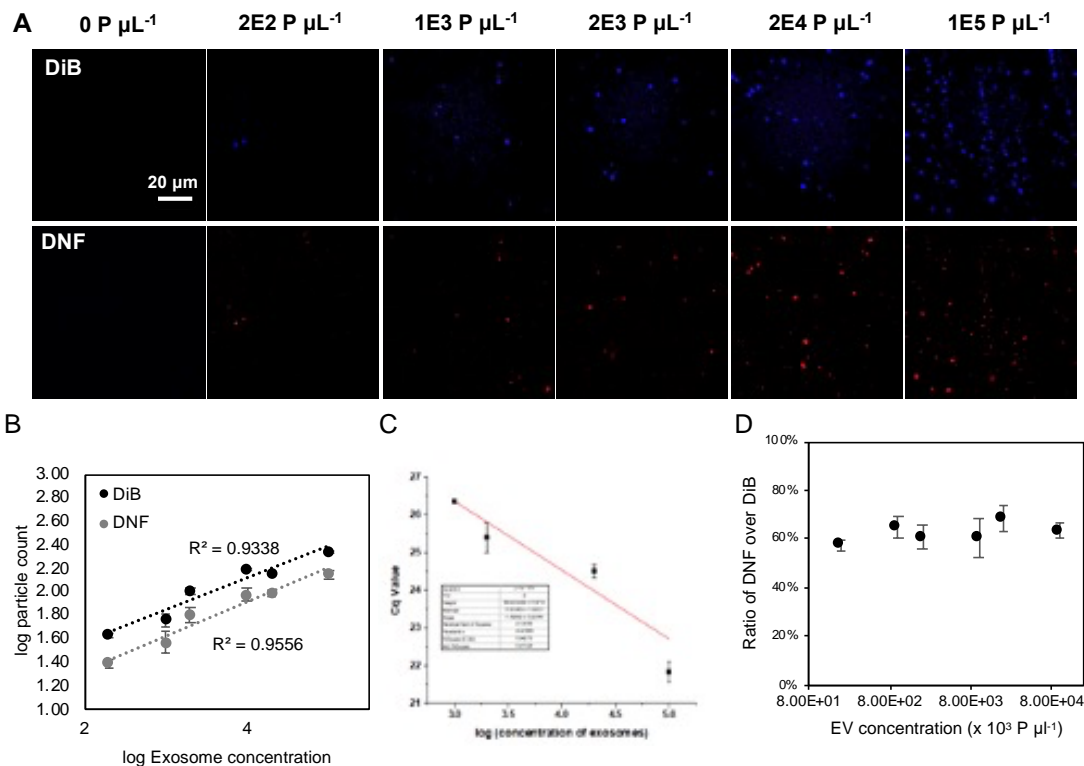


**Figure 4.23 Representative fluorescence microscopy imaging of EV staining by various DiB concentration.**

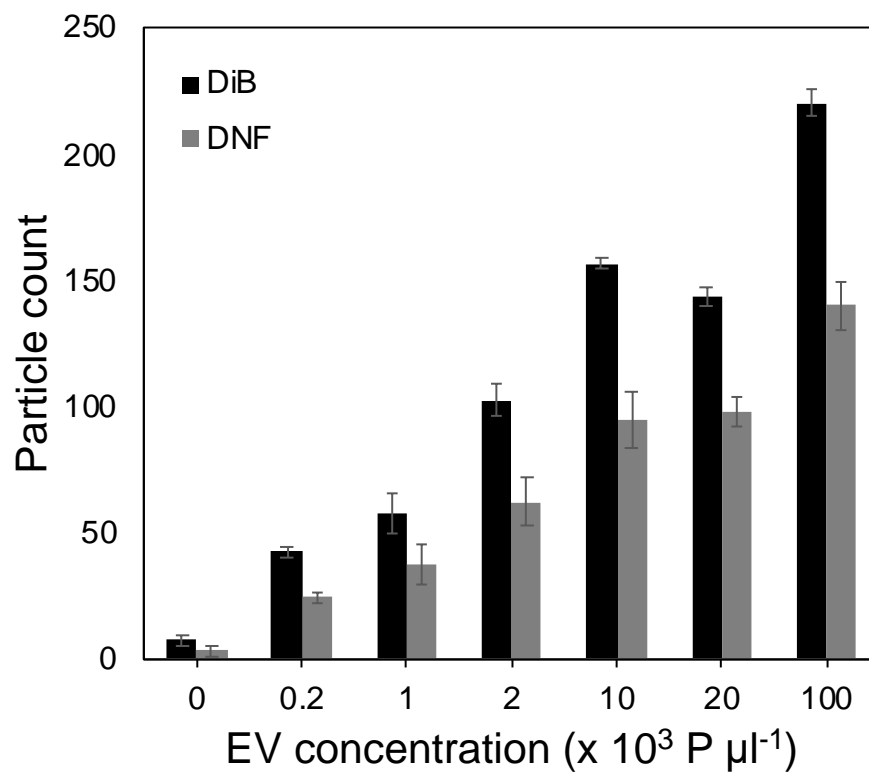


After reaction condition optimization, we used hairpin targeting miRNA-155 and miRNA-122 to test EV samples with various concentration using our assay. The particle counts acquired in the red channel was proportional to the EV concentration in the range of  $200 - 10^5$  particle/ $\mu\text{l}$  with high linear regression coefficient (Figure 4.24-4.27,  $R^2 = 0.9556$  for miR-155 and  $R^2 = 0.9364$  for miR-122). Using the  $3\sigma$  method, the limit of detection (LOD) for DNF labeling were 447 particle/ $\mu\text{l}$  for miR-155 and 6743 particle/ $\mu\text{l}$  for miR-122, 1000 times lower than that obtained by molecular beacons encapsulated cationic lipoplexes. What's more, the hairpin designs for miR-122 also showed single-base mismatch discrimination capability (Figure 4.26D). These results confirmed that we can “digitally” count the number of fluorescence particles for exosomal miRNA quantification with high sensitivity and high specificity.

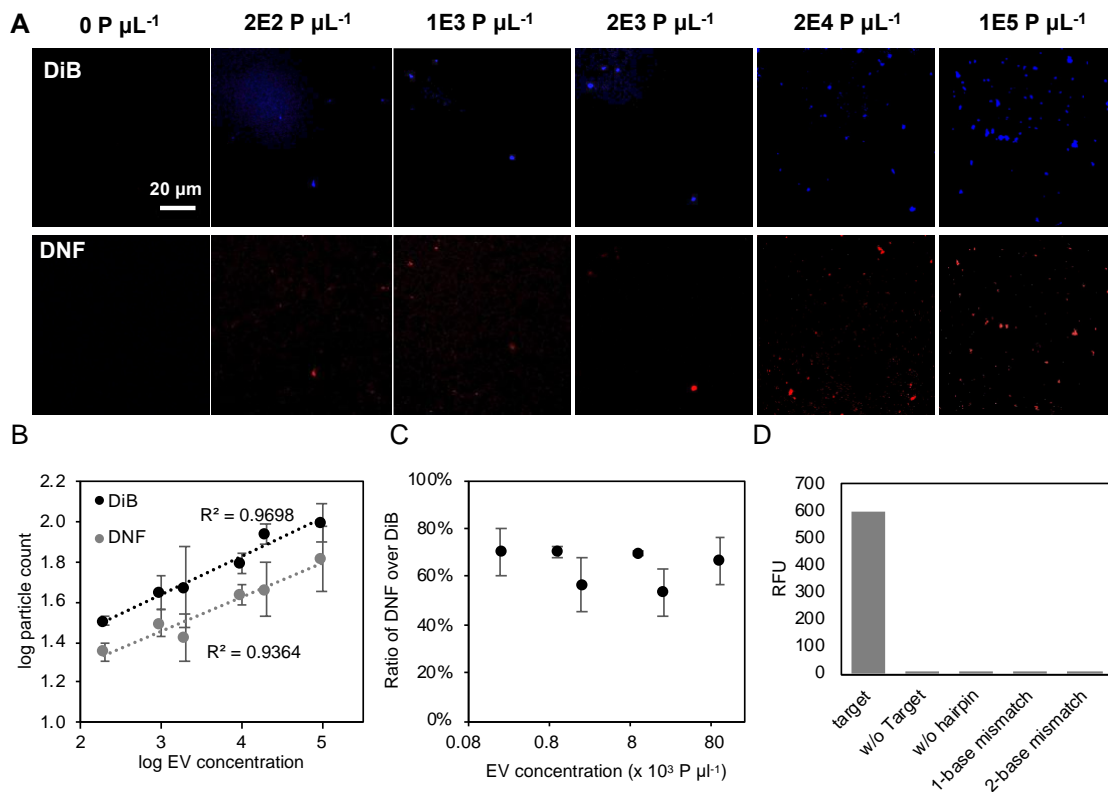
To avoid the variation in EV capture, we stained the EVs with the lipophilic fluorescent dye DiB. And the total EVs captured on the NSB can be directly counted. The DiB-stained EV shows a high linear regression coefficient ( $R^2 = 0.9338$  for miR-155 and 0.9698 for miR-122, Figure 4.24-4.27). The number of DiB-stained EV obtained in the blue channel of the CFM ( $P_{\text{DiB}}$ ) is supposed to be proportional to all the EVs captured on the NSB. Using  $P_{\text{DiB}}$  as the internal standard to normalize  $P_{\text{DNF}}$ , we can correct variations in EV input and capture efficiency. The ratio of  $P_{\text{DNF}}/P_{\text{DiB}}$  for miR-155 remained constant and  $\sim 60\%$  with different EV concentrations, revealing that  $\sim 60\%$  of this EV population carries miR-155 (Figure 4.24).



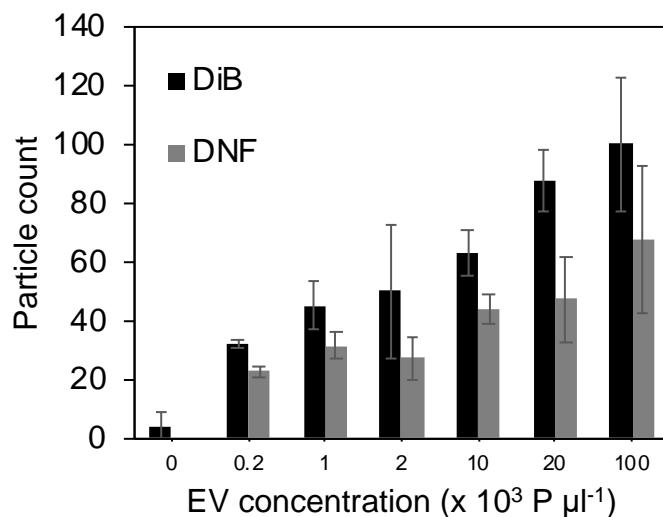
**Figure 4.24 Sensitivity test of our assay for miR-155 *in situ* detection.** A) Representative CFM images of EV labeled with DiB and miR-155-specific DNFs in EV-spiked solution with various EV concentration. All images share the same scale bar. B) Correlation of detectable EVs particle count using DiB (black) and miR-155-specific DNFs (grey) with EVs concentration in EV-spiked EV particle count for EV-spiked samples labeled with DiB or DNFs. C) Correlation of Cq values and log EV concentration obtained from RT-PCR. D) Ratio of  $P_{\text{DNFs}}/P_{\text{DiB}}$  measured across different EV input concentration. All error bars represent the standard deviations from two repeated measurements.



**Figure 4.25** The particle counts obtained from counting the DiB-stained or the miR-155 specific DNF-tagged EVs at different EV concentrations. All error bars represent the standard deviations from two repeated measurements.



**Figure 4.26 Sensitivity and specificity test of our assay for miR-122 *in situ* detection.** A) Representative CFM images of EV labeled with DiB and miR-122-specific DNFs in EV-spiked solution with various EV concentration. All images share the same scale bar. B) Correlation of detectable EVs particle count using DiB (black) and miR-122-specific DNFs (grey) with EVs concentration in EV-spiked EV particle count for EV-spiked samples labeled with DiB or DNFs. C) Ratio of  $P_{\text{DNFs}}/P_{\text{DiB}}$  measured across different EV input concentration. D) Specificity of RCA reaction using different target probes. All error bars represent the standard deviations from two repeated measurements.



**Figure 4.27** The particle counts obtained from counting the DiB-stained or the miR-122 specific DNF-tagged EVs at different EV concentrations. All error bars represent the standard deviations from two repeated measurements.

miRNA expression level could be an indicator for cancer diagnosis. Here, we chose EV derived from COLO1 cell line as our sample, and profile the miRNA expression level. Eight miRNAs were selected as our target models (Table 4.2). Based on the sequence of target miRNA, the hairpin probes were designed to trigger RNA after target binding (Table 4.3). Figure 4.28 showed the miRNA profiling of EVs derived from COLO1 cell line obtained from RT-PCR, which shows it has highest expression level of miR-155 and lowest expression level of miR-16. Based on the RT-PCR result, the concentration of miR-155 is about 3 copies per EV and that of miR-122 is about 0.0017 copies per EV. RT-PCR only provides the average miRNA concentration in the samples, which fails to reveal the relationship between miRNA distribution and its biological function. Our design takes advantage of a long ssDNA grown *in situ* inside each EV, so we can apply our assay to profile various miRNA by simply switching the recognition domain. We tested various

miRNA by labeling EV with DiB for total EV counting and DNF for target miRNA counting. The total EV particle counts are similar, while the number of EV carried various miRNA are different (Figure 4.29A and 4.29B). miR-155 has the highest particle ratio and miR16 is the lowest one. The result obtained from our assay are consistent with the RT-PCR result. A positive correlation ( $R^2 = 0.7569$ , Figure 4.29C) was detected between the  $P_{DNF}/P_{DiB}$  ratio and the miRNA concentration obtained by RT-PCR, further confirming that the ratio of  $P_{DNF}/P_{DiB}$  is proportional to the expression level of the target miRNA in EVs. What's more, our results reveal the distribution pattern of miRNA is high occupancy and high miRNA concentration for miR-155, while high occupancy and low miRNA concentration for miR122. The investigation of miRNA distribution pattern allows us to better understand the role of miRNA physiological and pathological process, and thereby improve the accuracy of cancer diagnosis.

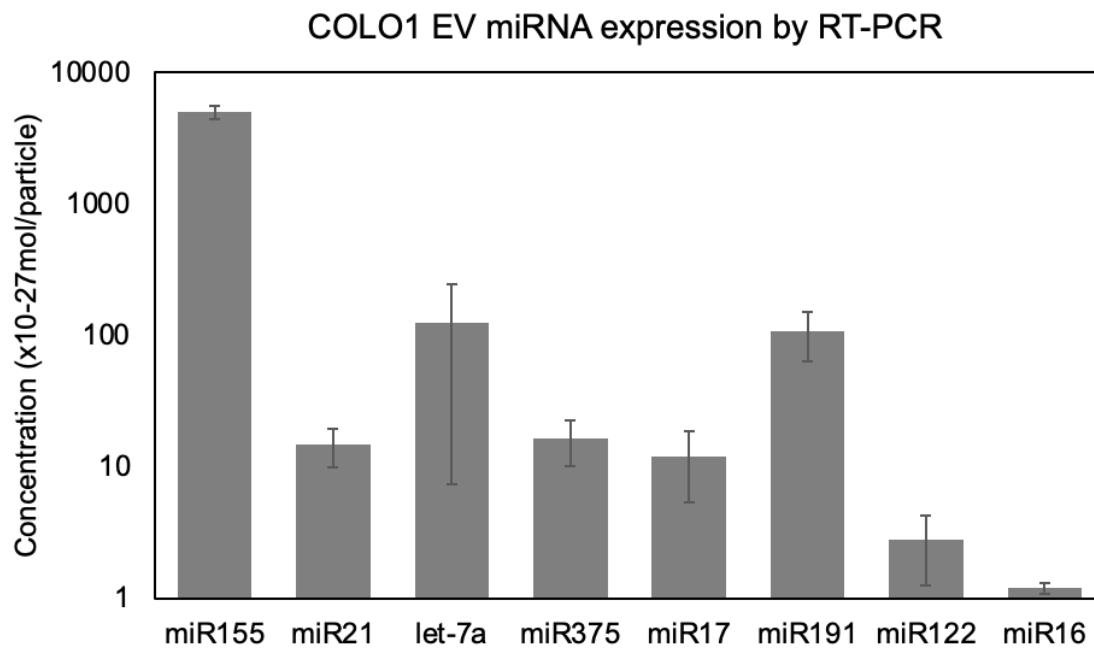
**Table 4.2 Target miRNA sequences used.**

Name	Sequences (5'-3')
miR-122	UGG AGU GUG ACA AUG GUG UUU G
miR-155	UU AAU GCU AAU CGU GAU AGG GGU
miR-21	UAG CUU AUC AGA CUG AUG UUG A
Let-7a	UGA GGU AGU AGG UUG UAU AGU U
miR-375	UUUGUUCGUUCGGCUCGCGUGA
miR-17	CAAAGUGCUUACAGUGCAGGUAG
miR-191	CAACGGAAUCCCAAAGCAGCUG
miR-16	UAGCAGCACGUAAAUAUUGGCG

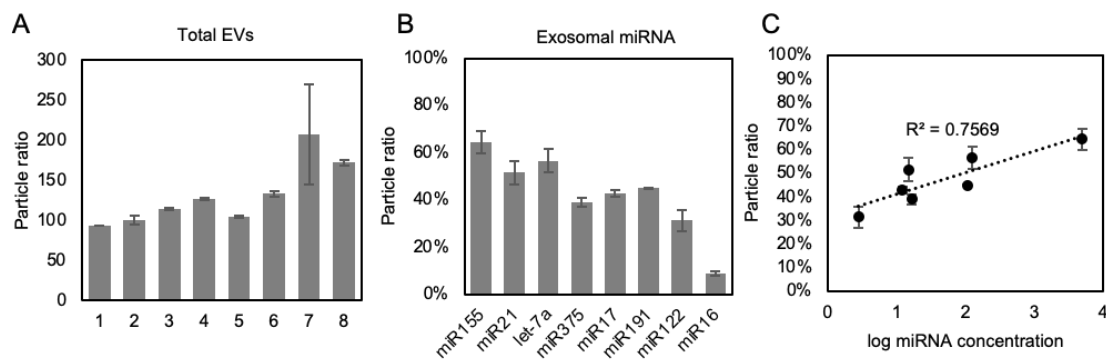
**Table 4.3 DNA sequences for hairpin probes used in our system.**

Name	Sequences (5'-3')
Hairpin for miR-122 (HP-122)	CAA ACA CCA TTG TCA CAC TCC AGT GTG TGA GTC TAG GAT TCG GCG TGT TAG CAT GGA GTG T
Hairpin for miR-155 (HP-155)	ACC CCT ATC ACG ATT AGC ATT AA G TCT CCC AGT CTA GGA TTC GGC GTG TTA GCA TTA ATG CTA A
Hairpin for miR-21 (HP-21)	TCA ACA TCA GTC TGA TAA GCT AGT GTG TGA GTC TAG GAT TCG GCG TGT TAG CAT AGC TTA TCA
Hairpin for let-7a(HP-let-7a)	AAC TAT ACA ACCTACTACTCA GT GTG TGA GTC TAG GAT TCG GCG TGT TAG CAT GAG GTA GT
Hairpin for miR-375 (HP-375)	TCA CGC GAG CCG AAC GAA CAA AGT GAG TGA GTC TAG GAT TCG GCG TGT TAG CAT TGT TCG
Hairpin for miR-17 (HP-17)	CTA CCT GCA CTG TAA GCA CTT TGG TGT GTG AGT CTA GGA TTC GGC GTG TTA GCA CAA AGT GC
Hairpin for miR-191 (HP-191)	CAG CTG CTT TTG GGA TTC CGT TGG TGT GTG AGT C TA GGA TTC GGC GTG TTA GCA CAA CGG AA
Hairpin for miR-16 (HP-16)	CGC CAA TAT TTA CGT GCT GCT A GT GTG TGA GTC TAG GAT TCG GCG TGT TAG CAT AGC AGC A

Underline sequences indicate complementary regions of the probes to form hairpin structure. Each hairpin includes a target miRNA recognition domain (red), and a trigger domain (blue) for growth of a long dsDNA via DNA hybridization cascade, connected by a hinge domain (grey).



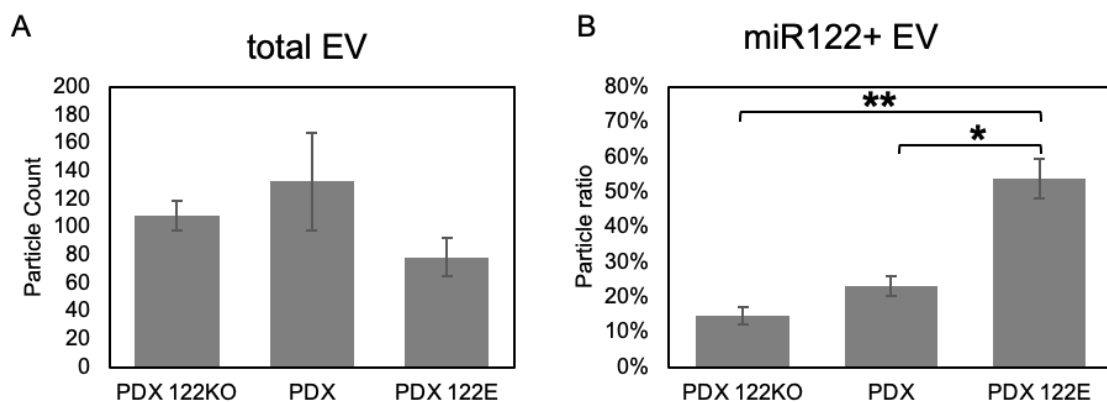
**Figure 4.28 Profiling of miRNA expression in EVs derived from COLO1 cell lines using RT-PCR.** All error bars represent the standard deviations from two repeated measurements.



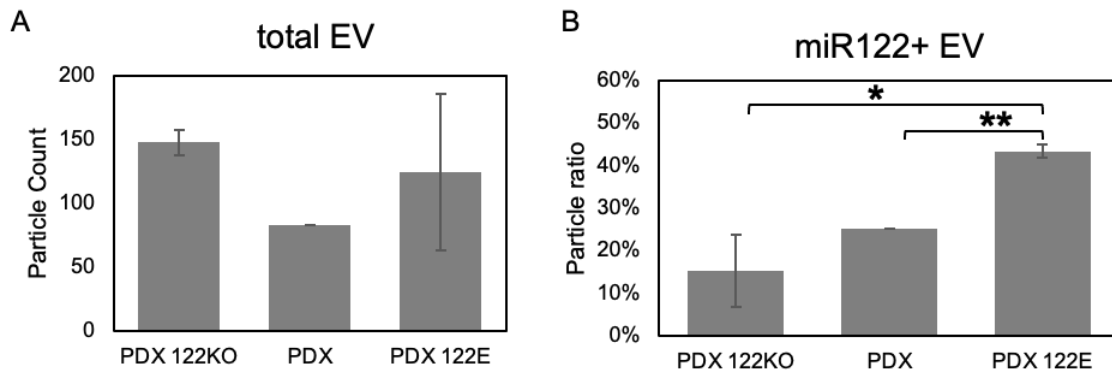
**Figure 4.29 Profiling of miRNA expression in EVs derived from COLO1 cell lines using our assay.** A) total EVs particle count. B) particle ratio for various Exosomal miRNA. C) correlation of particle ratio with log miRNA concentration. All error bars represent the standard deviations from two repeated measurements.



We then applied our assay to investigate the miR-122 expression level in EVs derived from PDX with various treatment: one with miR-122 knockdown (PDX 122 KO) and another with miR-122 overexpression (PDX 122E). Tetraspanin membrane protein, such as CD81, CD63 and CD9, are highly abundant on EV.<sup>35</sup> To capture all the EVs, we synthesized NSB carried with three kinds of antibodies targeting these three antigens. Therefore, the DiB labeled EV represented EV carried CD81, CD63 or CD9 (CD81<sup>+</sup>/CD63<sup>+</sup>/CD9<sup>+</sup> EVs).  $P_{DNF}/P_{DiB}$  ratio in PDX 122E was significantly higher than those in the normal PDX or PDX 122KO (Figure 4.30). In contrast, differentiation between PDX EVs with various treatment cannot be attained by the total counts of particles stained by DiB. Notably, when we used anti-CD24 antibody modified NSB to isolate EVs carried CD24 (CD24<sup>+</sup> EVs), and detected EVs carried both CD24 and miR-122, we observed a similar result (Figure 4.31). The  $P_{DNF}/P_{DiB}$  ratio in PDX 122E was significantly higher than those in the normal PDX or PDX 122KO. In contrast, differentiation between PDX EVs with various treatment cannot be attained by the total counts of particles stained by DiB.



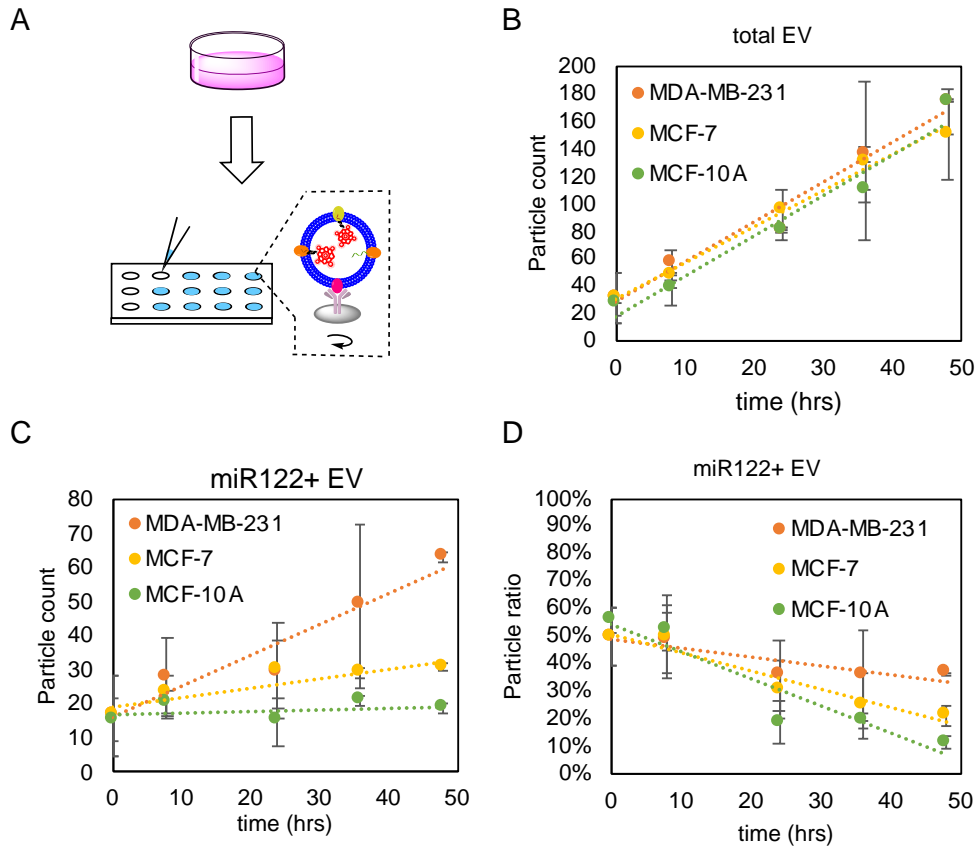
**Figure 4.30 Profiling of miR-122 expression in CD81<sup>+</sup>/CD63<sup>+</sup>/CD9<sup>+</sup> EVs derived from PDX cell lines with various treatment using our assay. A) total EVs particle count, and B) particle ratio for miR-122 in PDX EVs with various treatment. All error bars represent the standard deviations from two repeated measurements.**



**Figure 4.31 Profiling of miR-122 expression in CD24<sup>+</sup> EVs derived from PDX cell lines with various treatment using our assay.** A) total EVs particle count and B) particle ratio for miR-122 in PDX EVs with various treatment. All error bars represent the standard deviations from two repeated measurements.

Continuous monitoring the secretion of EV and enclosed miRNA expression in cell culture medium can provides vital insights for fundamental research and clinical applications.<sup>36</sup> However, the low EV concentration and limited amount of miRNA enclosed limit direct detection of EV miRNA. Our assay can isolate EV from cell culture medium using nano-stir bar and then detect EV miRNA with high sensitivity and high specificity, so it has a potential to monitor EV secretion in cell culture medium. To verify the ability of our assay to determine the miR-122-EV level secreted from breast cell lines, we analyzed the miR-122-EV levels in cell culture mediums from three breast cell lines (MDA-MB-231, MCF-7 and MCF-10A) using our assay every 12 hours. The EVs were captured directly using antibody modified NSB without any sample pretreatment. Our result showed that miR-122-EV level increased with time in the cell culture medium from MDA-MB-231, while remained steady in control cell lines (MCF-7 and MCF-10A, Figure 4.32). Our assay can significantly distinguished breast cancer cell line from normal breast

cell line by 36 hours cell culture. In contrast, total EV number increased with time for all three cell lines and the total EV number between various cell lines were almost the same.



**Figure 4.32 Profiling of time-based miR-122 expression in cell culture medium of three cell lines using our assay.** A) Schematic of miRNA detection in cell culture medium, B) total EVs particle count, C) particle count for miR-122, and D) particle ratio for miR-122 in different incubation times. All error bars represent the standard deviations from two repeated measurements.

#### 4.4. Conclusion

To summarize, we have developed a method to detect the miRNA cargos enclosed in individual EVs. This method employs nano-stir bars (NSB) for rapid EV capture and

isolation from biological fluids. They also permit confinement of miRNA cargos from the same EV onto the same NSB. In this way, DNA nanostructures can be constructed upon recognition of specific miRNA targets for analysis of the miRNA cargos carried by each EV. Again, EV differentiation by their cell of origin can be simply achieved by evaluating the exosomal miRNAs expression profiles among different EV samples. Moreover, our method can provide real-time monitoring of EV secretion and the enclosed miRNA cargos in cell culture medium, facilitating analysis of EV biogenesis and functions.

#### 4.5. Reference

---

- 1 S. Komatsu, J. Kiuchi, T. Imamura, D. Ichikawa, E. Otsuji, *J. Cancer Metastasis Treat.* **2018**, *4*, 36.
- 2 F. J. Nassar, G. Chamandi, M. A. Tfaily, N. K. Zgheib, R. Nasr, *Front. Med.* **2020**, *7*, 28.
- 3 Y. Toiyama, Y. Okugawa, J. Fleshman, C. R. Boland, A. Goel, *Biochim. Biophys. Acta* **2018**, *1870*, 274-282.
- 4 B. Zhou, K. Xu, X. Zheng, T. Chen, J. Wang, Y. Song, Y. Shao, S. Zheng, *Signal Transduct. Tar.* **2020**, *5*, 144.
- 5 R. Drula, L. F. Ott, I. Berindan-Neagoe, K. Pantel, G. A. Calin, *Cancers* **2020**, *12*, 2009.
- 6 G. Raposo, W. Stoorvogel, *J. Cell Biol.* **2013**, *200*, 373-383.
- 7 J. Lee, J. Choi, S. D. Chueng, T. Pongkulapa, L. Yang, H. Cho, J. Choi, K. Lee, *ACS Nano* **2019**, *13*, 8793-8803.
- 8 I. Krepelkova, T. Mrackova, J. Izakova, B. Dvorakova, L. Chalupova, R. Mikulik, O. Slaby, M. Bartos, V. Ruzicka, *Biotechniques* **2019**, *66*, 277-284.
- 9 T. Ouyang, S. Liu, Z. Han, Q. Ge, *Anal. Chem.* **2019**, *91*, 3179-3186.
- 10 E. A. Hunt, D. Broyles, T. Head, S. K. Deo, *Annu. Rev. of Anal. Chem.* **2015**, *8*, 217-237.
- 11 M. Kolanowska, A. Kubiak, K. Jazdzewski, A. Wójcicka, *miRNA Biogenesis* **2018**, *1823*, pp 87-101.
- 12 J. Zhao, C. Liu, Y. Li, Y. Ma, J. Deng, L. Li, J. Sun, *J. Am. Chem. Soc.* **2020**, *142*, 4996-5001.
- 13 L. Zhai, M. Li, W. Pan, Y. Chen, M. Li, J. Pang, L. Zheng, J. Chen, W. Duan, *ACS Appl. Mater. Interfaces* **2018**, *10*, 39478-39486.
- 14 W. Lu, Y. Chen, Z. Liu, W. Tang, Q. Feng, J. Sun, X. Jiang, *ACS Nano* **2016**, *10*, 6685-6692.

- 
- 15 S. Jiang, Q. Li, C. Wang, Y. Pang, Z. Sun, R. Xiao, *ACS Sens.* **2021**, *6*, 852-862.
  - 16 H. C. Yang, W. J. Rhee, *J. Clin. Mol.* **2021**, *10*, 319.
  - 17 J. H. Lee, J. A. Kim, M. H. Kwon, J. Y. Kang, W. J. Rhee, *Biomaterials* **2015**, *54*, 116-125.
  - 18 J. H. Lee, J. A. Kim, S. J. W. J. Rhee, *Biosens. Bioelectron.* **2016**, *86*, 202-210.
  - 19 J. Zhou, Z. Wu, J. Hu, D. Yang, X. Chen, Q. Wang, J. Liu, M. Dou, W. Peng, Y. Wu, W. Wang, C. Xie, M. Wang, Y. Song, H. Zeng, C. Bai, *Sci. Adv.* **2020**, *6*, eabc1204.
  - 20 Y. Yang, E. Kannisto, G. Yu, M. E. Reid, S. K. Patnaik, Y. Wu, *ACS Appl. Mater. Interfaces* **2018**, *10*, 43375-43386.
  - 21 X. Gao, S. Li, F. Ding, H. Fan, L. Shi, L. Zhu, J. Li, J. Feng, X. Zhu, C. Zhang, *Angew. Chem. Int. Ed.* **2019**, *58*, 8719-8723.
  - 22 X. Wang, J. Feng, H. Yu, Y. Jin, A. Davidson, Z. Li, Y. Yin, *Research* **2018**, *13*.
  - 23 M. Wang, L. He, W. Xu, X. Wang, Y. Yin, *Angew. Chem. Int. Ed.* **2015**, *54*, 7077-7081.
  - 24 Z. Li, J. Jin, F. Yang, N. Song, Y. Yin, *Nat. Commun.* **2020**, *11*, 2883.
  - 25 C. E. Yoo, G. Kim, M. Kim, D. Park, H. J. Kang, M. Lee, N. Huh, *Anal. Biochem.* **2012**, *431*, 96-8.
  - 26 D. W. Greening, R. Xu, H. Ji, B. J. Tauro, R. J. Simpson, *Methods Mol. Biol.* **2015**, *1295*, 179-209.
  - 27 J. Ko, E. Carpenter, D. Issadore, *Analyst.* **2016**, *141*, 450-460.
  - 28 R. A. Mathias, J. W. Lim, H. Ji, R. J. Simpson, *Methods Mol. Biol.* **2009**, *528*, 227-242.
  - 29 F. Momen-Heravi, L. Balaj, S. Alian, P. Mantel, A. E. Halleck, A. J. Trachtenberg, C. E. Soria, S. Oquin, C. M. Bonebreak, E. Saracoglu, J. Skog, W. P. Kuo, *Biol. Chem.* **2013**, *3894*, 1253-62.
  - 30 D. D. Taylor, S. Shah, *Methods* **2015**, *87*, 3-10.

- 
- 31 M. M. Ali, F. Li, Z. Zhang, K. Zhang, D. Kang, J. A. Ankrum, X. C. Le, W. Zhao, *Chem. Soc. Rev.* **2014**, *43*, 3324-3341.
- 32 J. Yao, K. Flack, L. Ding, W. Zhong, *Analyst* **2013**, *138*, 3121–3125.
- 33 Y. Jiang, M. Shi, Y. Liu, S. Wan, C. Cui, L. Zhang, W. Tan, *Angew. Chem.* **2017**, *56*, 11916–11920.
- 34 W. Yu, J. Li, C. Zuo, Y. Tao, S. Bai, J. Li, Z. Zhang, G. Xie, *Anal. Chim. Acta* **2019**, *1068*, 96-103.
- 35 G. Raposo, W. Stoorvogel, *J. Cell Biol.* **2013**, *200*, 373-383.
- 36 Y. Koi, Y. Tsutani, Y. Nishiyama, D. Ueda, Y. Ibuki, S. Sasada, T. Akita, N. Masumoto, T. Kadoya, Y. Yamamoto, R. Takahashi, J. Tanaka, M. Okada, H. Tahara, *Cancer Sci.* **2020**, *111*, 2104-2115.

## Chapter 5: Conclusion and Future Outlook

### 5.1 Conclusion

The focus of my research presented in this dissertation has been the development and optimization of methods for protein profiling and miRNA analysis of single EV. This includes the design and construction of DNA nanostructure using isothermal amplification methods, optimization of EV engineering using DNA nanostructures, and novel detection strategies.

In Chapter 2, a single-EV FCA technique to visualize individual EV in a conventional flow cytometer is presented. We designed a conformation-switchable probe to recognize exosomal membrane proteins. After recognition, the probe would trigger the hybridization chain reaction and produce a long double-strand DNA for EV engineering. We optimized reaction conditions and successfully applied them to detect individual EV using conventional flow cytometer. Our system can be easily adjusted to target different surface biomarkers by simply switching the aptamer sequence in the conformation-switchable DNA probe. We also achieved simultaneous recognition of dual surface markers on the same vesicle for EV differentiation among heterogeneous mixture.

In Chapter 3, a calibration-free technique to profile the surface protein contents on individual EVs is presented. We conjugated different affinity probes, such as aptamers, antibodies, and ligands, to recognize diverse targets located on the membrane of the EV. We designed and constructed DNA nanoflowers using rolling circle amplification, which not only enables single EV visualization by the diffraction-limited microscopes, but also greatly improves the sensitivity of EV detection. We optimized reaction conditions and



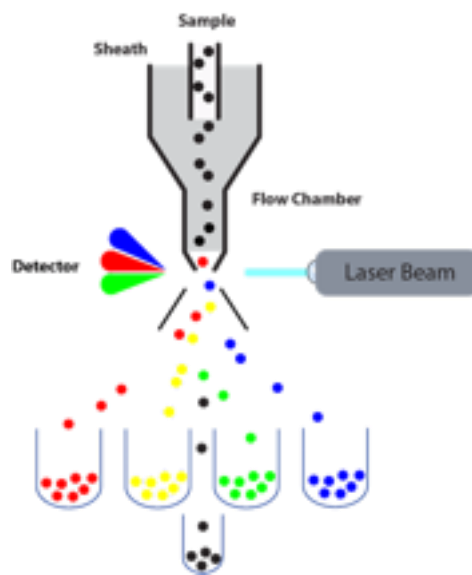
successfully applied them to profile exosomal protein expression in serum without sample pre-concentration. We also applied our method for co-localization of multiple markers on the same EV to improve EV differentiation.

In Chapter 4, an NSB-DNF technique for exosomal miRNA *in situ* detection is presented. We synthesized antibody functionalized nano-stir bar for EV isolation, which not only can capture one EV each time to achieve single EV analysis, but also can facilitate reactions using stirring function. After immunocapture and isolation, the EVs were treated with PFA and EDC to crosslink miRNA to exosomal proteins for *in situ* miRNA detection. We designed a hairpin probe to recognize target miRNAs. After recognition, the probe would trigger the rolling circle amplification and produce a DNA nanoflower for miRNA detection. The DNA nanoflower would bind to multiple dye to amplify signal, enabling exosomal miRNA *in situ* detection under confocal fluorescence microscopy (CFM). We optimized reaction conditions and successfully applied them to profile exosomal miRNA expression. We also applied our method for real-time monitoring of miRNA expression in cell culture medium.

## **5.2 Future Outlook**

In terms of future work, the single-EV FCA technique developed in Chapter 2 can be applied to target different surface biomarkers. Therefore, we can expand the target scopes and apply the single-EV FCA technique to detect more target proteins, such as EGFR,<sup>1</sup> EpCAM,<sup>2</sup> MUC1<sup>3</sup> and CD44.<sup>4</sup> All of them are promising cancer markers. Profiling of multiple surface markers can help gain in-depth insights into the molecular signatures of EV. This single-EV technique also can colocalize dual surface markers on the same

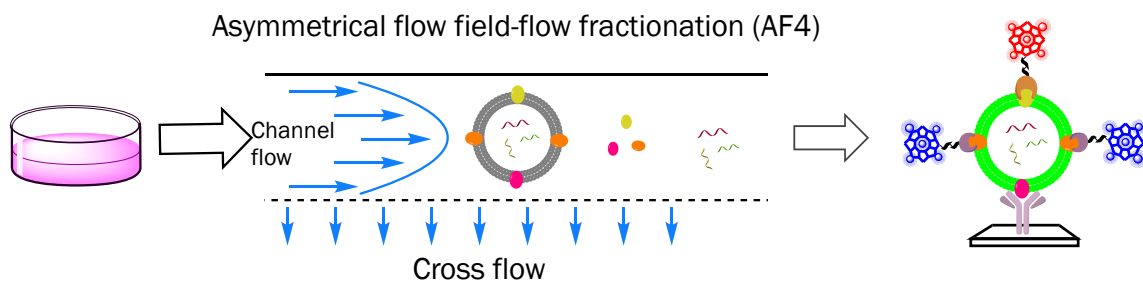
vesicle, so we can colocalize two surface markers of EV derived from various cell types. As a result, we would obtain flow plot with characteristic distribution pattern for each cell type. Based on their characteristic distribution patterns, we can differentiate them directly from the cell fluids, which can help better understanding the functions and secretion mechanism of EV. FCA can sort and collect cells based on surface marker profiles, so we can apply it to sort and collect EV under typical clinical lab settings (Figure 5.1). After collecting the EV with specific surface markers, we can further analyze the content of lipid and nucleic acid, which benefit clear correlation between EV composition and their biogenesis and functions.



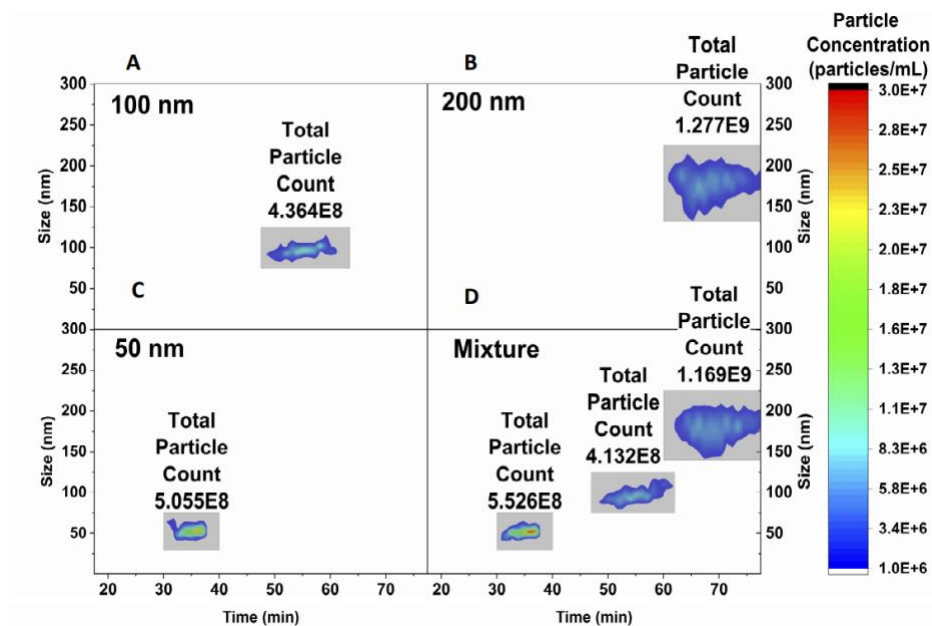
**Figure 5.1 FCA sort and collect cell based on surface marker profiles.** Figure reprinted from Ref.5.

The DNF-based protein microarray developed in Chapter 3 can profile multiple surface markers of EVs. We can couple it to asymmetrical flow field flow fractionation (AF4) and nanoparticle tracking analysis (NTA) to obtain more information of pure EV

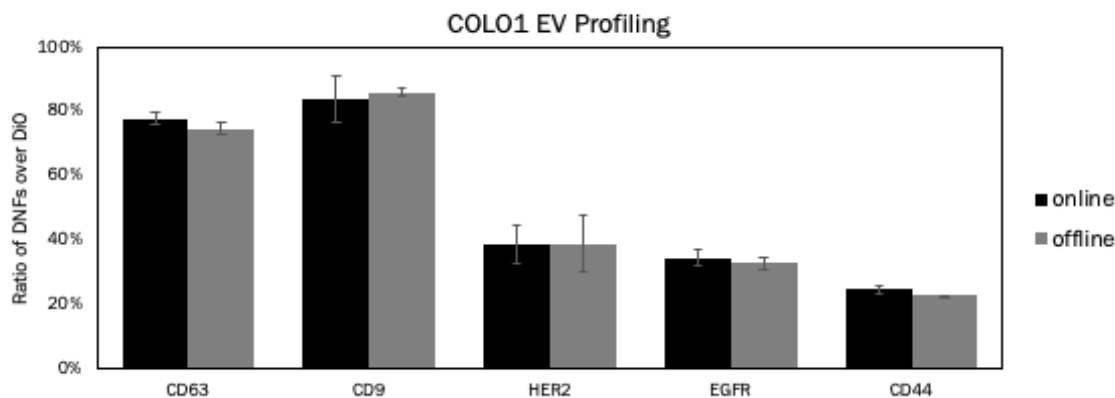
characterization (Figure 5.2). AF4 is a powerful technique to purify EVs. AF4 combines filtration with size-based separations. In this way, AF4 can separate nanomaterials with sizes ranging from nanometers to micrometers. Figure 5.3 showed that AF4 can separate 50, 100, and 200 nm polystyrene particles from the mixture.<sup>6</sup> No difference was found between the plots from injections of the mixed and single particle samples. These results support that our AF4 system can separate particles based on particle size. What's more, the EV purified from AF4 showed a similar protein profiling as the standard EV (Figure 5.3), proving that AF4 does not damage the vesicle and change the molecular contents. Therefore, we can use AF4 to isolate EV from cell culture medium or serum. AF4 would generate multiple eluted samples, so we can measure the surface markers of various elution. NTA can size and count nanoparticles down to ~ 30nm, so we can use NTA to measure the particle size and concentration of the eluted EV from AF4. By coupling AF4 and NTA with DNF-based protein assay (AF4/NTA/DNF), we can purify EV from biological fluid, size and count the purified EV, as well as immuno-profile their protein content. We can stimulate cell with nanoparticles or drug to alter EV secretion, and study the change of their particle concentration, size and protein content by this AF4/NTA/DNF technique.



**Figure 5.2 Schematic of AF4-NTA coupling immunoassay.**

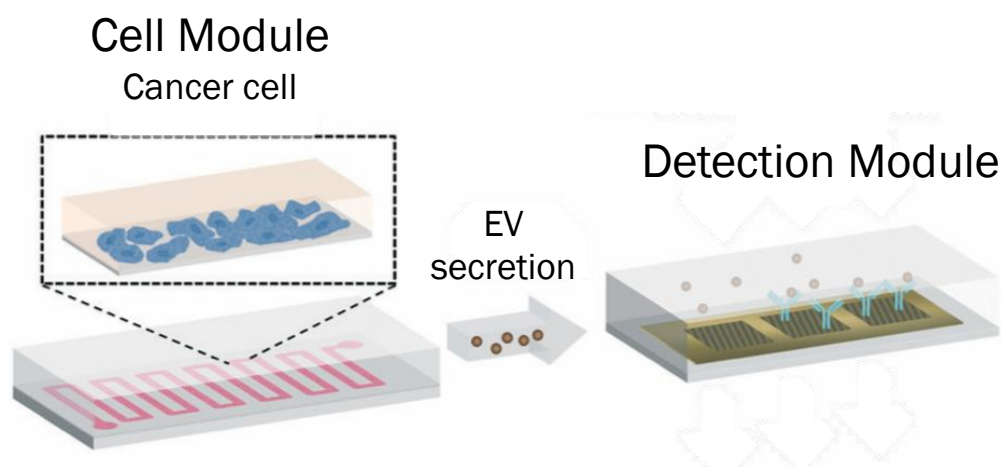


**Figure 5.3 Contour plots showing the single populations and mixed population injections.** Quantification is taken as the volume under the curve. The gray box highlights the quantification region for each peak. For total quantification, the peak area was multiplied by the detector volumetric flowrate (0.5 mL/min) to obtain total particle count. Figure reprinted from Ref.6. © 2020, American Chemical Society.



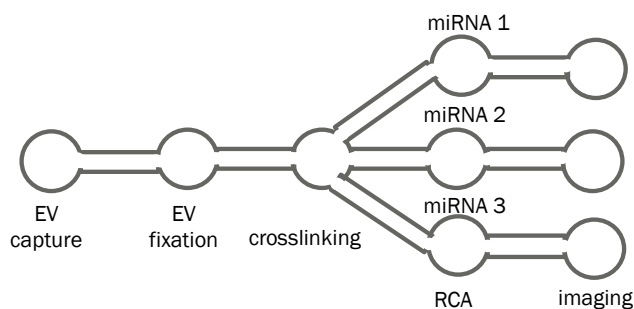
**Figure 5.4 Protein profiling of EV derived from COLO1 cell lines before and after AF4 separation.**

Another way to apply this DNF-based protein array would be design a microfluidic-integrated biosensor for real-time analysis of live cell secretion (Figure 5.5). This microfluidic-integrated biosensor would contain two microfluidic modules: the cell culture module and the protein detection module. The cell would grow in the cell culture module, in which the inlet tubing would introduce fresh culture media and the outlet tubing would deliver the old cell culture media into the protein detection module. For the protein detection module, antibodies would be immobilized on the array to capture the biomarkers secreted by the cancer cells, and the DNF decoration would enable the detection of biomarkers. By tracing the detectable particle count continuously, we can monitor the dynamic of cell secretion. Taking advantage of the multiplexing capability of this microfluidic-integrated biosensor, we can simultaneously analyze various protein content from different cell types by using multiple cell culture modules and protein detection modules.



**Figure 5.5 Schematic of a microfluidic-integrated biosensor for real-time analysis of live cell secretion.** Figure reprinted from Ref.7. © 2001, Royal Society of Chemistry.

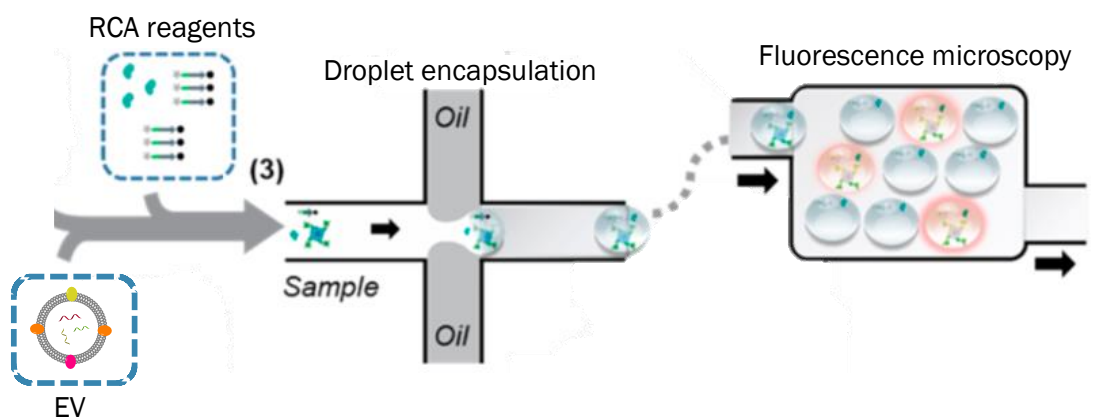
The NSB-DNF technique developed in Chapter 4 can be conducted in a microfluidic device for automation (Figure 5.6). The microfluidic device would be composed with five open wells and four closed channels. The first well would be sample capture, in which NSB would stir with EV samples for EV isolation. After 30 min incubation, the NSB would be moved to next well using magnetic field through the closed channel. In the second well, the captured EV would be treated with PFA for EV fixation. After that, the captured EV would be moved to next well for EDC crosslinking. After crosslinking, the EV would be moved to next well for RCA amplification. After RCA, the EV would be moved to the last well for detection. The microfluidic device can improve sample work-flow and reduce sample consumption. We can design a microfluidic device with multiple channels, which we can achieve multiple sample analysis simultaneously.



**Figure 5.6 Schematic of microfluidic device for automation.**

Another way to achieve exosomal miRNA detection would be develop a droplet microfluidic platform to encapsulate individual EVs into droplets that contain RCA reagent (Figure 5.7). We could fabricate a microfluidic device for droplet generation. This microfluidic device has two inlets, one inlet connects with a syringe contained reaction reagent, another connects with a syringe contained oil. By controlling the concentration of

EV and fluid rate of two syringes, individual EV can be encapsulated into droplets for single EV analysis. After generation of droplet contained single EV, RCA can be triggered in the presence of the target miRNA and product signal for detection. Generating microdroplets using oil-aqueous system enhance mixing and reaction rates.



**Figure 5.7 Schematic of droplet microfluidic platform.** Figure reprinted from Ref.8. © 2020, American Chemical Society.

### 5.3 Reference

---

- 1 B. R. Voldborg, L. Damstrup, M. Spang-Thomsen, H. S. Poulsen, *Ann. Oncol.* **1997**, *8*, 1197–1206.
- 2 M. Trzpis, P. M. J. McLaughlin, L. M. F. H. de Leij, M. C. Harmsen, *Am. J. Pathol.* **2007**, *171*, 386-395.
- 3 T. M. Horm, J. A. Schroeder, *Cell Adh. Migr.* **2013**, *7*, 187-198.
- 4 C. Chen, S. Zhao, A. Karnad, J. W. Freeman, *J. Hematol. Oncol.* **2018**, *11*, 64.
- 5 NIA IRP Flow Cytometry Unit. <https://www.irp.nia.nih.gov/branches/lmg/fcl/new-index.htm>.
- 6 G. B. Adkins, E. Sun, R. Coreas, W. Zhong, *Anal. Chem.* **2020**, *92*, 7071-7078.
- 7 X. Li, M. Soler, C. I. Özdemir, A. Belushkin, F. Yesilköy, H. Altug, *Lab Chip* **2017**, *17*, 2208-2217.
- 8 X. Yang, W. Liu, D. C. Chan, S. U. Ahmed, H. Wang, Z. Wang, C. R. Nemr, S. O. Kelley, *J. Am. Chem. Soc.* **2020**, *142*, 14805-14809.